AFRL-RY-WP-TR-2011-1197

CHAINS OF METAMATERIALS FOR GUIDING AND ANTENNA APPLICATIONS

Andrea Alu

The University of Texas at Austin

APRIL 2011
Final Report

AIR FORCE RESEARCH LABORATORY
SENSORS DIRECTORATE
WRIGHT-PATTERSON AIR FORCE BASE, OH 45433-7320
AIR FORCE MATERIEL COMMAND
UNITED STATES AIR FORCE

NOTICE AND SIGNATURE PAGE

AFRL-RY-WP-TR-2011-1197 HAS BEEN REVIEWED AND IS APPROVED FOR PUBLICATION IN ACCORDANCE WITH ASSIGNED DISTRIBUTION STATEMENT.

*//Signature// | //Signature//

DAVID D. CURTIS for ROBERT SHORE
Work Unit Manager, RYHA
Antenna Technology Branch
Electromagnetics Technology Division

DAVID D. CURTIS
Branch Chief, RYHA
Antenna Technology Branch
Electromagnetics Technology Division

*//Signature//

WILLIAM E. MOORE
Division Chief, RYH
Electromagnetics Technology Division

REPORT DOCUMENTATION PAGE			*Form Approved* *OMB No. 0704-0188*

The public reporting burden for this collection of information is estimated to average 1 hour per response, including the time for reviewing instructions, searching existing data sources, gathering and maintaining the data needed, and completing and reviewing the collection of information. Send comments regarding this burden estimate or any other aspect of this collection of information, including suggestions for reducing this burden, to Department of Defense, Washington Headquarters Services, Directorate for Information Operations and Reports (0704-0188), 1215 Jefferson Davis Highway, Suite 1204, Arlington, VA 22202-4302. Respondents should be aware that notwithstanding any other provision of law, no person shall be subject to any penalty for failing to comply with a collection of information if it does not display a currently valid OMB control number. **PLEASE DO NOT RETURN YOUR FORM TO THE ABOVE ADDRESS**.

1. REPORT DATE *(DD-MM-YY)* April 2011	2. REPORT TYPE Final	3. DATES COVERED *(From - To)* 21 September 2009 – 31 March 2011	

4. TITLE AND SUBTITLE CHAINS OF METAMATERIALS FOR GUIDING AND ANTENNA APPLICATIONS	5a. CONTRACT NUMBER FA8718-09-C-0061
	5b. GRANT NUMBER
	5c. PROGRAM ELEMENT NUMBER 62204F
6. AUTHOR(S) Andrea Alu	5d. PROJECT NUMBER 4916
	5e. TASK NUMBER HA
	5f. WORK UNIT NUMBER 4916HACR

7. PERFORMING ORGANIZATION NAME(S) AND ADDRESS(ES) The University of Texas at Austin Department of Electrical and Computer Engineering 1 University Station C0803 Austin, TX 78712	8. PERFORMING ORGANIZATION REPORT NUMBER

9. SPONSORING/MONITORING AGENCY NAME(S) AND ADDRESS(ES) Air Force Research Laboratory Sensors Directorate Wright-Patterson Air Force Base, OH 45433-7320 Air Force Materiel Command United States Air Force	10. SPONSORING/MONITORING AGENCY ACRONYM(S) AFRL/RYHA
	11. SPONSORING/MONITORING AGENCY REPORT NUMBER(S) AFRL-RY-WP-TR-2011-1197

12. DISTRIBUTION/AVAILABILITY STATEMENT
Approved for public release; distribution unlimited.

13. SUPPLEMENTARY NOTES
This report is the result of fundamental research authored by university. As such, the material does not require Public Affairs (PA) Office security and policy review prior to releasing the information to the public.

This report contains color.

14. ABSTRACT
Final report contains results produced within the effort sponsored by the U.S. Air Force Research Laboratory with Contract No. FA8718-09-C-0061. Focus was on the most relevant aspects of our findings, which was fully addressed during the effort: guided propagation and leaky-wave radiation along linear arrays of nanoparticles, also considering and modeling the realistic presence of technological disorder, comparison of the guidance properties along linear and planar arrays of nanoparticles and nanovoids in different realistic geometries, guided and leaky modes along parallel arrays of nanoparticles, propagation along periodic arrays of nanoparticles and their rigorous homogenization as metamaterials for a variety of applications of interest to the U.S. Air Force.

15. SUBJECT TERMS
Nanoparticles, metamaterial resonators, guided modes, periodic arrays, nanoantennas, leaky-wave antennas, optical waveguides

16. SECURITY CLASSIFICATION OF:			17. LIMITATION OF ABSTRACT:	18. NUMBER OF PAGES	19a. NAME OF RESPONSIBLE PERSON (Monitor)
a. REPORT Unclassified	b. ABSTRACT Unclassified	c. THIS PAGE Unclassified	SAR	130	David D. Curtis
					19b. TELEPHONE NUMBER *(Include Area Code)* N/A

Standard Form 298 (Rev. 8-98)
Prescribed by ANSI Std. Z39-18

Table of Contents

Abstract We report the main results produced within the effort sponsored by the U.S. Air Force Research Laboratory with Contract No. FA8718-09-C-0061. We focus on the most relevant aspects of our findings, which we have fully addressed during our effort: guided propagation and leaky-wave radiation along linear arrays of nanoparticles, also considering and modeling the realistic presence of technological disorder, comparison of the guidance properties along linear and planar arrays of nanoparticles and nanovoids in different realistic geometries, guided and leaky modes along parallel arrays of nanoparticles, propagation along periodic arrays of nanoparticles and their rigorous homogenization as metamaterials for a variety of applications of interest to the U.S. Air Force.

1. Executive Summary

In the present effort we have explored a variety of theoretical and numerical problems associated with wave propagation and radiation along periodic arrays of nanoparticles. Our extensive efforts have tackled several relevant problems in the following areas: (a) leaky- and guided modes along isolated and coupled arrays of metamaterial resonators and plasmonic nanoparticles; (b) quantification of the effect of degree of disorder in the propagation along linear arrays; (c) propagation along planar arrays of nanoparticles and voids in plasmonic substrates, and comparisons among different solutions for nanoscale light propagation and radiation; (d) rigorous modeling of the propagation along 3-D arrays of nanoparticles and their proper homogenization models. These results may have a variety of important applications of interest to the U.S. Air Force, in particular in the realization and design of sub-wavelength compact optical waveguides with optimized field confinement and propagation length, nanoantenna and leaky-wave radiation applications with optimized directivity, control of propagation and scattering from nanoscale structures and design of metamaterials with unconventional wave interaction. We have analyzed several geometries and designs with a variety of analytical and numerical methods, including full-wave numerical techniques, modeling in details the properties of the arrays in terms of frequency and spatial dispersion and of radiation and Ohmic losses. During this effort, we have developed novel analytical, theoretical and numerical tools for a thorough understanding of the propagation and radiation properties of arrays of nanoresonators in various frequency regimes of operation, even in the presence of realistic disorder. Our efforts have been successful not only from the research perspective, but we have also involved a few students and one postdoctoral researcher within this exciting project. In the following, we review some of the most relevant findings obtained in this work, as outlined in recent publications referred at the end of this report. Each section will contain one of the topics developed in the framework of this project and the main results obtained in this framework. The interested reader is referred to the series of publications that have been produced during this effort, which are reported in Section 9 of this report.

2. Methods, Assumptions and Procedures

In this effort we have used a variety of analytical techniques, including periodic Green's functions and analytical continuation in the complex domain, as well as numerical techniques, including finite-integration technique and finite-time-domain simulations. We detail more of our numerical approaches and efforts in the following sections, specifying their relevance in each part of our effort. We assume in the following sections an $e^{-i\omega t}$ time dependence for the electromagnetic fields, unless otherwise noted.

3. Propagation Along Linear Arrays of Nanoparticles: Effect of Disorder
a. Summary
Metallic nanoparticles are known to possess several exciting properties when interacting with light. Linear arrays of plasmonic nanoparticles, in particular, can support optical beam propagation with ultra-confined lateral cross-section (possibly much smaller than the free-space

1

wavelength of interest), surpassing by far the transverse size of regular optical fibers. Although in theory these waveguides may support relatively long propagation, in practical scenarios short propagation lengths have been measured. Absorption in plasmonic materials indeed plays a relevant role in this regard, but fabrication disorder has been also suspected to severely affect the overall propagation length.

During this effort, we have been able to quantify in a simple analytical expression the role of small imperfections in linear arrays of plasmonic nanoparticles, showing that the dominant effect of random Gaussian disorder on the propagation properties of these arrays is equivalent to an additional loss term in the metal. The total measured loss may therefore be associated with material absorption and to an additional factor that is directly proportional to the disorder variance and function of the phase velocity of the guided mode. Our results may not only affect the understanding of plasmonic nanoscale waveguides and quantify the role of technological disorder in optical communications, but they may also be extended to other periodic optical devices of interest, like photonic crystals and metamaterials, whose performance are often limited by inherent fabrication imperfections. Analogous concepts may be able to quantify their effect in various practical designs of interest.

b. Introduction

Exploring the science and applications of photonic crystals and metamaterials formed by periodic collections of inclusions has rapidly grown in interest and importance in recent years (see e.g., [1]). With a few exceptions (see, e.g., [2]-[7]), however, in majority of the theoretical contributions on this subject the role of disorders and imperfections due to inherent fabrication limitations are neglected, while, at the present state of the art, experimental efforts in metamaterial realization and measurement inevitably involve such problems. The sub-wavelength scale in which the constituent inclusions of a metamaterial are typically embedded in a host medium usually allows a homogenization procedure, suggesting that the intrinsic deviation from an ideal periodic arrangement may not play a fundamental role in the metamaterial performance. This disorder, however, should be taken into account for a complete and rigorous analysis of the metamaterial response, which may describe more closely the experimental conditions. A clear example of such limitations is seen when dealing with periodic lattices of inclusions and metamaterials: it is well known that an infinite periodic arrangement of lossless inclusions cancels out the scattering losses from each individual particle, ensuring a completely lossless bulk metamaterial [8], but the measured losses in metamaterials, manifested in the imaginary parts of extracted permittivity and permeability, are often higher than expected from purely theoretical considerations. The role of fabrication imperfections and random disorders enters directly into play in this scenario, generating incoherent superposition of scattered waves from the different inclusions, which results in energy decay for a wave traveling through the metamaterial sample. This energy "loss" has been often interpreted in the measurements as energy absorbed in the bulk sample, even though it is actually related mostly to incoherent scattering, rather than material absorption.

A different, but related problem that we have recently analyzed is represented by the analytical solutions for the eigenmodes supported by 1-D or 3-D periodic lattices of closely-packed plasmonic nanoparticles [9]-[10], which may support highly-confined guided modes and backward-wave propagation, with various potential applications for negative-index materials and laterally-confined waveguides. Also in this case, the chain periodicity allows total cancellation of

2

the scattering losses, supporting the propagation of low-loss eigenmodes (with loss only due to the material absorption in the particles). However, disorder is inherently associated with the realization of these chains: techniques for manufacturing large arrays of nanoparticles are currently available, but while they can ensure a good control on the average dimension of the particles, it may be more challenging to ensure a perfect alignment and positioning of each of them on a large scale. Since the assumption of ideally periodic arrangement of the particles has provided us with closed-form solutions for the propagation of such modes [9]-[10], which may also easily take into account the presence of Ohmic absorption, we may ask whether an extension of these analytical results may also model the intrinsic disorder expected in the fabrication process. More broadly, this may be applied to the general analysis of metamaterials, in order to quantitatively model how the deviation from ideal periodic arrangements of the inclusions may affect their potential application in realistic setups and devices.

In this section, we explore these concepts and in particular we study how the presence of disorder may be modeled in simple geometries like periodically arranged nanoparticles. In particular, we show how such disorder effects, when small enough, may be equivalently described as the effect of an additional "loss" in the materials forming the particles, directly related to the statistical variance of the disorder in the system, and may characterize both quantitatively and qualitatively the effects of imperfections in the realization of these metamaterials. These results may be further generalized to generic metamaterial lattices, providing relevant physical insights into the analysis of metamaterials for a practical realization.

It should be pointed out that other groups have recently analyzed the problem of disorders in metamaterials, both from theoretical and experimental points of view (see e.g., [2]-[5]), showing how these effects, although of second-order, may be relevant in some applications and how they are sometimes underestimated. An extensive amount of work, somehow related to these concepts, is also available for random disorder in photonic crystals and Anderson localization in random materials [11]-[16]. Here we concentrate on the problem of periodic arrays of plasmonic nanoparticles in order to derive a quantitative expression that may model this small disorder in closed form, with a first-order perturbation approach. Different from the other approaches presented in the literature relative to this problem, our analytical results allow us to theoretically quantify and model the small disorder in order to provide simple physical analogies and insights that could be later applied to metamaterial technology. A preliminary portion of these results has been presented in a recent conference talk [7] and these results have been recently published in

c. *Theoretical analysis*

Consider an infinite linear array of identical particles each characterized by an electric polarizability α_{ee} and periodically displaced along the z axis at distance d from each other (center-to-center distance). As shown in various recent papers on the problem [17]-[23], the guided eigenmodes supported by this periodic arrangement propagate along the array with an $e^{i\beta z}$ dependence, where β satisfies the following equations:

$$L: 6\sum_{N=1}^{\infty}\left[N^{-3}\overline{d}^{-3}\cos\left(N\overline{\beta}\overline{d}\right)e^{iN\overline{d}}\left(1-iN\overline{d}\right)\right] = \overline{\alpha}_{ee}^{-1}$$

$$T: -3\sum_{N=1}^{\infty}\left[N^{-3}\overline{d}^{-3}\cos\left(N\overline{\beta}\overline{d}\right)e^{iN\overline{d}}\left(1-iN\overline{d}-N^2\overline{d}^2\right)\right] = \overline{\alpha}_{ee}^{-1}$$

$$(1)$$

3

where $\bar{d} \equiv k_0 d$, $\bar{\beta} \equiv \beta / k_0$, $\bar{\alpha}_{ee} \equiv k_0^3 \alpha_{ee} / (6 \pi \varepsilon_0)$, $k_0 \equiv \omega \sqrt{\varepsilon_0 \mu_0}$, and ε_0, μ_0 are the background medium's permittivity and permeability, respectively. In Eq. (1) the nanoparticles forming the array are modeled as polarizable dipoles. The two equations refer to the two orthogonal polarizations for the eigenmodes of this system, i.e., respectively, longitudinal (Fig. 1a) and transverse (Fig. 1b) with respect to the axis of propagation [9].

Eq. (1) supports the possibility of no-damping sub-diffractive guided propagation in the limit of lossless plasmonic particles, since, as expected, the mathematical problem represented by (1) ensures a real-valued solution for any $1 < \beta < \pi / d$ under the lossless condition $\mathrm{Im}\left[\bar{\alpha}_{ee}^{-1}\right] = -1$ [9]. Therefore, similar to any periodic metamaterial, this geometry in the ideally periodic limit also ensures that, despite the scattering losses from each one of the nanoparticles, the overall behavior of the chain may have zero radiation losses.

The previous equations may fully take into account the general case in which the particles forming the array are lossy. In such case, complex solutions for β are required, with a corresponding decay in the direction of propagation. The summations in (1) are not strictly convergent in this situation [19], and an analytical continuation employing polylogarithm functions is required, obtaining the closed-form dispersion equations first introduced in [9]:

$$L : 3\bar{d}^{-3}\left[f_3\left(\bar{\beta},\bar{d}\right) - i\bar{d}\ f_2\left(\bar{\beta},\bar{d}\right) \right] = \bar{\alpha}_{ee}^{-1}$$
$$T : -\frac{3}{2}\bar{d}^{-3}\left[f_3\left(\bar{\beta},\bar{d}\right) - i\bar{d}\ f_2\left(\bar{\beta},\bar{d}\right) - \bar{d}^2 f_1\left(\bar{\beta},\bar{d}\right) \right] = \bar{\alpha}_{ee}^{-1} \qquad (2)$$

where $\quad f_N\left(\bar{\beta},\bar{d}\right) = Li_N\left(e^{i(\bar{\beta}+1)\bar{d}}\right) + Li_N\left(e^{-i(\bar{\beta}-1)\bar{d}}\right) \quad$ and $\quad Li_N\left(x\right) = \int_0^x \dfrac{Li_{N-1}(t)}{t}dt$, with

$Li_1\left(x\right) = -\ln\left(1-x\right)$ is the polylogarithm function, as defined in [24].

Let us suppose now that each of the particles in the linear array is not necessarily positioned at the designated location $z_N = N \cdot d$, but slightly shifted as $z_N = Nd + \delta_N$, where the set of real numbers $\delta_N \ll d$ represents quantitatively an imperfection or disorder in their position (see Fig. 1). Analogously, intrinsic fabrication limitations may generate uncontrollable small differences among the particles, and each of the polarizabilities involved in the summations (1) may be rewritten as $\alpha_N = \alpha_{ee}\left(1 + \varphi_N\right)$, with φ_N being a set of complex numbers.
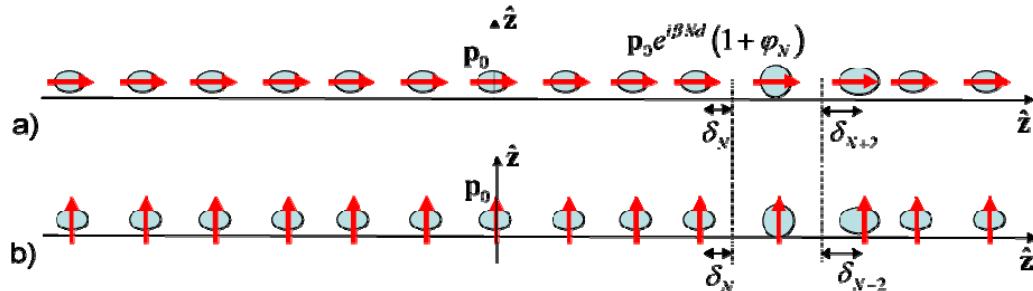
Figure 1 – Geometry of the propagation along 1-D linear chains of particles under the two orthogonal polarizations [(a) longitudinal, (b) transverse], considering random imperfections/disorders in the positioning of the particles.

In order to model the presence of disorder in this problem, we may assume that these imperfections are inherently random in nature and provide small perturbations from the ideal

4

design values. Under these assumptions, it may be reasonably expected that such quasi-periodic system may still be able to guide a mode with $e^{i\beta z}$ space dependence, where the disorder is anticipated to produce an analogously small perturbation in the guided wave number β. Here we aim to quantify this variation, and relate it to the expected degree of disorder.

The dispersion equations (1) have been obtained for the two polarizations in the ideally-periodic geometry by assuming that the induced dipole moments along the chain are in the form $\mathbf{p}_N = \mathbf{p}_0 e^{i\beta N d}$, with N being any integer (positive or negative) and $\mathbf{p}_0$ being the dipole moment induced on the particle located at the origin. Each $\mathbf{p}_N$ produces an electric field at the origin, with amplitude $\mathbf{E}_N = \underline{\mathbf{G}}(Nd) \cdot \mathbf{p}_N$, where $\underline{\mathbf{G}}(Nd)$ is the dipolar dyadic Green function. Imposing that the sum of the $\mathbf{E}_N$ would give rise to a total electric field at the origin self-sustaining a dipole moment $\mathbf{p}_0$ provides the dispersion equations (1)-(2), which may be solved for the guided wave number β once the array geometry is known. The presence of small disorder in the position of the particles has a perturbative effect to the original dispersion equation, which may be analyzed under a first-order approximation as the perturbation to the self-sustaining field at the location of $\mathbf{p}_0$. In this sense, the small disorder affects the evaluation of the dispersion equations in two distinct ways: the Green function is modified into $\underline{\mathbf{G}}(Nd + \delta_N)$, due to the variation of the distance of each of the particle from the origin, which causes an estimated variation in the induced field on the particle; moreover, the value of each of the dipole moments in the chain is also varied as $\mathbf{p}_N = \mathbf{p}_0 e^{i\beta(Nd + \delta_N)}$ by the variation in the particle position. The variation in the shape or electromagnetic properties of the particles may also be embedded in the estimation of the induced dipole moment of each particle, which corresponds quantitatively to the expression $\mathbf{p}_N = (1 + \varphi_N) \mathbf{p}_0 e^{i\beta(Nd + \delta_N)}$. Summing all these effects, each term in the summations in (1), therefore, takes the form:

$$
\begin{aligned}
L &: \left(\left|N\right|\overline{d} + \delta_N\right)^{-3} e^{i\overline{\beta}\left(N\overline{d} + \delta_N\right)} e^{i\left(\left|N\right|\overline{d} + \delta_N\right)} \left(1 - i\left|N\right|\overline{d} - i\delta_N\right)\left(1 + \varphi_N\right) \\
T &: \left(\left|N\right|\overline{d} + \delta_N\right)^{-3} e^{i\overline{\beta}\left(N\overline{d} + \delta_N\right)} e^{i\left(\left|N\right|\overline{d} + \delta_N\right)} \left(1 - i\left(\left|N\right|\overline{d} + \delta_N\right) - \left(\left|N\right|\overline{d} + \delta_N\right)^2\right)\left(1 + \varphi_N\right)
\end{aligned}
\tag{3}
$$

where N goes from $-\infty$ to ∞ and it takes into account of the contribution from each of the particles in the chain. In this modified form, the sums in the dispersion relations cannot be evaluated in any closed form, since each of their terms depend separately on random occurrences of δ_N and φ_N.

Rearranging the terms in the summation and expanding in Taylor series for δ_N, owing to the assumption of small disorder, we may formally rewrite the dispersion relations as in Eq. (2):

$$
\begin{aligned}
L &: 3\overline{d}^{-3}\left[f_3\left(\overline{\beta}, \overline{d}\right) - i\overline{d}\, f_2\left(\overline{\beta}, \overline{d}\right)\right] = \overline{\alpha}_L^{-1} \\
T &: -\frac{3}{2}\overline{d}^{-3}\left[f_3\left(\overline{\beta}, \overline{d}\right) - i\overline{d}\, f_2\left(\overline{\beta}, \overline{d}\right) - \overline{d}^2 f_1\left(\overline{\beta}, \overline{d}\right)\right] = \overline{\alpha}_T^{-1}
\end{aligned}
\tag{4}
$$

where the following expressions for the modified polarizabilities hold:

5

$$\bar{\alpha}_{L}^{-1}\big|_{T} = \bar{\alpha}_{ee}^{-1} - \sum_{N=-\infty}^{\infty} c_N \varphi_N + d_N \delta_N + d_N \delta_N \varphi_N + f_N \delta_N^2 .... \tag{5}$$

The coefficients c_N, d_N, f_N are the Taylor coefficients of (3). As an example, in the longitudinal polarization they take the form:

$$c_N = 3\left(|N|\bar{d}\right)^{-3} e^{i\bar{\beta}(N\bar{d})} e^{i(|N|\bar{d})} \left(1 - i|N|\bar{d}\right)$$

$$d_N = -3\left(N\bar{d}\right)^{-4} e^{i\bar{\beta}(N\bar{d})} e^{i(|N|\bar{d})} \left[3 - i(\bar{\beta}+3)N\bar{d} - (\bar{\beta}+1)(N\bar{d})^2\right] \tag{6}$$

$$f_N = 3\left(N\bar{d}\right)^{-5} e^{i\bar{\beta}(N\bar{d})} e^{i(|N|\bar{d})} \left[12 - 6i(\bar{\beta}+2)N\bar{d} - (\bar{\beta}+1)(\bar{\beta}+5)(N\bar{d})^2 + i(\bar{\beta}+1)^2(N\bar{d})^3\right]$$

Eq. (4)-(5) combine the effects of disorder along the chain in a single compact expression, accurate enough to evaluate the perturbation of the dispersion relations due to the random disorder in the chain in terms of a change in the "average polarizability" of the particles forming the array, allowing a quantitative evaluation of the effects of the disorder on the guided wave number. In other words, the disorder along the chain is "seen" by the propagating mode as a variation in the polarizability of the particles in an equivalent ideally-periodic array.

Due to the assumption of small disorder, the summation in (5) is expected to weakly perturb the solution of Eq. (4), and this is why the approach of summing the fields at the particle location is still applicable. In particular, in the limit of interest in which the particles are lossless or with low-loss (allowing low-damping modal propagation along the chain) it is straightforward to show that the perturbation in (5) principally affects the imaginary part of Eq. (4), which is identically satisfied in the limit of lossless particles. This implies that a reasonably small disorder weakly affects the phase velocity along the chain, but it may affect more considerably its damping coefficient (imaginary part of β).

Assuming that the random quantities δ_N and φ_N are Gaussian distributions with zero expected value and with variances σ_δ^2 and σ_φ^2, respectively, we may evaluate this expected variation on the effective polarizability of the particles as "seen" by the mode. The Gaussian hypothesis on the distribution of δ_N and φ_N represents a realistic assumption, since the disorder associated with technological limitations and imperfections may be reasonably assumed to be a stochastic process in which each occurrence of δ_N and φ_N is fairly independent from the others. Due to the zero mean value of δ_N and φ_N and their independence, the dominant term in the summation (5) for evaluating the expected values $\langle \bar{\alpha}_L^{-1} \rangle$ and $\langle \bar{\alpha}_T^{-1} \rangle$ is given by $f_N \delta_N^2$. The expected values may be evaluated in closed form using the variance theorem for the sum of Gaussian distributions and the properties of the polylogarithm function. Their expressions in closed form are given in the general case as:

6

$$\left\langle \overline{\alpha}_L^{-1} \right\rangle = \overline{\alpha}_{ee}^{-1} - \frac{3\sigma_\delta^2}{2\overline{d}^5} \begin{bmatrix} 12 f_5\left(\overline{\beta},\overline{d}\right) - 6i\overline{d}\left(\overline{\beta}+2\right) Li_4\left(e^{i(\overline{\beta}+1)\overline{d}}\right) + 6i\overline{d}\left(\overline{\beta}-2\right) Li_4\left(e^{-i(\overline{\beta}-1)\overline{d}}\right) + \\ -\overline{d}^2\left(\overline{\beta}+1\right)\left(\overline{\beta}+5\right) Li_3\left(e^{i(\overline{\beta}+1)\overline{d}}\right) - \overline{d}^2\left(\overline{\beta}-1\right)\left(\overline{\beta}-5\right) Li_3\left(e^{-i(\overline{\beta}-1)\overline{d}}\right) + \\ +i\overline{d}^3\left(\overline{\beta}+1\right)^2 Li_2\left(e^{i(\overline{\beta}+1)\overline{d}}\right) + i\overline{d}^3\left(\overline{\beta}-1\right)^2 Li_2\left(e^{-i(\overline{\beta}-1)\overline{d}}\right) \end{bmatrix}$$

$$\left\langle \overline{\alpha}_T^{-1} \right\rangle = \overline{\alpha}_{ee}^{-1} + \frac{3\sigma_\delta^2}{4\overline{d}^5} \begin{bmatrix} 12 f_5\left(\overline{\beta},\overline{d}\right) - 6i\overline{d}\left(\overline{\beta}+2\right) Li_4\left(e^{i(\overline{\beta}+1)\overline{d}}\right) + 6i\overline{d}\left(\overline{\beta}-2\right) Li_4\left(e^{-i(\overline{\beta}-1)\overline{d}}\right) + \\ -\overline{d}^2\left(\overline{\beta}^2+6\overline{\beta}+7\right) Li_3\left(e^{i(\overline{\beta}+1)\overline{d}}\right) - \overline{d}^2\left(\overline{\beta}^2-6\overline{\beta}+7\right) Li_3\left(e^{-i(\overline{\beta}-1)\overline{d}}\right) + \\ +i\overline{d}^3\left(\overline{\beta}+1\right)\left(\overline{\beta}+3\right) Li_2\left(e^{i(\overline{\beta}+1)\overline{d}}\right) + i\overline{d}^3\left(\overline{\beta}-1\right)\left(\overline{\beta}-3\right) Li_2\left(e^{-i(\overline{\beta}-1)\overline{d}}\right) + \\ +\overline{d}^4\left(\overline{\beta}+1\right)^2 Li_1\left(e^{i(\overline{\beta}+1)\overline{d}}\right) + \overline{d}^4\left(\overline{\beta}-1\right)^2 Li_1\left(e^{-i(\overline{\beta}-1)\overline{d}}\right) \end{bmatrix} \quad (7)$$

where we have applied the properties of the polylogarithms to evaluate the summation (5) in closed form. Even if the form of these expressions is quite complex, these solutions provide some interesting insights into the effect of disorder in these plasmonic chain waveguides.

It is seen in (7) that the main perturbation on the effective polarizability is given by the variance of the disorder in the position of the particles, as shown by (7). Random (and independent) variations in the geometry of the particles appear to compensate each other in the first-order approximation along the chain, not significantly affecting the expected value $\left\langle \overline{\alpha}^{-1} \right\rangle$, as it was also verified numerically in [4] for 3D metamaterials in a different geometry. The variance of the position disorder, however, which is a measure of the degree of disorder in the system, may significantly perturb the effective "average" polarizability of the particles as seen by the guided mode, since the scattering losses from each of the particles cannot be completely "canceled" by the other particles forming an ideally periodic array, producing residual scattering losses. For this reason, in the following sections we concentrate on the analysis of random disorder in the position of the nanoparticles, assuming for simplicity that they have the same size.

Due to the nature of Eq. (4), when low-loss particles and low-damping guided modes are considered, the main effect in the perturbation of (7) is in fact expected to be in the imaginary part of (7), which is a measure of the "losses" experienced by the mode. Similarly to what was done in [9], the properties of the polylogarithm functions allow a direct evaluation of this imaginary part. Using the properties:

7

$$\begin{cases} \text{Im}\left[Li_1\left(e^{i\theta} \right) \right] = \dfrac{(\pi - \theta)}{2} \\[3mm] \text{Re}\left[Li_2\left(e^{i\theta} \right) \right] = \dfrac{\pi^2}{6} - \dfrac{\theta(2\pi - \theta)}{4} \\[3mm] \text{Im}\left[Li_3\left(e^{i\theta} \right) \right] = \dfrac{\theta(\pi - \theta)(2\pi - \theta)}{12} \qquad 0 \le \theta \le 2\pi \\[3mm] \text{Re}\left[Li_4\left(e^{i\theta} \right) \right] = \dfrac{\pi^4}{90} - \dfrac{\pi^2\theta^2}{12} + \dfrac{\pi\theta^3}{12} - \dfrac{\theta^4}{48} \\[3mm] \text{Im}\left[Li_5\left(e^{i\theta} \right) \right] = \dfrac{\pi^4\theta}{90} - \dfrac{\pi^2\theta^3}{36} + \dfrac{\pi\theta^4}{48} - \dfrac{\theta^5}{240} \end{cases} \tag{8}$$

the following exact relations are obtained for the imaginary parts of the expected values of effective polarizabilities in the two polarizations:

$$\begin{aligned} \text{Im}\left[\left\langle \overline{\alpha}_L^{-1} \right\rangle \right] &= \text{Im}\left[\overline{\alpha}_{ee}^{-1} \right] - \sigma_\delta^2 \left(\frac{1 + 5\overline{\beta}^2}{10} \right) \\[3mm] \text{Im}\left[\left\langle \overline{\alpha}_T^{-1} \right\rangle \right] &= \text{Im}\left[\overline{\alpha}_{ee}^{-1} \right] - \sigma_\delta^2 \left(\frac{2 + 5\overline{\beta}^2}{10} \right) \end{aligned}, \tag{9}$$

under the assumption that $\text{Im}\left[\overline{\beta} \right]$ is negligible (low-damping guided modes). This result is formally consistent with the first-order approximation for the effect of disorder in photonic crystal waveguides derived in [14].

We reiterate that Eq. (9) applies only in the limit of small disorder, for which these results represent small perturbations of the solution in the ideally periodic scenario. In this limit, this result is of great interest for its inherent simplicity. In this context, it is noticed that this perturbative method is consistent with iterative techniques that take into account small disorders in periodic arrays, for which a recent application to periodic metamaterials has been presented in [6]. Although our method would numerically yield consistent results for any type of random disorder (with zero mean value), the advantage of our technique when applied to Gaussian disorder is that it provides a closed-form solution for the level of additional losses caused by the disorder, directly related to its variance, as shown in Eq. (9). This provides relevant physical insights into the effect of small disorder in periodic structures, as we further discuss in the following.

Without resorting to any further approximation, and considering the fully dynamic interaction in the infinite disordered array of particles, Eq. (9) indeed states that, independent of the average distance between the particles, the disorder in the positions of particles affects the modal propagation by adding an effectively additional loss, due to the incoherent scattering radiation from the particles, proportional to the variance of the disorder. Similarly to the closed-form solution obtained in the ideally-periodic chain for the imaginary part of the dispersion relations (4), which ensured power conservation along the chain [9], and for which $\text{Im}\left[\overline{\alpha}_{ee}^{-1} \right] = -1$, i.e., the particles are lossless and no-damping propagation is obtained, here we get another equally simple generalized expression that takes into account the presence of disorder along the chain

8

and adds another form of radiation damping, quantitatively related to the degree of disorder in the chain.

We note that the sign of the additional terms in (9) is strictly negative, ensuring that the disorder increases the damping factor of the modes whatever is the geometry of the chain and the nature of the disorder. For passive particles, in fact, $\text{Im}\left[\bar{\alpha}_{ee}^{-1}\right] = -1 - \bar{\alpha}_{loss}^{-1}$, with $\bar{\alpha}_{loss}^{-1} \geq 0$ [9]. Moreover, Eq. (9) is consistent with the physical expectation that an increase in the variance of the disorder would correspond to an increase in the damping factor of the guided modes, and that a tighter (and slower) propagation along the chain (increase in β) makes the propagation more sensitive to such imperfections. Another interesting feature of this result is associated with the fact that the transverse-polarization configuration, which ensures backward propagation, is slightly more sensitive to the disorder than the longitudinal-polarization propagation. This is consistent with our previous findings [9] that showed how this polarization has a slightly lower bandwidth and more sensitivity to losses than the forward-wave longitudinal propagation.

d. Numerical examples and validation

Figure 2, as a first example, shows the variation of $\text{Im}\left[\bar{\beta}\right]$ with the standard deviation σ_δ of the position disorder for a chain of silver particles, calculated using (9) and the results in [9]. Longitudinal polarization, which is the most appealing for guiding purposes, is considered here and in the following. Moreover, we concentrate on the positional disorder, which has been proven in the previous section to be the most significant mechanism of radiation loss. The chain is formed by silver spherical nanoparticles with average radius $a = 10\,nm$ and center-to-center average distance $d = 22\,nm$. We have evaluated this chain geometry considering experimental values of the silver permittivity available in the literature [25], and considering the inherent absorption and frequency dispersion (black solid line) of silver at optical frequencies. We have also added the red dashed curve, which neglects the absorption in the particles, in order to isolate the effect of disorder on the damping of the mode. The curves in this case have been evaluated at the free-space wavelength $\lambda_0 = 380\,nm$, which, following the analysis in [9], ensures the best guiding properties of the mode as the highest ratio between real and imaginary parts of $\bar{\beta}$. At this wavelength the permittivity of silver is $\varepsilon_{Ag} = -3.8 + i\,0.19$ [25].

As predicted by the previous analysis, increasing the disorder along the chain induces a perturbation of $\bar{\beta}$, mainly reflected in its imaginary part. Small deviations from the ideal position of the particles do not considerably perturb the guiding properties of the chain, and the absorption is usually dominated by the inherent ohmic absorption of metallic particles. Still, the sensitivity to disorder is well modeled by the theoretical considerations in this geometry.

Figure 3 shows a similar case, but for larger silver particles and correspondingly larger separation between the centers of the particles, highlighting the difference in the effect of disorder with a change in the geometry of the chain. In this case $a = 15\,nm$, $d = 33\,nm$ and $\lambda_0 = 390\,nm$, for which $\varepsilon_{Ag} = -3.9 + i\,0.19$.

It is evident how in this second scenario the effect of disorder is somehow lower. This is due to the fact that in this second scenario the particles are larger, and therefore less affected by the inherent Ohmic losses and effect of disorder, since the electric field is less concentrated in their

9

volume. Despite the mode being more confined around the chain (higher $\mathrm{Re}\left[\bar{\beta}\right]$) this second example ensures more robustness to Ohmic losses and to disorder, consistent with its inherent robustness reported in [9].
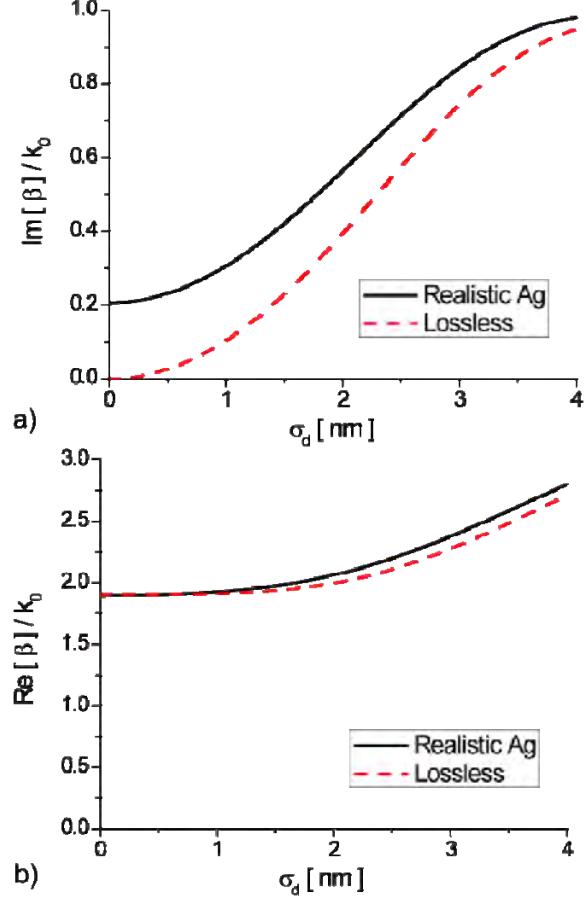
Figure 2 – Variation of imaginary (a) and real (b) parts of $\bar{\beta}$ as a function of the standard deviation of disorder along a chain of silver nanoparticles, considering (solid) and neglecting (dashed) Ohmic absorption. The radius of the particles is $a = 10\,nm$ and average distance between any two neighboring particles (center to center) is $d = 22\,nm$ at the free-space wavelength $\lambda_0 = 380\,nm$. Here and in the following the longitudinal polarization is considered.

Figure 4, as a confirmation of the validity of the previous theoretical results, reports the numerical simulations of a linear chain of particles with some disorder in which the location and the size of each particle has been perturbed from the original periodic geometry of Fig. 2. In particular, we have assumed a Gaussian random noise in the position of the particles with standard deviation $\sigma_\delta = 0.5\,nm$ and a deviation from the ideal radius of each particle $a = 10\,nm$ equal to $\sigma_a = 0.5\,nm$. The figure reports the calculated $\mathrm{Im}\left[\bar{\beta}\right]$ for the ideal chain without disorder and for the chain with added disorder, both evaluated using Eq. (4), corresponding to the black solid line and the red dashed line, respectively. Moreover, we have reported the calculations for a random chain, obtained by applying (1), (3) and truncating the summation to the first 20 elements (that is evaluating the eigen-wave number considering the contributions from the nearest 40 nanoparticles around the origin). As we already mentioned, the summation in

10

(1) is not strictly convergent when complex propagation constants are considered, due to the fact that the mode amplitude grows exponentially in one direction of the chain. This is consistent with any complex eigenmode solution (leaky-waves or lossy geometries), and this problem is usually solved with proper analytical continuation of the series in the complex domain, as in Eq. (4).
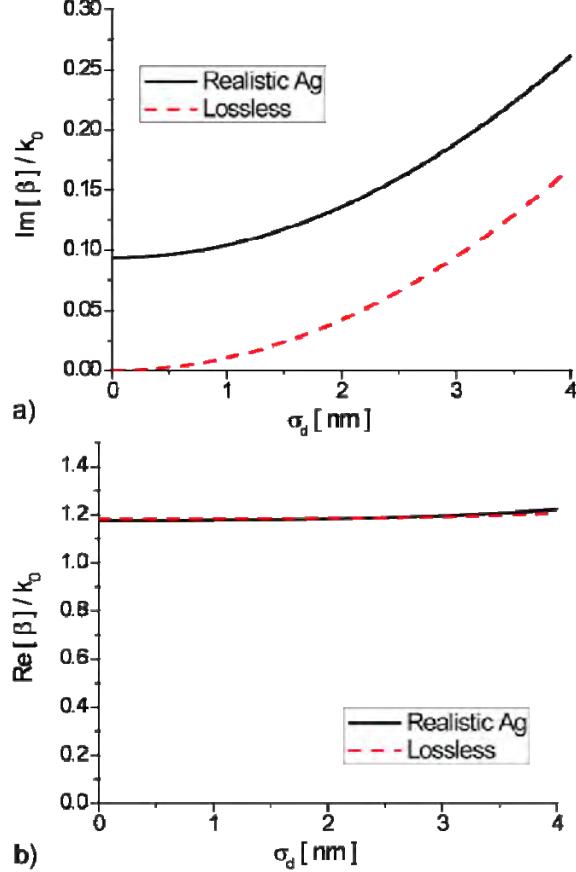
Figure 3 – Similar to Fig. 2, but for $a = 15\,nm$ and average distance $d = 33\,nm$ at the free-space wavelength $\lambda_0 = 390\,nm$.

Since now the summation is constituted by random variables, and it cannot be solved in closed-form, we have considered its solution obtained after proper truncation, which is a good approximation to the exact analytical continuation derived in (2). In this scenario, where each particle has a random deviation in position and size, the closed-form analytical solution cannot be derived, but the summation truncated to the first 20 elements provide a good agreement with our theoretical results that embed the effect of disorder in the closed-form expression (4)-(5), as evident from the figure. The residual oscillation with frequency, evident in Fig. 4, is related to the truncation effect, as shown by evaluating Eq. (1)-(3) in the case of no disorder and of increased losses using Eq. (4) (black and red dotted lines, respectively). It is evident that the line corresponding to the random chain (dotted blue line) agrees very well with the truncated dispersion relation obtained using the previous theoretical results. We have verified similar agreement when we change the number of elements considered in the truncated series.

Figure 5 shows the full-wave numerical simulations, performed with commercial electromagnetic software [26], simulating the chain geometry of Fig. 2 with (Fig. 5a) and

11

without (Fig. 5b) considering the disorder in the position of the particles, in the amount of $\sigma_\delta = 2\,nm$. These simulations refer to the wavelength $\lambda_0 = 400\,nm$, for which the silver permittivity is $\varepsilon_{Ag} = -4.56 + i\,0.22$ [25]. In particular, the figure reports a snapshot of the instantaneous magnetic field distribution orthogonal to the plane of the chain. It is evident from the figure how the guided mode along the chain, although supported in both cases, decays faster due to the presence of disorder, consistent with the results of the previous theory and with the presence of an effective additional loss factor in the particles forming the chains. In the figure we have also reported the plot of the longitudinal electric field amplitude sampled on a line parallel to the chain axis at a distance of $80\,nm$. Despite the sharp variations due to the granularity of the spheres, a clear exponential decay is visible in both cases in the figure, which is highlighted by the dashed lines in Fig. 5. We have extracted the effective $\mathrm{Im}\left[\bar{\beta}\right]$ from these simulations, which is given by:

no disorder: $\quad \mathrm{Im}\left[\bar{\beta}\right] = 0.22$

disorder: $\qquad \mathrm{Im}\left[\bar{\beta}\right] = 0.35$, (10)

respectively corresponding to the black (darker) and red (lighter) lines. As expected, these extracted values of $\mathrm{Im}\left[\bar{\beta}\right]$ are consistent with the values predicted by Eq. (9), despite the simplified dipolar approximation of our analytical model.
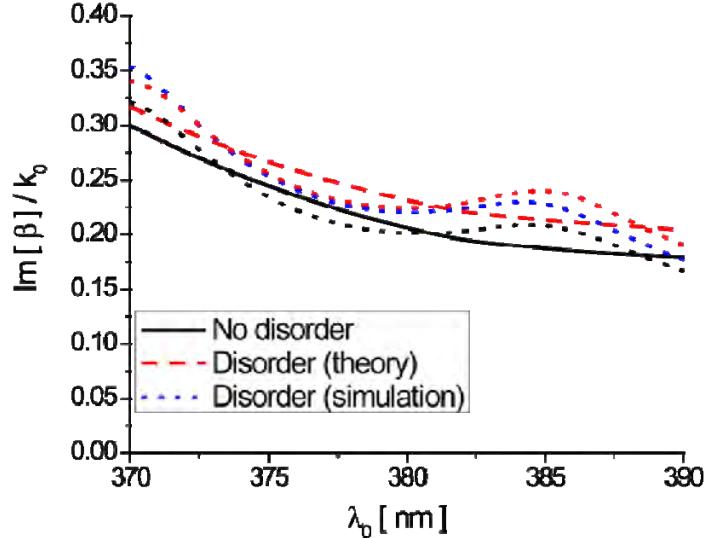
Figure 4 – Dispersion of $\mathrm{Im}\left[\bar{\beta}\right]$ for a guided mode along the chain of Fig. 2 in the three cases of: ideally periodic chain (black solid line), disordered chain using this theory (Eq. (9), red dashed) and disordered chain using a random array and Eq. (1)-(3) truncated to $N_{max} = 20$ (blue dotted). The disorder in the position of the particles has a standard deviation $\sigma_\delta = 0.5\,nm$, whereas the disorder in the size of the particles is embedded in the standard deviation for their radius $\sigma_a = 0.5\,nm$. For comparison, here we have also reported the solution of Eqs. (1)-(3) truncated to $N_{max} = 20$ for an ideally periodic chain (black dotted) and for the disordered chain using Eq. (9) (red dotted).

12
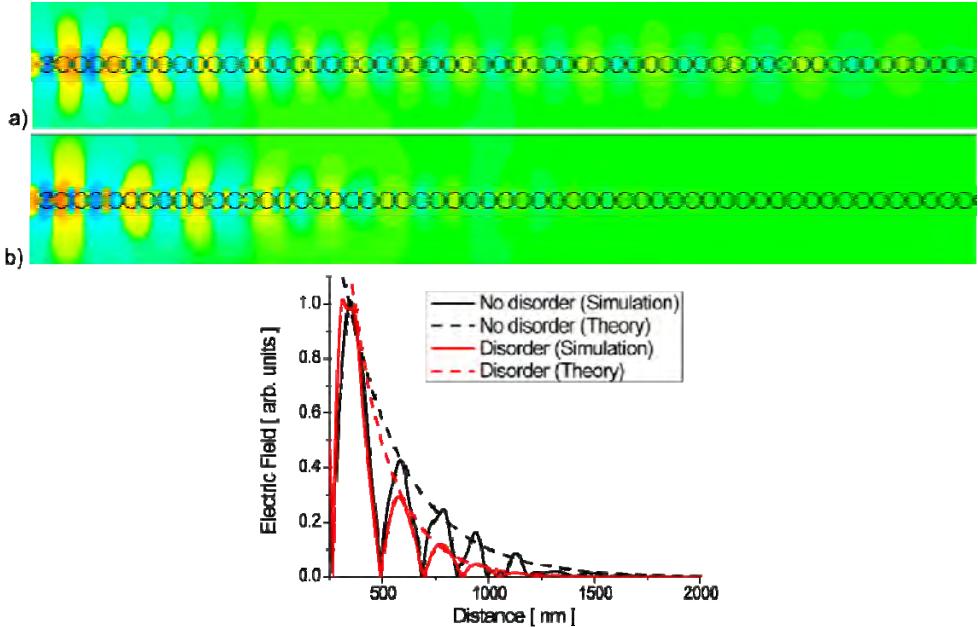
Figure 5 – Magnetic field distribution orthogonal to the plane of the chain for the geometry of Fig. 2 in the case of: (a) ideally (periodically) ordered particles and (b) with random disorder in the position of the particles with $\sigma_\delta = 2\,nm$. The plot reports the electric field distribution sampled on a line parallel to the chain axis, at a distance of $80\,nm$ (solid lines) and the corresponding exponential decays, consistent with our theoretical model.

e. Conclusions

The results in this manuscript confirm that the disorder in plasmonic waveguides and metamaterials may give rise to additional scattering losses that may be quantified as a function of the degree of disorder present in the periodic lattice. The geometry analyzed here, a linear array of plasmonic nanoparticles, has been selected for two reasons: the possibility of a closed-form analytical solution, generalizing the results of [9], and its inherent property that this geometry shares with the more general class of periodic metamaterials, i.e., supporting low-loss propagation by the means of cancellation of the radiation losses that an ideally periodic lattice ensures. It has been proven in various experimental setups that sub-diffraction optical waveguides like the one considered here, indeed suffer from the presence of losses, and signals cannot travel over few wavelengths in realistic scenarios with subwavelength cross-sectional size. The results presented here allow a proper quantification of the effects of small random disorder on the expected propagation distance and on the further increase in damping due to radiation losses. We believe this may be useful for the design and fabrication of these waveguides and of optical metamaterials based on similar concepts.

With similar arguments, these results may be extended to the 3D scenario of closely packed nanoparticles forming backward-wave metamaterials [10] and to the more general class of periodic metamaterials and photonic crystals. We may quantify the amount of expected scattering losses in a realistic plasmonic array or metamaterial affected by disorder associated with technological limitations and imperfections, justifying how the measured losses in such setups are often larger than those expected from purely theoretical predictions obtained under the assumptions of ideally-periodic configurations. It is interesting to underline that our theoretical results show quantitatively how to a first-order approximation small variations in the shape or electromagnetic properties of the inclusions are less important than an analogous disorder in their

13

position, for what concerns the overall electromagnetic behavior of the metamaterial setup and in particular its damping and absorption properties. To conclude, these results represent an important step in quantifying the radiation and scattering losses induced by disorder in plasmonic waveguides and periodic metamaterials.

4. Waveguiding Properties of Plasmonic Nanoparticles and Voids

a. Summary

In this section, we show our efforts in comparing different nanoscale waveguiding geometries involving plasmonic materials for sub-diffractive propagation at optical frequencies. Deriving closed-form analytical formulas to analyze the different structures, we show how the presence of a plasmonic background may produce robust, highly confined guided wave propagation as compared with the dual setups involving plasmonic particles in a transparent background. Advantages and disadvantages of different scenarios for realizing right-handed and left-handed propagation in one-dimensional (1D) and two-dimensional (2D) waveguides are highlighted and discussed.

b. Introduction

Plasmonic phenomena and their related applications have witnessed fantastic development in recent years. In particular, at optical frequencies where plasmonic materials are readily available in nature [27]-[28], various potential applications of plasmonic concepts have been recently proposed, including transport of optical energy with tight lateral confinement [29]-[56], left-handed wave propagation [57]-[60], and slow-light devices [61]-[63], just to name a few. As one such application, inspired by our idea of bringing the notion of circuit elements into optical frequencies [64], we have proposed and analyzed different geometries for realizing optical nanotransmission-lines in the form of chains of plasmonic nanoparticles [39] and nanorods [41] (1D propagation), planar plasmonic nanolayers [56] (2D), and plasmonic 3D nanoarrays of particles to form optical nanomaterials [40]. Bringing the notion of transmission-line from the radio frequencies (RF) and microwaves into optical frequencies may inspire the design of guided modes more tolerant to Ohmic absorption, less radiation losses and larger bandwidth of operation, all inherent properties of RF transmission lines. The different waveguiding geometries that we have recently proposed, all based on the peculiar properties of plasmonic materials at IR and optical frequencies, indeed allow, under proper conditions, reasonably long propagation distances with highly sub-diffractive lateral confinement of the guided beams and relatively larger bandwidth of operation.

Even if ideally the plasmonic nanowaveguides may be designed to totally suppress unwanted radiation [39]-[40], the presence of small disorder, Ohmic absorption and other unwanted imperfections may generate radiation losses in the transparent background, which affect the propagation distance of the guided beams [65]. For this reason, we have recently been interested in analyzing in detail the dual of these setups, i.e., analogous geometries employing dielectric waveguides surrounded by a plasmonic background material, in the form of arrays of voids or dielectrics, cylindrical voids, or dielectric nanolayers embedded in noble metals or other plasmonic materials as backgrounds, consistent with some recent analogous proposals [42]-[54]. Due to the opaqueness of such materials at optical frequencies, wave propagation in the background is forbidden and the corresponding radiation losses of the guided modes may be

14

reduced. The confinement of the guided beams inside the dielectrics or voids, which usually have lower loss, may also ensure a lower sensitivity to Ohmic absorption, which is another possible advantage of these dual configurations. This is of course valid as long as comparable field confinement is achieved, since large field concentration would always lead to larger sensitivity to absorption loss in both setups.

In general, a common trend in all the waveguiding geometries involving plasmonic effects may be emphasized: a trade-off between propagation length of the guided waves and the limitation on its lateral confinement and bandwidth. In this sense, a figure of merit, defined as the ratio of propagation distance versus beam cross section may be defined in order to sort out the most promising waveguiding geometries involving plasmonic materials at the frequency of interest. Moreover, the fact that the power inside plasmonic materials generally flows in a direction opposite to the modal phase velocity [56] allows one tailoring these waveguides to exhibit either forward- or backward-wave propagation (i.e., the group velocity being parallel or anti-parallel with the phase velocity of the mode), depending on whether the power is more concentrated in the plasmonic or in the dielectric region. Efficient and optimized backward-wave waveguides may play an important role in the framework of left-handed material research and sub-wavelength imaging, as discussed in Ref. [56].

In this section, after discussing the analytical properties of the guided modes in these different types of waveguides, we compare and contrast their properties, exploring which ones of the different proposed waveguiding geometries and solutions may be more robust to material absorption and radiation losses, and which ones exhibit a "better" bandwidth of operation.

c. *Plasmonic and dielectric cavities*

It is well known that a subwavelength plasmonic nanoparticle of radius a and permittivity ε may support a "quasi-static" resonance when $\mathrm{Re}[\varepsilon] < 0$ [28]. This phenomenon may be interpreted in terms of the nanocircuit concepts [64] as the intrinsic resonance between the nanoinductor elements represented by a plasmonic nanoparticle and the nanocapacitor constituted by its fringing fields in a background material with permittivity $\varepsilon_b > 0$. The specific values of the two nanocircuit elements, as described in Ref. [64], depend on the material parameters and the geometry of the nanoparticle, which determines the combined resonance condition. It is well known, for instance, that the resonance of a plasmonic nanosphere is obtained when:

$$\begin{vmatrix} j_n(ka) & y_n(k_b a) \\ \left[ka\, j_n(ka) \right]' / \varepsilon & \left[k_b a\, y_n(k_b a) \right]' / \varepsilon_b \end{vmatrix} = 0,$$

(11)

where j_n and y_n are spherical Bessel functions, depending on the resonant order n, $k = \omega\sqrt{\varepsilon\mu_0}$, $k_b = \omega\sqrt{\varepsilon_b\mu_0}$ (with the choice for the branch root of k_b satisfying the radiation condition at infinity) and μ_0 is the free-space permeability assumed to be the same in all the (non-magnetic) materials in our study. In the small-radii approximation, Eq. (11) is satisfied near the frequency for which $\mathrm{Re}[\varepsilon] \simeq -\dfrac{n+1}{n}\varepsilon_b$. Different resonant conditions may be achieved for different shapes

15

of the nanoparticle or with a multi-layered geometry [67]. For the dominant resonant mode, with $n = 1$, the corresponding resonance Q-factor may be calculated as:

$$Q = \frac{3}{2\left(k_0 a\right)^{-3} + 3\dfrac{\gamma}{f_0}},$$ (12)

where we have assumed a Drude-model dispersion for the nanosphere permittivity as $\varepsilon = \varepsilon_0 \left(1 - \dfrac{3f_0^2}{f\left(f + i\gamma\right)}\right)$, with f_0 being the resonance frequency. (Here, we are assuming that the plasma radian frequency for the spherical particle is $\omega_p = 2\pi\sqrt{3}f_o$.) The denominator in Eq. (12), proportional to the total losses in the system, is evidently given by the sum of two terms: the radiation losses, inversely proportional to the nanosphere volume, consistent with Ref. [66], and the ohmic absorption in the material, proportional to the damping frequency γ of the material. Even in an ideally lossless particle, the Q-factor in Eq. (12) would be indeed limited by the intrinsic radiation losses of the particle. For higher-order resonances the term in the denominator of (12) becomes $\left(k_0 a\right)^{-2n-1}$, implying smaller radiation losses and higher Q, as expected.

If we now reverse the role of inductors and capacitors, i.e., we analyze the dual geometry composed of a dielectric nanosphere with permittivity $\varepsilon > 0$ embedded in an ε-negative (ENG) background with permittivity $\varepsilon_b < 0$, the resonance is described by an analogous equation:

$$\begin{vmatrix} j_n\left(ka\right) & h_n^{(1)}\left(k_b a\right) \\ \left[ka\, j_n\left(ka\right)\right]' / \varepsilon & \left[k_b a\, h_n^{(1)}\left(k_b a\right)\right]' / \varepsilon_b \end{vmatrix} = 0,$$ (13)

where $h_n^{(1)}$ is the spherical Hankel function of first kind, which is purely imaginary for imaginary k_b (associated with the fact that the ENG background does not support wave propagation), and the field distribution is mainly concentrated in the dielectric nanosphere and at the plasmonic interface, decaying much more rapidly in the outside region. In this case, the expression for the Q-factor simplifies to:

$$Q \simeq \frac{f_0}{\gamma},$$ (14)

where we have assumed $\varepsilon_b = \varepsilon \left(1 - \dfrac{\dfrac{2n+1}{n+1}f_0^2}{f\left(f + i\gamma\right)}\right)$, which once again supports a resonance at frequency f_0. Eq. (14) is valid for any resonant order n.

It is interesting to see that such a cavity may support an extremely high-Q resonance, limited only by the inherent losses of the background material, since no radiation is involved in the unbounded plasmonic background. Interestingly, the cavity size is not limited by diffraction, i.e., in principle its dimension may be made arbitrarily small, since the field distribution would be

16

adjusted in order to remain concentrated around the plasmonic interface, with the Q as derived in Eq. (4), independent of the cavity volume or of the resonant order.

Figure 6 reports the variation of the electric field distribution induced on the surface of a glass spherical cavity embedded in the silver background, with radius $a = 5\,nm$, for a sample excitation. It is interesting to note how the different resonant peaks1 have similar operating bandwidths, since they are characterized by a similar Q-factor, as predicted by Eq. (14)[2].
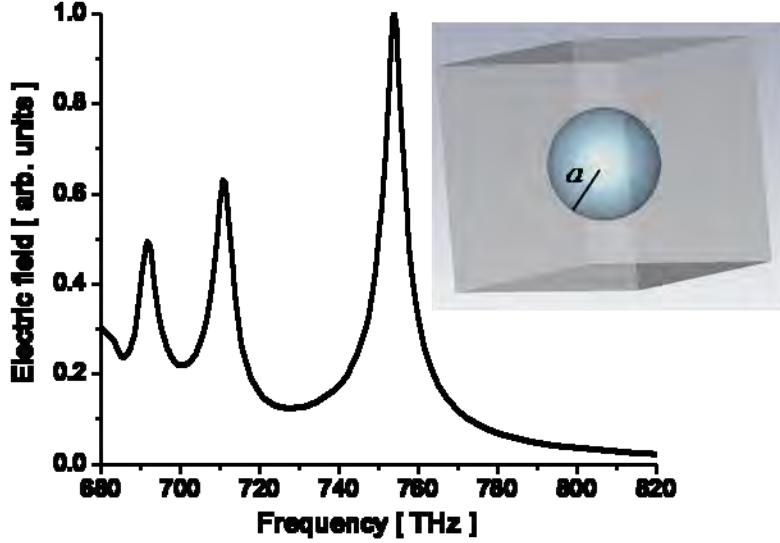
Figure 6 - Electric field amplitude on the surface of a glass cavity with radius $a = 5\,nm$ embedded in a silver background (considering realistic losses of silver).

d. *Chains of dielectric voids in an ENG background*

If the 0-D problem of a sub-wavelength dielectric cavity in an ENG background presents some interesting peculiarities, collections of such small cavities may give rise to other, even more exciting possibilities [42], [47], [50]. For instance, consider cascading several identical dielectric voids, of any arbitrary shape and material properties, in a linear array format, with center-to-center spacing $d > 2a$. The propagation along these arrays may be modeled analogously to the previous section and to Ref. [39], where we have solved analytically the propagation along linear arrays of plasmonic particles in free-space. In particular, when our technique in Ref. [39] is applied to this dual scenario, the dispersion equations for the guided modes supported by such arrays of nanovoids embedded in an ENG background become, in the limit of negligible losses:

$$L: \quad \sum_{N=1}^{\infty} \left[N^{-3} d^{-3} \cos(N\beta d) e^{-N|k_b|d} \left(1 + N|k_b|d \right) \right] = \pi \varepsilon_b \alpha_{ee}^{-1}$$

$$T: \quad \sum_{N=1}^{\infty} \left[N^{-3} d^{-3} \cos(N\beta d) e^{-N|k_b|d} \left(1 + N|k_b|d - N^2 |k_b|^2 d^2 \right) \right] = -2\pi \varepsilon_b \alpha_{ee}^{-1}$$

(15)

---

[1] As seen in Fig. 1, the $n = 1$ resonance arises around $755\,THz$, the other resonances arise in order when the frequency is lowered, consistent with Eq. (11).

[2] This is different from the behavior of a plasmonic nanoparticle embedded in a dielectric (e.g., air), where, due to radiation losses, the bandwidth of higher-order resonances is usually much narrower than the first-order resonance.

17

Respectively, for the longitudinal and transverse polarization (with respect to the array axis x, see the insets in Fig. 7a and Fig. 7b respectively), where β is the longitudinal wave number of the guided modes ($e^{i\beta x}$ spatial dependence) and α_{ee} is the generic electric polarizability of each individual nanovoid, consistent with Ref. [39]. Since the wave propagation is forbidden in the background material, the radiation from this array is automatically avoided in this geometry, and the coupling among distant elements is consistently minimized. In this lossless limit, Eq. (15) indeed ensures quick convergence and only a few terms should be considered for an accurate prediction of the guided wave number β. Introducing losses, however, Eq. (15) is not properly converging and an analytic continuation is necessary to handle the problem accurately. In this sense, the closed-form expressions may be derived, analogous to those derived in the previous section for the present dual geometry, as:

$$
\begin{aligned}
L:\quad & 3\overline{d}^{-3}\left[f_3\left(\overline{\beta},\overline{d}\right)+\overline{d}\,f_2\left(\overline{\beta},\overline{d}\right)\right]=\overline{\alpha}_{ee}^{-1} \\
T:\quad & -\frac{3}{2}\overline{d}^{-3}\left[f_3\left(\overline{\beta},\overline{d}\right)+\overline{d}\,f_2\left(\overline{\beta},\overline{d}\right)+\overline{d}^2 f_1\left(\overline{\beta},\overline{d}\right)\right]=\overline{\alpha}_{ee}^{-1}
\end{aligned}
\tag{16}
$$

with $\quad f_N\left(\overline{\beta},\overline{d}\right)=Li_N\left(e^{-(1+i\overline{\beta})\overline{d}}\right)+Li_N\left(e^{-i(1-i\overline{\beta})\overline{d}}\right), \quad Li_N\left(z\right)=\sum_{k=1}^{\infty}\dfrac{z^k}{k^N}, \quad \overline{\beta}=\beta/\left(-ik_b\right), \quad \overline{d}=-ik_b d$,

$\overline{\alpha}_{ee}=\dfrac{-ik_b^{\,3}}{6\pi\varepsilon_b}\alpha_{ee}$. Li_N is the polylogarithm function, which may be analytically continued in the complex plane following Refs. [39], [68].

Owing to the absence of radiation, these equations are much simpler to analyze than their counterparts derived in Ref. [39] for the transparent background scenario. When losses are absent, they are real-valued. When the losses are considered in general their imaginary part is simply associated with the ohmic absorption in the background (notice that due to the normalizations, when losses are considered the normalized distance $\overline{d}$ becomes a complex quantity). Due to the properties of $Li_N\left(z\right)$ and their derivatives (see Ref. [39] for details), Eq. (16) implies that in the longitudinal polarization the chain supports only "backward" modes (oppositely-signed phase and group velocities), whereas the modes are inherently "forward" for the transverse polarization. This is opposite to the dual scenario of arrays of plasmonic particles in a transparent background, consistent with the fact that in both polarizations we have effectively interchanged the roles of nanoinductors and nanocapacitors (in the longitudinal polarization, the equivalent circuit model for this geometry consists of series capacitors and shunt inductors, like in a left-handed transmission line[69], whereas for transverse modes we have series inductors and shunt capacitors, as in a regular transmission line supporting forward wave propagation). Eq. (16) determines the conditions on the polarizability of each individual cavity and on the spacing among them, so that such arrays may support propagation. In particular, the range of guidance for the two polarizations may be written in closed-form by considering the properties of $Li_N\left(z\right)$ and the fact that, due to its periodicity, the array may support propagation in the range $0<\overline{\beta}<\pi$. The range of guided wave propagation as a function of α_{ee} may be interestingly written in closed form as:

18

$$L: \quad \frac{6}{\bar{d}^3}\left[Li_3\left(-e^{-\bar{d}}\right)+\bar{d}\,Li_2\left(-e^{-\bar{d}}\right)\right]<\bar{\alpha}_{ee}^{-1}<\frac{6}{\bar{d}^3}\left[Li_3\left(e^{-\bar{d}}\right)+\bar{d}\,Li_2\left(e^{-\bar{d}}\right)\right]$$

$$T: \quad \frac{-3}{\bar{d}^3}\left[Li_3\left(e^{-\bar{d}}\right)+\bar{d}\left(Li_2\left(e^{-\bar{d}}\right)+\bar{d}\left[\bar{d}-\ln\left(e^{\bar{d}}-1\right)\right]\right)\right]<\bar{\alpha}_{ee}^{-1}< \quad , \quad (17)$$

$$< \frac{-3}{\bar{d}^3}\left(Li_3\left(-e^{-\bar{d}}\right)+\bar{d}\,Li_2\left(-e^{-\bar{d}}\right)-\bar{d}^2\ln\left(1+e^{-\bar{d}}\right)\right)$$

valid in the limit of zero losses.
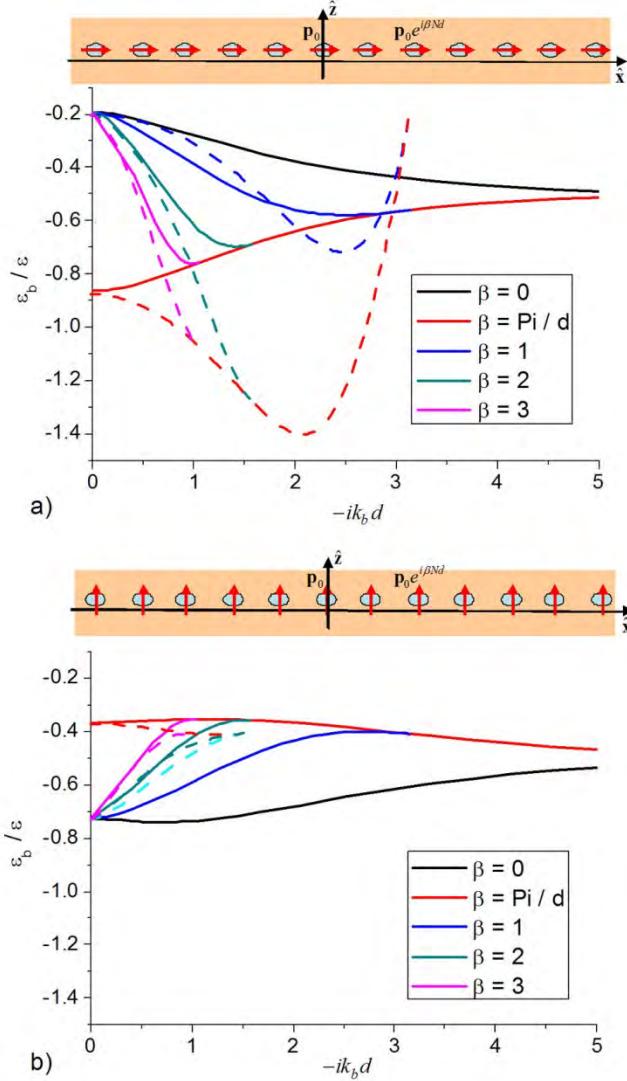
Figure 7 - Regions of guidance (between the black and red lines) for arrays of nanovoids in an unbounded plasmonic background for the two polarizations, as a function of the normalized distance $\bar{d}$ for fixed ratio $d/a=2.1$.

These results are valid for any shape of the nanovoids, since they are written in terms of the generic polarizability α_{ee}. For a homogenous spherical void of permittivity ε, we have $\bar{\alpha}_{ee}^{-1} \simeq \frac{3}{2}\left(-ik_b a\right)^{-3}\frac{\varepsilon+2\varepsilon_b}{\varepsilon-\varepsilon_b}$ and this allows plotting the conditions (17) in terms of the ratio $\varepsilon_b/\varepsilon$, as reported in Figure 7 for the case of $d=2.1a$. The solid lines in the figure are relative to the

19

current scenario (i.e., voids embedded in the ENG background), whereas the dashed lines refer to the dual case of plasmonic particles in a transparent background (consistent with the analogous plots in Ref. [39]). The regions of guidance are delimited by the loci $\bar{\beta} = 0$ and $\bar{\beta} = \pi / \bar{d}$ (notice that in this geometry, for which propagation is forbidden in the background material, also fast modes with $\bar{\beta} < 1$ may propagate without losses, like inside a regular waveguide at RF, differently from the case of plasmonic particles that are required to radiate away when $\beta < k_b$).

In the plot other curves for specific values of $\bar{\beta}$ within the guidance region are also shown. Since $\varepsilon_b < 0$ and $d\varepsilon_b / d\omega > 0$ for passivity requirements [70], both plots confirm that longitudinal modes are necessarily backward (Fig. 7a) and transverse modes are forward (Fig. 7b), opposite to the dual configuration in Ref. [13].

Some other interesting features are evident in these plots: in principle there is no limit on the distance between the nanovoid cavities to support propagation, even if, for large enough distance, propagation is allowed only very near the resonant frequency of the individual cavities (for which $\varepsilon_b = -\varepsilon / 2$). This may substantially enlarge the relative region of propagation when compared with the dual configuration of plasmonic particles (dashed lines), particularly for the transverse polarization (in Ref. [39] it was proven analytically that arrays of plasmonic particles in a transparent background may support propagating modes with no radiation losses only for $\bar{d} < \pi$). It should be noticed, however, that for large distances the supported modes are very fast ($\bar{\beta} \simeq 0$) and this propagation region may become sensitive to the material absorption in the background. For closer and closer particles, the range of values of permittivities of dielectric voids for which propagation is admissible gets relatively larger, consistent with the tight coupling among the individual resonances in the chain, and therefore relatively larger bandwidths of propagation are expected, compared to the dual geometry, due to absence of radiation loss from the array. In the limit of $\bar{d} \to 0$, the regions of guidance coincide for the two dual geometries, since in this case quasi-static considerations hold [39].

Figure 8, as an example, shows the dispersion of the guided modes for a chain of spherical SiC voids embedded in a silver background with $a = 5\,nm$ and $d = 10.5\,nm$, considering realistic values of permittivity (including dispersion and losses) for both materials [27],[71]. In particular, here the silver is modeled using a Drude model with plasma frequency $f_p = 2.175\,PHz$ and damping frequency $\gamma = 435\,THz$. The figure reports the real and imaginary parts of the normalized guided wave number β / k_0, with $k_0 = \omega \sqrt{\varepsilon_0 \mu_0}$. Fig. 8a reports the comparison between the dispersion curves in the ideally lossless scenario (neglecting loss in silver, solid lines) and the case in which losses are considered (dashed). As expected, their influence is most visible near the edges of the pass-band, since the group velocity is lower. The thin dashed line in this panel represents the dispersion of the curve $\text{Re}[\beta] = \pi / d$, which coincides with the stop-band for these guided modes, as again expected. Fig. 8b reports the imaginary part of the normalized guided wave number in the two polarizations, also reporting the level of absorption in dB / λ_0, where $\lambda_0 = 2\pi / k_0$. It is clear that realistically these guided beams cannot propagate over multiple wavelengths, but this is expected, considering the level of confinement represented by the large value of $\text{Re}[\beta]$.

20
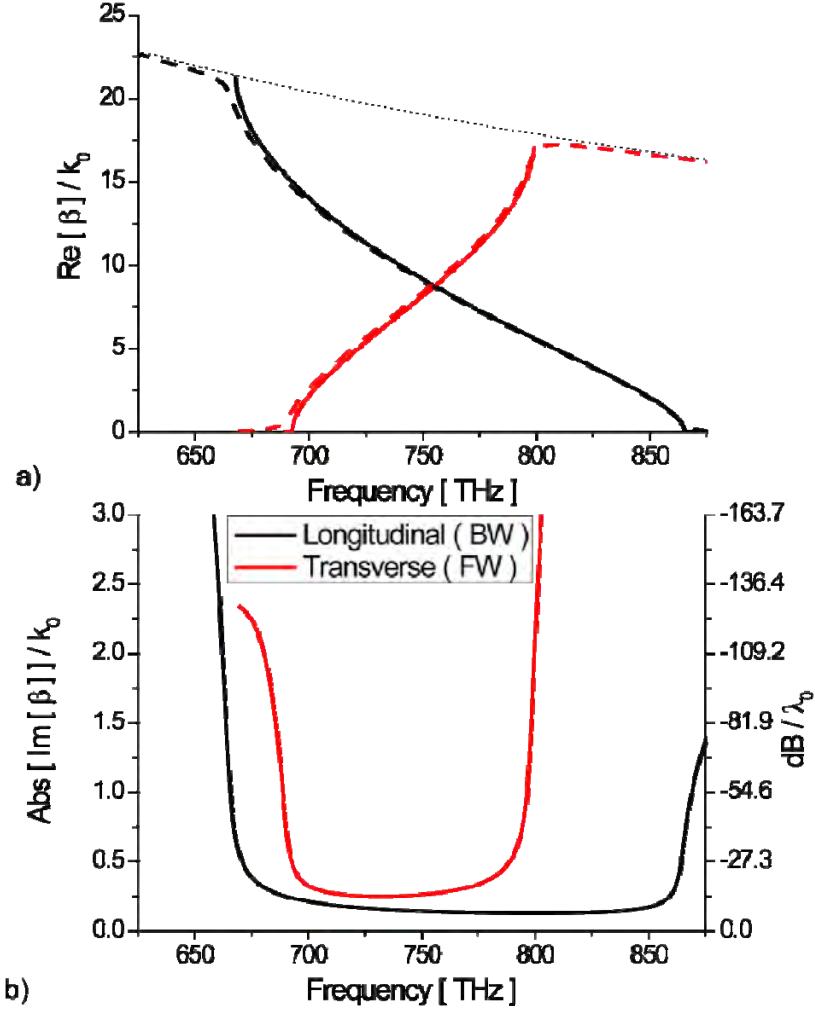
Figure 8 - Dispersion of the real (a) and imaginary (b) part of β, normalized to k_0, for a linear array of *SiC* voids of radius $a = 5\,nm$ in a silver background with $d = 10.5\,nm$. The thin dotted line corresponds to the condition $\beta = \pi / d$, which is the upper limit for modal propagation, whereas the dashed lines refer to the case in which material losses are neglected.

It is evident that the dispersion of β versus frequency supports the backward (forward) propagation of longitudinal (transverse) modes, with the derivative $\partial\beta / \partial\omega$ confirming the previous discussion. The bandwidth for longitudinal modes is slightly larger than for the transverse modes, consistent with the dual scenario [39], implying that in this geometry backward-wave propagation is actually more robust than forward-wave propagation, in terms of bandwidth and losses (Fig. 8b). The possibility of relatively low-loss propagation over a relatively wide bandwidth is feasible, consistent with the transmission-line analogy at radio-frequencies. Another advantage of this dual configuration, with respect to plasmonic particles in a transparent background, is the suppression of the spurious transverse mode with forward properties [39] that limits the bandwidth of the transverse backward-wave mode in the dual geometry. Here its presence is avoided due to the absence of propagation in the background material. In the figure the dashed lines refer to the case in which material losses are neglected, exhibit the fact that their presence does not sensibly affect the phase velocity of guided modes

21

($\text{Re}[\beta]$, Fig. 8a), but it simply affects the propagation distance ($\text{Im}[\beta]$, Fig. 8b). As noticed in panel a), and consistent with the dual scenario [39], losses are more significant in the regions where slow-wave propagation arises, i.e., near the edges of the propagation band, where the group velocity $\partial \omega / \partial \beta \simeq 0$.

e. *Dielectric nanorod in an ENG background*

In the limit in which the dielectric nanovoids analyzed in the previous section are closely packed together, they may constitute a homogeneous 1D cylindrical nanorod of radius a surrounded by an ENG background, as investigated, e.g., in Ref. [55]. The properties of the dual configuration, i.e., a plasmonic nanorod used as waveguide, have been thoroughly investigated by various groups in several papers (e.g., Refs. [41],[72]) and the analytical framework is the same when plasmonic materials form the background. In particular, the dispersion equation for a mode with generic azimuthal order n supported by a nanorod with permittivity ε and radius a is given by:

$$
\left[\frac{\varepsilon}{\sqrt{k^2 - \beta^2}} \frac{J_n'\left(\sqrt{k^2 - \beta^2}a\right)}{J_n\left(\sqrt{k^2 - \beta^2}a\right)} - \frac{\varepsilon_b}{\sqrt{k_b^2 - \beta^2}} \frac{H_n'^{(1)}\left(\sqrt{k_b^2 - \beta^2}a\right)}{H_n^{(1)}\left(\sqrt{k_b^2 - \beta^2}a\right)} \right] \cdot
$$

$$
\cdot \left[\frac{1}{\sqrt{k^2 - \beta^2}} \frac{J_n'\left(\sqrt{k^2 - \beta^2}a\right)}{J_n\left(\sqrt{k^2 - \beta^2}a\right)} - \frac{1}{\sqrt{k_b^2 - \beta^2}} \frac{H_n'^{(1)}\left(\sqrt{k^2 - \beta^2}a\right)}{H_n^{(1)}\left(\sqrt{k^2 - \beta^2}a\right)} \right] = .
$$

$$
= n^2 \frac{\beta^2}{k_b^2 a^2} \left(\frac{1}{k^2 - \beta^2} - \frac{1}{k_b^2 - \beta^2} \right)^2
$$

(18)

Still sub-diffraction propagation may be obtained and, not surprisingly, the properties of the chain configuration analyzed in the previous section do appear in the modes guided by these cylindrical nanovoids. In particular, the longitudinal polarization in the array of voids corresponds to the azimuthally symmetric TM_0 mode (both with backward-wave properties), whereas the transverse polarization in the chain corresponds to the forward hybrid quasi-TM_1 mode, consistent with the results in Ref. [41]. The important difference between these two geometries arises in the frequency band in which propagation is supported. If the array of nanovoids supports propagation in a frequency band centered around the resonance of each nanovoid (for the homogeneous sphere case when $\varepsilon_b \simeq -\varepsilon / 2$), the local geometry is drastically changed when the array of inclusions merges into a single infinite nanorod, shifting the propagation band around the plasmonic frequency of the nanorod, which happens for a homogeneous cylinder near $\varepsilon_b = -\varepsilon$ for any order $n > 0$. This is shown in Fig. 9, where we have reported the propagation properties, in both polarizations, of a cylindrical nanorod made of *SiC* in a silver background, with $a = 5\,nm$, consistent with the example in Fig. 8. The plots confirm the correspondence between the cylindrical guided modes and polarization of the modes in the arrays described in the previous section, showing how the cylindrical geometry may provide another possibility for obtaining highly confined guided wave propagation in specific frequency bands of interest with relatively long propagation distances.
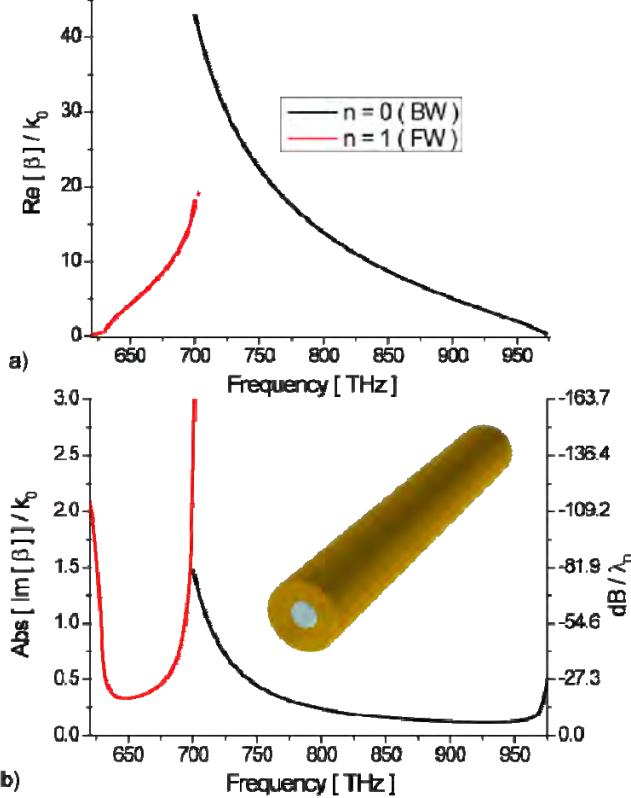
Figure 9 - Dispersion of the real (a) and imaginary (b) part of β, normalized to $\mathrm{Re}\left[-ik_b\right]$ calculated at the central frequency, for a cylindrical nanorod made of *SiC* with radius $a = 5\,nm$ embedded in an unbounded silver background.

We compare more thoroughly the guidance properties of the 1D waveguides analyzed in these two subsections in the following. It would be interesting to compare more thoroughly the propagation along nanovoid arrays and the dual geometry of plasmonic nanoparticle arrays, as well as nanorods and cylindrical nanovoids. In part, we also address this comparison in the following section. However, it is worth noting that it is not straightforward to establish a fair and universal criterion to compare these different waveguide geometries. On the one hand, a thorough comparison would require keeping the same shape of the waveguide and using the same materials, with similar level of losses. However, as it is clear after comparing the dispersion bands in Fig. 7, the guidance regions in these two complementary scenarios would fall in very different frequency bands. For instance, for the longitudinal mode of the arrays of nanovoids in Fig. 8, propagation is expected in the green-blue bands, whereas the dual setup of silver nanoparticles in a *SiC* background would support propagation in the red spectrum. This drastic difference is of course reflected in substantially different properties of the involved plasmonic materials, which affect the overall propagation lengths. Similar considerations are applicable in the case of cylindrical rods.

f.   2D arrays of nanovoids

The extension of the analytical solution presented in Ref. [39] and above to the 2D array of nanoparticles and nanovoids may be performed following the analytical technique that we have

23

recently applied to study the propagation in 3D arrays of plasmonic particles [40], based on the acceleration technique presented in Ref. [73]. In this 2D geometry, Eq. (16) becomes:

$$L: 3\bar{d}_x^{-3}\left[f_3\left(\bar{\beta}_x,\bar{d}_x\right) - i\bar{d}_x f_2\left(\bar{\beta}_x,\bar{d}_x\right)\right] +$$

$$-\sum_{n=1}^{\infty}\sum_{m=-\infty}^{\infty}\frac{\left(\bar{\beta}_x+\dfrac{2\pi m}{\bar{d}_x}\right)^2-1}{\pi\bar{d}_x}K_0\left[n\bar{d}_y\sqrt{\left(\bar{\beta}_x+\dfrac{2\pi m}{\bar{d}_x}\right)^2-1}\right]\cos\left[n\bar{d}_y\bar{\beta}_y\right] = \bar{\alpha}_{ee}^{-1}$$

$$T: 3\bar{d}_x^{-3}\left[f_3\left(\bar{\beta}_x,\bar{d}_x\right) - i\bar{d}_x f_2\left(\bar{\beta}_x,\bar{d}_x\right)\right] +$$

$$-\sum_{n=1}^{\infty}\sum_{m'=-\infty}^{\infty}\frac{\left(\bar{\beta}_x+\dfrac{2\pi m}{\bar{d}_x}\right)^2-1}{\pi\bar{d}_x}K_0\left[n\bar{d}_y\sqrt{\left(\bar{\beta}_x+\dfrac{2\pi m}{\bar{d}_x}\right)^2-1}\right]\cos\left[n\bar{d}_y\bar{\beta}_y\right] +$$

$$-\frac{\bar{\beta}_x^2-1}{2\bar{d}_x\bar{d}_y}\left[\begin{array}{l}\dfrac{1}{\sqrt{\bar{\beta}_x^2+\bar{\beta}_y^2-1}}+\sum_{n'=-\infty}^{\infty}\left(\bar{\beta}_x^2+\left(\bar{\beta}_y^2+\dfrac{2\pi n}{\bar{d}_y}\right)^2-1\right)^{-1/2}+\\[4mm] -\sum_{n=1}^{\infty}\left(\dfrac{\bar{d}_y}{\pi n}+\dfrac{\bar{d}_y^3\left(2\bar{\beta}_y^2-\bar{\beta}_x^2+1\right)}{8\pi^3 n^3}\right)+\xi(3)\dfrac{\bar{d}_y^3\left(2\bar{\beta}_y^2-\bar{\beta}_x^2+1\right)}{8\pi^3 n^3}+\\[4mm] +\dfrac{\bar{d}_y}{\pi}\left(\ln\dfrac{\bar{d}_y\left|\bar{\beta}_x^2-1\right|}{4\pi}+\gamma\right)+i\dfrac{\bar{d}_y}{2}\end{array}\right] = \bar{\alpha}_{ee}^{-1} \tag{19}$$

where β_x,β_y are the components of the propagation wave vector in the *x-y* array plane and d_x, d_y are the spacing distances (i.e. the periodicities in the x and y directions). These formulas are equally valid both for 2D arrays of plasmonic nanoparticles and of nanovoids in a plasmonic background, once again in terms of the individual polarizability of each inclusion $\bar{\alpha}_{ee}^{-1}$. The convergence of the summations in (19) is very fast (few terms are needed for convergence) and the equations are also valid for complex values of $\bar{\beta}$ (due to ohmic absorption or radiation losses in the transparent background case).

The properties of these chains are analogous to those highlighted in Section 2b for the 1D case, even if the operational bandwidth and robustness to losses may be worsened in the transverse polarization when the parallel chains get too close to each other, consistent with our findings in 3D arrays [40]. In the case of nanovoids in a background material, in this 2D case the transverse propagation also implies forward-wave modes and longitudinal propagation corresponds to backward propagation. Longitudinal modes are generally more robust to losses and have a slightly larger frequency bandwidth, and in both scenarios the propagation band is centered around the resonant frequency of the individual inclusions, similar to the 1D arrays.

g. Planar nanolayers

Similar to the 1D geometry, when the nanoparticles or nanovoids are closely packed together, the 2D structure resembles, in the limit, a single planar nanolayer with thickness $2a$, corresponding to the geometry thoroughly analyzed in Ref. [56]. The corresponding dispersion relation for the *TM* modes may be split into even and odd operation, with conditions:

$$
\begin{aligned}
even: \ \tanh\left[\sqrt{\beta^2 - \omega^2\varepsilon\mu_0}\ a\right] &= -\frac{\varepsilon}{\varepsilon_b}\frac{\sqrt{\beta^2 - \omega^2\varepsilon_b\mu_0}}{\sqrt{\beta^2 - \omega^2\varepsilon\mu_0}} \\
odd: \ \coth\left[\sqrt{\beta^2 - \omega^2\varepsilon\mu_0}\ a\right] &= -\frac{\varepsilon}{\varepsilon_b}\frac{\sqrt{\beta^2 - \omega^2\varepsilon_b\mu_0}}{\sqrt{\beta^2 - \omega^2\varepsilon\mu_0}}
\end{aligned}
\tag{20}
$$

As we have shown in Ref. [56], this geometry also fully supports the nanocircuit interpretation, acting as an infinite cascade of nanoinductors and nanocapacitors arranged in series or in parallel as a function of the polarization of the local electric field. In particular, the longitudinal polarization in the 2D nanochain/nanovoids problem corresponds to the odd *TM* modes in the planar layer geometry, and correspondingly transverse polarization corresponds to the even modes. This is confirmed by the backward (forward) nature of the odd (even) modes in the metal-insulator-metal geometry [56]. Moreover, in this case the propagation band is generally located around the resonance of the layer (when $\varepsilon_b = -\varepsilon$), even if usually the bandwidths over which propagation takes place in this planar layer geometry are very large. In the following section, we compare the different types of plasmonic waveguides that we have introduced in this section, highlighting the differences among them and the potentials that they may offer for different applications.

h. Figure of merit for different plasmonic waveguides: 1D propagation

Following Sections 2b-c, 1D plasmonic waveguides may be envisioned as linear arrays of plasmonic nanoparticles in a transparent background, nanovoids in a plasmonic background, and cylindrical nanorods. In all these scenarios, the field distribution away from the interface between plasmonic and dielectric materials decays as $K_i\left(\sqrt{\beta^2 - \omega^2\varepsilon_b\mu_0}\ \rho\right)$, where ρ is the radial coordinate with respect to the axis of propagation, $K_i(.)$ is the modified Hankel function and $i = 1$ for azimuthally symmetric modes (the longitudinal mode in the array geometries and the TM_0 modes in the cylindrical structures), whereas $i = 2$ for the transverse polarization and the hybrid quasi-TM_1 modes [39]-[41]. This allows one to evaluate the beam cross section as the distance ρ_0 for which the field amplitude is decreased to e^{-1} of its value at $\rho = a$. It is clear that ρ_0 decreases for larger $\text{Re}[\beta]$, since the mode is more concentrated around the waveguide. Not surprisingly, decreasing the waveguide radius a for a given frequency, $\text{Re}[\beta]$ increases, in principle without any limit, supporting the possibility of highly confined sub-diffractive guided wave propagation.

25

On the other hand, we may define the attenuation length L as the propagation length along the x axis for which the modal field has decreased to e^{-1} of its original value due to ohmic (and in general radiation) losses. It is noted that, due to the same definition of β, $L = \left(\text{Im}[\beta] \right)^{-1}$.
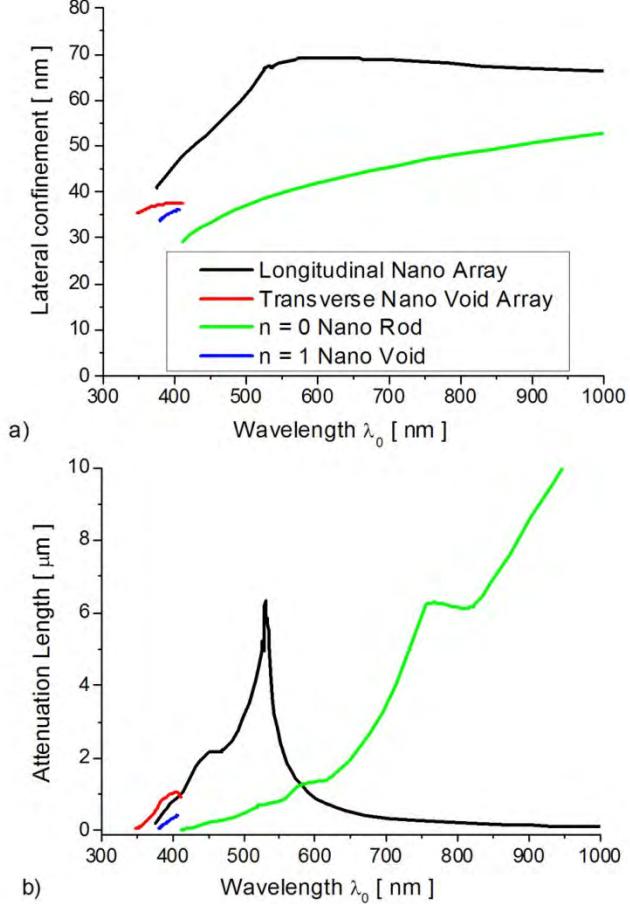
Figure 10. Dispersion of the lateral confinement (a) and attenuation length (b) for four different forward-wave 1-D waveguides employing silicon-nitride and silver with $a = 25\,nm$.

As a first example, in Fig. 10 we compare the guidance properties of four different 1D forward-wave waveguides composed of silver Ag (as the plasmonic material) and silicon-nitride Si_3N_4 (as the dielectric), in particular for the cases of: (a) silver nanoparticles embedded in the silicon-nitride background with longitudinal polarization, (b) silicon-nitride nanovoids in silver background with transverse polarization, (c) silver nanorod in silicon-nitride background with TM_0 mode, and (d) a silicon-nitride nanocylinder in silver background with quasi-TM_1 hybrid mode. It is important to stress that for a fair comparison of the different performance of these different waveguides, in this section we have used the experimental values of the silver permittivity as extracted from Ref. [27]. This is different from the simplified Drude model used in the previous section, which does not take into account the interband transitions of silver in the near-UV. We have preferred the Drude model in the previous section because it provides a clearer and more predictable behavior with frequency, providing some intuitive insights into the effect of frequency dispersion on the modal propagation of these sub-diffractive modes.

26

However, in this section we use realistic experimental values of silver permittivity, to ensure the higher accuracy of these results even near the UV band.

In Fig. 10a we plot the variation of the lateral confinement ρ_0 versus the operation wavelength (in free-space) λ_0, whereas in Fig. 10b we report the corresponding variation of the attenuation length L. In all these examples the radius of the waveguide is $a = 25\,nm$ and for the array cases the distance between neighboring spherical inclusions is $d = 2.1a$. Several features are evident from these plots: first of all, in all these geometries it is possible to confine the propagating beam, over a given frequency band, in a cross section much smaller than the usual diffraction limit ($\lambda_0 / 2$). These sub-diffractive beams may propagate over several wavelengths without diffraction and with relatively low damping, despite the strong concentration of the guided beam and the material absorption (and possibly radiation in the cases of transparent backgrounds).
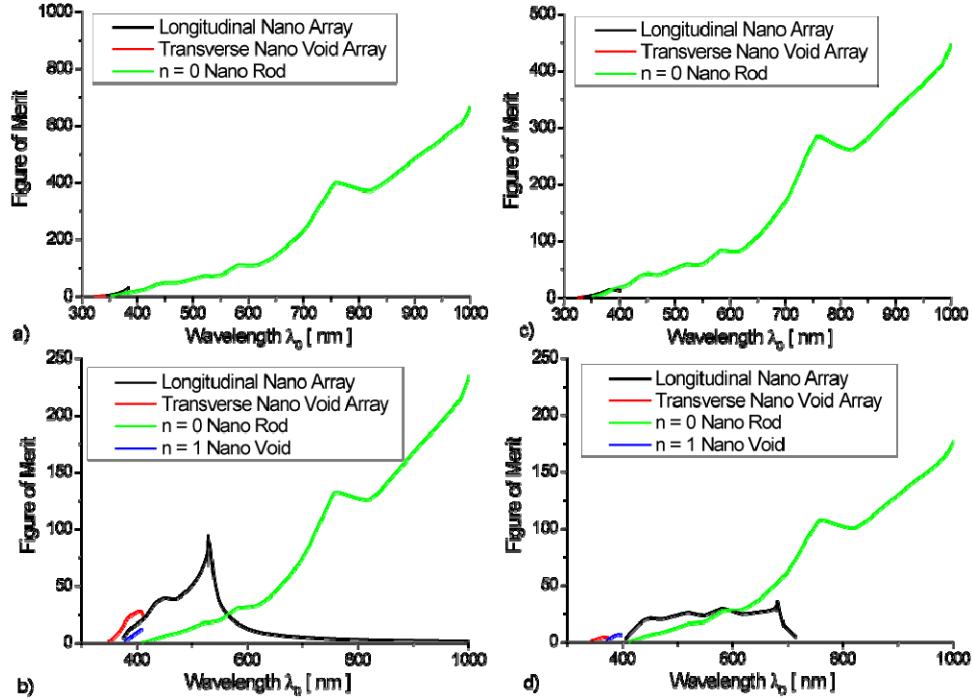
Figure 11 - Figure of merit for the four classes of forward-wave 1D waveguides in Fig. 10 (when available) for four different scenarios: (a) silver and free-space with $a = 25\,nm$; (b) silver and silicon-nitride with $a = 25\,nm$ (corresponding to Fig. 10); (c) silver and free-space with $a = 5\,nm$; (d) silver and silicon-nitride with $a = 5\,nm$.

The available bandwidth is usually much larger for cylindrical waveguides, whereas the propagation along chain of particles is usually possible only over a relatively narrower bandwidth (still large enough for many applications) around the resonance frequency of the inclusions composing the array, which in this case happens near the wavelength for which $\varepsilon_{Ag} = -2^{\pm 1}\varepsilon_{Si_3N_4}$ (with the plus minus depending on whether the silver composes the inclusions or the background). Depending on the frequency band and the application of interest, arrays of particles or cylindrical waveguides may be more or less appealing. For instance, in this geometry the array of nanovoids appears very suitable in the optical frequency range, providing the longest propagation distance together with a good beam confinement. At lower frequencies, the

27

cylindrical plasmonic nanorod seems the most suitable solution for this combination of materials, due also to the larger bandwidth of propagation.

A clear general trend is evident in Fig. 10, which applies to all these classes of plasmonic waveguides: a trade-off should be sought between beam lateral confinement and attenuation length. Even if in principle there is not an upper limit to the value of $\mathrm{Re}[\beta]$ (and therefore to the beam lateral confinement), the value of $\mathrm{Im}[\beta]$ indeed usually grows accordingly, effectively limiting the possibility of realizing highly confined ultra-sub-diffractive waveguides with reasonably long attenuation lengths. In the following, therefore, we define a figure of merit as the ratio $F = L / \rho_0$, in order to effectively compare waveguides with different sizes and geometries.

Figure 11, for instance, compares, when available, the four different scenarios of Fig. 10 using two different dielectric materials (free-space, Fig. 11a,c; silicon-nitride, Fig. 11b,d) and two different radii ($a = 25\,nm$, Fig. 11a,b; $a = 5\,nm$, Fig. 11c,d). For each panel only some waveguides may support a propagating mode with sufficient robustness to propagation despite the material absorption, as indicated in the legend. Even though the trends are consistent in the four panels, important differences arise. For instance, a larger radius usually allows reaching larger figures of merit, due to the lower field concentration in the plasmonic materials. Moreover, the free-space as dielectric ensures larger figures of merit at low frequencies, since the mode can be more spread (with lower beam concentration) in the transparent region, even though the chain configuration in the plasmonic background may achieve relatively large figures of merit at optical wavelengths.
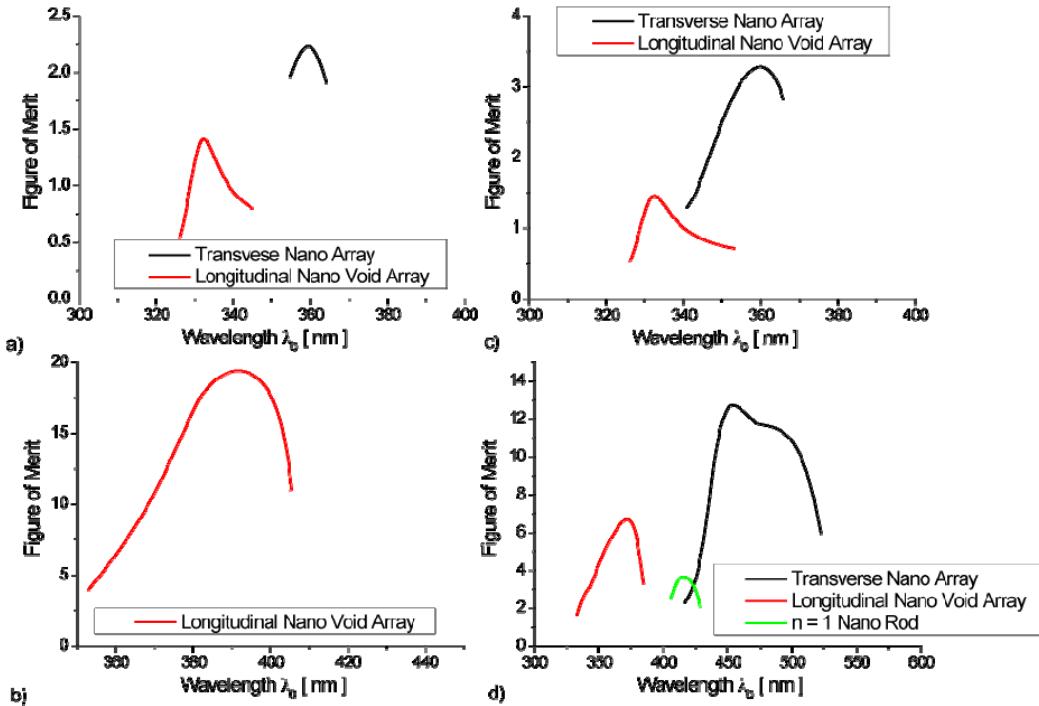
Figure 12. Similar to Fig. 11, but for four backward-wave 1D waveguides (dual of those in Fig. 11, when available) for: (a) silver and free-space with $a = 25\,nm$; (b) silver and silicon-nitride with $a = 25\,nm$ (corresponding to Fig. 10); (c) silver and free-space with $a = 5\,nm$; (d) silver and silicon-nitride with $a = 5\,nm$.

28

Figure 12 refers to the backward modes supported by the dual geometries or polarizations, employing the same materials. In this case, the modes are supported only by some combinations, since backward modes are usually more challenging to be supported. However, consistent with Fig. 8, for small radii the nanovoid linear array supports a fairly robust longitudinal mode with backward-wave properties that may achieve, over a reasonable bandwidth, considerable figures of merit, as reported in Fig. 12b. This may provide some interesting possibility to realize left-handed nanotransmission lines at optical frequencies. The cylindrical rods, on the other hand, do not easily support backward modes with sufficient robustness to losses. If the interest is merely in field confinement and propagation length, the best option and the largest figure of merit is usually obtained with forward-mode waveguides.
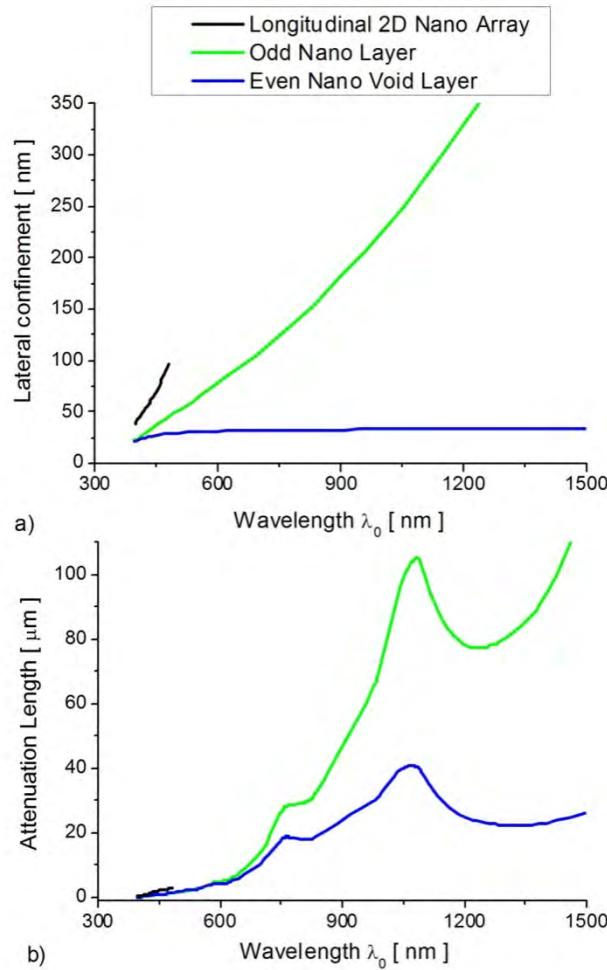
Figure 13. Similar to Fig. 10, but for 2D geometries, dispersion of the lateral confinement (a) and attenuation length (b) for three different forward-wave 2-D waveguides employing silicon-nitride and silver with $a = 25 nm$.

i. *Figure of Merit for Different Plasmonic Waveguides: 2D propagation*

We may perform an analogous analysis for the different types of 2D waveguides, i.e., 2D planar arrays of nanoparticles or nanovoids and planar nanolayers with different combinations of plasmonic and dielectric materials. In this scenario, the field distribution decays in the transverse

29

direction as $e^{-\sqrt{\beta^2 - k_b^2}\, z}$, therefore $\rho_0 = a + \left(\sqrt{\mathrm{Re}[\beta]^2 - k_b^2}\right)^{-1}$. In the case of 2D arrays of inclusions, sufficiently small $d_x = d_y$ ensure isotropic propagation in two dimensions, analogous to the planar layers. In the following, for comparison, we analyze this situation.

Figure 13 reports the dispersion of ρ_0 and L for three classes of plasmonic 2D forward waveguides, consisting of a planar array of silver nanoparticles in a silicon-nitride background (with longitudinal polarization), a silver planar nanolayer surrounded by silicon-nitride (odd mode) and a Si_3N_4 nanolayer in a silver background (even mode). For the planar array of nanoparticles we have assumed isotropic guidance properties, i.e., same interspacing $d_x = d_y = 2.1a$ in the plane of propagation. In all the cases $a = 25\,nm$ is the nanosphere radius or the half-thickness of the nanolayer. The dual scenario of silicon-nitride voids in a silver background does not support a forward mode with sufficiently low damping in this configuration, so it has not been reported in the figure.
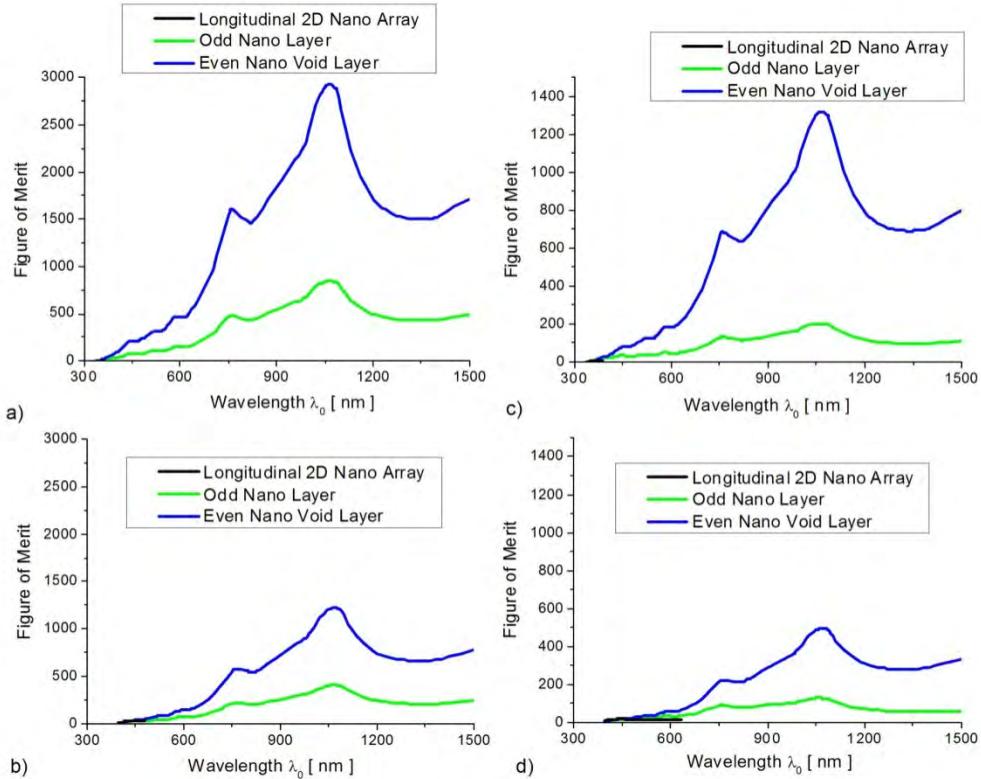
Figure 14. Similar to Fig. 11, but for three forward-wave 2D waveguides for: (a) silver and free-space with $a = 25\,nm$; (b) silver and silicon-nitride with $a = 25\,nm$ (corresponding to Fig. 8); (c) silver and free-space with $a = 5\,nm$; (d) silver and silicon-nitride with $a = 5\,nm$.

It is noticed that the propagation properties are analogous to the 1D case, even if the bandwidth and guidance properties of the arrays of nanoinclusions are somehow worsened by the coupling between closely packed parallel arrays. The plasmonic nanolayer geometry may achieve very long propagation distances, at the expenses of worse beam confinement. On the other hand, in the infrared the dielectric planar gap in a silver background performs well, similar to a parallel-plate waveguide, confining the field in a sub-diffractive quasi-TEM mode with long propagation

30

distances. In the 2D scenario this parallel-plate silver configuration seems the most adequate for guidance and in this sense the advantages of a plasmonic background, as outlined in the previous sections, are evident in Fig. 13.

Figure 14 shows the figure of merit dispersion for four different geometries, consistent with the results of Fig. 11, but for the 2D case. Here it is even more evident how the plasmonic background allows confinement in the waveguide in a sub-diffractive region, still ensuring sufficiently low-damping. At optical frequencies the 2D arrays of nanovoids may also be employed in this configuration with good performance. (As an aside, it should be noted that the central frequency for the propagation band in the array geometries may be tailored at will by changing the geometry of each inclusion, or the involved materials, as outlined in the previous section. In this geometry the resonance between silver and air or silicon-nitride happens in the visible, but THz plasmonic materials, like silicon carbide, or multi-layered particles, may shift the propagation band at will).
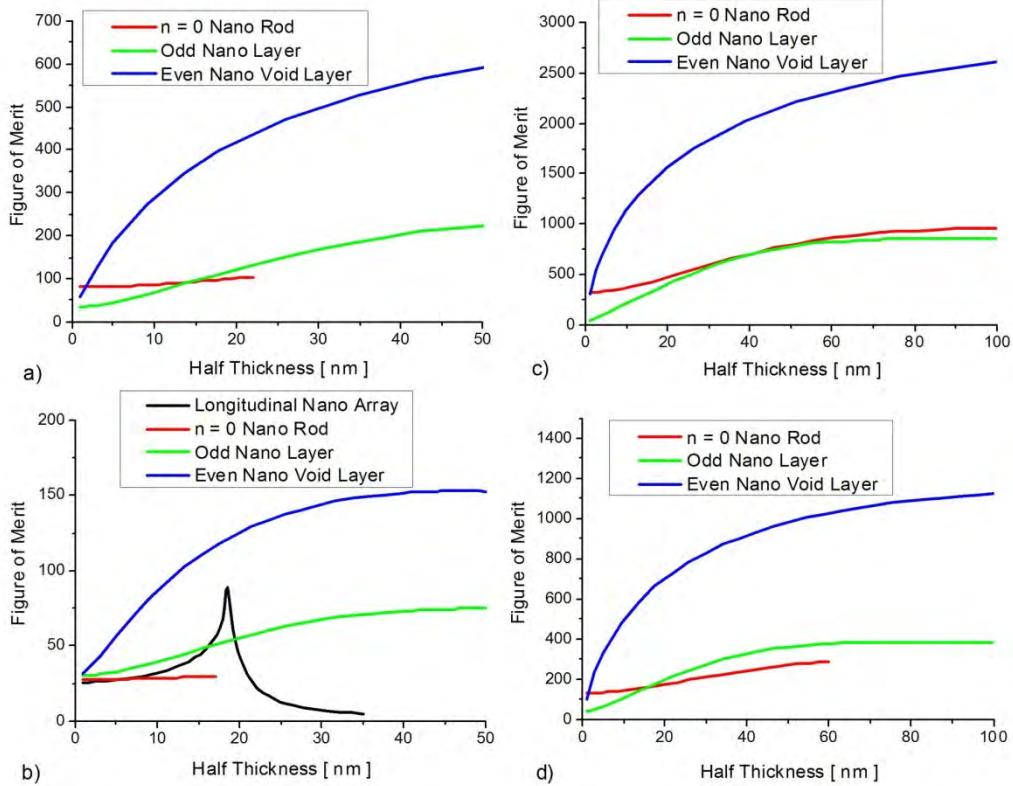
Figure 15. Variation of the figure of merit for forward 1D and 2D waveguides as a function of the half-thickness a for: (a) silver and free-space at $\lambda_0 = 600\,nm$; (b) silver and silicon-nitride at $\lambda_0 = 600\,nm$ (corresponding to Fig. 13); (c) silver and free-space at $\lambda_0 = 1.5\,\mu m$; (d) silver and silicon-nitride at $\lambda_0 = 1.5\,\mu m$.

As a last example, Fig. 15 shows the variation of F, for the classes of forward waveguides in 1D and 2D geometries, with the half thickness a of the waveguide, for the same combinations of materials as in the previous examples. The panels refer to an optical wavelength ($\lambda_0 = 600\,nm$, Fig. 10a-b) and a typical telecommunication wavelength ($\lambda_0 = 1.5\,\mu m$, Fig. 10c-d). These charts show how the figure of merit tends to increase for larger waveguides and it is in general larger at

31

lower frequencies and for $Si_3N_4 - Ag$ combinations. The potential advantages of a plasmonic background in guidance and confinement are evident also in these charts.

j. Conclusions

We have considered and compared in this section eight different solutions for guiding optical beams with highly confined sub-diffractive cross-sections and reasonable propagation distance, comparing their potential advantages and drawbacks. In particular, we have compared, both in 1D and 2D geometries, plasmonic waveguides embedded in a transparent background, and the dielectric waveguides in a plasmonic background, showing how the latter may arguably provide better figures of merit in terms of propagation distances versus lateral cross-section. The analogies and differences between arrays of particles and continuous rods and layers have been outlined, showing how the latter may provide wider guidance bands, whereas the former may show larger figures of merit and propagation lengths, but more limited bandwidth of operation concentrated around the resonances of the inclusions composing the arrays. These results may be of interest for the design and realization of plasmonic waveguides, with potentials in optical communications and nanocircuit applications.

5. Radiation and Leaky-Waves along Linear Arrays

a. Summary

We analyze in this section the leaky-wave properties of linear arrays of plasmonic nanoparticles. It is shown that such periodic arrays may support two orthogonal leaky-wave propagation regimes, respectively with longitudinal and transverse polarization. Using closed-form dispersion relations derived in the complex domain, consistent with the previous sections, we analyze their properties in the leaky-wave regime and we derive general conditions under which a nanoparticle array with sub-wavelength lateral cross section may support a radiating leaky mode with directive properties, conical radiation, frequency scanning and sufficiently long propagation distance, paving the way to potential applications as a leaky-wave optical nanoantenna with sub-diffractive properties. Realistic designs and configurations are presented, considering the material dispersion and absorption of optical materials, for which we determine propagation distance, near-field distribution and far-field leaky-wave radiation pattern.

b. Introduction

The miniaturization of electronic and optical devices is one of the main challenges in modern communications and computer technology. Various concepts and devices, well-established in microwave engineering, have been transplanted to optical frequencies, at which the characteristic size and operating wavelength are orders of magnitude smaller, and frequency bandwidths are proportionally larger. One successful example is represented by optical nanoantennas [74]-[82], which have been inspired in recent years by well-established concepts at radio frequencies[83]. As another example, in microwave technology the electromagnetic properties of periodic structures play a crucial role in several devices. Various periodic structures, such as slot arrays and frequency selective surfaces, are widely applied as antennas and filters. Recent advances in nanotechnology have made possible to extend also these concepts to optical frequencies, where periodic structures, arrays and nanoscale metamaterials have been recently investigated for a variety of applications.

As one of the interesting applications of periodic arrays at radio frequencies for radiation applications, leaky-wave antennas are a well-established technology that provides directive radiation and frequency beam scanning [83]-[85]. The recent application of metamaterial concepts has provided novel possibilities for leaky-wave antenna design and operation at microwave frequencies [86]-[88]. Translating these concepts to the optical domain may open new areas in optical communications, control of radiation and optical computing. In this regard, periodic arrays of nanoparticles have already been considered by various groups as optical waveguides with confined beams, overcoming the optical diffraction limit [89]-[98]. Dielectric waveguides are generally limited by diffraction to have a transverse cross section comparable with the wavelength, as guided optical beams tend to spread in the background material when the waveguide is too thin [99]. However, the use of plasmonic materials, and arrays of subwavelength plasmonic nanoparticles in particular [89]-[98], may overcome this limitation and confine a guided optical beam over a transverse cross-sections significantly smaller than the wavelength, supporting sub-diffractive propagation with relevant applications in optical computing and communications.

This same nanoparticle array, which is realizable within available nanofabrication technology, may also provide an interesting way of realizing leaky-wave nanoantennas with sub-wavelength lateral cross-section and directive radiation at a specific angle in the far-field. Our group has theoretically investigated in the past guided-wave propagation along linear chains of plasmonic and metamaterial particles as optical nanotransmission lines with sub-diffractive properties [100]. Our contribution to this problem consisted in the derivation of a closed-form dispersion relation for real and complex dipolar modes supported by such arrays, with the only approximation being the neglect of multipoles of higher order than the dominant dipolar contribution from each particle. In particular, this formulation makes it possible to deal with the presence of realistic losses and damping for the guided modes, extending previous analyses that were limited to real wave numbers to the complex domain by an analytic continuation technique [100]. Similarly, this technique may be applied to problems involving radiation losses, coming into play when the wave energy is not totally guided along the particle chain, but partially leaked out, as it happens in leaky modes.

As mentioned above, the idea of energy leakage is widely applied in microwave engineering to design directive radiators with beam scanning capabilities. A leaky mode is a fast eigenmode of the structure with complex wave number, whose real part is less than the free-space wave number [101]. This ensures that the energy is not confined along the array, and the Poynting (power flux) vector points towards the lateral direction. Provided that the imaginary part of the leaky wave number is sufficiently small, the radiation from the chain may become very directive, producing a conical directive beam at a given angle from the array axis. At microwaves, leaky-wave antennas are usually obtained by perturbing a guided wave with periodic defects, as in a periodically loaded micro-strip line [102]-[104]. It is challenging, however, to produce defects within a sub-wavelength transverse cross-section, since in such case they tend to weakly interact with the mode of interest, which is usually weakly confined. This is another clear symptom of the diffraction limit of guided beams in free-space. For this reason, the leaky-wave antenna transverse cross section is usually comparable with the wavelength of operation. In optics, surface plasmons may be able to confine the energy within sub-wavelength cross-sections, and there has been some interest in using energy leakage from thin plasmonic films for near field microscopy [105]-[107].

In this work, stemming from our previous analysis of guided modes along periodic linear arrays of sub-wavelength nanoparticles, as reported in part in the previous sections, we analyze the potential of this geometry to support leaky-waves with directive radiation properties in the optical regime, even in the limit in which it has sub-wavelength (i.e., not limited by the diffraction limitations mentioned above) lateral cross section, in order to form a sub-diffractive optical leaky-wave nanoantenna. This may lead to the possibility to connect distant points of an optical nanocircuit board [108] and create point-to-point links at the nanoscale. In this context, interest in tailoring the optical radiation from linear and planar arrays of nanoparticles, forming Yagi-Uda nanoantenna arrays [109]-[110] or planar reflectarrays [111]-[112], has been recently discussed in several exciting papers. In the following, we derive relevant design parameters and underline the fundamental and general limitations and challenges to the practical realization of leaky-wave nanoantennas as linear arrays of plasmonic nanoparticles. It should be mentioned that an extensive analysis of the complex modes supported by 1-D, 2-D and 3-D arrays of magnetodielectric particles has been recently reported [113], including some aspects of the leaky-wave propagation along sub-wavelength arrays of dielectric and magnetodielectric spheres with large index of refraction. Our general analysis is focused here on plasmonic nanoparticle arrays, which may ensure the application of these concepts at optical frequencies and may provide inherent advantages associated with their anomalous light interaction.
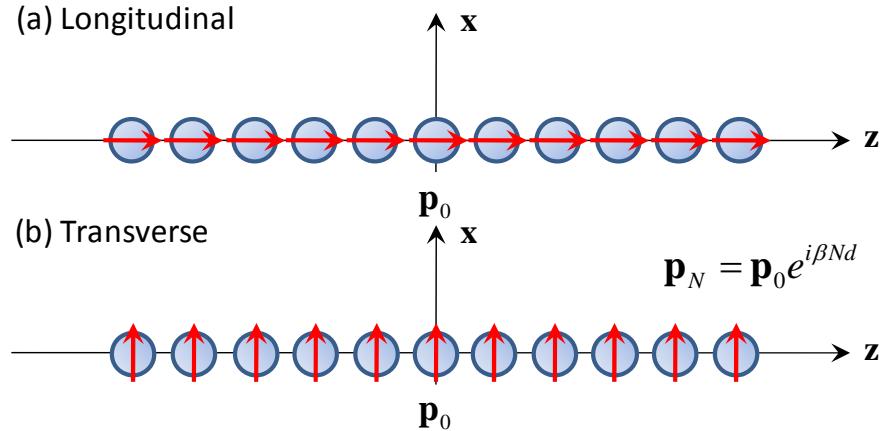
Figure 16 - Geometry under consideration: a linear array of polarizable nanoparticles supporting a longitudinal (a) or a transverse (b) eigenmode.

c. *Theoretical formulation*

Consider an infinite linear array of particles oriented along the z axis, periodically located at $z = Nd$, with d being the center-to-center distance and N being any positive or negative integer, consistent with the geometry analyzed in Ref. [100]. Provided that the nanoparticle size is much smaller than the wavelength of operation, as assumed in the previous sections, its wave interaction is dominated by the dipolar scattering and each element may be safely modeled as a polarizable dipole, fully characterized by its electric polarizability α_{ee}. As commonly done [114], and consistent with the analytical theory in Ref. [100], if $\mathbf{p}_0 = \alpha_{ee}\mathbf{E}_0$ is the dipole moment induced by a local electric field $\mathbf{E}_0$ on the particle at $z = 0$, it is possible to derive a self-sustained eigensolution traveling along the array in the form $\mathbf{p}_N = \mathbf{p}_0 e^{i\beta Nd}$, under an $e^{-i\omega t}$ time convention. Here, β is the complex propagation factor, fully characterizing its propagation and

34

radiation properties. As reported in several papers on the topic [90]-[100], the complete eigenmode spectrum may be split into longitudinal and transverse polarizations, consistent respectively with Fig. 16(a) and Fig. 16(b). The dispersion relations for these two polarizations may be respectively written [100], consistent with the previous sections:

$$L: 3\bar{d}^{-3}\left[f_3\left(\bar{\beta},\bar{d}\right) - i\bar{d} \, f_2\left(\bar{\beta},\bar{d}\right)\right] = \bar{\alpha}_{ee}^{-1}$$

$$T: -\frac{3}{2}\bar{d}^{-3}\left[f_3\left(\bar{\beta},\bar{d}\right) - i\bar{d} \, f_2\left(\bar{\beta},\bar{d}\right) - \bar{d}^2 f_1\left(\bar{\beta},\bar{d}\right)\right] = \bar{\alpha}_{ee}^{-1}$$

(21)

where $\bar{d} \equiv k_0 d$, $\bar{\beta} \equiv \beta/k_0$, $\bar{\alpha}_{ee} \equiv k_0^3 \alpha_{ee}/(6\pi\varepsilon_0)$, $k_0 \equiv \omega\sqrt{\varepsilon_0\mu_0}$, and ε_0, μ_0 are the permittivity and permeability of background medium, respectively. In addition:

$$f_N\left(\bar{\beta},\bar{d}\right) = \mathrm{Li}_N\left(e^{i(\bar{\beta}+1)\bar{d}}\right) + \mathrm{Li}_N\left(e^{-i(\bar{\beta}-1)\bar{d}}\right)$$

(22)

and $\mathrm{Li}_N(x)$ is the polylogarithm function, as defined in Ref. [116]. Due to the inherent periodicity of the Floquet modes of the linear chain, we limit our analysis to the principal period $\left|\mathrm{Re}\left[\bar{\beta}\right]\right| \leq \pi/\bar{d}$.

The form of dispersion relation (21) is valid for any real or complex value of β, ensuring that it may be employed to study guided [100] as well as leaky-wave propagation along the linear chains. In our previous work, we have discussed guided propagation along arrays of extremely sub-wavelength particles, showing that the condition $\mathrm{Im}\left[\bar{\alpha}_{ee}^{-1}\right] = -1$ is required for the involved nanoparticles to support a real solution for β (guided modes with no decay) [100]. This condition is identically met for passive dipolar particles only when absorption may be neglected [114],[117], as physically expected, and it implies that $\mathrm{Re}\left[\bar{\beta}\right] \geq 1$ in Eq. (21). If the lossless condition is not satisfied ($\mathrm{Im}\left[\bar{\alpha}_{ee}^{-1}\right] < -1$), then absorption takes place in the nanoparticle array and the eigenwave numbers are necessarily complex, whose imaginary part is associated with the damping caused by Ohmic loss.

Even in the lossless scenario, however, complex solutions are allowed when $\left|\mathrm{Re}\left[\bar{\beta}\right]\right| < 1$ (fast leaky modes), when $1 < \left|\mathrm{Re}\left[\bar{\beta}\right]\right| < \pi/\bar{d}$ (complex modes) or when $\left|\mathrm{Re}\left[\bar{\beta}\right]\right| = \pi/\bar{d}$ (stop-band). In the following, we are interested in leaky modes with sufficiently low $\mathrm{Im}\left[\bar{\beta}\right]$, which may provide directive radiation and sustained propagation over a reasonable electrical length, analogous to the operation of microwave leaky-wave antennas [83]. For $\bar{d} < \pi$ (sufficiently tight arrays, which is required for leaky radiation, as we note in the following), the first-order Bloch mode dominates the far-field pattern, which may be therefore evaluated by simply assuming an averaged current line distribution along the z axis with amplitude $-i\omega\mathbf{p}_0 e^{i\beta z}/d$, consistent with Ref. [115]. In this case, the magnetic potential $\mathbf{A}$ may be written in the two polarizations as:

$$\mathbf{A} = \frac{\omega\mu_0\mathbf{p}_0}{4d} H_0^{(1)}\left(\sqrt{k_0^2 - \beta^2}\rho\right)e^{i\beta z}$$

(23)

35

where ρ is the radial coordinate in the suitable cylindrical reference system with axis along the cylinder. The electric and magnetic far-field distributions may be easily derived as $\mathbf{H} = \nabla \times \mathbf{A} / \mu_0$, $\mathbf{E} = \nabla \times \mathbf{H} / (-i\omega\varepsilon_0)$.

This implies that a complex value of β necessarily requires a non-zero power flux and phase propagation along the radial direction. In particular, for $\mathrm{Im}[\beta]$ sufficiently small, Eq. (23) represents a standard guided-wave mode for $\mathrm{Re}[\beta] > k_0$, with exponential decay rate in the radial direction given by Ref. [100]:

$$\begin{cases} L: & K_1\left(\sqrt{\mathrm{Re}[\beta]^2 - k_0^2}\,\rho\right) \\ T: & K_2\left(\sqrt{\mathrm{Re}[\beta]^2 - k_0^2}\,\rho\right) \end{cases} \tag{24}$$

and a leaky mode when $\mathrm{Re}[\beta] < k_0$, with conical beam radiation at an angle $\theta = \cos^{-1}\left[\mathrm{Re}\left[\bar{\beta}\right]\right]$ from the z axis. In such case, the decay rate is the one of a cylindrical wave $1/\sqrt{\rho}$ and the corresponding intensity pattern is well approximated by [84]:

$$I(\theta) = \frac{\sin^2\theta}{\left(\cos\theta - \mathrm{Re}\,\bar{\beta}\right)^2 + \left(\mathrm{Im}\,\bar{\beta}\right)^2}. \tag{25}$$

The radiation beamwidth of the main conical lobe is calculated as:

$$BW = 2\,\mathrm{Im}\,\bar{\beta} / \sin\theta_0, \tag{26}$$

which ensures that the directivity of radiation, a measure of how oriented and narrow the far-field radiation pattern is towards the desired direction, is inversely proportional to $\mathrm{Im}\left[\bar{\beta}\right]$.

It should be emphasized in this context that a complex solution of Eq. (21) implies in principle a diverging distribution of the induced dipole distribution along the array, which may raise some questions about the validity of its analytical continuation in the complex domain. It is noticed, however, that similar concerns arise any time we deal with complex eigensolutions of the wave equation, i.e., in regular leaky-wave configurations, or even in surface-wave propagation along lossy interfaces. Similar to such cases, this divergence arises only because of the assumption of an infinite array. Leaky-wave solutions do not represent proper contributions to the radiated spectrum of the chain, but they indeed dominate the steepest-descent approximation in specific angular regions of the visible spectrum, and therefore they constitute an accurate and effective description of the far-field distribution of the chain in a variety of realistic applications [83]. In practice, their divergence does not constitute an issue, since we are interested in solutions with small $\mathrm{Im}[\beta]$ and finite chain lengths, for which the localized excitation (which may be represented by an emitting molecule or a quantum dot in this scenario at optical frequencies) is at a finite location along the array [118].

36
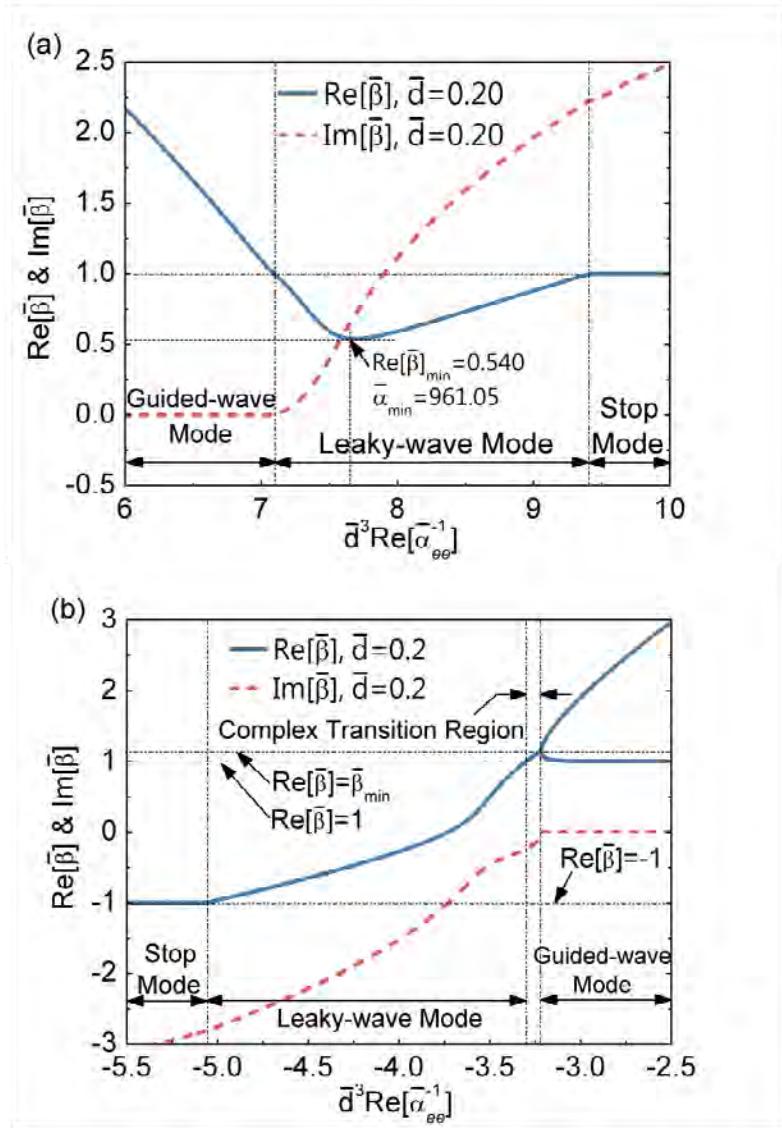
Figure 17 - Variation of complex $\bar{\beta}$ in (a) longitudinal and (b) transverse polarization versus the normalized inverse polarizability of the nanoparticles composing the array. Here we consider a normalized center-to-center distance $\bar{d} = 0.2$.

d. General properties of the leaky-wave eigensolution

In this section, we report our investigation on the general properties of the complex solutions of Eq. (21), with special attention to the leaky-wave regime. In order to make the analysis very general, we focus in this section on the variation of complex $\bar{\beta}$ with the normalized quantity $\text{Re}\left[\bar{\alpha}_{ee}^{-1}\right]$, which compactly describes the general properties of the individual nanoparticles forming the array. It is noticed, in particular, that $\text{Im}\left[\bar{\alpha}_{ee}^{-1}\right]$ is simply associated with the absorption properties of the particles, and it is forced to be $\text{Im}\left[\bar{\alpha}_{ee}^{-1}\right] = -1$ when the particles are lossless. The available degrees of freedom to tailor the leaky-wave properties of the array are

37

therefore compactly represented, to within the dipolar approximation, by $\mathrm{Re}\left[\bar{\alpha}_{ee}^{-1}\right]$, which is a function of the geometrical and material properties of the nanoparticles. In the next sections, we will provide specific examples of nanoparticle geometries that may synthesize the required values of $\mathrm{Re}\left[\bar{\alpha}_{ee}^{-1}\right]$ obtained in this section.

As a first example, in Figure 17 we report the variation of complex $\bar{\beta}$ as a function of the normalized parameter $\bar{d}^3\,\mathrm{Re}\left[\bar{\alpha}_{ee}^{-1}\right]$, for an interparticle distance $\bar{d}=0.2$. We consider here lossless particles with $\mathrm{Im}\left[\bar{\alpha}_{ee}^{-1}\right]=-1$. As seen in Fig. 17(a), the longitudinally polarized eigenmodes have a smooth transition from the guided-wave to the leaky-wave region at $\mathrm{Re}\left[\bar{\beta}\right]=1$. The lossless nature of the particles ensures $\mathrm{Im}\left[\bar{\beta}\right]=0$ in the guided region $\mathrm{Re}\left[\bar{\beta}\right]>1$. As the wave number enters the region $\mathrm{Re}\left[\bar{\beta}\right]<1$, the imaginary part starts increasing, due to the conical radiation of the leaky mode at an angle $\theta_0=\cos^{-1}\left[\mathrm{Re}\left[\bar{\beta}\right]\right]$. It is recognized that the guided modes in this longitudinal polarization are inherently forward in nature, since the slope $\partial\mathrm{Re}\left[\bar{\beta}\right]/\partial\mathrm{Re}\left[\bar{\alpha}_{ee}^{-1}\right]$ is negative. As explicitly proven in Ref. [100], in fact, the slope of the curves in Fig. 17 is directly related to whether the modes are forward (negative slope) or backward (positive), which directly determines the sign of $\partial\mathrm{Re}\left[\beta\right]/\partial\omega$ for passive particles in regions in which $\mathrm{Im}\left[\bar{\beta}\right]$ is negligible.

Also in the leaky-wave regime, for low $\mathrm{Im}\left[\bar{\beta}\right]$ negative slope is preserved, but, for the value $\bar{\alpha}_{ee}^{-1}=\bar{\alpha}_{\min}^{-1}$, the real part of $\bar{\beta}$ reaches a minimum at $\bar{\beta}_{\min}$ and then returns to $\mathrm{Re}\left[\bar{\beta}\right]=1$. Similar arguments apply in the low-damping region $\bar{\alpha}_{ee}^{-1}>\bar{\alpha}_{\min}^{-1}$, ensuring that the supported longitudinal leaky-wave modes are forward, improper[119] in nature, as also verified by the fact that $\mathrm{Re}\left[\bar{\beta}\right]/\mathrm{Im}\left[\bar{\beta}\right]>0$, (phase and group velocities are parallel with each other) in the region with small $\mathrm{Im}\left[\bar{\beta}\right]$. This follows from the modal dependence $e^{i\beta z}$, which ensures that the phase propagation is in the same direction as the power flow and energy decay, under the condition $\mathrm{Re}\left[\bar{\beta}\right]/\mathrm{Im}\left[\bar{\beta}\right]>0$.

The level of radiation damping monotonically increases with $\mathrm{Re}\left[\alpha_{ee}^{-1}\right]$, implying that the range $\mathrm{Re}\left[\alpha_{ee}^{-1}\right]<\alpha_{\min}^{-1}$ is preferable for more directive radiation. This is physically expected, since this is the region closer to the resonance of the individual nanoparticles composing the array, which always arises at $\mathrm{Re}\left[\alpha_{ee}^{-1}\right]=0$. Longitudinal leaky modes are inherently supported for positive values of $\mathrm{Re}\left[\alpha_{ee}^{-1}\right]$, due to their forward nature, since causality requires[100] $\dfrac{\partial\mathrm{Re}\left[\alpha_{ee}^{-1}\right]}{\partial\omega}\leq 0$.

It is worth noticing that the point of minimum $\mathrm{Re}\left[\bar{\beta}\right]=\bar{\beta}_{\min}$ arises close to the crossing $\mathrm{Re}\left[\bar{\beta}\right]=\mathrm{Im}\left[\bar{\beta}\right]$ in the plot of Fig. 17a. This point may be considered the cut-off of the leaky-

38

wave regime, since for $\bar{\alpha}_{ee}^{-1} > \alpha_{\min}^{-1}$ the leaky-wave radiation is damped by rapid longitudinal decay, and its directivity is very limited. The occurrence of a cut-off for leaky modes close to where $\mathrm{Re}\left[\bar{\beta}\right] = \mathrm{Im}\left[\bar{\beta}\right]$ is well known in a variety of leaky-wave antennas[85], and it is verified in this geometry for different values of $\bar{d}$ in Fig. 18. It is interesting to note that this cut-off arises here around the region of minimum $\bar{\beta}$.

In the transverse polarization (Fig. 17b), the guided confined branch (right in the figure) is inherently backward in nature, since $\partial \mathrm{Re}\left[\bar{\beta}\right] / \partial \mathrm{Re}\left[\bar{\alpha}_{ee}^{-1}\right] > 0$, due to similar arguments as outlined above, and consistent with analogous findings in thin plasmonic films [120]-[121] and optical metamaterials [122]. As outlined in Ref. [100], a second, less confined, forward branch is also present in the guided regime, of less interest from the practical point of view, since it is very similar to a plane wave traveling unperturbed in the background with very limited confinement. A complex branch stems from the contact point between these two guided modes, which enters the leaky-wave regime for sufficiently negative $\mathrm{Re}\left[\alpha_{ee}^{-1}\right]$. The dispersion of $\mathrm{Re}\left[\bar{\beta}\right]$ with frequency in this regime decreases monotonically from +1 to -1, for decreasing $\mathrm{Re}\left[\alpha_{ee}^{-1}\right]$, crossing the axis $\mathrm{Re}\left[\bar{\beta}\right] = 0$. For this specific value of inverse polarizability, the leaky mode passes from backward proper [123] (for less negative $\mathrm{Re}\left[\alpha_{ee}^{-1}\right]$) to forward improper operation. It is evident that in this polarization we are mostly interested in the backward region, which ensures smaller damping factor $\mathrm{Im}\left[\bar{\beta}\right]$. As expected, also in this polarization the most interesting region arises closer to the resonance of the individual nanoparticles, i.e., here for less negative values of $\mathrm{Re}\left[\alpha_{ee}^{-1}\right]$. The leaky-wave branch is connected to the guided branches through a complex modal regime, which is typical of a transition between leaky-wave modes and a two-branch guided-wave regime [85]. In this transition region, the mode does not radiate and propagates with complex wave number, whose real part is very close to the one of free-space, and non-zero imaginary part.

It is interesting to stress that the inherent backward propagation of guided and leaky-wave modes with transverse polarization may be appealing in the framework of negative-index propagation, and this guided regime has been exploited to realize double-negative metamaterials in the visible [120]-[122]. In terms of leaky-wave radiation, backward radiation may be of interest to increase the degrees of freedom in tailoring and directing the optical radiation, but, as we show in the following, it is intrinsically less efficient than the forward longitudinal mode. Farther from resonance, outside the leaky-wave regime, both polarizations have a stop-band region with $\left|\mathrm{Re}\left[\bar{\beta}\right]\right| = 1$, in which the imaginary part grows in magnitude, the propagation is evanescent in nature and the damping is significantly large. In the following, we analyze more in detail the dispersion of the leaky-wave modes as a function of the interparticle distance $\bar{d}$ and of the nanoparticle polarizability, with the goal of optimizing the leaky-wave radiation in the two polarizations, and of analyzing the fundamental limitations and possibilities of leaky radiation at optical frequencies.

i. *Longitudinally polarized modes*

Consistent with Fig 17(a), $\text{Re}\left[\bar{\beta}\right]=1$ constitutes the boundary between guided-wave and leaky-wave operation for longitudinal polarization. Formally, the leaky-wave regime is bounded by the following conditions on the nanoparticle inverse polarizability:

$$\xi(3)+Cl_3\left(2\bar{d}\right)+\bar{d}\,Cl_2\left(2\bar{d}\right)<\frac{\bar{d}^3\,\text{Re}\left[\bar{\alpha}_{ee}^{-1}\right]}{3}<\text{Re}\left[f_3\left(\bar{\beta},\bar{d}\right)-i\bar{d}f_2\left(\bar{\beta},\bar{d}\right)\right]\Big|_{\substack{\bar{\beta}\in\mathbb{C}\\\text{Re}\left[\bar{\beta}\right]=1}},\qquad(27)$$

where $f_N\left(\bar{\beta},\bar{d}\right)$ are defined in (22), $Cl_N\left(\theta\right)$ are the Clausen's functions [116], which are real for real argument and $\zeta(.)$ is the Riemann Zeta function. The left-hand side has been written in closed-form using the properties of the polylogarithm functions for real argument:

$$\begin{cases}Li_1\left(e^{i\theta}\right)=Cl_1\left(\theta\right)+i\dfrac{\left(\pi-\theta\right)}{2}\\[2mm]Li_2\left(e^{i\theta}\right)=\dfrac{\pi^2}{6}-\dfrac{\theta\left(2\pi-\theta\right)}{4}+i\,Cl_2\left(\theta\right)\qquad 0\le\theta\le2\pi\,.\\[2mm]Li_3\left(e^{i\theta}\right)=Cl_3\left(\theta\right)+i\dfrac{\theta\left(\pi-\theta\right)\left(2\pi-\theta\right)}{12}\end{cases}\qquad(28)$$
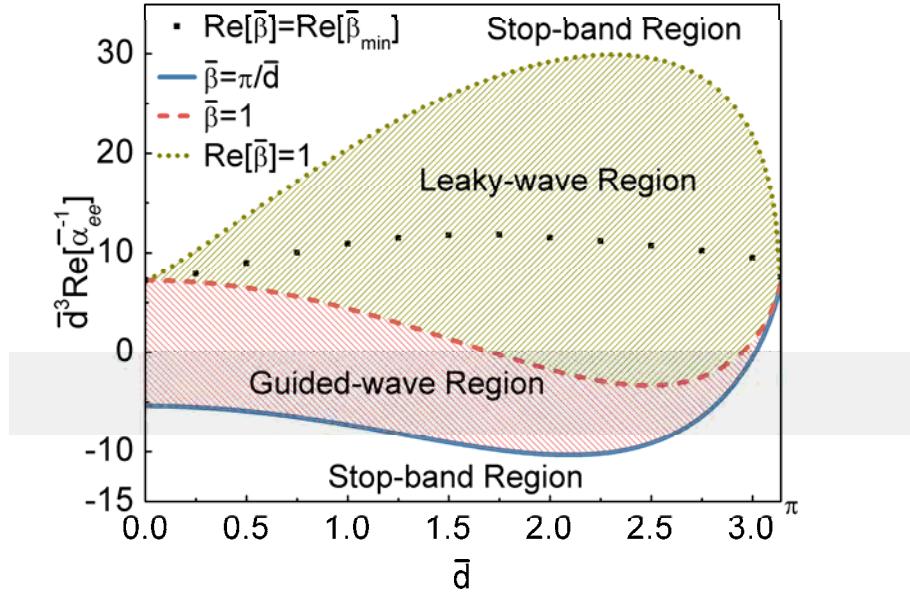
Figure 18 - Guided- and leaky-wave regions for longitudinal polarization. The solid blue and dashed red curves are respectively the loci of real solutions $\bar{\beta}=\pi/\bar{d}$ and $\bar{\beta}=1$, which delimit the guided-wave regime. The dotted green line defines the upper limit of the leaky-wave regime. The black dots denote the locus $\text{Re}\left[\bar{\beta}\right]=\bar{\beta}_{\min}$, which may be considered the cut-off of the leaky-wave regime.

Figure 18 shows a map of the different ranges of guided-wave, leaky-wave radiation, or stop-band, as a function of $\bar{d}$ and $\mathrm{Re}\left[\bar{\alpha}_{ee}^{-1}\right]$. The dashed red line in this plot represents the locus $\bar{\beta}=1$, which separates the guided-wave propagation (below) and leaky-wave radiation (above). The dotted green line represents the upper boundary of the leaky-wave regime, for which $\bar{\beta}\in\mathbb{C}$ and $\mathrm{Re}\left[\bar{\beta}\right]=1$. In this plot, we have also considered the locus $\mathrm{Re}\left[\bar{\beta}_{\min}\right]$ (black dotted line), which may be considered the cut-off for leaky-wave propagation, as discussed above. The solid blue line corresponds to $\bar{\beta}=\pi/\bar{d}$, which is the lower boundary of the guided regime. The regions above the leaky-wave region and below the guided-wave region are stop-band regions, where modes decay very fast along z, and are not of interest for guidance or radiation purposes.
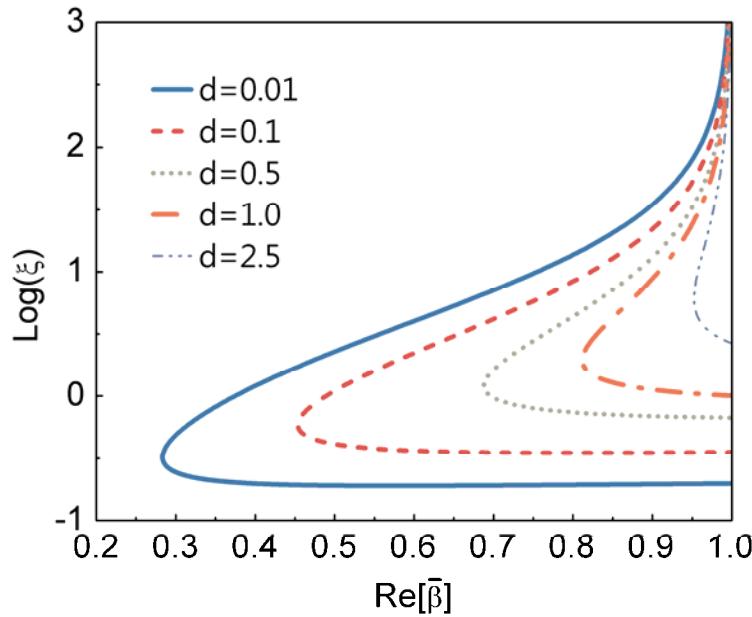

Figure 19 - Variation of the ratio $\xi=\mathrm{Re}\left[\bar{\beta}\right]/\mathrm{Im}\left[\bar{\beta}\right]$ for the supported leaky-wave modes of the nanoparticle chain of Fig. 16 for longitudinal polarization, varying the center-to-center distance.

It is seen how all the boundary curves converge at $\bar{d}=\pi$ which represents the maximum interparticle distance for supporting guided or leaky modes along arrays of sub-wavelength nanoparticles. Moreover, the leaky-wave region widens up around $\bar{d}=2$ and it is centered above the resonance condition for the individual nanoparticles $\mathrm{Re}\left[\bar{\alpha}_{ee}^{-1}\right]=0$. In the limit $\bar{d}\to 0$, the leaky-wave range Eq. (27) tends to a single point with value $\bar{d}^3\,\mathrm{Re}\left[\bar{\alpha}_{ee}^{-1}\right]=6\zeta(3)\simeq 7.21$, implying that too closely packed chains provide a very limited leaky-wave radiation bandwidth.

One of the relevant figures of merit for leaky modes is the ratio $\xi=\mathrm{Re}\left[\bar{\beta}\right]/\mathrm{Im}\left[\bar{\beta}\right]$. A lower $\mathrm{Re}\left[\bar{\beta}\right]$ may be desirable for radiation closer to the normal to the array, but this is usually accompanied by a larger $\mathrm{Im}\left[\bar{\beta}\right]$, which implies shorter propagation distance, and inherently lower directivity. As mentioned above, the cut-off of the leaky mode may be defined by $\xi=1$.

Overall, a larger value of ξ ensures larger directivity and radiation farther from the array axis, both desirable features of a leaky-wave antenna.

Figure 19 shows the variation of $\log \xi$ versus $\text{Re}\left[\bar{\beta}\right]$ for different values of interparticle distance. The ratio ξ tends to infinity for $\text{Re}\left[\bar{\beta}\right] \simeq 1$, since we are operating near the guided-wave regime and lossless particles are being considered here. This region is characterized by endfire radiation, consistent with the limit of a surface mode propagating along the chain. A wider range of $\text{Re}\left[\bar{\beta}\right]$ implies that energy may be coupled into a broader angular spectrum, which is more appealing for antenna applications. Fig. 19 confirms that better ratios ξ and wider variation along $\text{Re}\left[\bar{\beta}\right]$ may be obtained by choosing a smaller value of $\bar{d}$. This is to be expected, since the nanoparticles in this regime are tightly coupled, ensuring more flexibility in terms of guidance and radiation. Consistent with Fig. 17, however, the available bandwidth of leaky-wave operation shrinks down for smaller values of $\bar{d}$. It should be stressed, in addition, that small interparticle distance necessarily requires nanoparticles with smaller diameters, which in turn implies higher individual Q factors and more sensitivity to losses. We discuss these aspects in the following section, when we consider specific models for the nanoparticle geometry.

ii.   Transversely polarized modes

Transversely polarized leaky modes behave quite differently. As discussed above, guided-wave and leaky-wave regions are separated by a complex transition region, not present in the longitudinal polarization. By setting $\text{Re}\left[\bar{\beta}\right] = \pm 1$ and solving for the corresponding $\text{Im}\left[\bar{\beta}\right]$ in Eq. (21), we can obtain the range of polarizability values that support leaky-wave propagation in this regime. This condition may be formally expressed as:

$$\left[f_3\left(\bar{\beta},\bar{d}\right) - i\bar{d}\, f_2\left(\bar{\beta},\bar{d}\right) - \bar{d}^2 f_1\left(\bar{\beta},\bar{d}\right) \right]\Big|_{\text{Re}\left[\bar{\beta}\right]=-1}$$
$$< -\frac{2}{3}\bar{d}^3 \bar{\alpha}_{ee}^{-1} < \left[f_3\left(\bar{\beta},\bar{d}\right) - i\bar{d}\, f_2\left(\bar{\beta},\bar{d}\right) - \bar{d}^2 f_1\left(\bar{\beta},\bar{d}\right) \right]\Big|_{\text{Re}\left[\bar{\beta}\right]=1} \quad , \tag{29}$$

where $f_N\left(\bar{\beta},\bar{d}\right)$ are defined in (22).

Figure 20 shows the different modal regions for transversely polarized modes as a function of $\bar{d}$ and $\bar{\alpha}_{ee}^{-1}$, analogous to Fig. 18. Like the longitudinal case, the leaky-wave regime converges to a single point for $\bar{d} \to 0$, implying that also in this polarization the leaky-wave regime is of narrow bandwidth for very tight nanoparticles. On the other extreme, towards $\bar{d} = \pi$, the modal region widens, ensuring a relatively broad range of normalized polarizability values that support leaky modes. As we will point out in the following, however, the corresponding $\text{Im}\left[\bar{\beta}\right]$ is rather large for this range of interparticle distance.

Figure 21 shows the variation of ξ with the array properties in this polarization, analogous to Fig. 19. It is evident comparing the two figures that it is more challenging to obtain a reasonably large figure of merit in this polarization. As anticipated earlier, the region of most interest is

42

localized in the backward-wave region, for positive $\text{Re}\left[\bar{\beta}\right]$ (right portion of Fig. 21). Due to the presence of a complex transition region between guided-wave and leaky-wave modes, in this polarization the imaginary part $\text{Im}\left[\bar{\beta}\right]$ is not negligible even for values $\text{Re}\left[\bar{\beta}\right] \simeq 1^-$, and the ratio ξ is never remarkably large. These results confirm the general dispersion properties of transverse modes highlighted in Fig. 17b.
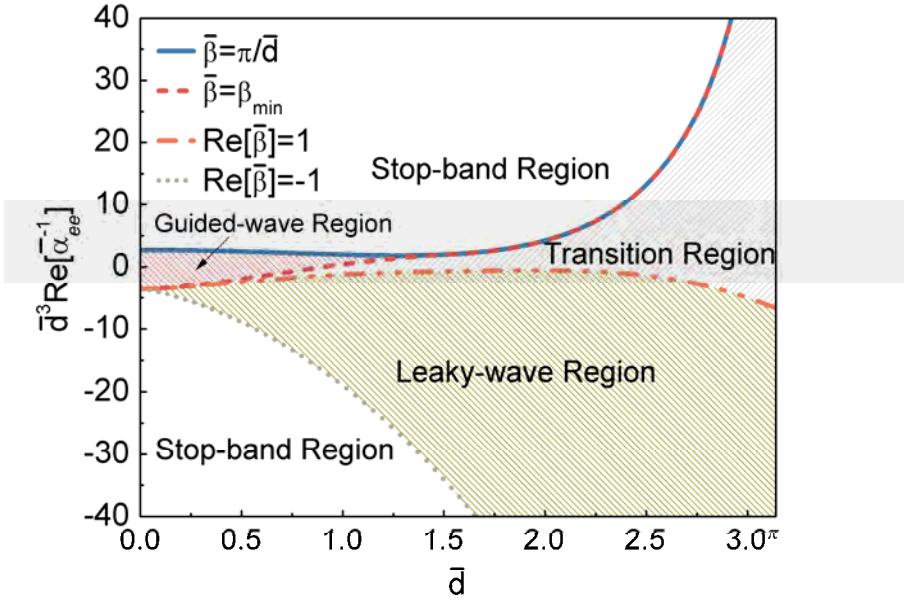

Figure 20 - Analogous to Fig. 18, guided- and leaky-wave regions for transversely polarized modes.
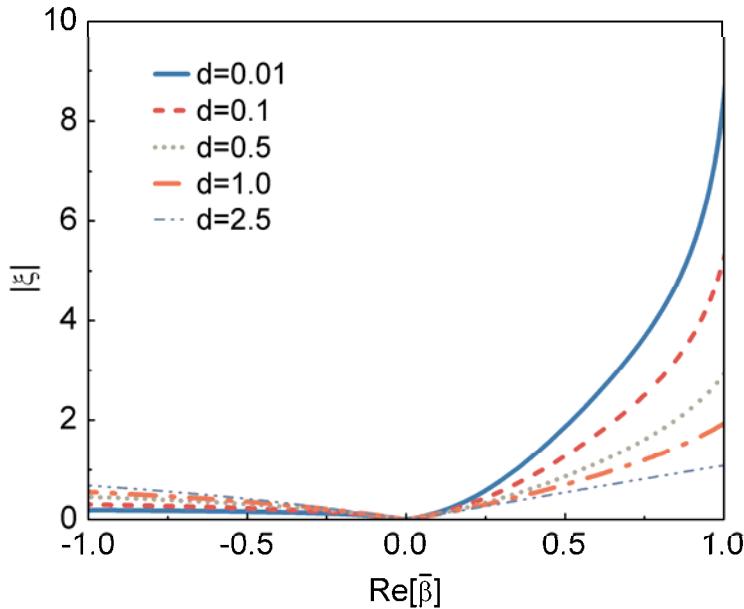
Figure 21. (Color online) Analogous to Fig. 19, variation of ξ vs. $\text{Re}\left[\bar{\beta}\right]$ for transversely polarized leaky modes, varying the center-to-center distance.

43

Before concluding this section, it should be mentioned that some of the general modal features highlighted here for linear arrays of nanoparticles may be obtained in thin plasmonic films, in the limit in which the array density increases. This is consistent with recent analyses of complex modes along such geometries [106], which have also highlighted the presence of backward-wave propagation [120]-[121] for transverse polarization, consistent with the general results presented here.
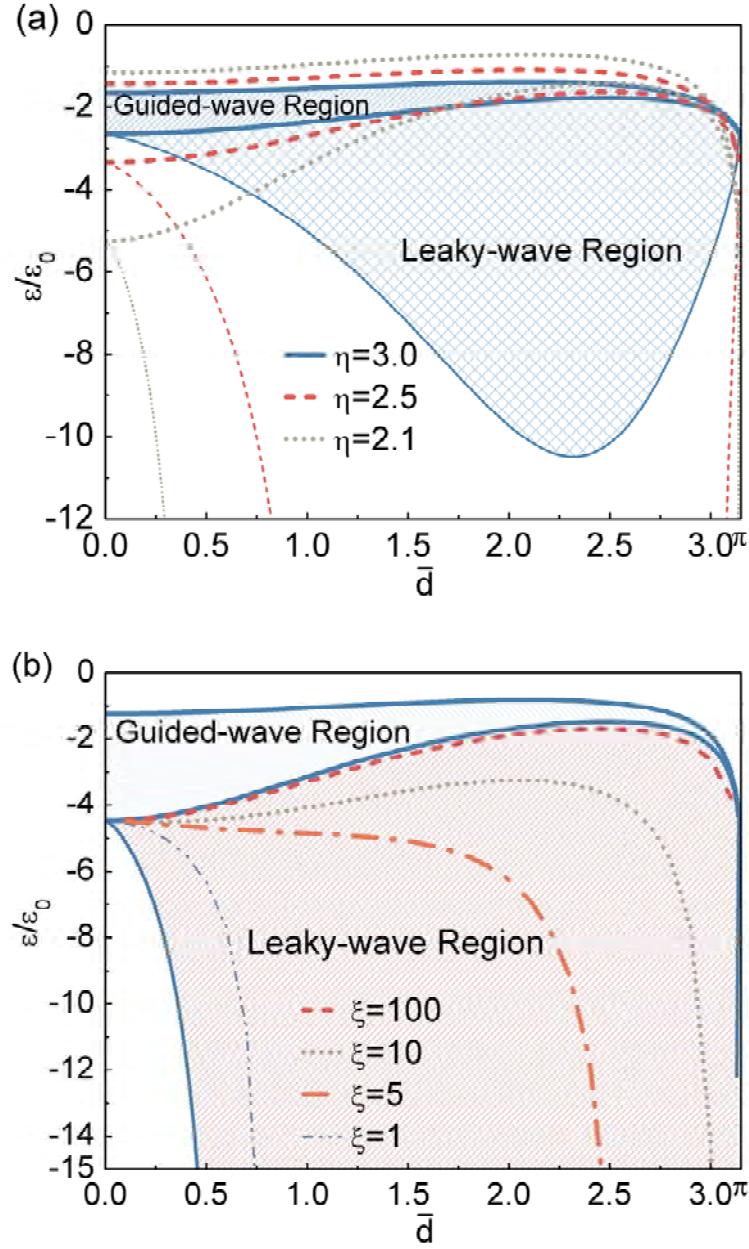
Figure 22 - (a) Guided-wave and leaky-wave regions for longitudinal polarization, as a function of nanosphere permittivity and interparticle distance. The guided-wave regime is supported between the bold lines, while the leaky-wave region is bounded by thinner lines. (b) Loci of constant $\xi = \mathrm{Re}\left[\bar{\beta}\right]/\mathrm{Im}\left[\bar{\beta}\right]$ in the leaky-wave region for $\eta = 2.2$. Blue solid lines delimit the guided-wave and leaky-wave regions.

44

e. Realistic models for nanoparticles

In the previous section, we have analyzed the general conditions and limitations for leaky-wave propagation along sub-wavelength nanoparticle chains, considering a general model for the nanoparticle polarizability. In particular, we have shown that longitudinal forward leaky-wave modes may provide better directivity properties than transverse modes, due to their significantly larger value of ξ for the same interparticle distance. Moreover, we have outlined the range of $\text{Re}\left[\bar{\alpha}_{ee}^{-1}\right]$ required to sustain leaky-wave radiation. In this section, we will consider realistic nanoparticle geometries to apply the previous general results to several practical designs for optical leaky-wave arrays.

In practice, $\text{Re}\left[\bar{\alpha}_{ee}^{-1}\right]$ is determined by the specific design and shape of the nanoparticles forming the array. In the case of spherical nanoparticles of radius a and permittivity ε, for instance, we obtain [100]:

$$\text{Re}\left[\bar{\alpha}_{ee}^{-1}\right] \simeq \frac{3}{2}\left(k_0 a\right)^{-3}\frac{\varepsilon + 2\varepsilon_0}{\varepsilon - \varepsilon_0}, \tag{30}$$

in the quasi-static limit of interest here. Other possible geometries of interest may be represented by coated spheres, with permittivities ε_1 and ε_2 and ratio of inner to outer radius γ, for which:

$$\text{Re}\left[\bar{\alpha}_{ee}^{-1}\right] \simeq \frac{3}{2}\left(k_0 a\right)^{-3}\frac{2\gamma^3\left(\varepsilon_2 - \varepsilon_1\right)\left(\varepsilon_2 - \varepsilon_0\right) - \left(\varepsilon_1 + 2\varepsilon_2\right)\left(\varepsilon_2 + 2\varepsilon_0\right)}{\gamma^3\left(\varepsilon_2 - \varepsilon_1\right)\left(2\varepsilon_2 + \varepsilon_0\right) - \left(\varepsilon_1 + 2\varepsilon_2\right)\left(\varepsilon_2 - \varepsilon_0\right)}, \tag{31}$$

or nanodiscs of radius a, height γa and permittivity ε, for which the transverse polarizability is [124]:

$$\text{Re}\left[\bar{\alpha}_{ee}^{-1}\right] \simeq \frac{9}{4}\left(k_0 a\right)^{-3}\left[\frac{1}{\gamma} - \frac{1}{\left(1-\gamma^2\right)^{3/2}}\left(\frac{\sqrt{1-\gamma^2}}{\gamma} - \arctan\frac{\sqrt{1-\gamma^2}}{\gamma}\right) + \frac{2/\gamma}{\varepsilon/\varepsilon_0 - 1}\right]. \tag{32}$$

It is evident that there is a wide range of flexibility in the shape and material properties of the nanoparticles to tailor the value of $\text{Re}\left[\bar{\alpha}_{ee}^{-1}\right]$ at the frequencies of interest. In the following, we focus on homogeneous nanospheres [Eq. (30)] and analyze how their design parameters affect the leaky-wave dispersion. Analogous results may be derived for different shapes and geometries.

Before analyzing in detail the nanosphere problem, it is relevant to highlight a common trend in the previous formulas (30)-(32): as expected, the value of $\text{Re}\left[\bar{\alpha}_{ee}^{-1}\right]$ tends to diverge for small nanoparticles $\left(k_0 a\right) \to 0$. This is to be expected, since a small nanoparticle is usually very far from its individual resonance $\text{Re}\left[\bar{\alpha}_{ee}^{-1}\right] = 0$. On the other hand, leaky-wave radiation requires finite values of $\text{Re}\left[\bar{\alpha}_{ee}^{-1}\right]$, as shown in the previous section. This implies that the operation of these leaky-wave nanoantennas with sub-diffractive lateral cross section will arise in the frequency range for which the numerator in the right-hand side of Eqs. (30)-(32) is close to zero, i.e., near a plasmonic resonance for the specific shape of interest. For larger $\bar{d}$ this condition

45

becomes more and more stringent, since $\text{Re}\left[\bar{\alpha}_{ee}^{-1}\right]$ is required to be closer to zero. This is reflected in a general trade-off between size of these leaky-wave antennas and their bandwidth and robustness to the presence of loss and disorder. We discuss these aspects in further detail, specifically applied to spherical nanoparticles, in the following.

i. Leaky-wave modal dispersion with the nanosphere permittivity

For spherical nanoparticles, we may use Eq. (30) to determine the range of permittivities ε that may allow leaky-wave propagation along the nanoparticle chain. Figure 22a shows the longitudinal guided and leaky modal regions in the diagram of $\varepsilon/\varepsilon_0$ vs. $\bar{d}$, for different values of the nanosphere radius a. The different curves refer to different ratios $\eta = d/a$ and we have used shadowing to highlight the guided-wave and leaky-wave regions in the case $\eta = 3$. As it may be seen, the leaky-wave region requires more negative permittivity values than the guided-wave region, which is centered at the resonance condition of the individual nanospheres $\varepsilon = -2\varepsilon_0$. Denser chains support a wider range of permittivities to achieve leaky-wave propagation, since the permittivity range gets wider for smaller values of η (of course there is a geometrical limit of $\eta > 2$ to consider in the design). This is reflected in wider bandwidths, as negative permittivity is necessarily dispersive with frequency [125]. Consistent with the previous section, in the mathematical limit $\bar{d} \to 0$ leaky waves are not supported, but the permittivity region rapidly widens up for slightly larger values of $\bar{d}$. Fig. 22b shows the loci of constant $\xi = \text{Re}\left[\bar{\beta}\right]/\text{Im}\left[\bar{\beta}\right]$ for $\eta = 2.2$, as an example. Consistent with the results of the previous section, it is seen that low attenuation rate is achieved close to the boundary of the guided-wave mode region, corresponding to end-fire radiation. However, relatively large values of ξ may be achieved even farther away from the guided-wave regime, which may provide conical radiation off-axis. Moreover, the natural permittivity dispersion of metals may provide frequency scanning for the conical beams radiated by the chain.

Figure 23 shows analogous plots for the transverse polarization. Due to the backward nature of guided and leaky modes in this polarization, less negative values of permittivity are required as compared to the guided regime. Also in this case, by decreasing the value of η the leaky-wave operation broadens in bandwidth. Comparing Figs. 22 and 23, it is seen that longitudinal leaky modes have a broader leaky-wave region and comparatively larger values of ξ, implying that they may outperform the transverse backward-wave leaky modes in terms of directivity and bandwidth of operation. These results are consistent with the discussion in the previous section, but applied here specifically to the nanosphere geometry.

ii. Effects of absorption and material loss

In this section we relax the assumption that material absorption and losses are negligible in the materials composing the chain, i.e., $\text{Im}\left[\bar{\alpha}_{ee}^{-1}\right] < -1$. This is a relevant aspect to consider, since negative permittivity, required to support subdiffractive leaky-wave operation, is usually combined with finite absorption [125]. Material losses are known to play a relevant role in plasmonic devices with subwavelength cross sections, such as nanoparticle waveguides [100],

46

[126]-[127]. In the case of lossy materials, the quasi-static inverse polarizability is related to the complex permittivity $\varepsilon = \varepsilon_r + i\varepsilon_i$ as:

$$\text{Re}\left[\bar{\alpha}_{ee}^{-1}\right] = \frac{3}{2}(k_0 a)^{-3} \frac{(\varepsilon_r + 2\varepsilon_0)(\varepsilon_r - \varepsilon_0) + \varepsilon_i^2}{(\varepsilon_r - \varepsilon_0)^2 + \varepsilon_i^2}$$

$$\text{Im}\left[\bar{\alpha}_{ee}^{-1}\right] = -1 - \frac{9}{2}(k_0 a)^{-3} \frac{\varepsilon_0 \varepsilon_i}{(\varepsilon_r - \varepsilon_0)^2 + \varepsilon_i^2}$$

(33)

For low-loss particles, of interest here, ε_i is small and the associated additional contribution to $\text{Im}\left[\bar{\alpha}_{ee}^{-1}\right]$ provides a first-order perturbation of the lossless results derived above.
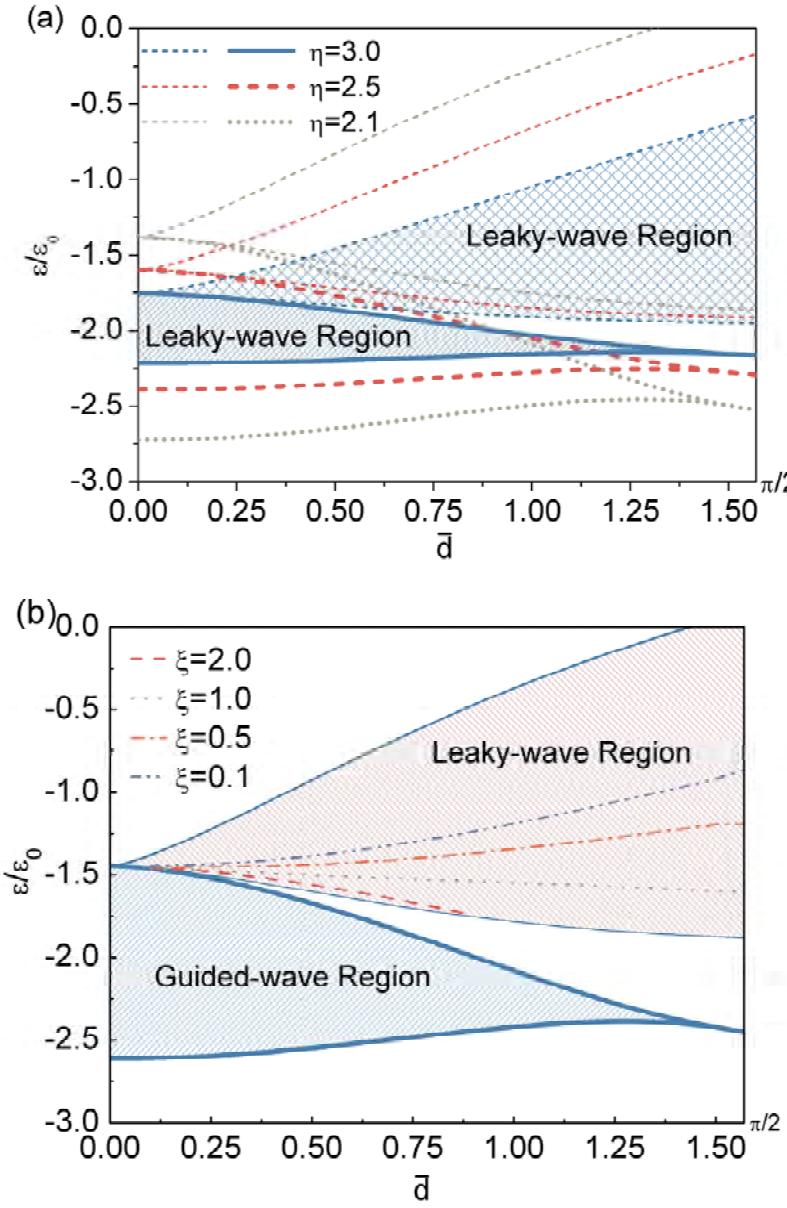

Figure 23 - Analogous to Fig. 22, but for transverse polarization.

47

Figure 24 shows the dispersion of $\mathrm{Re}\left[\bar{\beta}\right]$ and $\mathrm{Im}\left[\bar{\beta}\right]$ versus ε_r for longitudinally polarized modes, for $\bar{d} = 0.1$, $\eta = d/a = 2.1$ and different levels of material absorption ε_i. It is interesting to see how in the guided-wave region a moderate increase of ε_i principally affects $\mathrm{Im}\left[\bar{\beta}\right]$, as expected, but leaves unaltered $\mathrm{Re}\left[\bar{\beta}\right]$ and correspondingly the phase velocity. Since the transition towards the leaky-wave regime is continuous for this polarization, the presence of material loss implies a reduction of the achievable values of ξ, even near the guided-wave region. In the leaky-wave region, however, the trend is opposite: $\mathrm{Im}\left[\bar{\beta}\right]$ is not sensibly altered, being mainly dominated by radiation losses (the mode is less confined to the particles), and the additional small loss mainly affects the angle of radiation and $\mathrm{Re}\left[\bar{\beta}\right]$. It is worth noticing that a complex-valued transition region may arise for relatively larger values of ε_i, for which $\mathrm{Re}\left[\bar{\beta}\right] = 1$.
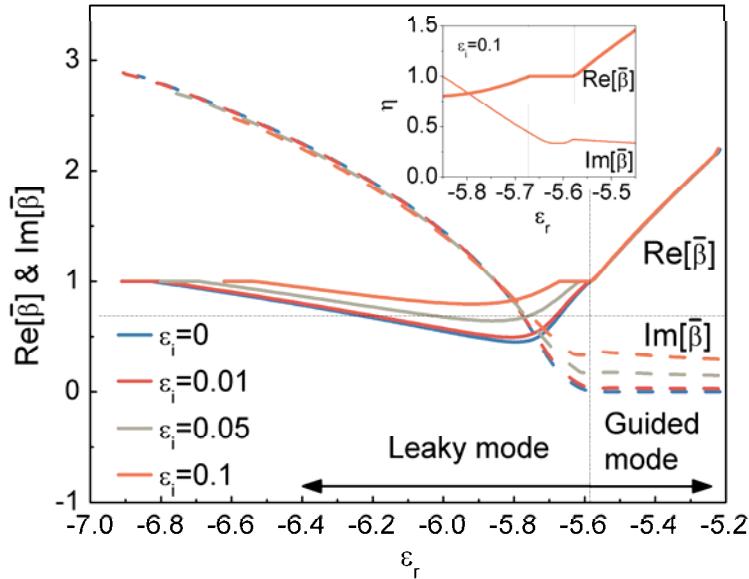

Figure 24 - Variation of $\mathrm{Re}\left[\bar{\beta}\right]$ and $\mathrm{Im}\left[\bar{\beta}\right]$ for $\bar{d} = 0.1$ and $\eta = d/a = 2.1$ in the longitudinal polarization regime, varying the imaginary part of permittivity. The inset plot shows a zoom in the transition region for the case $\varepsilon_i = 0.1$.

A zoom of this transition region for $\varepsilon_i = 0.1$ is reported in the inset of Fig. 24. The figure confirms that realistic levels of absorption in optical materials may provide the possibility to realize nanoantennas with sub-diffractive lateral cross section able to sustain such longitudinal leaky modes with directive radiation properties.

Figure 25 shows the variation of ξ for increased material absorption in the case of $\eta = d/a = 2.1$ and $\bar{d} = 0.1$, both for longitudinal (a) and transverse (b) polarization. The loss effect is more evident in the longitudinal case, since the transverse polarization has much larger radiation losses. Still, the levels of ξ, and correspondingly of directivity, achieved in the

48

longitudinal polarization remain substantially larger than in the transverse case, even after considering realistic absorption levels.
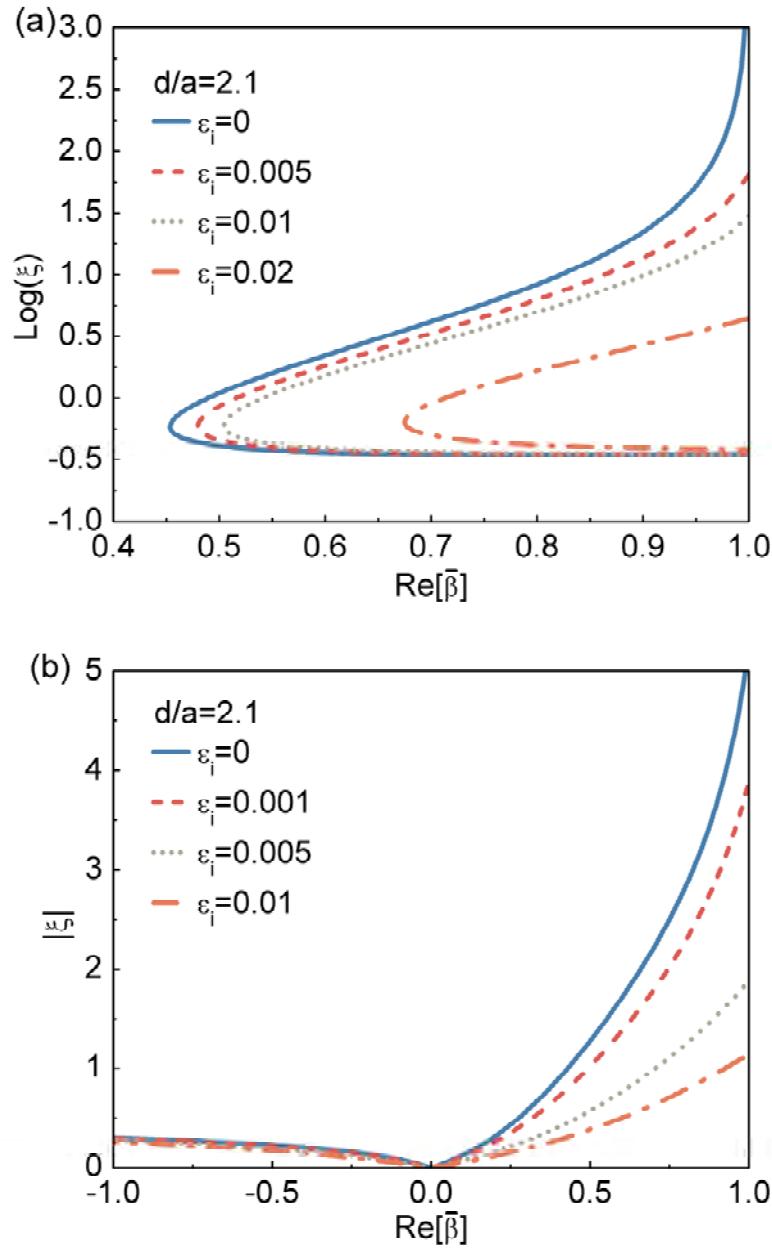
Figure 25 - Variation of ξ for different levels of material loss ε_i in longitudinal (a) and transverse (b) polarization. In both plots, we have considered $\eta = d/a = 2.1$ and $\bar{d} = 0.1$.

iii.   Realistic plasmonic materials

The results of the previous subsection imply that chains of metamaterial or plasmonic nanoparticles with negative permittivity and moderate losses may provide a promising mean to realize a leaky-wave nanoantenna with subwavelength transverse cross-section. For this purpose,

49

noble metals, or combinations of noble metals and dielectrics, may be chosen to realize such nanochains, following the design guidelines represented by Eqs. (30)-(32).
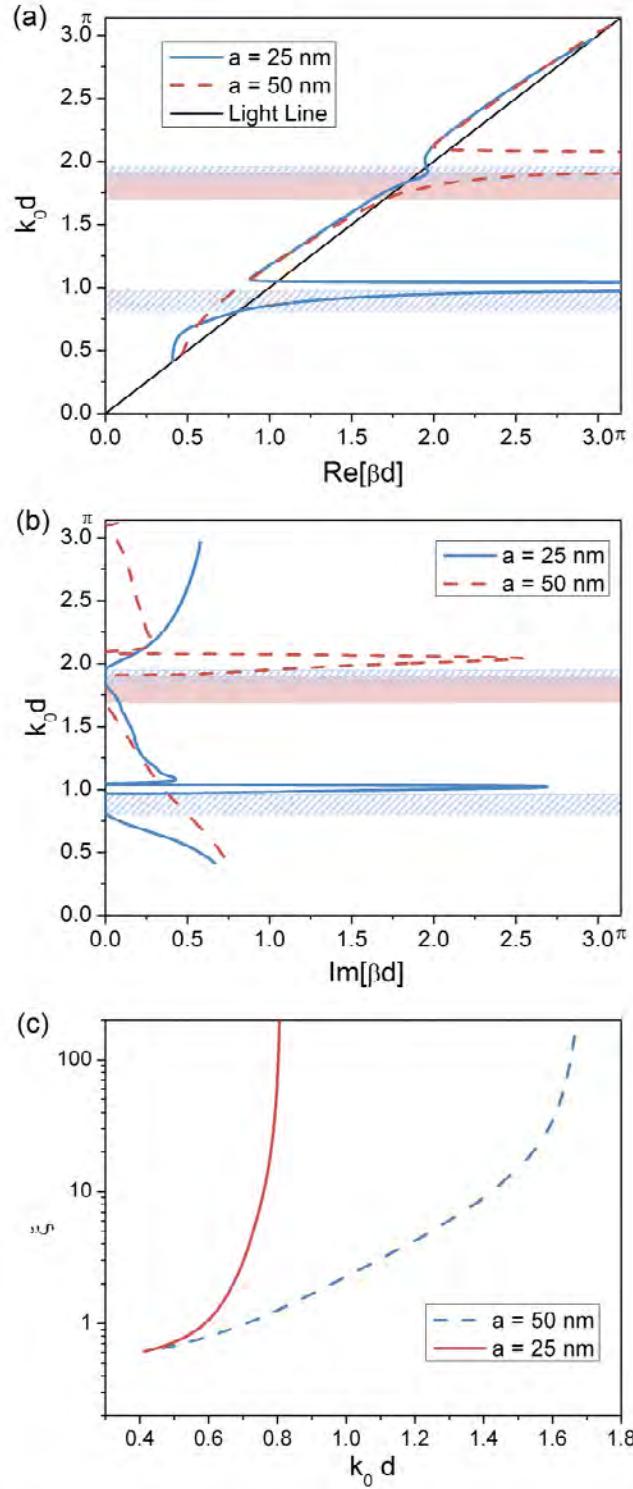
Figure 26 - $\bar{\beta}d$ vs k_0d diagrams and ξ for longitudinal modes supported by silver arrays with $\eta = 2.1$.

Metallic nanoparticles made of silver or gold, for instance, have shown moderate guidance properties in the optical regime [93]. In this subsection, we consider the realistic properties of noble metals in the realization of these nanoantennas. For simplicity, we focus on nanospheres and on longitudinally polarized modes, which ensure better radiation performance and more robustness to the effect of absorption in the materials under consideration.
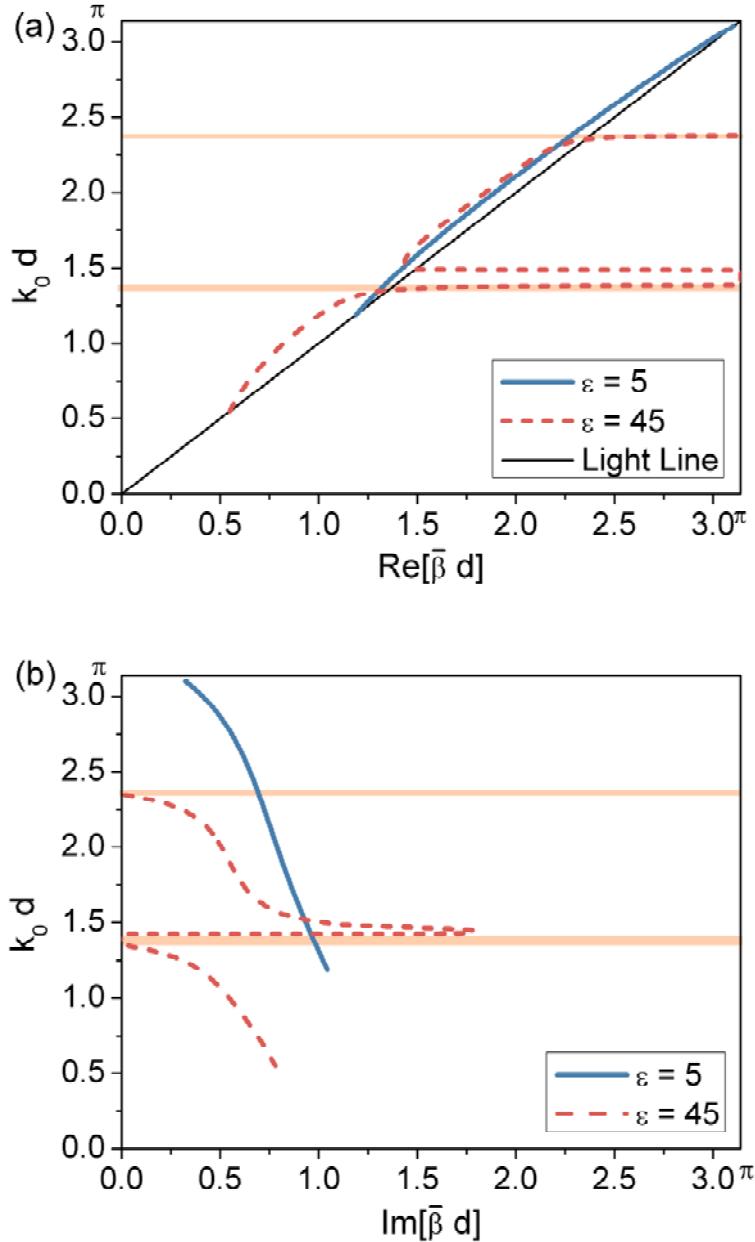

Figure 27 - $\bar{\beta}d$ vs $k_0 d$ diagrams for longitudinal modes supported by dielectric arrays with $\eta = 2.1$.

Figure 26 shows the complex dispersion relations βd - $k_0 d$ for linear arrays composed of silver nanospheres, considering experimental values of permittivity [128], frequency dispersion and loss. In this case, we have chosen $\eta = 2.1$ and nanosphere radii of 25 (blue solid line) and 50 nm (red dashed). Fig 26a reports the real part of βd and Fig. 26b the corresponding imaginary part. It is seen that larger particles may provide wider bandwidth of leaky-wave radiation, due to the inherently larger period, and they are inherently more robust to the presence of loss, consistent with analogous results in the guided region [100]. The shadowed regions in the figure indicate these guidance regions.

Fig. 26c reports the calculated values of ξ for the leaky-wave operation. Significantly large values may be achieved near the endfire radiation, despite the presence of loss and the overall sub-diffractive lateral cross-section of these nanoantennas. These results are particularly encouraging for the realization of these concepts using arrays of subwavelength silver nanoparticles.

iv. Comparison with dielectric nanosphere arrays

The previous results imply that plasmonic nanoparticles may represent a promising means for the realization of sub-diffractive leaky-wave nanoantennas. In this subsection we compare their performance with the one of dielectric nanoparticles, focusing in the range $\bar{d} < \pi$. Complex-wave propagation along arrays of spheres with large values of constitutive parameters has been considered in Ref. [113]. Figure 27 shows the dispersion of complex modes along a dense array ($\eta = 2.1$) of dielectric spheres with $\varepsilon = 5\varepsilon_0$ and with $\varepsilon = 45\varepsilon_0$. For consistency with the previous results, we show only guided modes supported by the induced electric dipoles along the array for longitudinal polarization, although for large dielectric constants magnetic modes are also available. Fig. 27a and 27b report the dispersion diagrams for $\mathrm{Re}\left[\bar{\beta}\right]$ and the corresponding $\mathrm{Im}\left[\bar{\beta}\right]$, respectively. For the low permittivity spheres (blue line), guided modes are not available in this low-frequency regime, as expected, and a small complex branch is visible near the light line. Since we are far from resonance, however, the value of ξ is always less than unity, implying poor radiation properties, as expected. Drastically increasing the nanosphere permittivity it is possible to induce electric dipole resonances, despite the sub-wavelength size of the particles. In this situation, guided-wave and leaky-wave regimes are available, and the dispersion diagrams are characterized by narrow guided-wave regions (highlighted by the shadowed regions) connected by leaky-wave branches. In some frequency ranges, significant directivity may be achieved, although the radiation is limited to grazing angles, close to the light line in the diagrams of Fig. 27. It is evident that large permittivity spheres may be also effective in supporting sub-diffractive leaky radiation, although the efficiency and directivity values achieved in this example are lower than for plasmonic particles and it may be challenging to realize such large values of permittivity at visible wavelengths. Plasmonic materials with the required values of permittivity, on the contrary, are naturally available at these frequencies, and their dispersion may naturally provide a larger degree of frequency scanning compared to large permittivity materials. We discuss these features further in the next section.
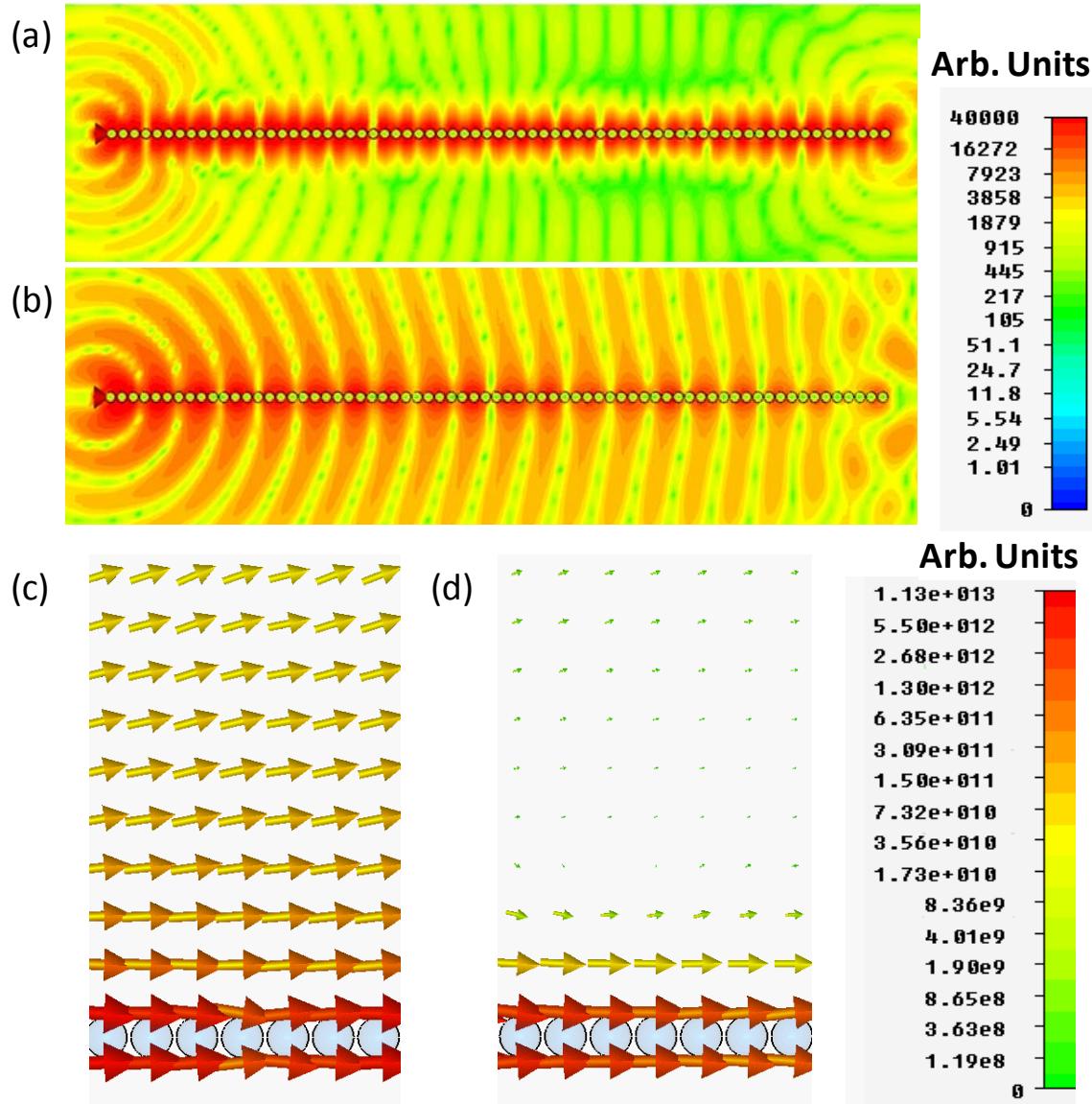
Figure 28 - Magnetic field and power flow distribution for a nanoparticle chain operating in the leaky-wave regime [(a) and (c), at 690nm wavelength] and in the guided propagation regime [(b) and (d), at 600nm].

f. *Full-wave numerical simulations*

In the previous sections, we have used the analytical formulation (21) to derive the fundamental properties of leaky-wave propagation and radiation along infinite arrays of subwavelength plasmonic nanoparticles to within a dipolar approximation. In this section, we validate the previous analytical model by simulating realistic finite arrays of silver nanoparticles with finite-integration technique commercial software [129], in order to determine the radiation patterns of such leaky modes in a practical realization, considering also the complete multipolar coupling among closely spaced nanoparticles.

53

In our numerical simulations, we have fixed the particle size to $a = 50\,\text{nm}$, center-to-center distance $d = 110\,\text{nm}$, and we have used a Drude permittivity model $\varepsilon = \varepsilon_\infty - \dfrac{f_p^2}{f\left(f - i\gamma\right)}$, with $\varepsilon_\infty = 5.0$, $f_p = 2175\,\text{THz}$ and $\gamma = 4.35\,\text{THz}$, which describes with good approximation the silver dispersion in the range of frequencies of interest [130]. The overall length of the chain is $L = 7\,\mu\text{m}$, sufficiently long to ensure that significant part of the power coupled to the leaky mode has been radiated. The array is excited by an optical source (i.e., an emitting molecule or a quantum dot) longitudinally polarized along the array axis, to ensure proper coupling with the longitudinal leaky modes supported by the array.

We have verified in our simulations that the dispersion of leaky-wave and guided modes along the array is qualitatively consistent with our analytical predictions. Clearly, the nature of our analytical technique neglects higher-order multipolar coupling between the closely spaced nanoparticles, which is reflected in a quantitative difference in the prediction of the frequency range for leaky-wave radiation, but qualitatively the results are in good agreement with the previous sections. As an example, Figure 28a reports the normal magnetic field distribution at the operating wavelength $\lambda_0 = 690\,\text{nm}$, which is in the leaky-wave regime for this array. Similarly, Fig. 28b reports the corresponding distribution at $\lambda_0 = 600\,\text{nm}$, for which the chain is in its guided regime. It is evident that the permittivity dispersion of silver allows tuning the guidance properties of the supported mode from a slow mode with short guided wavelength, as in Fig. 28b, confined along the structure, to a much faster mode, which produces leaky-wave radiation in free-space with conical directive properties. The difference in phase velocity between the two simulations is striking, considering that the free-space wavelength difference between the two cases is only 15%, and it is consistent with our analytical theory. Away from the chain, the leaky-wave (Fig 28a) couples to free-space radiation, drastically different from the guided propagation in Fig. 28b, which decays exponentially far away from the chain axis. The leaky-wave far-field extends laterally and propagates with oblique wave fronts, consistent with the previous analytical results. Figs. 28c and 28d show a zoom in the dashed regions of the two panels of Figs. 28a and 28b, reporting the power flow (Poynting vector) distribution. The power flow shows significant lateral energy leakage in the leaky-wave scenario of Fig. 28c. In contrast, at the wavelength $\lambda_0 = 600\,\text{nm}$ (Fig. 28d), the power flow is confined and bounded parallel to the chain, rapidly decaying away from its axis. It is remarkable that these full-wave results qualitatively confirm with very good precision the analytical results in the previous sections, and in particular the possibility to create a leaky-wave nanoantenna composed of subwavelength nanoparticles composed of realistic plasmonic materials. The fact that our full-wave results take into account the full coupling among the neighboring particles, and not just their dipolar (dominant) contribution, slightly shifts the guidance and leaky-wave frequency ranges from our analytical predictions in Fig. 26, but qualitatively these results confirm the possibilities noted in the previous sections.
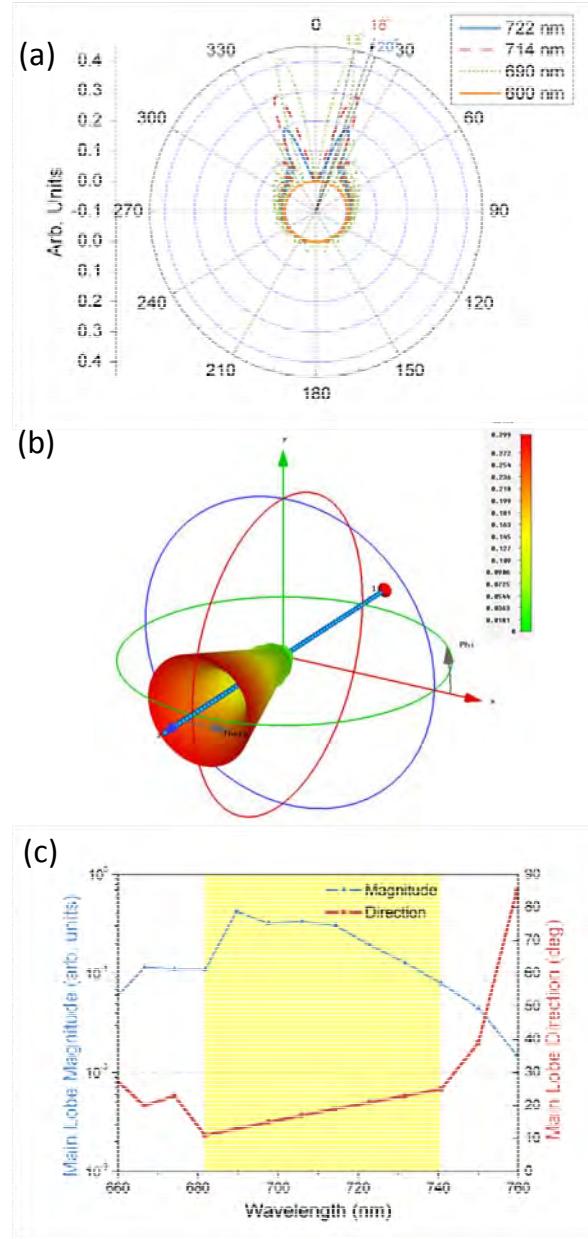
Figure 29 - (a) Far-field radiation patterns vs. wavelength of operation. At 722 nm (solid blue line), 714 nm (dashed red line) and 690nm (dotted green line), directional far-field radiation patterns are obtained, pointing at 20°, 18°, and 13° respectively. At 600nm, the guided-wave mode does not significantly contribute to the far-field radiation. (b) Calculated three-dimensional leaky-wave radiation pattern at the wavelength of 690nm. (c) Scanning of the main lobe radiation pattern (magnitude and main direction) versus wavelength. The highlighted region corresponds to leaky-wave operation.

Figure 29(a) shows the corresponding far-field radiation patterns in the E plane at various wavelengths. It is seen that, in the leaky-wave regime, the conical beam may scan the angle with frequency, as predicted in the previous sections. The patterns show a significant directivity that may be tuned by changing the frequency of operation (i.e., the material permittivity). It is seen that, consistent with the previous analytical results, better directivity is achieved for radiation closer to the chain axis, for which ξ is larger. The scan of the main lobe direction with frequency confirms the forward nature of these longitudinal leaky-wave modes, as predicted by

Approved for public release; distribution unlimited.

the previous analysis. For comparison, the radiation at $\lambda_0 = 600\,\text{nm}$ is very poor, due to the guided-wave properties of the chain at this wavelength. The subdiffractive nature and subwavelength period of the chain ensure absence of significant side lobes. These results confirm the realistic possibility of using a silver nanoparticle chain as a leaky-wave nanoantenna. Different nanoparticle size and geometry may be used to tune and shift the leaky-wave operation at different wavelengths.Figure 29b reports the three-dimensional far-field radiation pattern at 714 nm, together with the geometry of the chain, to highlight the directive conical radiation at 18 degrees from the chain axis, consistent with Fig. 29a. Smaller side lobes are visible, associated to the finite length of the chain. As reported in Fig. 29c, the nanoparticle chain supports a smooth linear scanning region between the wavelengths of 680 to 740 nm (highlighted in the figure), which delimit the leaky-wave operation of this nanoantenna. Tunability and beam scanning at the same frequency may be envisioned by considering electro-optical materials or proper nonlinearities in the nanoparticles.

g. Conclusions

In this section, we have provided a detailed analysis of the general leaky-wave radiation properties of linear arrays of subwavelength plasmonic nanoparticles. Using closed-form analytical dispersion relations for real and complex modes supported by such chain, we have analyzed its leaky-mode properties and the most general conditions required to support this regime with large directivity and robust frequency response, in the limit of subwavelength nanoparticles composing the array.

In particular, we have shown that the longitudinal polarization is the best candidate for achieving significantly directive conical radiation with scanning capabilities in this regime, and that the transverse polarization may support backward-wave radiation. We have also considered the effects of varying the center-to-center distance, the material properties and the possible presence of material dispersion and loss, specializing our general analysis to realistic plasmonic materials and providing comparison with analogous dielectric arrays. Our analysis shows that plasmonic materials may provide a robust route to leaky-wave radiation at optical frequencies, adding more flexibility over the leaky-wave properties of thin plasmonic films. We have also validated our results with full-wave simulations, analyzing the leaky-wave propagation and radiation along silver nanosphere arrays of finite length. Our full-wave simulations have confirmed that plasmonic leaky-wave nanoantennas with sub-diffractive lateral cross section may indeed lie within the realm of current nanotechnology and may be applied to novel devices for optical communications and computing.

6. Coupling and Guided Propagation along Parallel Arrays of Nanoparticles
a. Summary

In this section, we derive a dynamic closed-form dispersion relation for the analysis of the entire spectrum of guided wave propagation along coupled parallel linear arrays of plasmonic nanoparticles, operating as optical "two-line" waveguides. Compared to linear arrays of nanoparticles, our results suggest that these waveguides may support more confined beams with comparable or even longer propagation lengths, operating analogously to transmission-line segments at lower frequencies. Our formulation fully takes into account the entire dynamic interaction among the infinite number of nanoparticles composing the parallel arrays,

56

considering also realistic presence of losses and the frequency dispersion of the involved plasmonic materials, providing physical insights into the guidance properties that characterize this geometry.

b. Introduction

Linear chains of plasmonic (silver or gold) nanoparticles have been suggested as optical waveguides in several recent papers [131]-[141], as outlined in the previous sections. Owing to design flexibility and relatively easy construction within current nanotechnology, the realization of such ultracompact waveguides has been thoroughly studied and analyzed in the past few years. However, the recent experimental realizations of such devices at the nanoscale have revealed challenges due to severe sensitivity to material absorption and to inherent disorder. The guided beam cannot usually travel longer than few nanoparticles before its amplitude is lost in the noise. This is mainly due to the fact that linear arrays of small nanoparticles have the property to concentrate the optical energy in a sub-wavelength region of space, in large part filled by lossy metal. If this is indeed appealing in terms of power concentration and for enhancing the nanoscale interaction with light, it also has the clear disadvantage of strong sensitivity to material and radiation losses. In general, there is a well-known trade-off between energy concentration and confinement and robustness to loss in several plasmonic waveguide geometries [142]. As we have noted in [143], a bare conducting wire at low frequencies has analogous limitations: although metals are much more conductive and less lossy in radio frequencies, connecting two points in a regular circuit with a single wire would still produce unwanted spurious radiation and sensitivity to metal absorption. This problem, which is much amplified at optical frequencies due to the poorer conductivity and higher loss of metals in the visible, is simply approached at low frequencies by closely pairing two parallel wires (or, which is the same, placing a ground plane underneath the conducting trace), forming the well-known concept of a transmission-line that provides a return path for the conduction current. Analogously, applying the nanocircuit concepts [144]-[145], we have recently put forward ideas to realize optical nanotransmission-line waveguides in different geometries [146]-[147], which have been proven to be more robust to material and radiation losses and may provide wider bandwidth of operation. In particular, one such idea consists in pairing together two parallel arrays of plasmonic nanoparticles, suggesting that the coupling among the guided modes may improve the guidance performance. In [143] we have shown that this is indeed the case: operating with the antisymmetric longitudinal mode, such parallel chains may indeed confine the beam in the background region between the chains, leading to large power confinement without significantly affecting the robustness to material absorption and radiation losses as compared to the isolated array scenario. In particular, we have shown that operating with these modes near the light-line would, in many senses, lead to operation close to a regular transmission-line at low frequencies, but available in the visible regime.

Here, we present a complete, closed-form dynamic solution for the dispersion of the eigenmodes supported by parallel chains, fully taking into account the coupling among the infinite number of particles composing the two-chain array, even in the presence of material absorption, radiation losses and frequency dispersion. This derivation allows us to discuss the complete spectrum of guided modes supported by this geometry and analyze the differences among different polarizations and the analogies with the isolated chain geometry. The results confirm the validity of the analogy between these parallel arrays of nanoparticles and optical transmission lines, and they provide further insights into the operation and the large spectrum of modes guided by these

57

paired arrays of nanoparticles. Applications for low-loss optical communications, optical switching, nonlinearity enhancement and sub-wavelength imaging devices are envisioned.

c. Dispersion Relations for Guided Propagation

Consider the geometry of Fig. 30, i.e., two identical linear arrays of plasmonic nanoparticles with radius a, period $d > 2a$ and interchain distance $l > d$. This geometry has been preliminarily analyzed in [143] for its longitudinally polarized antisymmetric guided modes, where it was shown that the coupling between the chains, limited in that analysis to its dominant contribution coming from the averaged current density on the chain axes, was expected to generate the splitting of the regular longitudinal mode guided by an individual linear array into two coexisting longitudinal modes, respectively, with symmetric and antisymmetric field distributions and polarization properties, as sketched in Fig. 30. The antisymmetric mode is the one corresponding to transmission-line operation [143], as outlined in the introduction, for which two antiparallel displacement current flows are supported by the parallel chains. A similar modal propagation has been analyzed in [137] for a related distinct geometry, consisting of longitudinal dipoles placed over a perfectly conducting plane. Also our analysis of quadrupolar chains [147] may, in the limit of $l \rightarrow 0$, have some analogies with this antisymmetric operation. In the following, we rigorously approach the general problem of modal dispersion along the parallel chains of Fig. 30, extending our general analysis in [140] valid for one isolated chain. Our formulation fully takes into account the entire coupling among the infinite nanoparticles composing the pair of arrays and the possible presence of material absorption, radiation losses and frequency dispersion.
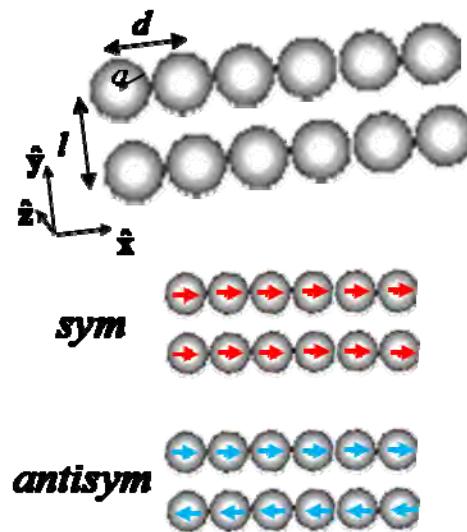
Figure 30 – Geometry of the problem: a pair of linear arrays of plasmonic nanoparticles as an optical two-line waveguide. The sketch reports the polarization properties of quasi-longitudinal modes with symmetric and antisymmetric properties.

We model each nanoparticle in the coupled array of Fig. 30 as a polarizable dipole with polarizability α, an assumption that is valid as long as $a \ll \lambda_b$, with λ_b being the wavelength of operation in the background material, consistent with the assumptions in the previous sections. For simplicity, we assume a scalar polarizability, implying that the particles are isotropic

58

(nanospheres, easy to realize as colloidal metal particles), or for more general shapes focusing on one specific field polarization. It is relevant to stress that the dipolar approximation represents a good assumption for small nanoparticles, and in particular in the case of nanospheres, due to their inherent symmetries. We have verified that this approximation holds very well even in the limit of very small gaps, as those considered in the following examples [140]. The use of additional multipolar orders, as considered, e.g., in [148], may increase the accuracy of the calculation, but also complicate some of the physical insights outlined in the following.

For a single isolated chain, the spectrum of supported eigenmodes may be split into longitudinal and transverse polarization with respect to the chain axis $\hat{\mathbf{x}}$ [140] (see previous sections). In particular, for $e^{i\beta x}$ propagation, the corresponding guided wave number β satisfies the following closed-form dispersion relations, respectively, for longitudinal and transverse modes:

$$L = 3\bar{d}^{-3}\left[f_3\left(\bar{\beta},\bar{d}\right) - i\bar{d}\, f_2\left(\bar{\beta},\bar{d}\right) \right] - \bar{\alpha}^{-1} = 0$$

$$T = -\frac{3}{2}\bar{d}^{-3}\left[f_3\left(\bar{\beta},\bar{d}\right) - i\bar{d}\, f_2\left(\bar{\beta},\bar{d}\right) - \bar{d}^2 f_1\left(\bar{\beta},\bar{d}\right) \right] - \bar{\alpha}^{-1} = 0$$

(34)

where $f_N\left(\bar{\beta}, \bar{d}\right) = Li_N\left(e^{i(\bar{\beta}+1)\bar{d}}\right) + Li_N\left(e^{-i(\bar{\beta}-1)\bar{d}}\right)$, $Li_N\left(z\right) = \sum_{k=1}^{\infty} \frac{z^k}{k^N}$ is the polylogarithm function of order N [149] and all the quantities have been normalized, consistent with [140], as $\bar{d} = k_b d$, $\bar{\beta} = \beta / k_b$, $\bar{\alpha} = k_b^3 \alpha / \left(6\pi\varepsilon_b\right)$, with $k_b = 2\pi / \lambda_b$ being the background wave number and ε_b the corresponding permittivity.

These equations fully take into account the dynamic coupling among the infinite number of particles composing the linear chain. They are real-valued for lossless particles (for which $\text{Im}\left[\bar{\alpha}^{-1}\right] = -1$ [140]), supporting guided modes with $\bar{\beta} > 1$, but they are also fully valid in the complex domain when realistic material losses are considered, making it possible to evaluate the realistic damping factors associated with material absorption and radiation losses. They can be applied also to the leaky-wave modal regime, for which $\text{Re}\left[\bar{\beta}\right] < 1$ and the chain radiates as an antenna in the background region [150].

When l is finite in Fig. 30, i.e., there are two parallel chains, their mutual coupling produces a modification of their guidance properties, which may be taken into account by considering the polarization fields induced by the electric field from each chain on the other. The fields radiated by each chain may be expanded into cylindrical waves, allowing us to write the general closed-form expressions for the coupling coefficients between the two chains.

Without loss of generality, we can assume that the particles composing the first chain, located at $y = 0$, are polarized by an eigenmodal wave with dipole moments $\mathbf{p}_1 e^{i\beta md}$, where $m \in \Im$ is the integer index for each nanoparticle of the chain. The equivalent current distribution on the x axis may be written as:

$$\mathbf{J}\left(x\right) = -i\omega\mathbf{p}_1 \sum_{m=-\infty}^{\infty} e^{i\beta md}\delta\left(x - md\right),$$

(35)

59

where $\delta(.)$ is the Dirac delta function. The fields radiated by such current distribution may be expanded into cylindrical waves and may be used to evaluate the coupling coefficients between one chain and the other, with dipole moments $\mathbf{p}_2 e^{i\beta md}$ located at $y = l$, yielding:

$$C_{xx} = -\frac{3}{\overline{d}} \sum_{m=-\infty}^{\infty} \overline{b}_m^2 K_0\left[\overline{b}_m \overline{l}\right]$$

$$C_{xy} = C_{yx} = -\frac{3i}{\overline{d}} \sum_{m=-\infty}^{\infty} \sqrt{\overline{b}_m^2 + 1}\, \overline{b}_m K_1\left[\overline{b}_m \overline{l}\right]$$

$$C_{yy} = \frac{3}{\overline{l}\overline{d}} \sum_{m=-\infty}^{\infty} \left(\overline{b}_m^2 + 1\right)\overline{l} K_0\left[\overline{b}_m \overline{l}\right] + \overline{b}_m K_1\left[\overline{b}_m \overline{l}\right] \,, \tag{36}$$

$$C_{zz} = \frac{3}{2\overline{d}} \sum_{m=-\infty}^{\infty} \left(\overline{b}_m^2 + 2\right) K_0\left[\overline{b}_m \overline{l}\right] - \overline{b}_m^2 K_2\left[\overline{b}_m \overline{l}\right]$$

$$C_{xz} = C_{zx} = C_{yz} = C_{zy} = 0$$

where $\overline{b}_m = \sqrt{\left(\overline{\beta} + \frac{2\pi m}{\overline{d}}\right)^2 - 1}$ and $K_m[.]$ are the modified Bessel functions of order m and $\overline{l} = k_b l$. The generic coupling coefficient C_{ij} expresses the polarization along j on one chain induced by the i-polarized dipoles on the other chain. The summations in (36) have very fast convergence, and the dominant term ($m = 0$) is usually sufficient to take into account the dominant contribution to the coupling, an approximation that is consistent with the approach we used in [143]. The numerical results shown in the following sections have been obtained by considering the first ten terms in the summations (36), even though full convergence has been usually achieved after the first one or two terms. The form of the coupling coefficients in (36) ensures that longitudinal (directed along x) and transverse modes polarized along y are coupled through C_{xy}, whereas transverse modes polarized along z are not coupled with the orthogonal polarizations.

The complete closed-form dispersion relation for the eigenmodes supported by the parallel chains may be written as:

$$\det \begin{pmatrix} L & 0 & C_{xx} & C_{xy} \\ 0 & T & C_{xy} & C_{yy} \\ C_{xx} & -C_{xy} & L & 0 \\ -C_{xy} & C_{yy} & 0 & T \end{pmatrix} \det \begin{pmatrix} T & C_{zz} \\ C_{zz} & T \end{pmatrix} = 0\,, \tag{37}$$

or, in a more compact form:

$$\left[\left(L \pm C_{xx}\right)\left(T \mp C_{yy}\right) + C_{xy}^2\right]\left(T \pm C_{zz}\right) = 0\,. \tag{38}$$
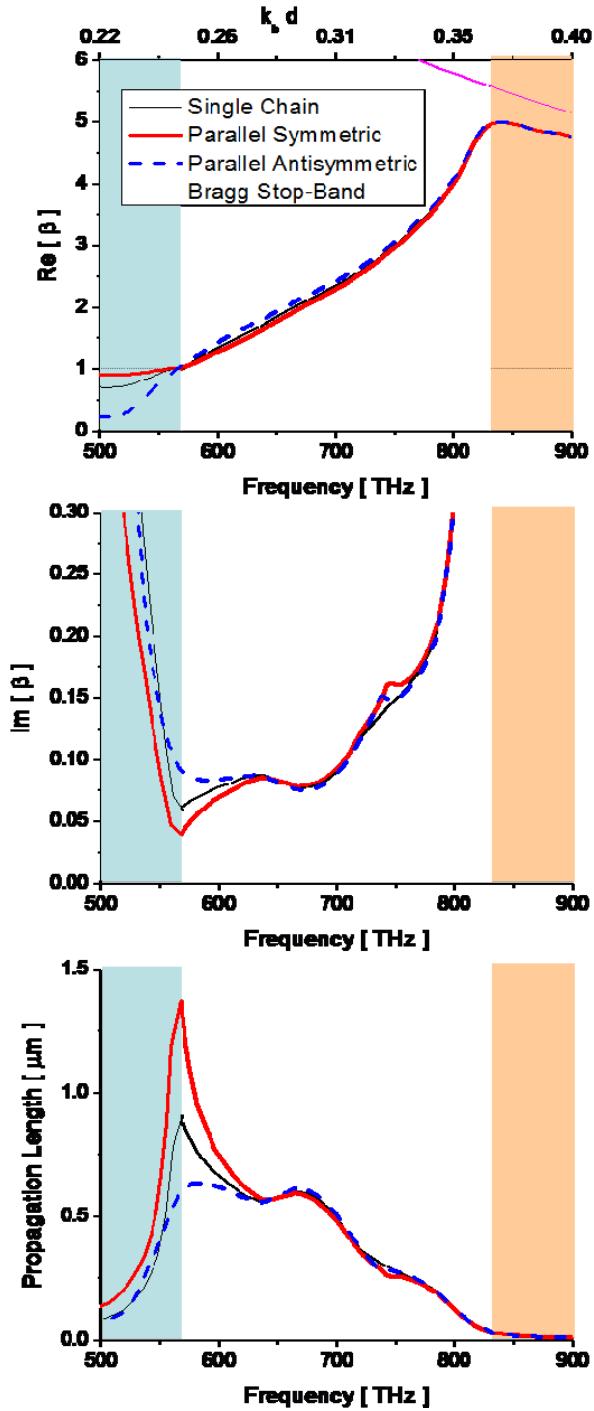
Figure 31 – Modal dispersion for the quasi-longitudinal modes supported by two parallel chains with interchain distance $l = 50\,\text{nm}$. The dispersions are compared to that of an isolated chain (thin solid line). The lighter blue shadowed region refers to leaky-wave propagation, whereas the darker orange region refers to the first Bragg stop-band.
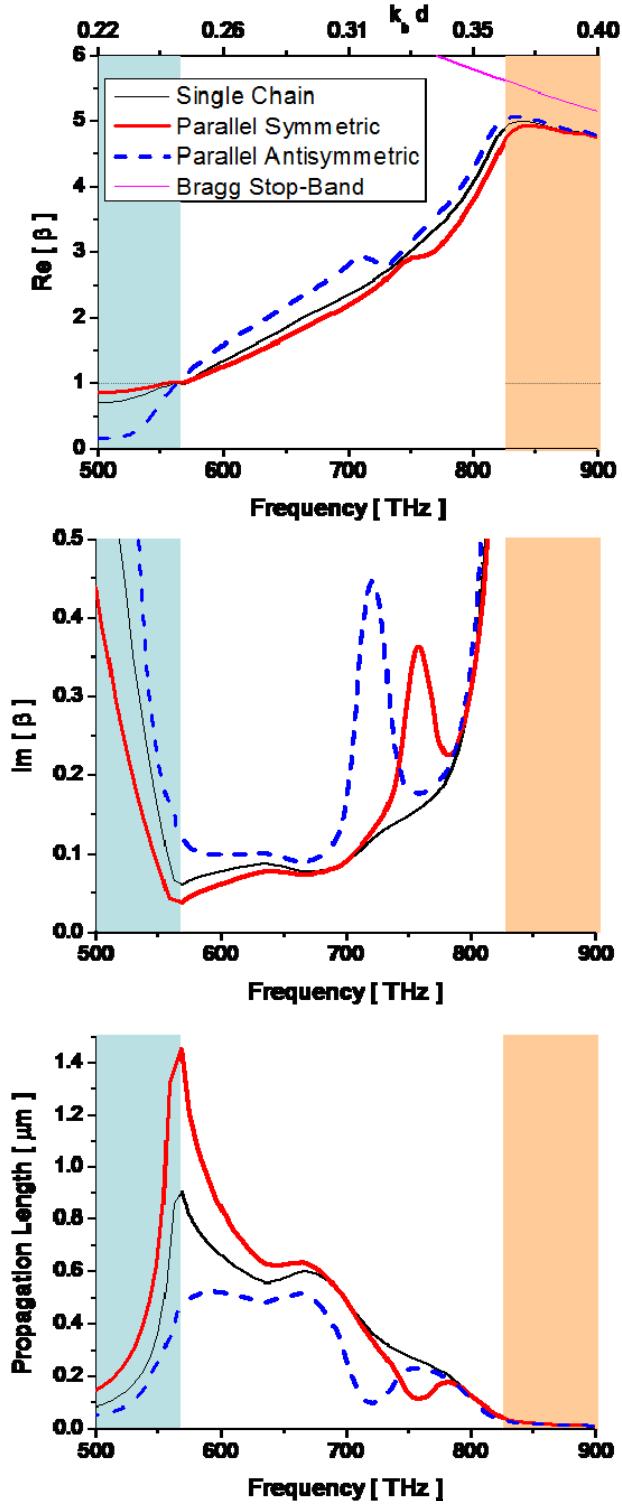
Figure 32 – Similar as in Fig. 31, modal dispersion for the quasi-longitudinal modes supported by two parallel chains with interchain distance $l = 30\,\text{nm}$.

The left-hand side in Eq. (38) consists of the product of two terms: the first determines the dispersion of the coupled modes polarized in the xy plane (among which the quasi-longitudinal

antisymmetric modes considered in [143]), whereas the second determines the purely-transverse modes polarized along z. This dispersion equation is completely general and it fully takes into account the entire dynamic interaction among the infinite particles composing the two parallel chains. Since the coupling coefficients (36) tend rapidly to zero for increased l, Eq. (38) represents the perturbation of the original transverse and longitudinal modes supported by the two linear chains independently given by $L = 0$ and $T = 0$ respectively [140], produced by the coupling coefficients C. In particular, it is seen that each of the three orthogonal polarizations (along x, y, z) splits into two branches due to the coupling between the chains, one with symmetric and the other with antisymmetric properties (consistent with the sketch in Fig. 30), leading to six modal branches of guided modes, some of which supported at the same frequency. In particular, the modes in the xy plane are mixed together (i.e., the parallel chains do not support purely longitudinal or purely y – polarized modes, but they do support purely transverse z – polarized modes). In the limit of lossless particles, since L and T are real for any $\bar{\beta} \geq 1$ [140], by inspecting Eq. (38) we notice that the parallel chains still support lossless guided propagation for any $1 \leq \bar{\beta} \leq \pi / \bar{d}$. In the following, we analyze in details the modal properties of this setup in its different regimes of operation.

d. Guided Modes of Parallel Chains of Silver Nanospheres

In this section we consider the different regimes of guided propagation supported by the parallel chains of Fig. 30, considering realistic optical materials composing the plasmonic nanoparticles. In the case of a chain of homogeneous spherical particles of radius a and permittivity $\varepsilon = \varepsilon_r + i\varepsilon_i$, their normalized polarizability satisfies the following relations [140]:

$$\mathrm{Re}\left[\bar{\alpha}^{-1}\right] = \frac{3}{2}\left(k_b a\right)^{-3} \frac{\varepsilon_r + 2\varepsilon_b}{\varepsilon_r - \varepsilon_b}$$

$$\mathrm{Im}\left[\bar{\alpha}^{-1}\right] = -1 - \frac{9\varepsilon_i}{2} \frac{\varepsilon_b \left(k_b a\right)^{-3}}{\left(\varepsilon_r - \varepsilon_b\right)^2 + \varepsilon_i^2} \qquad (39)$$

This polarizability model is analogous to the classic quasi-static polarizability definition for a small sphere, with the addition of radiation loss (as from the -1 term in $\mathrm{Im}\left[\bar{\alpha}^{-1}\right]$), to comply with energy conservation. Since the guided modes are perturbations of the longitudinal and transverse modes supported by the isolated chains, there is no need to analyze here again in full detail how variations in the chain geometry, i.e., in a, d and/or the involved materials, may affect the guidance of the parallel chains, since we have already extensively studied how these changes affect the guidance of isolated chains in [140]. In the following, therefore, we focus on one specific realistic design of the chains and we employ the exact formulation developed in the previous section to characterize the modal properties of two of such parallel arrays coupled together. In the following, we focus on colloidal silver nanospheres embedded in a glass background ($\varepsilon_b = 2.38\,\varepsilon_0$).We use experimental data available in the literature to model the silver permittivity at optical frequencies [27] and we assume $a = 10\,\mathrm{nm}$ and $d = 21\,\mathrm{nm}$ for the two chains. In general, we can predict that larger separation distances for same particle size are expected to weaken the guidance properties of the array and reduce the bandwidth of operation and robustness to loss, whereas particles with larger size have the opposite effect.

63

i. *Quasi-longitudinal propagation (forward modes)*

An isolated linear chain of plasmonic nanoparticles supports forward-wave longitudinal guided modes ($x-$polarized), satisfying the dispersion relation $L=0$, over the frequency regime for which:

$$6\left[Cl_3\left(\bar{d}+\pi\right)+\bar{d}\,Cl_2\left(\bar{d}+\pi\right)\right]<\bar{d}^3\,\mathrm{Re}\left[\bar{\alpha}^{-1}\right]<3\left[\xi(3)+Cl_3\left(2\bar{d}\right)+\bar{d}\,Cl_2\left(2\bar{d}\right)\right],\qquad(40)$$

where $Cl_N\left(\theta\right)$ are Clausen's functions [149] and $\xi(.)$ is the Riemann Zeta function. For the case at hand (silver nanoparticles, $a=10\,nm$ and $d=21\,nm$), such modal regime is supported over a relatively wide range of frequencies between $550\,THz$ and $850\,THz$, as shown in Fig. 31 (thin solid black line). In particular, in the figure we plot: (a) the real and (b) the imaginary parts of the normalized $\bar{\beta}$ and (c) the propagation length, i.e., the distance traveled by the guided mode before its amplitude is e^{-1} of the original value, which is equal to $\mathrm{Im}\left[\beta\right]^{-1}$. The shadowed regions at the sides of the plots delimit the leaky-wave region (left-side, lighter blue shadowed region), for which $\mathrm{Re}\left[\bar{\beta}\right]<1$ and the mode radiates in the background region [154], and the stop-band region (right side, darker shadow, brown), where $\mathrm{Re}\left[\bar{\beta}\right]=\pi/\bar{d}$ when lossless particles are considered and the mode is evanescent in nature. In between these two regions, as defined by Eq. (40), the modes are guided and $\mathrm{Im}\left[\beta\right]$, i.e., the damping factor, is only associated with material losses, since in the limit of lossless particles the mode would not radiate and $\mathrm{Im}\left[\beta\right]=0$. In the leaky-wave region (lighter blue shadow) the damping is larger, due to additional radiation losses [150], whereas in the stop-band (darker shadow) the mode does not propagate and it is reflected back by the chain due to Bragg reflection (the ideal Bragg stop-band line $\mathrm{Re}\left[\bar{\beta}\right]=\pi/\bar{d}$ is shown in Fig. 31 as the thin pink line). Near the light line ($\mathrm{Re}\left[\bar{\beta}\right]\simeq1$) the mode is poorly guided by an isolated chain, but its propagation length may reach relatively large values, around $1\,\mu m$.

In the same figure we plot the variation of these dispersion diagrams in the case of two coupled parallel chains separated by a finite distance l. In this case, the longitudinal modes are coupled with each other, also polarizing the chains with a small transverse component along y, consistent with the value of C_{xy}. The longitudinal mode dispersion splits into two quasi-longitudinal branches, one with symmetric and the other with antisymmetric properties with respect to $x-$ polarization (as sketched in Fig. 30). The two modes satisfy, respectively, the following dispersion relations, consistent with Eq.(38):

$$
\begin{aligned}
sym: &\quad \left(L+C_{xx}\right)\left(T-C_{yy}\right)+C_{xy}{}^2=0 \\
antisym: &\quad \left(L-C_{xx}\right)\left(T+C_{yy}\right)+C_{xy}{}^2=0
\end{aligned}
,\qquad(41)
$$

providing the following constraints on the polarization eigenvectors for the two chains [obtained by calculating the eigen-vectors associated with Eq. (37)]:

64

$$sym: \begin{cases} \mathbf{p}_1 \cdot \hat{\mathbf{x}} = \mathbf{p}_2 \cdot \hat{\mathbf{x}} \\ \mathbf{p}_1 \cdot \hat{\mathbf{y}} = -\mathbf{p}_2 \cdot \hat{\mathbf{y}} \end{cases}$$

$$antisym: \begin{cases} \mathbf{p}_1 \cdot \hat{\mathbf{x}} = -\mathbf{p}_2 \cdot \hat{\mathbf{x}} \\ \mathbf{p}_1 \cdot \hat{\mathbf{y}} = \mathbf{p}_2 \cdot \hat{\mathbf{y}} \end{cases} . \tag{42}$$
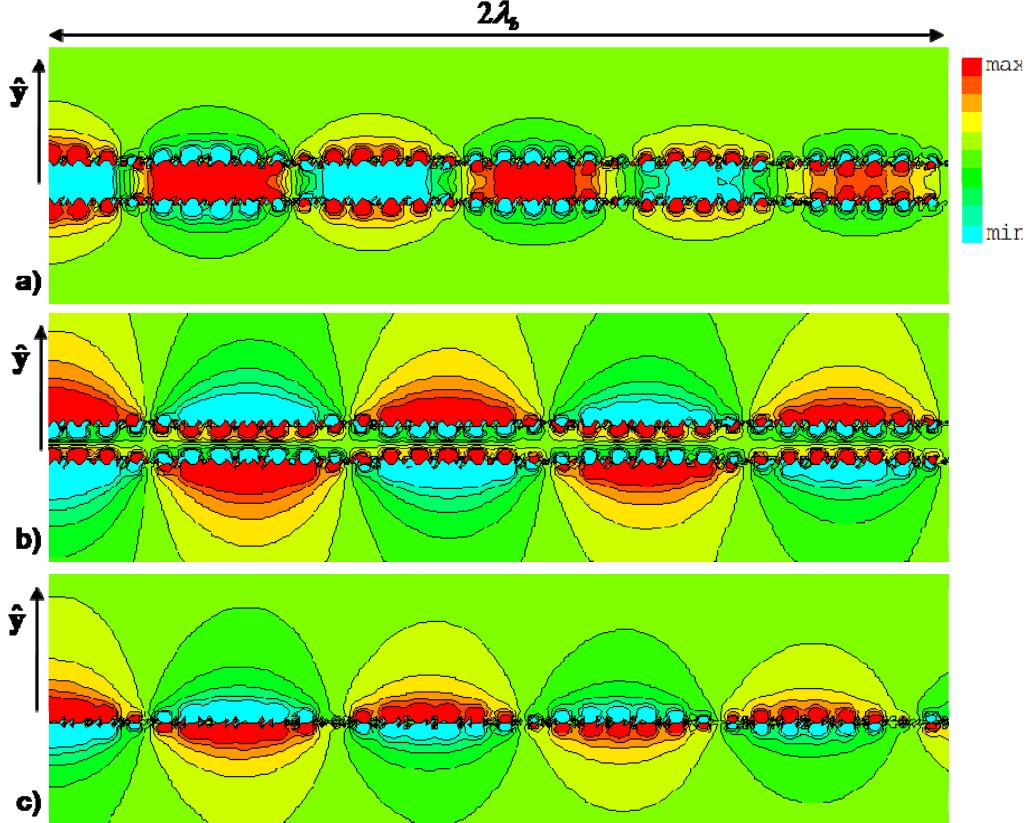

Figure 33 – (Color online). Magnetic field distribution (snapshot in time) for the chains of Fig. 32 at frequency $f = 585\,THz$. (a) antisymmetric mode, (b) symmetric mode, (c) isolated chain. All the plots are drawn with the same color scale bar (normalized to the modal amplitude at the left of the figure). The total length of the simulated region is $2\lambda_b$.

Figure 31 shows as a first example the dispersion of symmetric and antisymmetric modes for $l = 50\,nm$. It is noticed that the small coupling between the chains slightly perturbs the dispersion of the modes, causing the antisymmetric mode (blue dashed line, with polarization currents oppositely flowing along the chains) to have slightly larger real and imaginary parts of $\bar{\beta}$ with respect to the unperturbed longitudinal mode supported by an isolated chain (light solid line) in the guided regime. Conversely, the symmetric mode (thick red solid line) supports slightly lower values of $\mathrm{Re}\left[\bar{\beta}\right]$. The perturbation is stronger near the light line and in the leaky-wave region, since the mode is less confined around each chain in this regime. The symmetric operation allows an increase of the propagation length of up to $1.5\,\mu m$, since the coupling between the parallel chains with polarization currents flowing in the same direction can boost up the mode. On the other hand, the antisymmetric operation has slightly lower propagation lengths, but this is accompanied with the important advantage of much stronger field confinement, as we note in the

65

Approved for public release; distribution unlimited.

following. The derivative $\partial \operatorname{Re}\left[\bar{\beta}\right]/\partial\omega > 0$ ensures that the modes supported in this regime are all forward-wave, and this is also confirmed by the condition $\operatorname{Im}\left[\bar{\beta}\right] > 0$, which ensures that phase and group velocity are parallel with each other for both modes.

As an aside, it should be noted that in the leaky-wave region (blue lighter shadow in the left) the forward-wave modes are improper in nature [154], implying that the dominant cylindrical wave radiated by the chain grows with the distance from the chain instead of decaying. This implies that for a correct evaluation of the modal properties and the field distribution generated in this forward-leaky mode regime, the formulas of Eq. (36) for the index $m = 0$ need to be corrected using the Hankel functions of second order instead of the modified K_n functions.

Figure 32 shows analogous results for closer chains, with $l = 30\,nm$. It is seen that the perturbation from the isolated chain is now stronger and the coupling between the modes generates some isolated resonant regions of stronger absorption, which are associated with stronger transversely polarized components of the field. Still, near the light line propagation lengths are relatively large.

Figure 33 shows the calculated orthogonal magnetic field distribution (snapshot in time) on the xy plane for the modes supported by the chains of Fig. 32 ($l = 30\,\mathrm{nm}$) at the frequency $f = 585\,THz$, near the light line. The figure emphasizes how the modal distribution is quite different in the three scenarios, even if the guided wave numbers are similar. Fig. 33a corresponds to antisymmetric propagation, for which the two chains support the eigenvector polarizations $\mathbf{p}_1 = \hat{\mathbf{x}} + (0.14i - 0.008)\hat{\mathbf{y}}$, $\mathbf{p}_2 = -\hat{\mathbf{x}} + (0.14i - 0.008)\hat{\mathbf{y}}$, consistent with Eq. (42). The corresponding normalized wave number at this frequency is $\bar{\beta}_{asym} = 1.38 + i\,0.1$. It can be seen how the magnetic field is very much confined in the tiny background region delimited by the two chains, similar to the field propagation in a regular transmission-line at low frequencies. Also the electric field is mainly transverse in the region between the chains, supporting the transverse electromagnetic configuration, again typical of a transmission-line mode. This regime of operation, whose interesting properties we have already described in details in [143], may lead to relatively low-loss optical guidance with ultra-confined properties in the space between the chains, similar to an optical nanotransmission-line. This functionality may be particularly appealing for optical switching, nanoscale field interaction, sensing and nonlinearity enhancements.

Fig. 33b, on the other hand, refers to the symmetric mode for the same parallel chains. In this case $\mathbf{p}_1 = \hat{\mathbf{x}} + (0.08i - 0.003)\hat{\mathbf{y}}$, $\mathbf{p}_2 = \hat{\mathbf{x}} - (0.08i - 0.003)\hat{\mathbf{y}}$ and $\bar{\beta}_{sym} = 1.13 + i\,0.053$. The currents flowing along the chains are now parallel with each other, producing fields very much spread all around the outside background region and weak field concentration in between them. This operation is equivalent to two parallel current flows, leading to small fields in between them. A single linear chain has analogous guidance properties, shown in Fig. 33c (for comparison, in this third example the chain is positioned at the same location as the lower chain in the other two panels). In this case the mode is purely longitudinal and $\bar{\beta}_{single} = 1.18 + i\,0.072$, implying weak guidance.

Comparing the three field plots (notice that for fair comparison they have been calculated with the same color scale and under the same initial amplitude excitation), it becomes evident that the

66

antisymmetric longitudinal operation allows for a much stronger confinement of the field, with comparable propagation length. By field confinement here, we consider the field decay away from the array axis, which is always of a higher rate for the anti-symmetric longitudinal mode compared to an isolated chain or the symmetric mode. By increasing the distance between the chains, as in the examples of Fig. 31, we achieve similar confinement in the region between the chains with reduced attenuation. In addition to a quantitatively larger field confinement achieved with the antisymmetric mode (compared to the isolated chain, despite the larger transverse physical cross section of the parallel chain geometry), this operation ensures larger confinement in between the two chains, which is particularly appealing for applications aiming at enhancing the nanoscale optical interaction.

These properties are not only limited to the modes operating near the light line, but they are also valid for higher frequencies and more confined modes. For instance, in Fig. 34 we show the magnetic field plots for the same chains, operating at $f = 680\,THz$. At these frequencies, as seen in Fig. 32, the three cases have similar levels of absorption and more confined slow-wave modes. The antisymmetric excitation is characterized in this case by $\mathbf{p}_1 = \hat{\mathbf{x}} + (0.37\,i - 0.038)\hat{\mathbf{y}}$, $\mathbf{p}_2 = -\hat{\mathbf{x}} + (0.37\,i - 0.038)\hat{\mathbf{y}}$ and $\bar{\beta}_{asym} = 2.42 + i\,0.091$. Its field distribution (Fig. 34a) still shows strong confinement between the two chains, where a "quasi-uniform" magnetic field may propagate as if guided by a transmission-line. The wave is slower than in the case of Fig. 4, due to increased $\mathrm{Re}\left[\bar{\beta}\right]$, but the level of absorption is still quite good and the mode can propagate for over two wavelengths with no strong attenuation. The symmetric operation, for which $\mathbf{p}_1 = \hat{\mathbf{x}} - (0.158\,i - 0.082)\hat{\mathbf{y}}$, $\mathbf{p}_2 = \hat{\mathbf{x}} + (0.158\,i - 0.082)\hat{\mathbf{y}}$ and $\bar{\beta}_{sym} = 1.9 + i\,0.074$, once again provides worse field confinement, as expected. In this case (Fig. 34b) the field is spread around the chains and is very weak in the region between the two chains. Similar spreading is noticeable in the single isolated chain configuration of Fig. 34c, with $\bar{\beta}_{single} = 2.06 + i\,0.077$. We note that the field spreading in the region around the chains would also be more sensitive to radiation losses produced by disorder and technological imperfections. This is consistent with our findings in [141], in which we have quantitatively modeled the possible presence of disorder along such periodic arrays in terms of effective additional loss in the polarizability coefficient. We predict that the antisymmetric transmission-line operation of the parallel chains may produce more robust optical guidance confined in the region between the chains compared to the symmetric operation or the isolated chain.

From the previous examples, it is evident that in this regime the modes guided by the parallel chains are quasi-longitudinal with a spurious transverse polarization, arising from the coupling, which is nearly 90° out of phase with respect to the longitudinal polarization. In Fig. 35, for the parallel chains of Fig. 31 and 32 we have calculated the level of transverse cross-polarization (defined as the ratio of the longitudinal to transverse component of $\mathbf{p}$) induced on the particles due to coupling, as a function of frequency. It is evident that its level increases for closer chains, as expected, and it is larger for antisymmetric modes. In the region of enhanced absorption that we have noticed in Fig. 32, the corresponding level of cross-polarization is also very high, implying that at some resonance frequencies the transverse polarization may be even higher than the longitudinal one, noticeably affecting the chain guidance. As expected, in these regimes the losses are inherently larger. The coupling is minimal near the light line and in the leaky-wave and stop-band regimes, and reaches its maximum somewhere inside the guidance region, whose

67

position in frequency varies depending on the distance between the chains and the mode of operation.
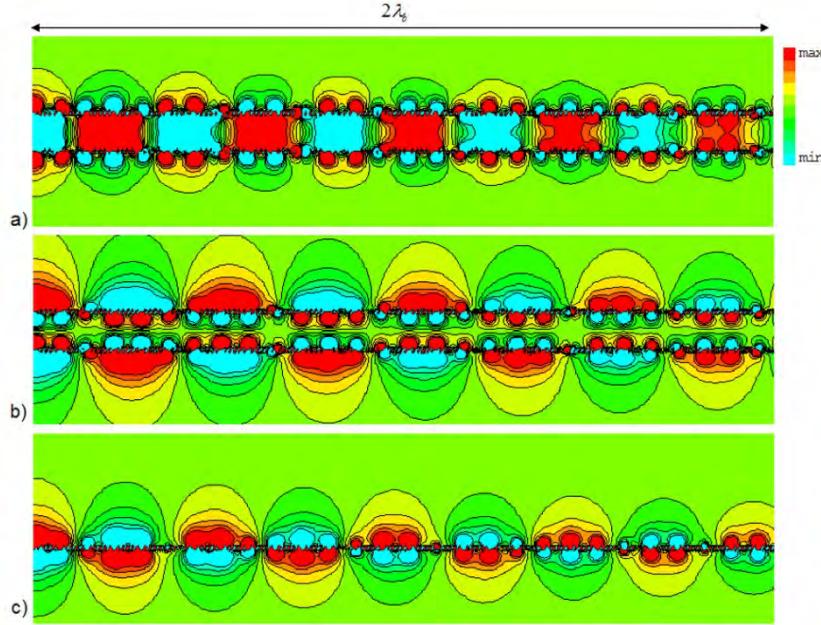

Figure 34 – Similar to Fig. 33, magnetic field distribution (snapshot in time) for the chains of Fig. 32 at frequency $f = 680 THz$: (a) antisymmetric mode, (b) symmetric mode, (c) isolated chain.
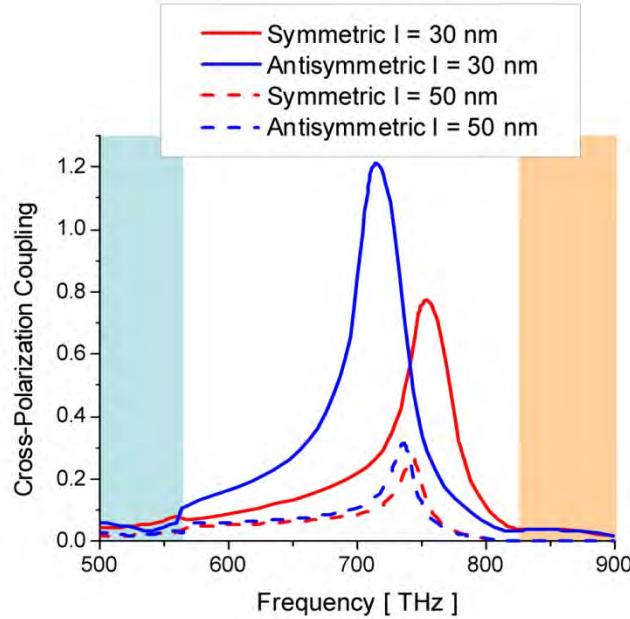

Figure 35 –Magnitude of the transverse cross-polarization for the chains of Figs. 31 and 32, operating in their quasi-longitudinal forward-wave regime.

68

ii. Quasi-transverse y-polarized propagation (backward modes)

We have discussed in [140] that a single isolated linear chain may also support transversely polarized guided modes, satisfying the exact dispersion relation $T = 0$. In this case, the condition on the particle polarizability is:

$$\bar{d}^3 \bar{\alpha}_{min}^{-1} < \bar{d}^3 \operatorname{Re}\left[\bar{\alpha}^{-1}\right] < -3\left[Cl_3\left(\bar{d} + \pi\right) + \bar{d}\, Cl_2\left(\bar{d} + \pi\right) - \bar{d}^2 Cl_1\left(\bar{d} + \pi\right)\right], \quad (43)$$

where $\bar{\alpha}_{min}^{-1}$ is defined in [140]. In this regime the isolated chain always supports two distinct modes at the same frequency, both with the same transverse polarization: one is guided along the chain and has backward-wave properties, the other is weakly guided, with forward-wave properties and $\operatorname{Re}\left[\bar{\beta}\right] \simeq 1$ (this eigenmode is basically a simple plane wave traveling in the background region, weakly polarizing the nanoparticles. This is not of interest for guidance purposes [140], but it is still discussed here for sake of completeness). For the geometry at hand, transversely-polarized propagation is supported over the frequencies between $650\,THz$ and $800\,THz$, in part overlapping with the longitudinally-polarized regime, as shown in Fig. 36 (thin black line), consistent with Eq. (43). Remarkable differences are noticed between longitudinal and transverse polarization: the confined transverse mode is backward in nature, explaining the negative slope of $\operatorname{Re}\left[\bar{\beta}\right]$ versus frequency and the negative sign of $\operatorname{Im}\left[\bar{\beta}\right]$. Correspondingly, the bandwidth is more limited and losses are higher, as is usually the case for backward-wave waveguides. As a consequence, the leaky-wave operation arises now at the upper boundary of the guided regime (lighter shadowed region in Fig. 36) [150], whereas the Bragg stop-band is positioned at the lower-end of the guidance band (darker shadow).

Due to modal coupling in the xy plane, when the coupling between parallel chains is considered, the quasi-transverse modes still satisfy the dispersion relations (41) and the polarization eigenvectors obey the same relations (42). It should be noticed, however, that in this regime the modes are quasi-transverse, and therefore the antisymmetric mode now corresponds to parallel $y-$polarized chains, whereas the symmetric mode supports anti-parallel polarization along y, consistent with (42), as sketched in Fig. 34.

Figure 36 shows the dispersion of symmetric and antisymmetric quasi-transverse modes for $l = 50\,nm$. Once again, the relatively small coupling between the chains produces a minor perturbation of the original backward-wave purely-transverse mode, which causes the antisymmetric mode to have slightly lower real and slightly larger imaginary part of $\bar{\beta}$. Conversely, the symmetric mode supports slightly larger values of $\operatorname{Re}\left[\bar{\beta}\right]$. As in the previous section, the coupling is stronger near the light line and in the leaky-wave region (lighter shadow), as expected. Also in this scenario the symmetric operation allows longer propagation lengths, even if in this case the $y-$polarized currents are oppositely oriented (see Fig. 37).

Compared to quasi-longitudinal forward modes, the propagation length is significantly reduced for these confined modes, due to the backward-wave nature of these modes and their transverse polarization. Of course, following the results in [140], the propagation length may be somewhat increased and optimized by increasing the size of the nanoparticles and/or reducing the interparticle distance d. Compared to backward-mode supported by isolated chains, these results show that the coupling between two parallel chains may increase the propagation length of

69

backward-wave optical nanowaveguides, simultaneously improving their field confinement in the space between the two lines, which may be of interest for several applications.
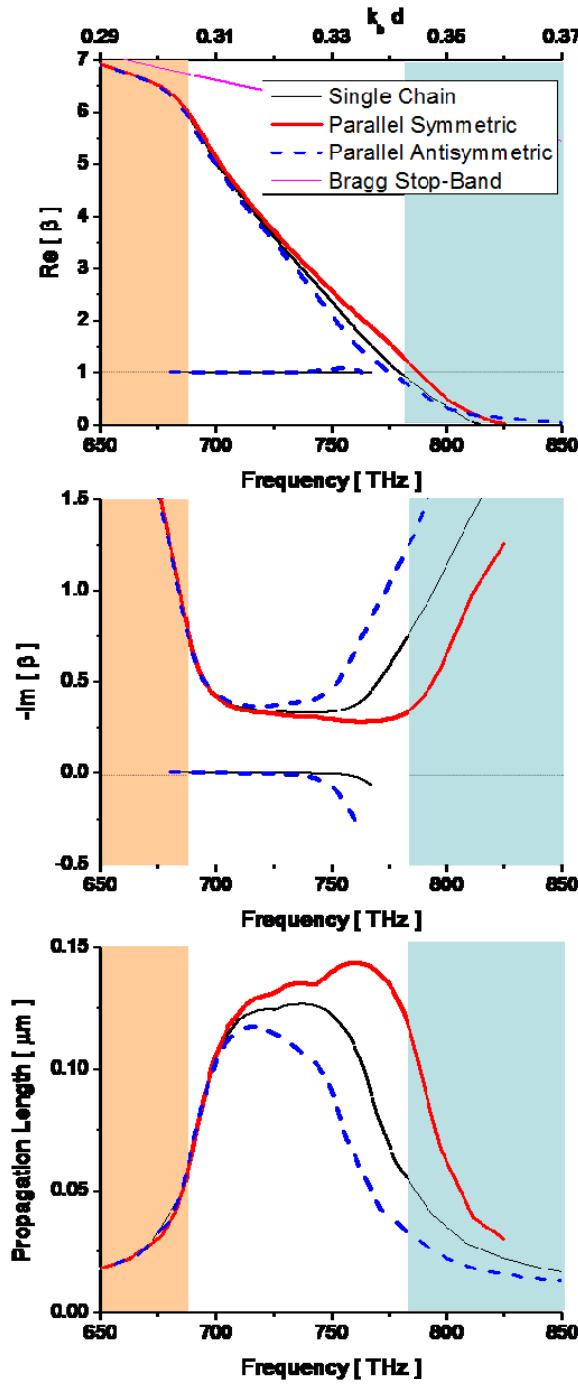

Figure 36 – Analogous to Fig. 31, modal dispersion for the quasi- transverse y − polarized modes supported by two parallel chains with interchain distance $l = 50\,\text{nm}$. In the antisymmetric polarization, as well as in the isolated chain, it is evident the presence of a second quasi-transverse mode with weakly guided properties, explaining the presence of two distinct branches.

70

Figure 38 shows analogous results in the case of closer chains ($l = 30\,\text{nm}$). Also in this case, the perturbation from the isolated chain is stronger and the bandwidth of backward operation may be increased by using two parallel chains in the symmetric mode. Here leaky modes (lighter shadow) are proper in nature and therefore Eqs. (36) also apply to this regime in the way they are written. Both in Fig. 36 and 38, for completeness, we also show the modal branch associated with the weakly guided forward-wave transverse mode, which is visible very close to the light line (thin solid line very close to the $\text{Re}\left[\bar{\beta}\right] = 1$ line in both plots). Consistent with its forward-wave properties, $\text{Im}\left[\bar{\beta}\right] > 0$ for this mode. As outlined above, this mode is of minor interest for guidance purposes, since it is a minor perturbation of a plane wave traveling in the background region, very weakly affected by the presence of the chains. It is noticed, as expected, that this second branch is present only for the antisymmetric modes, whose y–polarization is in the same direction for both chains. Indeed, in Figs. 36 and 38 one can see a second branch for the blue dashed lines, near the light line, corresponding to the weakly guided forward mode traveling in the background (not of interest here).

Figure 39 shows the magnetic field for these backward-wave modes as in Fig. 38 at the frequency $f = 700\,THz$. In the antisymmetric case (Fig. 39a) $\mathbf{p}_1 = \left(0.076 - 0.12i\right)\hat{\mathbf{x}} + \hat{\mathbf{y}}$, $\mathbf{p}_2 = -\left(0.076 - 0.12i\right)\hat{\mathbf{x}} + \hat{\mathbf{y}}$ and $\bar{\beta}_{asym} = 3.95 - i\,0.46$; in the symmetric case $\mathbf{p}_1 = \left(0.02 - 0.016i\right)\hat{\mathbf{x}} - \hat{\mathbf{y}}$, $\mathbf{p}_2 = \left(0.02 - 0.016i\right)\hat{\mathbf{x}} + \hat{\mathbf{y}}$ and $\bar{\beta}_{sym} = 5.88 - i\,0.72$; for the isolated chain $\bar{\beta}_{single} = 5.036 - i\,0.42$. The field distributions in some senses resemble the one for quasi-longitudinal modes, but the presence of a dominant transverse polarization does not allow an analogous strong transmission-line confinement in this backward-wave regime for the antisymmetric modes. Still, the plots confirm that relatively long backward-wave propagation (over one wavelength) is achievable using coupled parallel chains.

Figure 40 shows the level of longitudinal cross-polarization for the chains of Figs. 36 and 38. In this scenario, the cross-polarization is in general lower than for quasi-longitudinal modes and it is stronger for symmetric modes. Once again, the cross-polarization is stronger for closely coupled chains and it has some resonant peaks in the middle of the guidance region, for which the damping is correspondingly increased.
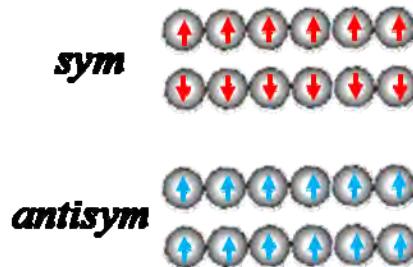

Figure 37 – Polarization properties of the symmetric and antisymmetric quasi-transverse modes supported by parallel chains as in Fig. 30.
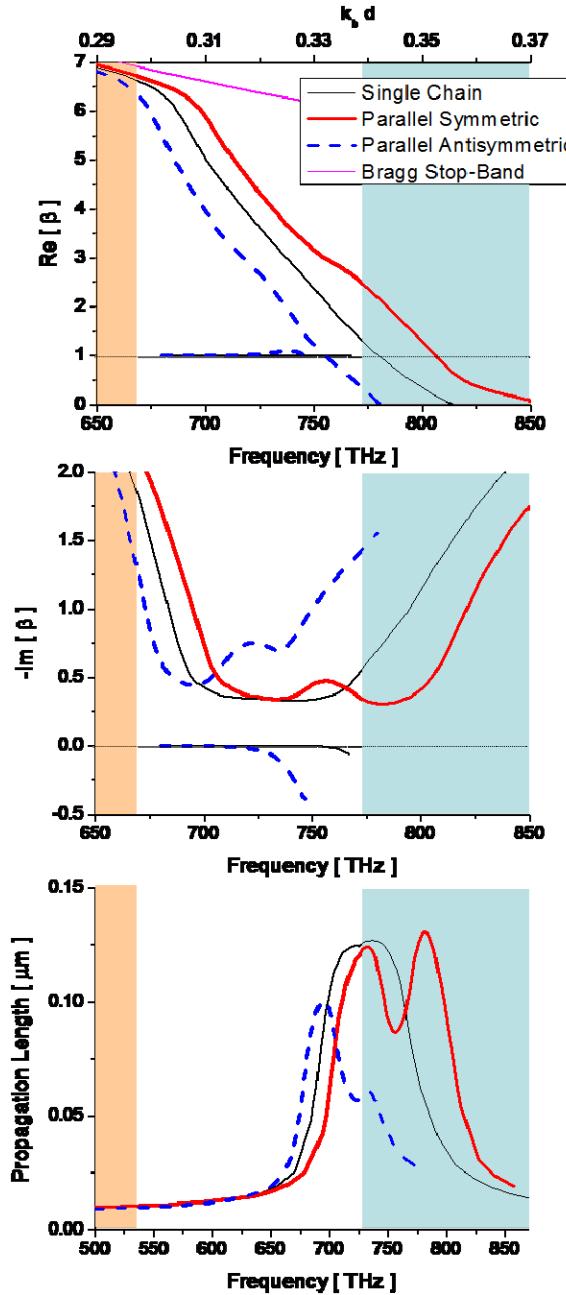
Figure 38 – Similar to Fig. 36, modal dispersion for the quasi- transverse y – polarized modes supported by two parallel chains with interchain distance $l = 30\,\text{nm}$.

iii. *Purely transverse z-polarized propagation (backward modes)*

When the chains are polarized along $\hat{\mathbf{z}}$ the supported modes are purely transverse, consistent with (37). Due to symmetry, the properties for isolated chains are identical to those described in the previous section, and therefore here we discuss how the coupling may have a different effect on the backward-wave guidance properties in this polarization. The coupling coefficient C_{zz} splits the transverse modal branch of propagation into two modes, with dispersion relations:

$$sym: \qquad T + C_{zz} = 0$$
$$antisym: \qquad T - C_{zz} = 0 \text{,} \qquad\qquad (44)$$

providing the following constraints on the polarization eigenvectors for the two chains:

$$sym: \qquad \mathbf{p}_1 \cdot \hat{\mathbf{z}} = \mathbf{p}_2 \cdot \hat{\mathbf{z}}$$
$$antisym: \qquad \mathbf{p}_1 \cdot \hat{\mathbf{z}} = -\mathbf{p}_2 \cdot \hat{\mathbf{z}} \text{.} \qquad\qquad (45)$$
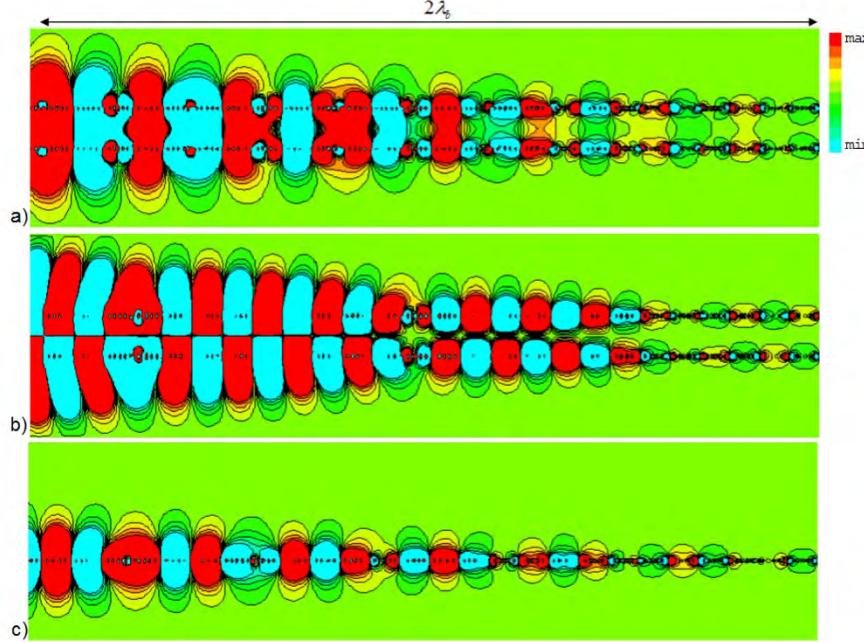
Figure 39 – Magnetic field distribution (snapshot in time) for the chains of Fig. 38 at frequency $f = 700 THz$. (a) antisymmetric mode, (b) symmetric mode, (c) isolated chain.
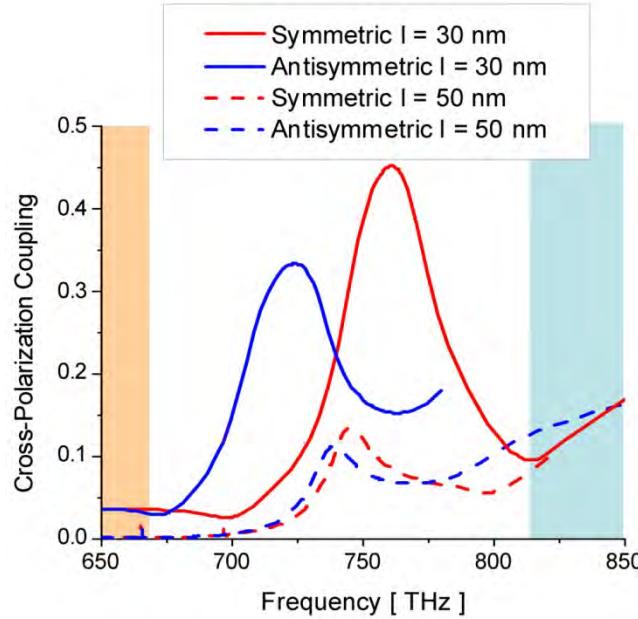
Figure 40 – Amplitude of the longitudinal cross-polarization for the chains of Figs. 36 and 38, operating in the quasi-transverse regime.

73
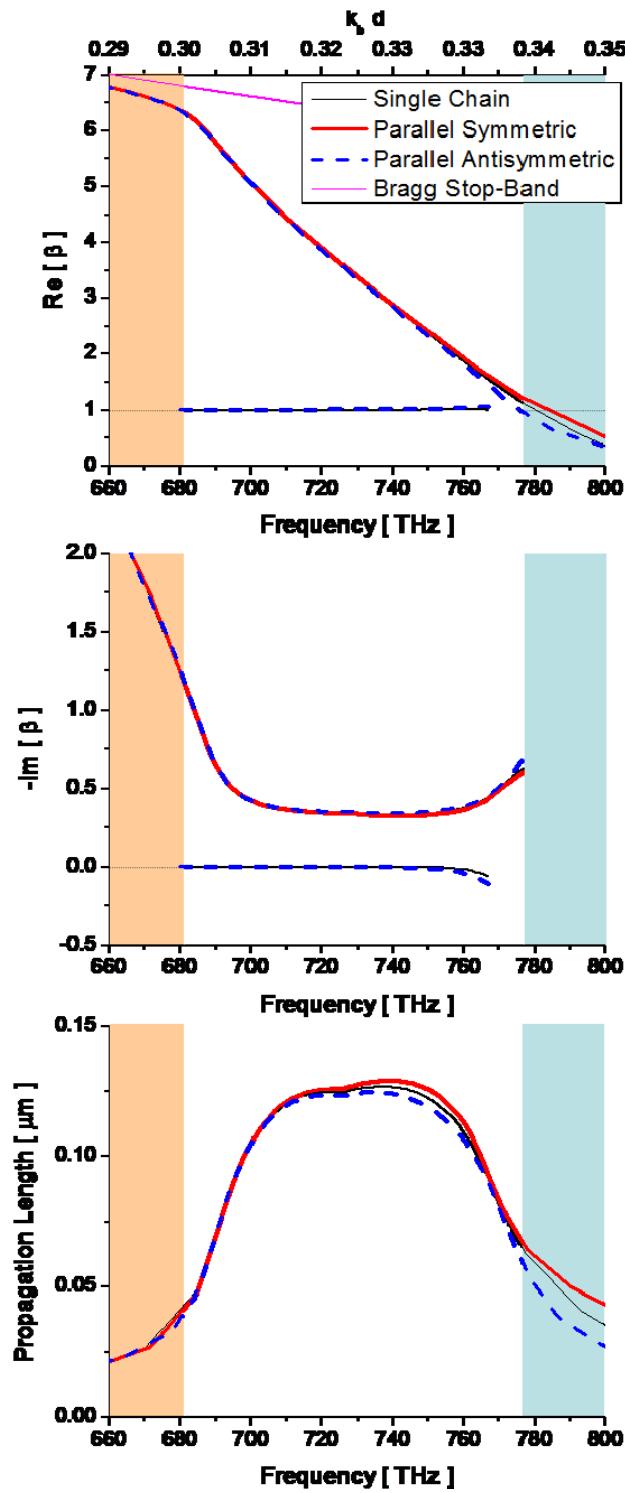
Figure 41 – Analogous to Fig. 31 and Fig. 36, modal dispersion for the quasi- transverse z – polarized modes supported by two parallel chains with interchain distance $l = 50\,\text{nm}$.
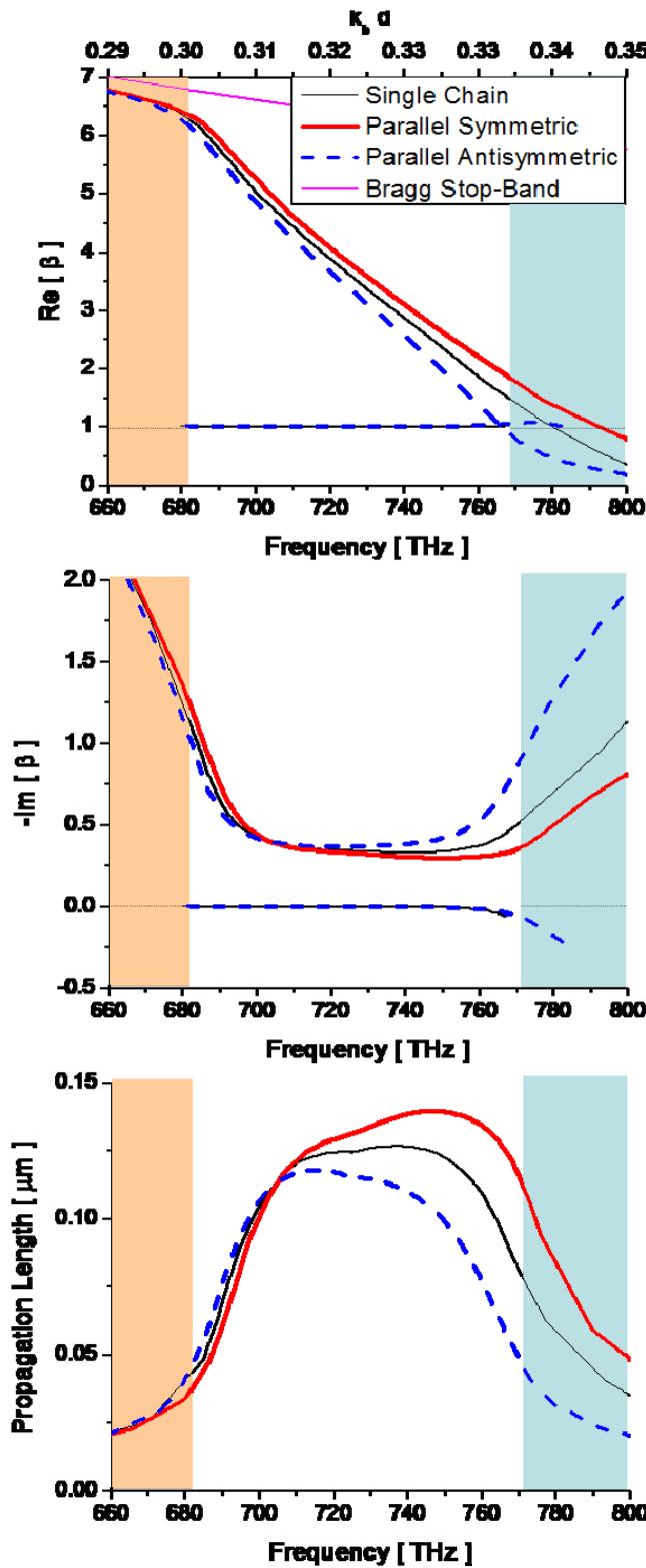
Figure 13 – (Color online). Similar to Fig. 12, modal dispersion for the quasi- transverse z-polarized modes supported by two parallel chains with interchain distance $l = 30\,\text{nm}$.

75

Figure 41 shows the dispersion of symmetric and antisymmetric transverse modes for $l = 50\,nm$. Here, for the same distance as in Figs. 31 and 36, the coupling perturbs the propagation properties even less as compared to the isolated chains.

Also in this case, symmetric modes allow slightly longer propagation lengths near the light line, where the coupling is stronger. Increasing the coupling ($l = 30\,nm$), as in Fig. 42, the perturbation is stronger, even if the trend is similar as in the previous scenario. Similar to the quasi-transverse propagation considered in the previous section, these purely transverse modes are also backward in nature and support leaky-wave propagation in the upper frequency regime and Bragg stop-band in the lower one. Moreover in this case the anti-symmetric transverse mode (consistent with the definition in Fig. 37) supports two distinct branches, one of which with very weakly guided properties near the light line.

Figure 43 shows the calculated orthogonal electric field distribution in the xy plane for the modes of Fig. 41 at the frequency $f = 750\,THz$. In this case the modes are purely transversely polarized and the guided wave numbers are respectively $\bar{\beta}_{asym} = 1.987 - 0.42i$, $\bar{\beta}_{sym} = 2.64 - 0.296i$, $\bar{\beta}_{single} = 2.36 - 0.34i$, consistent with Fig. 42. The field confinement in this polarization is not drastically different from that of an isolated chain, as evident from the figure, and the main advantage of using parallel chains may reside in the longer propagation distance of symmetric modes near the light line.
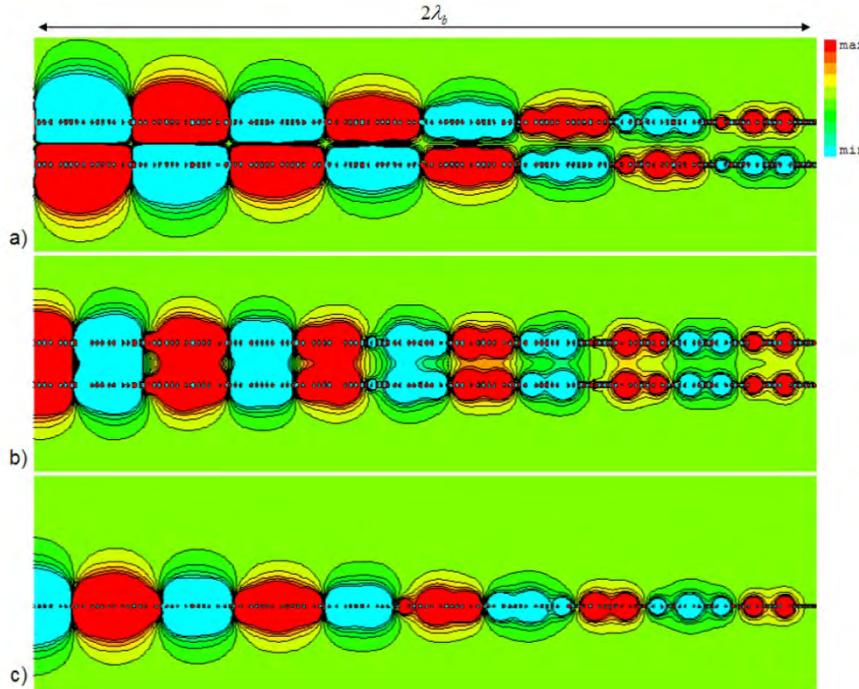
Figure 43 – (Color online). Electric field distribution (snapshot in time) for the chains of Fig. 41 at frequency $f = 750\,THz$. (a) antisymmetric mode, (b) symmetric mode, (c) isolated chain.

### e. Conclusions

We have presented in this section a fully general and complete theoretical formulation for the analysis of the dynamic coupling between two parallel linear chains of plasmonic nanoparticles

operating as optical waveguides. These chains may support up to eight different guided modes with different polarization properties in the same range of frequencies, which we have fully analyzed here. We have shown that, compared to linear arrays, these waveguides may support relatively longer propagation lengths and ultra-confined beams, operating analogously to transmission-line segments at lower frequencies. In particular, our results confirm that, by operating near the light line with antisymmetric quasi-longitudinal modes, we may achieve relatively long propagation lengths (of several wavelengths) and ultraconfined beam traveling, similar to a transmission-line, in the background region sandwiched between the two antisymmetric current flows guided by the chains. It should be stressed that the designs considered here are based on ultrasmall nanospheres, with the aim of large concentration of light in a sub-wavelength region. This choice inherently produces relatively short propagation lengths, in part improved by the parallel chain configuration. Large field confinement, even at the expenses of moderate propagation distances, may be appealing in a variety of applications, i.e., nonlinearity enhancement, sensing, optical switching and nanoscale interaction with light, as in optical nanocircuits [144]-[145]. On the other hand, longer propagation distances may be achieved by considering larger particles or lower frequencies of operation for which metals are more conductive, as discussed for isolated chains in [140] and in the previous sections. We believe that these results may be of great interest for optical connections with sub-wavelength lateral cross-section in a variety of new generation optical devices of interest to U.S. Air Force.

7. Rigorous First-Principle Homogenization Theory of Metamaterials

a. Summary

We introduce in this section a first-principle homogenization theory for periodic metamaterials composed of arbitrary dielectric, magnetic and/or conducting inclusions. We derive closed-form analytical expressions for the effective constitutive parameters of the metamaterial array, pointing out the relevance of inherent spatial dispersion effects, present even in the long wavelength limit. Our results clarify the limitations of quasi-static homogenization models and the proper physical meaning of effective metamaterial parameters. In particular, we outline the physical reasons behind the necessity of considering magneto-electric coupling in the homogenized constitutive relations, even in the case of metamaterials formed by center-symmetric inclusions. These results may be of great interest for U.S. Air Force applications of nonconventional materials and artificial materials in realistic systems and devices.

b. Introduction

The electromagnetic homogenization of natural and artificial materials has a long-standing tradition [155]-[160] and several theories are available to properly define macroscopic averaged quantities representing the effective constitutive parameters of periodic or random collections of molecules or inclusions. The same way in which we define permittivity and permeability of natural materials, by averaging out irrelevant microscopic fluctuations of the fields at the atomic or molecular level, also in the field of artificial materials and mixtures, homogenization and mixing rules have been put forward over the years in order to avoid solving for the complex electromagnetic interaction among a large number of inclusions [160]. Homogenized descriptions of natural and artificial materials can hold only in the long-wavelength regime, i.e., for effective wavelengths and averaged field variations much larger than the material granularity.

77

Within these limits, however, such descriptions have proven to be accurate and of great advantage for analysis and design purposes.

With the advent of metamaterials [161], i.e., artificial materials with anomalous and exotic electromagnetic response, the necessity of more advanced concepts and improved homogenization models has become evident, since often the topological and/or resonant properties of the inclusions and building blocks do not allow a description of their properties in terms of simple averaging procedures. Often, the exotic metamaterial properties are inherently based on these anomalous features, which cannot be captured by simple homogenization schemes inspired to natural materials. The necessity for improved homogenization models has been outlined in several recent papers on the topic [162]-[179], which describe different approaches to the problem.

The simplest homogenization method is represented by retrieval techniques, which postulate the equivalence between a complex metamaterial array and a uniform slab of same thickness with unknown constitutive parameters, often limited to permittivity and permeability [180]-[182]. This simple approach regularly provides non-physical dispersion of these constitutive parameters, in particular near the inclusion resonances, yielding complex values of permittivity and permeability that violate basic passivity and causality constraints [183]. The typical presence of "anti-resonant" artifacts in the dispersion of the effective constitutive parameters, wrong sign of the imaginary part and wrong slope of the real part of the extracted parameters are all clear signs of the inadequacy of such simple homogenization approaches when applied to resonant artificial materials, as discussed in [184].

These anomalies have been generically related to strong spatial dispersion effects present in metamaterials, which should be taken into account in more refined homogenization models. In this context, analytical and semi-analytical methods have been put forward to address the homogenization in a more rigorous fashion. Generalized Clausius-Mossotti techniques have been extended to the case of complex inclusions, including bianisotropic effects, possible presence of spatial dispersion and accurate modeling of the interaction among inclusions [167]-[175]. As another successful approach, averaging a planar sheet of inclusions and then considering the mutual interaction among parallel layers as a Bloch lattice has been proposed as a venue to derive physically sound effective constitutive parameters [162]-[166]. In these schemes too, however, effects of spatial dispersion can often generate artifacts in the extracted effective parameters, which are not easily explained on physical grounds.

In order to circumvent these issues, an interesting approach to the homogenization of periodic arrays of dielectric inclusions [176]-[179] has been put forward based on the model that commonly describes optical crystals [185], i.e., introducing a generalized permittivity tensor that includes all the polarization effects, including artificial magnetism and possible bianisotropy. Although this technique is applicable to a wide class of dielectric metamaterials with periodic features, it often may not be intuitive to relate weak spatial dispersion effects in the generalized permittivity tensor to magnetic or bianisotropic effects, and it may be more desirable to describe these effects in terms of local permeability or chirality parameters. In addition, in this description the generalized permittivity tensor explicitly depends on the wave number even for local materials, making it more challenging to apply the usual boundary conditions and the solution of dispersion relations.

In most circumstances, it may be safely assumed that for frequencies well below the inclusion resonances, for which both the background wavelength and the effective guided wavelength are

78

significantly larger than the average array granularity, local or quasi-local constitutive parameters should be sufficient to characterize the metamaterial response, and strong spatial dispersion effects may be negligible. There are, however, examples of metamaterial geometries that contradict this general assumption, such as the wire medium [186] or dense arrays of plasmonic nanoparticles [169], [176], which show spatial dispersion effects even for longer wavelengths. In addition to these effects, anomalous bianisotropic coupling due to lattice effects has been pointed out in recent papers [174]-[175].

Inspired by all these issues, in the following we develop a general and rigorous first-principle theory for the homogenization of periodic metamaterials composed of arbitrary magnetodielectric and/or conducting inclusions. We use a homogenization approach consistent with [176],[185], but generalized to the case of an array comprised of arbitrary electric and magnetic materials and to the presence of arbitrary sources. We show that it is indeed possible to derive a fully consistent homogenization model for metamaterial arrays, which rigorously takes into account their complex wave interaction, that does not depend on the external source excitation and that converges to quasi-local constitutive parameters in the long-wavelength limit. Our analysis highlights the reasons and physical mechanisms behind artifacts and non-physical features arising in common homogenization models, showing that a rigorous analysis of the array coupling inherently requires considering frequency and spatial dispersion effects at the lattice level, even when higher-order multipolar interaction or bianisotropic effects within the unit cell are negligible. These effects modify the usual form of effective local constitutive parameters and they may be associated with a direct manifestation of the finite phase velocity with respect to the array granularity, becoming particularly relevant for more densely packed, and possibly resonant, metamaterials. Our findings establish the foundations of a physically meaningful and rigorous description of a wide class of metamaterials, in particular when the density of inclusions is not small and classic homogenization models, like Clausius-Mossotti relations [160], lose their accuracy even in the long wavelength regime. In addition, we shed new light into the physics of metamaterials and the meaning of effective constitutive relations to describe their complex wave interaction.

c. General Homogenization Theory for Metamaterial Arrays

In this section, starting from first-principle considerations, we develop a general and rigorous homogenization model for periodic arrays of arbitrarily shaped dielectric, magnetic and/or conducting inclusions, extending the approach commonly used in optical crystals [185] and dielectric metamaterials [176] to arbitrary materials and arbitrary form of excitation. We will show that this general description reduces to a quasi-local constitutive representation in the long-wavelength limit. For simplicity of notation, we assume a cubic lattice with period d, but extension to arbitrary lattices may also be envisioned. The most general description of a periodic array in its linear operation may be developed, without loss of generality, in the Fourier domain [185]. Our goal is to derive the general form of macroscopic constitutive relations for any arbitrary pair $(\omega, \boldsymbol{\beta})$, relating spatially averaged field quantities that vary as $e^{i\boldsymbol{\beta}\cdot\mathbf{r}}e^{-i\omega t}$. In general, only a limited set of eigen-vectors $\boldsymbol{\beta}$ are supported by the array at a given frequency ω in absence of impressed sources. These correspond to the eigen-modes of the system. Therefore, we will assume the presence of impressed sources with specific $e^{i\boldsymbol{\beta}\cdot\mathbf{r}}e^{-i\omega t}$ plane-wave like dependence, uniformly distributed all over the array. This ensures an averaged space-time distribution of the induced fields with the same $e^{i\boldsymbol{\beta}\cdot\mathbf{r}}e^{-i\omega t}$ dependence. In practice, it may be

79

challenging to practically realize a distribution of uniformly impressed sources within a metamaterial array, so this excitation should be seen as a test excitation to isolate the response in the Fourier domain, or as the Fourier expansion of embedded sources with realistic space-time distribution. We will specialize these results to the eigen-modal scenario (source-free modes) later in the paper.

In the most general case, the microscopic field distribution [187] at any point in the array satisfies

$$\nabla \times \mathbf{E}(\mathbf{r}) = i\omega\mu_0 \mathbf{H}(\mathbf{r}) + i\omega\mathbf{M}(\mathbf{r}) - \mathbf{K}_{ext} e^{i\boldsymbol{\beta}\cdot\mathbf{r}}$$
$$\nabla \times \mathbf{H}(\mathbf{r}) = -i\omega\varepsilon_0 \mathbf{E}(\mathbf{r}) - i\omega\mathbf{P}(\mathbf{r}) + \mathbf{J}_{ext} e^{i\boldsymbol{\beta}\cdot\mathbf{r}} \quad , \tag{46}$$

where $\mathbf{E}(\mathbf{r})$, $\mathbf{H}(\mathbf{r})$ are the local electric and magnetic fields, $\mathbf{P}(\mathbf{r})$ is the local polarization vector, $\mathbf{M}(\mathbf{r})$ is the local magnetization vector, $\mathbf{J}_{ext}$ and $\mathbf{K}_{ext}$ are complex vectors of independently impressed distributed electric and magnetic current density sources with explicit plane wave dependence $e^{i\boldsymbol{\beta}\cdot\mathbf{r}}$, and ε_0, μ_0 are the background permittivity and permeability, repectively. Due to the linearity of the problem, we have suppressed in (46) the $e^{-i\omega t}$ time dependence. In the presence of electric or magnetic conductors, the induced current densities $\mathbf{J}_{ind}$, $\mathbf{K}_{ind}$ are implicitly embedded into $\mathbf{P}(\mathbf{r}) = i\mathbf{J}_{ind}(\mathbf{r})/\omega$ and $\mathbf{M}(\mathbf{r}) = i\mathbf{K}_{ind}(\mathbf{r})/\omega$ in Eq. (46) .

The distributed impressed source distributions may also be seen as sustaining impressed fields with the same $e^{i\boldsymbol{\beta}\cdot\mathbf{r}} e^{-i\omega t}$ plane-wave dependence and therefore complex amplitudes satisfying

$$i\boldsymbol{\beta} \times \mathbf{E}_{ext} = i\omega\mu_0 \mathbf{H}_{ext} - \mathbf{K}_{ext}$$
$$i\boldsymbol{\beta} \times \mathbf{H}_{ext} = -i\omega\varepsilon_0 \mathbf{E}_{ext} + \mathbf{J}_{ext} \quad . \tag{47}$$

Notice that the arbitrary choice of $\mathbf{J}_{ext}$ and $\mathbf{K}_{ext}$ in (46) implies that the complex amplitudes of impressed fields $\mathbf{E}_{ext}$ and $\mathbf{H}_{ext}$ are independent of each other. This will be very important to ensure the general validity of the effective homogenization model proposed here, as discussed below.

Due to the periodicity of the crystal, we may write Eq. (46) in the $e^{i\boldsymbol{\beta}\cdot\mathbf{r}} e^{-i\omega t}$ Fourier domain

$$i\boldsymbol{\beta} \times \bar{\mathbf{E}} = i\omega\mu_0 \bar{\mathbf{H}} + i\omega\bar{\mathbf{M}} - \mathbf{K}_{ext}$$
$$i\boldsymbol{\beta} \times \bar{\mathbf{H}} = -i\omega\varepsilon_0 \bar{\mathbf{E}} - i\omega\bar{\mathbf{P}} + \mathbf{J}_{ext} \quad , \tag{48}$$

where the bar denotes the averaging operation $\bar{\mathbf{E}} = \dfrac{1}{d^3} \int_V \mathbf{E}(\mathbf{r}) e^{-i\boldsymbol{\beta}\cdot\mathbf{r}} d\mathbf{r}$, and similarly for all the other vectors in Eq. (48). This averaging procedure, consistent with [185], [176], filters out the dominant contribution to the local field $\mathbf{E}(\mathbf{r})$, varying as $\bar{\mathbf{E}}e^{i\boldsymbol{\beta}\cdot\mathbf{r}}$, of interest for a macroscopic homogenized description of the array. Eq. (48) effectively relates the complex amplitudes of the spatially averaged macroscopic field quantities, which all vary with an $e^{i\boldsymbol{\beta}\cdot\mathbf{r}} e^{-i\omega t}$ space-time dependence due to the chosen form of impressed excitation and the linearity of the problem.

80

Inspecting Eq. (48), one may be tempted to define spatially averaged displacement vectors $\bar{\mathbf{B}} = \mu_0\bar{\mathbf{H}} + \bar{\mathbf{M}}$ and $\bar{\mathbf{D}} = \varepsilon_0\bar{\mathbf{E}} + \bar{\mathbf{P}}$, and the associated constitutive relations $\bar{\mathbf{B}} = \underline{\boldsymbol{\mu}}_g \cdot \bar{\mathbf{H}}$, $\bar{\mathbf{D}} = \underline{\boldsymbol{\varepsilon}}_g \cdot \bar{\mathbf{E}}$, which would generalize the metamaterial homogenization approach used in [185], [176] to the case of magnetodielectric materials. However, this macroscopic description would have several shortcomings: the effective permittivity and permeability coincide with ε_0 or μ_0 if the inclusions are formed by purely magnetic ($\mathbf{P}(\mathbf{r}) = \bar{\mathbf{P}} = \mathbf{0}$) or dielectric ($\mathbf{M}(\mathbf{r}) = \bar{\mathbf{M}} = \mathbf{0}$) materials, respectively. This implies that artificial magnetic or polarization effects, stemming from the rotation of electric and magnetic polarization respectively, remain hidden as spatial dispersion effects in the permittivity or permeability tensors. In particular, $\underline{\boldsymbol{\varepsilon}}_g$ coincides with the generalized permittivity defined in [176] in the case of dielectric inclusions. This description, therefore, cannot converge to a local constitutive model in the long-wavelength limit in the presence of artificial magnetic or dielectric effects (e.g., for split-ring resonators), of most interest for metamaterial applications.

i. Multipolar expansion

In order to overcome this problem, we assume that the unit cell is sufficiently smaller than the wavelength of operation to ensure that the induced microscopic polarization and magnetization vectors vary slowly within each unit cell. In such circumstances, it is possible to expand $\bar{\mathbf{P}}$ in Taylor series around the origin of each unit cell, to obtain [188]

$$\bar{\mathbf{P}} = \frac{1}{d^3}\int_V \mathbf{P}(\mathbf{r})e^{-i\boldsymbol{\beta}\cdot\mathbf{r}}d\mathbf{r} =$$

$$= \frac{1}{d^3}\left[\begin{array}{c} \int_V \mathbf{P}(\mathbf{r})d\mathbf{r} + i\boldsymbol{\beta}\times\int_V \frac{\mathbf{r}\times\mathbf{P}(\mathbf{r})}{2}d\mathbf{r} - \frac{i\boldsymbol{\beta}}{2}\cdot\int_V\left[\mathbf{r}\mathbf{P}(\mathbf{r})+\mathbf{P}(\mathbf{r})\mathbf{r}\right]d\mathbf{r} + \\[2mm] -\boldsymbol{\beta}\times\int_V \frac{\mathbf{r}\times\mathbf{P}(\mathbf{r})\times\mathbf{r}}{6}d\mathbf{r}\times\boldsymbol{\beta} + \frac{\boldsymbol{\beta}}{2}\times\left[\boldsymbol{\beta}\cdot\int_V\frac{\left[\mathbf{r}\times\mathbf{P}(\mathbf{r})\right]\mathbf{r}+\mathbf{r}\left[\mathbf{r}\times\mathbf{P}(\mathbf{r})\right]}{3}d\mathbf{r}\right] + ... \end{array}\right] = , \quad (49)$$

$$= \mathbf{P}_E - \frac{\boldsymbol{\beta}\times\mathbf{M}_E}{\omega\mu_0} - \frac{i\boldsymbol{\beta}}{2}\cdot\underline{\mathbf{Q}}_E^e + \frac{\boldsymbol{\beta}}{i\omega}\times\left[\bar{\mathbf{P}}_E' \times\boldsymbol{\beta} - \frac{\boldsymbol{\beta}\cdot\mathbf{Q}_E^m}{2}\right] + ...$$

where

$$\mathbf{P}_E = \frac{1}{d^3}\int_V \mathbf{P}(\mathbf{r})d\mathbf{r}$$

$$\mathbf{M}_E = -\frac{i\omega\mu_0}{d^3}\int_V \frac{\mathbf{r}\times\mathbf{P}(\mathbf{r})}{2}d\mathbf{r}$$

$$\underline{\mathbf{Q}}_E^e = \frac{1}{d^3}\int_V\left[\mathbf{r}\mathbf{P}(\mathbf{r})+\mathbf{P}(\mathbf{r})\mathbf{r}\right]d\mathbf{r} \qquad (50)$$

$$\mathbf{P}_E' = -\frac{i\omega}{d^3}\int_V \frac{\mathbf{r}\times\mathbf{P}(\mathbf{r})\times\mathbf{r}}{6}d\mathbf{r}$$

$$\underline{\mathbf{Q}}_E^m = -\frac{i\omega}{d^3}\int_V \frac{\left[\mathbf{r}\times\mathbf{P}(\mathbf{r})\right]\mathbf{r}+\mathbf{r}\left[\mathbf{r}\times\mathbf{P}(\mathbf{r})\right]}{3}d\mathbf{r}$$

81

represent the first electric and magnetic multipole moments associated with the induced electric polarization distribution $\mathbf{P}(\mathbf{r})$. In particular, $\mathbf{P}_E$, $\mathbf{M}_E$ are the fist-order contribution to the electric and magnetic dipole moments, respectively, $\underline{\mathbf{Q}}_E^e$, $\underline{\mathbf{Q}}_E^m$ are the electric and magnetic quadrupole moment cntributions, $\mathbf{P}_E'$ is the third-order contribution to the electric dipole moment. The subscript E indicates the origin of these multipole moments, associated to the electric polarization. We can apply analogous considerations to the induced magnetization $\mathbf{M}(\mathbf{r})$

$$\bar{\mathbf{M}} = \mathbf{M}_H + \frac{\boldsymbol{\beta} \times \mathbf{P}_H}{\omega \varepsilon_0} - \frac{i\boldsymbol{\beta}}{2} \cdot \underline{\mathbf{Q}}_H^m + \frac{\boldsymbol{\beta}}{i\omega} \times \left[\mathbf{M}_H' \times \boldsymbol{\beta} + \frac{\boldsymbol{\beta} \cdot \underline{\mathbf{Q}}_H^e}{2} \right] + \dots , \tag{51}$$

with analogous definitions for the corresponding multipole moments

$$\mathbf{M}_H = \frac{1}{d^3} \int_V \mathbf{M}(\mathbf{r}) \, d\mathbf{r}$$

$$\mathbf{P}_H = \frac{i\omega \varepsilon_0}{d^3} \int_V \frac{\mathbf{r} \times \mathbf{M}(\mathbf{r})}{2} \, d\mathbf{r}$$

$$\underline{\mathbf{Q}}_H^m = \frac{1}{d^3} \int_V \left[\mathbf{r}\mathbf{M}(\mathbf{r}) + \mathbf{M}(\mathbf{r})\mathbf{r} \right] d\mathbf{r} \tag{52}$$

$$\mathbf{M}_H' = -\frac{i\omega}{d^3} \int_V \frac{\mathbf{r} \times \mathbf{M}(\mathbf{r}) \times \mathbf{r}}{6} \, d\mathbf{r}$$

$$\underline{\mathbf{Q}}_H^e = \frac{i\omega}{d^3} \int_V \frac{\left[\mathbf{r} \times \mathbf{M}(\mathbf{r}) \right] \mathbf{r} + \mathbf{r} \left[\mathbf{r} \times \mathbf{M}(\mathbf{r}) \right]}{3} \, d\mathbf{r}$$

and the subscript H refers to the magnetic origin of these multipole moments.

Using the previous expansions, we may write Eq. (48) in the interesting form

$$i\boldsymbol{\beta} \times \left[\bar{\mathbf{E}} - \frac{\mathbf{P}_H}{\varepsilon_0} - i\boldsymbol{\beta} \times \mathbf{M}_H' + \frac{i\boldsymbol{\beta}}{2} \cdot \underline{\mathbf{Q}}_H^e \right] = i\omega \left(\mu_0 \bar{\mathbf{H}} + \mathbf{M}_H - \frac{i\boldsymbol{\beta}}{2} \cdot \underline{\mathbf{Q}}_H^m \right) - \mathbf{K}_{ext}$$

$$i\boldsymbol{\beta} \times \left[\bar{\mathbf{H}} - \frac{\mathbf{M}_E}{\mu_0} - i\boldsymbol{\beta} \times \mathbf{P}_E' - \frac{i\boldsymbol{\beta}}{2} \cdot \underline{\mathbf{Q}}_E^m \right] = -i\omega \left[\varepsilon_0 \bar{\mathbf{E}} + \mathbf{P}_E - \frac{i\boldsymbol{\beta}}{2} \cdot \underline{\mathbf{Q}}_E^e \right] + \mathbf{J}_{ext} \tag{53}$$

in which we have neglected the effects of higher order multipole moments (beyond the electric and magnetic quadrupole moments) in Eqs. (49), (51).

ii. *Proper definition of averaged fields*

Eq. (53) ensures that, by correcting the definition of the averaged fields as follows:

$$\mathbf{E}_{av} = \bar{\bar{\mathbf{E}}} - \frac{\mathbf{P}_H}{\varepsilon_0} - i\boldsymbol{\beta} \times \mathbf{M}'_H + \frac{i\boldsymbol{\beta}}{2} \cdot \underline{\mathbf{Q}}^e_H$$

$$\mathbf{H}_{av} = \bar{\bar{\mathbf{H}}} - \frac{\mathbf{M}_E}{\mu_0} - i\boldsymbol{\beta} \times \mathbf{P}'_E - \frac{i\boldsymbol{\beta}}{2} \cdot \underline{\mathbf{Q}}^m_E$$

$$\mathbf{D}_{av} = \varepsilon_0 \bar{\bar{\mathbf{E}}} + \mathbf{P}_E - \frac{i\boldsymbol{\beta}}{2} \cdot \underline{\mathbf{Q}}^e_E$$

$$\mathbf{B}_{av} = \mu_0 \bar{\bar{\mathbf{H}}} + \mathbf{M}_H - \frac{i\boldsymbol{\beta}}{2} \cdot \underline{\mathbf{Q}}^m_H$$

$$(54)$$

the macroscopic (averaged) Maxwell's equations take the expected form

$$i\boldsymbol{\beta} \times \mathbf{E}_{av} = i\omega\mathbf{B}_{av} - \mathbf{K}_{ext}$$

$$i\boldsymbol{\beta} \times \mathbf{H}_{av} = -i\omega\mathbf{D}_{av} + \mathbf{J}_{ext}$$

$$(55)$$

for any arbitrary pair $(\omega, \boldsymbol{\beta})$.

The definition of averaged fields as given in (54) solves the issues outlined above in reference to Eq. (48) and ensures the proper representation of artificial electric and magnetic effects, making sure that the constitutive relations of the metamaterial tend to local parameters in the long-wavelength limit, even in presence of artificial magnetic or polarization effects. In other words, this averaging procedure, based on a rigorous first-principle approach, properly takes into account weak forms of spatial dispersion associated with artificial magnetism and polarization, at the basis of common metamaterial effects, and it allows their description in a local framework. Eq. (54) shows that the proper form of averaged electric and magnetic fields $\mathbf{E}_{av}$ and $\mathbf{H}_{av}$ is obtained after correcting the spatial microscopic averages $\bar{\bar{\mathbf{E}}}$ and $\bar{\bar{\mathbf{H}}}$ for the possible presence of these artificial effects, associated with the rotation of $\mathbf{P}$ and $\mathbf{M}$. This ensures that they are correctly attributed to local constitutive parameters in the long-wavelength limit. In the presence of only dielectric and conducting inclusions $(\mathbf{M}(\mathbf{r}) = \mathbf{0})$, $\mathbf{E}_{av} = \bar{\bar{\mathbf{E}}}$ and $\mathbf{B}_{av} = \mu_0 \bar{\bar{\mathbf{H}}}$, ensuring that $\mathbf{E}$ and $\mathbf{B}$ are the direct source fields, consistent with rigorous homogenization for optical crystals and dielectric metamaterials [185],[176]. Similarly, if only magnetization is present at the microscopic level, then $\mathbf{H}_{av} = \bar{\bar{\mathbf{H}}}$ and $\mathbf{D}_{av} = \varepsilon_0 \bar{\bar{\mathbf{E}}}$ are the source fields to be spatially averaged, as shown in [178]. Eq. (54) represents a generalization of these techniques in the case of magnetodielectric arrays, for which both averaged fields $\mathbf{E}_{av}$, $\mathbf{H}_{av}$ need to be corrected for the possible presence of artificial electric and magnetic effects. This is the only way to ensure that these weak spatial dispersion effects are properly taken into account within a local homogenization description.

iii. Relations between averaged fields

In the general case, the constitutive relations relating the averaged displacement vectors $\mathbf{D}_{av}$, $\mathbf{B}_{av}$ to the averaged field vectors $\mathbf{E}_{av}$, $\mathbf{H}_{av}$ inherently depend on $\boldsymbol{\beta}$, implying that spatial dispersion effects associated with higher-order multipole contributions are present. In the long wavelength limit of interest here, however, it is expected that the distributions of $\mathbf{P}(\mathbf{r})$, $\mathbf{M}(\mathbf{r})$ may be described simply in terms of electric and magnetic dipole moments, which is the case

83

when the unit cell is sufficiently smaller than the wavelength of operation, and the inclusions are not too densely packed. In such circumstances, the explicit effects of spatial dispersion disappear in Eq. (54):

$$
\begin{aligned}
\mathbf{E}_{av} &= \bar{\mathbf{E}} - \mathbf{P}_H / \varepsilon_0 \\
\mathbf{H}_{av} &= \bar{\mathbf{H}} - \mathbf{M}_E / \mu_0 \\
\mathbf{D}_{av} &= \varepsilon_0 \bar{\mathbf{E}} + \mathbf{P}_E \\
\mathbf{B}_{av} &= \mu_0 \bar{\mathbf{H}} + \mathbf{M}_H
\end{aligned}
\tag{56}
$$

and the constitutive relations relating averaged displacement and field vectors may be written in the local form

$$
\begin{aligned}
\mathbf{D}_{av} &= \varepsilon_0 \mathbf{E}_{av} + \mathbf{P}_E + \mathbf{P}_H = \varepsilon_0 \mathbf{E}_{av} + \mathbf{P}_{av} \\
\mathbf{B}_{av} &= \mu_0 \mathbf{H}_{av} + \mathbf{M}_H + \mathbf{M}_E = \mu_0 \mathbf{H}_{av} + \mathbf{M}_{av}
\end{aligned}
\tag{57}
$$

where we have combined averaged polarization and magnetization stemming from electric and magnetic effects into $\mathbf{P}_{av}$ and $\mathbf{M}_{av}$. As an aside, this relation rigorously proves from first-principle considerations that the electric and magnetic contributions are simply additive within the unit cell in the dipolar limit, which in turn implies that we can alternatively describe the complex unit cell interaction in terms of point-dipoles. In other words, the following theory may be also obtained in a more streamlined version by considering lattices of electric and magnetic point-dipoles to describe the complex inclusions in each unit cell.

Combining Eq. (57) and (47) into (55), we can write a general relation between averaged and external fields and averaged polarization and magnetization vectors,

$$
\begin{aligned}
i\boldsymbol{\beta} \times (\mathbf{E}_{av} - \mathbf{E}_{ext}) &= i\omega \mu_0 (\mathbf{H}_{av} - \mathbf{H}_{ext}) + i\omega \mathbf{M}_{av} \\
i\boldsymbol{\beta} \times (\mathbf{H}_{av} - \mathbf{H}_{ext}) &= -i\omega \varepsilon_0 (\mathbf{E}_{av} - \mathbf{E}_{ext}) - i\omega \mathbf{P}_{av}
\end{aligned}
\tag{58}
$$

These equations may be further manipulated to yield

$$
\begin{aligned}
\left[k_0^2 + \boldsymbol{\beta} \times \boldsymbol{\beta} \times \right] (\mathbf{E}_{av} - \mathbf{E}_{ext}) &= -k_0^2 \frac{\mathbf{P}_{av}}{\varepsilon_0} + k_0 \eta_0 \boldsymbol{\beta} \times \frac{\mathbf{M}_{av}}{\mu_0} \\
\left[k_0^2 + \boldsymbol{\beta} \times \boldsymbol{\beta} \times \right] (\mathbf{H}_{av} - \mathbf{H}_{ext}) &= -k_0^2 \frac{\mathbf{M}_{av}}{\mu_0} - \frac{k_0}{\eta_0} \boldsymbol{\beta} \times \frac{\mathbf{P}_{av}}{\varepsilon_0}
\end{aligned}
\tag{59}
$$

where $k_0 = \omega \sqrt{\varepsilon_0 \mu_0}$ and $\eta_0 = \sqrt{\mu_0 / \varepsilon_0}$.

Henceforth, for simplicity of notation, we consider only averaged and impressed field distributions that are transverse-electromagnetic (TEM) waves propagating along the direction $\hat{\boldsymbol{\beta}}$ (where the hat indicates a unit vector). It may be proven that this is the case for isotropic unit cells and lattices, as we assume in the following, when $\hat{\boldsymbol{\beta}}$ is along one of the lattice axes or, more generally, for any propagation direction in the limit $k_0 d \ll 1$. A more general tensorial notation may be used for arbitrary propagation, but is not adopted here in the interest of notational simplicity. In this situation, Eq. (59) may be compactly written as follows,

84

$$\mathbf{E}_{av} = \mathbf{E}_{ext} + \frac{k_0^2}{\beta^2 - k_0^2} \frac{\mathbf{P}_{av}}{\varepsilon_0} - \frac{\beta k_0}{\beta^2 - k_0^2} \eta_0 \hat{\boldsymbol{\beta}} \times \frac{\mathbf{M}_{av}}{\mu_0}$$
$$\mathbf{H}_{av} = \mathbf{H}_{ext} + \frac{k_0^2}{\beta^2 - k_0^2} \frac{\mathbf{M}_{av}}{\mu_0} + \frac{\beta k_0}{\beta^2 - k_0^2} \frac{\hat{\boldsymbol{\beta}}}{\eta_0} \times \frac{\mathbf{P}_{av}}{\varepsilon_0}$$

$$(60)$$

This is a very general result, which relates the averaged and external fields for any $(\omega, \boldsymbol{\beta})$ pair and holds for any metamaterial array and any combination of electric and magnetic excitations. Observe that, analogous to the way both electric and magnetic induced currents contribute to the electric and magnetic averaged polarization effects in (57), both averaged polarization and magnetization vectors contribute to the averaged electric and magnetic fields. In other words, an inherent form of magnetoelectric coupling at the unit cell level stems from weak spatial dispersion effects when $\beta \neq 0$, associated with finite phase velocity across each unit cell. Eq. (60) defines a general relation among averaged and impressed fields, which is independent on the specific nature of the metamaterial inclusions. In the following section, we use these results and introduce the inclusion into the picture, in order to derive the first-principle effective constitutive parameters of an arbitrary metamaterial.

iv.   Effective constitutive parameters

After having established the proper definition of averaged fields and their general relations, we are now ready to derive a macroscopic homogenized description of the array, once we relate averaged polarization and magnetization vectors to the local fields, as a function of the specific inclusion geometry. Since we are assuming that dipolar terms are dominant, we may compactly describe the unit cell response in terms of its polarizability coefficients, which relate the induced electric and magnetic dipole moments in the unit cell $\mathbf{p}_{000} = d^3 \mathbf{P}_{av}$ and $\mathbf{m}_{000} = d^3 \mathbf{M}_{av}$ to the local fields at its center,

$$\mathbf{p}_{000} = \varepsilon_0 \alpha_e \mathbf{E}_{loc} - \varepsilon_0 \alpha_{em} \eta_0 \hat{\boldsymbol{\beta}} \times \mathbf{H}_{loc}$$
$$\mathbf{m}_{000} = \mu_0 \alpha_m \mathbf{H}_{loc} - \mu_0 \alpha_{em} \frac{\hat{\boldsymbol{\beta}} \times \mathbf{E}_{loc}}{\eta_0},$$

$$(61)$$

where α_e, α_m and α_{em} are the electric, magnetic and magneto-electric polarizability coefficients, respectively. All these coefficients have dimensions of an inverse volume, and they are considered scalar here due to the assumptions of TEM propagation and isotropic unit cell. In addition, in writing Eq. (61) we have implicitly assumed that the inclusions are reciprocal.

The fields $\mathbf{E}_{loc}$ and $\mathbf{H}_{loc}$ represent the local fields at the center of the unit cell in absence of the inclusion. They are due to the superposition of the impressed fields $\mathbf{E}_{ext}$, $\mathbf{H}_{ext}$ and the induced fields scattered from inclusions in the rest of the array, that is,

$$\mathbf{E}_{loc} = \mathbf{E}_{array} + \mathbf{E}_{ext} = C \frac{\mathbf{p}_{000}}{\varepsilon_0} - \eta_0 C_{em} \hat{\boldsymbol{\beta}} \times \frac{\mathbf{m}_{000}}{\mu_0} + \mathbf{E}_{ext}$$
$$\mathbf{H}_{loc} = \mathbf{H}_{array} + \mathbf{H}_{ext} = C \frac{\mathbf{m}_{000}}{\mu_0} + \frac{C_{em}}{\eta_0} \hat{\boldsymbol{\beta}} \times \frac{\mathbf{p}_{000}}{\varepsilon_0} + \mathbf{H}_{ext}.$$

$$(62)$$

85

The interaction constants C and C_{em} may be evaluated using the dipolar radiation from the generic unit cell at $\mathbf{r}_{lmn} = (ld, md, nd)$ and applying the Floquet condition $\mathbf{p}_{lmn} = \mathbf{p}_{000}e^{i\boldsymbol{\beta}\cdot\mathbf{r}_{lmn}}$, $\mathbf{m}_{lmn} = \mathbf{m}_{000}e^{i\boldsymbol{\beta}\cdot\mathbf{r}_{lmn}}$:

$$C = \sum_{(l,m,m)\neq(0,0,0)} \hat{\mathbf{p}} \cdot \underline{\mathbf{G}}_{ee}(\mathbf{r}_{lmn}) e^{i\boldsymbol{\beta}\cdot\mathbf{r}_{lmn}} \cdot \hat{\mathbf{p}}$$
$$C_{em} = \sum_{(l,m,m)\neq(0,0,0)} \hat{\mathbf{p}} \cdot \underline{\mathbf{G}}_{em}(\mathbf{r}_{lmn}) e^{i\boldsymbol{\beta}\cdot\mathbf{r}_{lmn}} \cdot \hat{\mathbf{m}} \text{,}$$

(63)

where $\underline{\mathbf{G}}_{ee}(\mathbf{r}_{lmn})$ and $\underline{\mathbf{G}}_{em}(\mathbf{r}_{lmn})$ are the electric and magneto-electric dyadic Green's functions [189] and $\hat{\mathbf{p}}$, $\hat{\mathbf{m}}$ are unit vectors oriented along $\mathbf{p}_{000}$ and $\mathbf{m}_{000}$. Fast converging expressions for these summations are available in [168]-[169], [173].

Combining Eqs. (61)-(62), we may now derive a general relation between impressed fields and averaged polarization vectors:

$$\mathbf{E}_{ext} = d^3\left(\frac{1}{\alpha_e + \alpha_{em}^2/\alpha_m} - C\right)\frac{\mathbf{P}_{av}}{\varepsilon_0} + \eta_0 d^3\left(\frac{\alpha_{em}}{\alpha_e\alpha_m + \alpha_{em}^2} + C_{em}\right)\hat{\boldsymbol{\beta}}\times\frac{\mathbf{M}_{av}}{\mu_0}$$
$$\mathbf{H}_{ext} = d^3\left(\frac{1}{\alpha_m + \alpha_{em}^2/\alpha_e} - C\right)\frac{\mathbf{M}_{av}}{\mu_0} + \frac{d^3}{\eta_0}\left(\frac{\alpha_{em}}{\alpha_e\alpha_m + \alpha_{em}^2} - C_{em}\right)\hat{\boldsymbol{\beta}}\times\frac{\mathbf{P}_{av}}{\varepsilon_0} \text{,}$$

(64)

which, substituted in (60), provides the important relations

$$\mathbf{E}_{av} = \left[\frac{d^3\alpha_m}{\alpha_e\alpha_m + \alpha_{em}^2} - d^3 C_{int}\right]\frac{\mathbf{P}_{av}}{\varepsilon_0} + \left[\frac{d^3\alpha_{em}}{\alpha_e\alpha_m + \alpha_{em}^2} + d^3 C'_{em}\right]\eta_0\hat{\boldsymbol{\beta}}\times\frac{\mathbf{M}_{av}}{\mu_0}$$
$$\mathbf{H}_{av} = \left[\frac{d^3\alpha_e}{\alpha_e\alpha_m + \alpha_{em}^2} - d^3 C_{int}\right]\frac{\mathbf{M}_{av}}{\mu_0} + \left[\frac{d^3\alpha_{em}}{\alpha_e\alpha_m + \alpha_{em}^2} - d^3 C'_{em}\right]\frac{\hat{\boldsymbol{\beta}}}{\eta_0}\times\frac{\mathbf{P}_{av}}{\varepsilon_0} \text{.}$$

(65)

Here we have used the reduced interaction constants

$$C_{int} = C - \left[\frac{1}{d^3}\frac{k_0^2}{\beta^2 - k_0^2}\right]$$
$$C'_{em} = C_{em} - \left[\frac{1}{d^3}\frac{\beta k_0}{\beta^2 - k_0^2}\right] \text{,}$$

(66)

which respectively coincide with $\hat{\mathbf{p}}\cdot\underline{\mathbf{C}}_{int}\cdot\hat{\mathbf{p}}$ and $\hat{\mathbf{p}}\cdot\underline{\mathbf{C}}_{e,m}\cdot\hat{\mathbf{m}}$ derived in [176] using an alternative spectral-domain representation.

Eq. (65) represents another important result, since it shows, directly from first-principle considerations, that it is possible to establish a general relation between averaged electric and magnetic fields and averaged polarization vectors [as defined in (56)], which depends on the array period and the polarizability coefficients for any given pair $(\omega, \boldsymbol{\beta})$, but is completely independent on the relative amplitude of the impressed sources $\mathbf{J}_{ext}$, $\mathbf{K}_{ext}$. This is a fundamental property of this homogenization theory, since a proper description of the metamaterial

86

interaction in homogenized form cannot depend on the type and form of external excitation, as commonly happens in less rigorous homogenization models.

The relations in (65) also show that there is an inherent form of magnetoelectric coupling (usually negligible in natural materials) relating $\mathbf{E}_{av}$ to the rotation of $\mathbf{M}_{av}$ and $\mathbf{H}_{av}$ to the rotation of $\mathbf{P}_{av}$. As expected, part of this coupling is associated with the presence of α_{em}, which represents the possible bianisotropy within the unit cell, stemming from asymmetric or non-centered inclusions [191]. However, Eq. (65) predicts that, even when inclusions are perfectly center-symmetric and with no inherent bainisotropy, a form of magneto-electric coupling is still expected, associated with the presence of C'_{em}. This additional coupling term is due to lattice effects and the finite value of β. We will discuss the implications of this coupling in more detail in the following.

Using (57), we can finally write for the constitutive relations of the metamaterial array:

$$
\begin{aligned}
\mathbf{D}_{av} &= \varepsilon_0 \mathbf{E}_{av} + \mathbf{P}_{av} = \varepsilon_{eff} \mathbf{E}_{av} - \left(\chi^e_{eff} + \chi^o_{eff} \right) \hat{\boldsymbol{\beta}} \times \mathbf{H}_{av} \\
\mathbf{B}_{av} &= \mu_0 \mathbf{H}_{av} + \mathbf{M}_{av} = \mu_{eff} \mathbf{H}_{av} - \left(\chi^e_{eff} - \chi^o_{eff} \right) \hat{\boldsymbol{\beta}} \times \mathbf{E}_{av}
\end{aligned}
\tag{67}
$$

with

$$
\begin{aligned}
\varepsilon_{eff} &= \varepsilon_0 \left[1 + \frac{d^{-3} \left[\alpha^{-1}_{m(eff)} - C_{int} \right]}{\left(\alpha^{-1}_{e(eff)} - C_{int} \right) \left(\alpha^{-1}_{m(eff)} - C_{int} \right) - C'^2_{em} + \alpha^2_{em(eff)}} \right] \\
\mu_{eff} &= \mu_0 \left[1 + \frac{d^{-3} \left(\alpha^{-1}_{e(eff)} - C_{int} \right)}{\left(\alpha^{-1}_{e(eff)} - C_{int} \right) \left(\alpha^{-1}_{m(eff)} - C_{int} \right) - C'^2_{em} + \alpha^2_{em(eff)}} \right], \\
\chi^e_{eff} &= \frac{1}{c_0} \frac{d^{-3} \alpha_{em(eff)}}{\left(\alpha^{-1}_{m(eff)} - C_{int} \right) \left(\alpha^{-1}_{m(eff)} - C_{int} \right) - C'^2_{em} + \alpha^2_{em(eff)}} \\
\chi^o_{eff} &= \frac{1}{c_0} \frac{d^{-3} C'_{em}}{\left(\alpha^{-1}_{e(eff)} - C_{int} \right) \left(\alpha^{-1}_{m(eff)} - C_{int} \right) - C'^2_{em} + \alpha^2_{em(eff)}}
\end{aligned}
\tag{68}
$$

where $c_0 = 1 / \sqrt{\varepsilon_0 \mu_0}$, $\alpha^{-1}_{e(eff)} = \alpha_m / \Delta$, $\alpha^{-1}_{m(eff)} = \alpha_e / \Delta$, $\alpha^{-1}_{em(eff)} = \alpha_{em} / \Delta$ and $\Delta = \left(\alpha_e \alpha_m + \alpha^2_{em} \right)$ [in the absence of magnetoelectric coupling at the unit cell level $\alpha_{em} = 0$ and $\alpha_{e(eff)} = \alpha_e$, $\alpha_{m(eff)} = \alpha_m$].

v. *General properties of the effective constitutive parameters*

These expressions represent general closed-form effective constitutive parameters obtained from first-principle considerations. They are valid for any pair $(\omega, \boldsymbol{\beta})$ and any form of external excitation $\mathbf{J}_{ext}$, $\mathbf{K}_{ext}$, ensuring that this homogenized description does not depend on the specific impressed field distribution in each unit cell, but it is the inherent response of the metamaterial as a bulk to a given arbitrary level of electric and/or magnetic excitation. It is noticed, in particular,

87

that the ratio of averaged fields E_{av} / H_{av}, i.e., the local wave impedance, inherently depends on the specific choice of impressed sources $\mathbf{J}_{ext}$, $\mathbf{K}_{ext}$, following Eq. (58), as expected in presence of arbitrary impressed sources. However, the constitutive parameters defined in Eq. (68) do not depend on this ratio, thus compactly including the macroscopic polarization and magnetization properties of the array for arbitrary excitation.

Effective permittivity and permeability are found in closed form in the first two expressions (68). These generalize the Clausius-Mosotti homogenization formulas [159]-[160], [176] by rigorously taking into account the coupling among the inclusions and their polarization properties. More importantly, this theory demonstrates the inherent presence of the magneto-electric coupling via the coefficients χ_{eff}^{e} and χ_{eff}^{o} in Eq. (67)-(68). The first portion of the bianisotropy coefficient χ_{eff}^{e}, even with respect to β, is associated with the magneto-electric effects at the inclusion level, and satisfies the usual reciprocity constraints for bulk materials. An additional contribution to χ_{eff}, odd with respect to β, is associated to inherent magneto-electric coupling effects at the lattice level. These latter effects cannot be generally neglected. Even in the case of center-symmetric inclusions, for which $\alpha_{em} = 0$, this latter contribution is present as long as $C'_{em} \neq 0$. The presence of this odd bianisotropy coefficient has been pointed out theoretically and numerically in [174]-[175], and the present theory explains its physical nature and relevance from first-principle considerations: χ_{eff}^{o} is a weak spatial dispersion effect associated with the finite phase velocity of mode propagation along the array, not negligible even in the long-wavelength limit as we show in the following numerical examples (Section 8). Its nature is associated with the inherent asymmetry introduced by the phase propagation across the unit cell, and this explains why, at first sight, its occurrence in (67) does not appear to satisfy the reciprocity relation for local bianisotropic materials. Its odd response with respect to β ensures however that, by reversing the direction of propagation for given frequency, its contribution also changes sign, ensuring that the constitutive relations (67) are effectively describing a reciprocal medium. This shows the drastic difference between the bianisotropy stemming from lattice effects χ_{eff}^{o} and the one associated with an actual magneto-electric coupling at the inclusion level χ_{eff}^{e}. Its relevance in the homogenization of metamaterials and in restoring the physical meaning of their constitutive parameters has been discussed in further detail in [184].

Due to the inherent properties of the summations in (63), which for real β satisfy [168]-[169], [173], [176]

$$\text{Im}[C] = k_0^3 / (6\pi)$$
$$\text{Im}[C_{em}] = 0$$

(69)

and the lossless conditions on the polarizability coefficients [190]

$$\text{Im}[\alpha_e^{-1}] = \text{Im}[\alpha_m^{-1}] = k_0^3 / (6\pi)$$
$$\text{Im}[\alpha_{em}] = 0$$

,

(70)

it is recognized that all the constitutive parameters in (68) are real for lossless particles and real β, as required in lossless bianisotropic materials, satisfying power conservation.

Before concluding this section, it is worth stressing that the closed-form expressions (68) for the effective parameters of the array apply to any plane-wave like field distribution in the homogenized material, any form of excitation and any pair $(\omega, \boldsymbol{\beta})$, representing an accurate first-principle homogenization model for the metamaterial array. The derived parameters are, in the general case, still weakly dependent on β, as a symptom of spatial dispersion. However, they tend to local parameters in the long-wavelength limit (small β). The present general theory highlights that, in addition to artificial magnetism and polarization effects stemming from weak spatial dispersion, the rigorous consideration of the coupling within the array requires additional magneto-electric coefficients, even in the case of center-symmetric inclusions. In the following section, we consider the special case of eigen-modal solution, without external impressed sources.

d. Eigen-Modal Propagation and Equivalent Constitutive Parameters

In the eigen-modal case, i.e., in the absence of external distributed sources, Eq. (64) ensures that non-trivial solutions are available only for specific instances of $\boldsymbol{\beta}(\omega)$, satisfying the array dispersion relation

$$\left(\alpha_{e(eff)}^{-1} - C\right)\left(\alpha_{m(eff)}^{-1} - C\right) = C_{em}^2 - \alpha_{em(eff)}^2. \tag{71}$$

The corresponding eigenvectors, again solving Eq. (64), satisfy

$$\frac{\mathbf{p}_{000} \cdot \hat{\mathbf{p}}}{\mathbf{m}_{000} \cdot \hat{\mathbf{m}}} = \frac{P_{av}}{M_{av}} = \frac{1}{\eta_0} \frac{C_{em} + \alpha_{em(eff)}}{\alpha_{e(eff)}^{-1} - C} = \frac{1}{\eta_0} \frac{\alpha_{m(eff)}^{-1} - C}{C_{em} - \alpha_{em(eff)}}, \tag{72}$$

which provides a specific constraint on the ratio P_{av} / M_{av} in this source-free case, function only of the frequency and the array geometry.

Rearranging Eq. (67) and (58), in this regime we may also write

$$i\boldsymbol{\beta} \times \mathbf{E}_{av} = i\omega \frac{\mu_{eff}}{1 - \dfrac{c_0 \left(\chi_{eff}^o - \chi_{eff}^e\right)}{\beta / k_0}} \mathbf{H}_{av} = i\omega \mu_{eq} \mathbf{H}_{av}$$

$$i\boldsymbol{\beta} \times \mathbf{H}_{av} = -i\omega \frac{\varepsilon_{eff}}{1 - \dfrac{c_0 \left(\chi_{eff}^o + \chi_{eff}^e\right)}{\beta / k_0}} \mathbf{E}_{av} = -i\omega \varepsilon_{eq} \mathbf{E}_{av} \tag{73}$$

which shows that the eigen-modal propagation may be described in terms of equivalent permittivity and permeability parameters ε_{eq}, μ_{eq}, which embed the magneto-electric coupling effects as a form of weak spatial dispersion. Their validity is strictly limited to eigen-modal propagation, since the ratio P_{av} / M_{av} is in general a function of the impressed distributed sources. The description of the array in terms of equivalent parameters is particularly attractive in the absence of bianisotropic effects at the inclusion level ($\alpha_{em} = \chi_{eff}^e = 0$), for which the residual magneto-electric coupling associated with lattice effects may be embedded into equivalent permittivity and permeability related to the effective parameters through the

89

normalization factor $1 - \dfrac{c_0 \chi_{eff}^o}{\beta / k_0}$. This shows that classic homogenization models that aim at describing metamaterial arrays in terms of permittivity and permeability (see, e.g., [166]-[173]) effectively extract these equivalent parameters, that inherently contain a form of weak spatial dispersion when χ_{eff}^o is not negligible. It is evident that this may easily translate into inconsistencies and lack of physical meaning in the extracted or retrieved parameters, as discussed more in detail in [184]. It is also worth stressing that these parameters are inherently a function of the specific ratio P_{av} / M_{av} in (72), i.e., they are forced to change when impressed sources are present in the array, in sharp contrast with the effective constitutive relations, derived in (68) on first-principle physical grounds.

i. Secondary parameters and relation between equivalent and effective descriptions

It follows straightforwardly from (73) that the dispersion relation $\beta(\omega)$ may be re-written as

$$\beta^2 = \omega^2 \mu_{eq} \varepsilon_{eq}, \tag{74}$$

which, after using Eqs. (68) and (66), is proven to coincide with Eq. (71).

In addition, we can define the effective characteristic impedance of the array for eigen-modal propagation:

$$\eta_{eff} = \frac{E_{av}}{H_{av}} = \sqrt{\frac{\mu_{eq}}{\varepsilon_{eq}}} = \sqrt{\frac{\mu_{eff}}{\varepsilon_{eff}}} \sqrt{\frac{\beta / k_0 - c_0 \left(\chi_{eff}^o + \chi_{eff}^e \right)}{\beta / k_0 - c_0 \left(\chi_{eff}^o - \chi_{eff}^e \right)}}. \tag{75}$$

In the absence of bianisotropic effects in the inclusion $\alpha_{em} = \chi_{eff}^e = 0$ and the last side in Eq. (75) simply becomes

$$\eta_{eff} = \frac{E_{av}}{H_{av}} = \sqrt{\frac{\mu_{eq}}{\varepsilon_{eq}}} = \sqrt{\frac{\mu_{eff}}{\varepsilon_{eff}}}. \tag{76}$$

In absence of bianisotropy, therefore, the characteristic impedance is not directly affected by magnetoelectric coupling at the lattice level, and the same characteristic impedance is obtained using either the ratio of effective or equivalent parameters. Using Eq. (67), we may write in the general case

$$\frac{P_{av}}{M_{av}} = \frac{\left(\varepsilon_{eff} - \varepsilon_0 \right) \eta_{eff} + \left(\chi_{eff}^e + \chi_{eff}^o \right)}{\left(\mu_{eff} - \mu_0 \right) - \eta_{eff} \left(\chi_{eff}^e - \chi_{eff}^o \right)}, \tag{77}$$

which, for $\alpha_{em} = \chi_{eff}^e = 0$, may be also written as

$$\frac{P_{av}}{M_{av}} = \eta_{eff} \frac{\varepsilon_{eq} - \varepsilon_0}{\mu_{eq} - \mu_0}. \tag{78}$$

Eqs. (74) and (78) coincide with the classic retrieval procedures used to determine effective permittivity and permeability of a metamaterial sample from their secondary parameters, i.e.,

90

their eigen-modal wave number β and characteristic impedance η_{eff} [173], [182]. This implies that the equivalent parameters derived in (73) from first-principle considerations coincide with those retrieved after assuming that the metamaterial may be described by a simple model consisting of permittivity and permeability, effectively embedding the effects of χ_{eff}^o into the equivalent parameters. In souce-free problems in which the sources are all outside the metamaterial sample, as in classic retrieval schemes, it is tempting to put aside the magneto-electric coupling coefficient χ_{eff}^o, and use the equivalent parameters to model the array scattering. This is indeed possible, and from the scattering point of view the effective and equivalent description is perfectly equivalent in this source-free scenario, since the secondary parameters of the supported eigen-mode coincide in the two descriptions. However, our theory shows that the equivalent parameter description has a limited physical meaning and it should not be used to characterize the electric and magnetic response of the metamaterial, since it hides an inherent form of magneto-electric coupling. It is not surprising that the frequency dispersion of the equivalent parameters may contain non-physical artifacts and not satisfy passivity, reciprocity or causality constraints typical of local parameters [184].

As a final remark with respect to retrieval procedures, it is worth noticing that, even at frequencies where spatial dispersion and magneto-electric coupling are negligible and we can write

$$
\begin{aligned}
\mathbf{D}_{av} &= \varepsilon_{eq}\mathbf{E}_{av} \\
\mathbf{B}_{av} &= \mu_{eq}\mathbf{H}_{av}
\end{aligned}
,
$$

(79)

as in a natural material, our theory shows that the averaged fields are effectively related to the microscopic polarization fields through Eq. (56), i.e., standard retrieval techniques implicitly assume

$$
\begin{aligned}
\varepsilon_{eq} &= \frac{\varepsilon_0\overline{\mathbf{E}}+\mathbf{P}_E}{\overline{\mathbf{E}}-\mathbf{P}_H/\varepsilon_0} \\
\mu_{eq} &= \frac{\mu_0\overline{\mathbf{H}}+\mathbf{M}_H}{\overline{\mathbf{H}}-\mathbf{M}_E/\mu_0}
\end{aligned}
.
$$

(80)

In other words, the nature of the averaged polarization currents within each unit cell, whether electric or magnetic, inherently affects the definition of averaged fields used to calculate equivalent or effective constitutive parameters, and weak spatial dispersion effects associated with artificial magnetism or polarization have a different role (contributing to $\mathbf{E}_{av}$ and $\mathbf{H}_{av}$) than the direct polarization and magnetization vectors (contributing to $\mathbf{D}_{av}$ and $\mathbf{B}_{av}$). This should be considered an implicit assumption of standard retrieval techniques for metamaterials.

e. Long-Wavelength Limit and Relations with Approximate Homogenization Models

For sufficiently long wavelength and away from the inclusion resonances, under the conditions $k_0d \ll 1$, $\beta d \ll 1$, the magneto-electric coupling effect becomes negligible, implying that

$$
C_{em}' \simeq 0, \ \chi_{eff}^o \simeq 0.
$$

(81)

Under this simple condition, and in the absence of bianisotropic effects at the inclusion level $\alpha_{em} = 0$, the array may be described by simple constitutive parameters

$$\varepsilon_{eff} = \varepsilon_{eq} = \varepsilon_0 \left(1 + \frac{d^{-3}}{\alpha_e^{-1} - C_{int}} \right)$$

$$\mu_{eff} = \mu_{eq} = \mu_0 \left(1 + \frac{d^{-3}}{\alpha_m^{-1} - C_{int}} \right), \tag{82}$$

which coincide with generalized Clausius-Mossotti relations fully taking into account the coupling among the inclusions [176]. Under condition (81) and $\alpha_{em} = 0$, we find for the eigenmodal solution:

$$\beta = \pm\omega\sqrt{\mu_{eff}\varepsilon_{eff}}$$

$$\frac{p}{m} = \eta_{eff} \frac{\varepsilon_{eff} - \varepsilon_0}{\mu_{eff} - \mu_0}, \tag{83}$$

which is exactly coincident with Eqs. (74) and (78) for equivalent parameters, ensuring that ε_{eq} and μ_{eq}, as well as the retrieval method [173], are coincident with this first-principle definition of effective constitutive parameters in the absence of impressed sources, after the relevant assumption that magneto-electric coupling effects stemming from spatial dispersion in C'_{em} may be neglected.

If also C_{int} may be considered independent of β in the long-wavelength limit, then

$$C_{int}\left(\omega, \beta \to 0\right) = \frac{1}{3d^3} + j\frac{k_0^3}{6\pi}, \tag{84}$$

which proves that Eqs. (82) and this homogenization method convege to local classic Clausius-Mossotti formulas for periodic arrays [158]-[160] when $\omega, \beta \to 0$. In the following numerical examples, we show that this assumption does not necessarily hold even in the very long wavelength regime, and that the rigorous homogenization approach introduced here may provide results significantly different from quasi-static approaches even for $k_0 d < 1$, $\beta d < 1$.

f. Spatial Dispersion and Extreme Metamaterial Parameters

At the other limit, metamaterials are of most practical interest when their constitutive parameters assume extreme (very large, very low or negative) values, which usually arise around the inclusion resonances. The homogenization model described here is very general, and in principle applicable to any value of ω, β. However, the same definition of homogenized parameters, as those presented in the previous section, inherently neglects the array granularity. This is particularly relevant near these resonances, since, despite a small $(k_0 d)$, the effective eigen-modal wavelength may become comparable with the period as (βd) increases. Although these resonant regions are quite limited in bandwidth for passive inclusions in the long-wavelength

92

regime, it is in these regions that the effects of χ_{eff}^o and of inherent spatial dispersion are most relevant.

i. Near-zero effective material parameters

Limiting ourselves to the lossless scenario for clarity, consider first the low-index regions, for which $\beta d \simeq 0$ for finite $k_0 d$, of interest in a variety of applications [192]-[197]. This includes ε-near-zero, μ-near-zero and low-index metamaterials. In this frequency range, β passes from imaginary to real values, since one of the two equivalent parameters crosses the real axis. For $\beta = 0$, $C'_{em} = \chi_{eff}^o = 0$ and their value also goes from imaginary to real. This makes sure that ε_{eq} and μ_{eq} stay real (and one of them negative) in Eq. (73), also when $\beta \in \Im$. As shown in some of the following numerical examples, crossing this zero-index region provides significant deviations between the equivalent parameters $\left(\varepsilon_{eq}, \mu_{eq}\right)$ and the effective parameters $\left(\varepsilon_{eff}, \mu_{eff}\right)$, as a symptom of inherent spatial dispersion, consistent with the results in [179]. It should be stressed that, surprisingly enough, in this region β, C'_{em}, χ_{eff} are all very close to zero, implying very long effective wavelengths and weak magneto-electric coupling; however, the ratio χ_{eff}^o / β (corresponding to κ_{eff} in the notation of [184]), crucial for determining the effect of spatial dispersion in the denominator of (73), is not necessarily small, providing relevant non-local effects in the equivalent parameters.

ii. Effective parameters near the bandgap regions

Another region of interest for metamaterial applications is the one near the edge of the lattice bandgap, for which $\beta d \simeq \pi$. Around this region, large positive or negative values of permittivity and permeability may be obtained, of interest in a variety of applications [171], [198]-[199]. It is evident that in this scenario the interaction of the electromagnetic wave with the inclusions may become very complex, and an averaged description may not provide much insight into the physical behavior of an eigenmode that flips its phase within the individual unit cell. In particular, inside the bandgap the same definition of constitutive parameters is not meaningful, and they become complex even for lossless inclusions. It is relevant to study, however, the transition between the homogenization regime and the bandgap region, where extreme metamaterial parameters are expected. It is in this transition region that this rigorous homogenization technique becomes particularly important, since here weak spatial dispersion effects become very relevant, even in the long-wavelength limit $k_0 d < 1$. Exactly at the bandgap edge the periodic properties of C_{em} require that [176]

$$C_{em}\left(\beta = \pi / d\right) = 0 \qquad \forall \omega. \tag{85}$$

For center-symmetric inclusions ($\alpha_{em} = 0$), this implies that the general dispersion relation (71) simplifies into

$$\left[\alpha_e^{-1} - C\left(\omega, \pi / d\right)\right]\left[\alpha_m^{-1} - C\left(\omega, \pi / d\right)\right] = 0, \tag{86}$$

93

which implies that a bandgap may be reached, in the long-wavelength limit for which C is small, exclusively near an electric or a magnetic resonance, for which one of the two $\alpha^{-1} = C$. It follows directly from (68), (73) that at such resonance one of the equivalent parameters

$$\mu_{eq} = \mu_0 \ (\text{for } \alpha_e^{-1} = C) \text{ or } \varepsilon_{eq} = \varepsilon_0 \ (\text{for } \alpha_m^{-1} = C), \tag{87}$$

unless the two resonances are degenerate, as considered in the following section. Correspondingly, using (74), the other equivalent parameter has to become

$$\varepsilon_{eq} = \varepsilon_0 \frac{\pi^2}{(k_0 d)^2} \ (\text{for } \alpha_e^{-1} = C) \text{ or } \mu_{eq} = \mu_0 \frac{\pi^2}{(k_0 d)^2} \ (\text{for } \alpha_m^{-1} = C). \tag{88}$$

For instance, if the bandgap associated with a magnetic resonance is considered, as it is the case for the first resonance of a dielectric inclusion (see example 2 in the following numerical section), the eigen-wave number β and the corresponding effective permeability μ_{eff} rapidly increase from lower frequencies when approaching the array resonance, until they hit the bandgap for $\alpha_m^{-1} = C$. At this frequency $\varepsilon_{eq} = \varepsilon_0$, $\mu_{eq} = \mu_0 \dfrac{\pi^2}{(k_0 d)^2}$, and therefore, using (73)

$$\begin{aligned}
\frac{\varepsilon_{eff}}{\varepsilon_0} &= 1 - \frac{c_0 \chi_{eff}^o}{\pi / (k_0 d)} \\
\frac{\mu_{eff}}{\mu_0} &= \frac{\pi}{k_0 d} \left(\frac{\pi}{k_0 d} - c_0 \chi_{eff}^o \right)
\end{aligned}. \tag{89}$$

Eq. (75) is indeed satisfied by Eq. (89), and it implies

$$\frac{\eta_{eff}}{\eta_0} = \frac{\beta}{k_0} = \frac{\pi}{(k_0 d)}, \tag{90}$$

which suggests that, independent on the geometry of the inclusions, at the bandgap edge the normalized characteristic impedance simply coincides with the normalized wave number. An analogous derivation for bandgaps at an electric resonance provides the inverse of Eq. (90). It is evident that in this regime χ_{eff}^o may not be neglected and indeed its effect is comparable, if not larger, than the one of ε_{eff} and μ_{eff}. In this frequency range the equivalent parameters (73) lose their physical meaning and strongly diverge from the effective parameters (68), as discussed in further detail in [184].

It is evident from this discussion that regions with extreme (very large, very low or negative) metamaterial parameters are those for which the present homogenization technique is most relevant. We show in the following numerical examples how this rigorous model may correctly model the exotic features of metamaterials within these frequency bands, capturing the weak spatial dispersion effects that are usually at the root of inconsistencies in approximate and less rigorous homogenization models.

g. *The Special Case of Matched Inclusions and Degenerate Resonances*

A special situation of interest arises in the case in which the electric and magnetic resonances of the inclusions are degenerate, as it may happen for matched inclusions, which support combined electric-magnetic resonances at the same frequency [171],[173],[196]. These are particularly relevant for realizing double negative metamaterials with matched properties. Under this condition, it is evident that $\alpha_e = \alpha_m = \alpha$ (at least over a given range of frequencies of interest) and, under the assumption $\alpha_{em} = 0$, the eigen-modal dispersion relation (71) simplifies into

$$\alpha^{-1} = C \pm C_{em}. \tag{91}$$

Correspondingly, Eq. (72) always yields, as expectable

$$m/p = \eta_0. \tag{92}$$

The effective constitutive parameters are simplified into

$$\frac{\varepsilon_{eff}}{\varepsilon_0} = \frac{\mu_{eff}}{\mu_0} = \left(1 + \frac{d^{-3}\left(\alpha^{-1} - C_{int}\right)}{\left(\alpha^{-1} - C_{int}\right)^2 - C'^{\,2}_{em}}\right),$$

$$c_0 \chi^o_{eff} = \frac{d^{-3} C'_{em}}{\left(\alpha^{-1} - C_{int}\right)^2 - C'^{\,2}_{em}} \tag{93}$$

and

$$\beta^2 = k_0^2 \frac{\varepsilon_{eq}}{\varepsilon_0} = k_0^2 \frac{\mu_{eq}}{\mu_0}, \tag{94}$$

$$\eta_{eff} = \eta_0$$

ensuring that effective and equivalent parameters are matched, as expected.

The eigen-solution β of (91) is necessarily bounded within the principal period $\left|\mathrm{Re}[\beta]\right| < \pi/d$ for the homogenization to hold. In the lossless limit of interest here, the matched condition ensures that there are no finite bandgaps for the real branches of β, and its dispersion bands are connected to each other at the branchcuts for which $\left|\mathrm{Re}[\beta]\right| = \pi/d$. The absence of bandgaps in the eigen-modal dispersion is particularly interesting, since it implies that the effective parameters are always real defined, producing peculiar dispersion phenomena in this special circumstance. In particular, at the branch cuts, using (85) we get

$$\alpha^{-1} = C\left(\omega,\ \beta = \pi/d\right). \tag{95}$$

Using (93) and (66), under this condition we find the interesting relations

$$\frac{\varepsilon_{eff}}{\varepsilon_0} = \frac{\mu_{eff}}{\mu_0} = 0$$

$$c_0 \chi^o_{eff} = \frac{\varepsilon_{eq}}{\varepsilon_0} = \frac{\mu_{eq}}{\mu_0} = \frac{\pi}{d} \tag{96}$$

which always hold at branch-cut points $\left|\operatorname{Re}[\beta]\right| = \pi / d$. Notice that in this special case Eqs. (87) -(88) do not hold. Although the effective permittivity and permeability are zero, the magneto-electric coefficient is large, and it makes sure that the dispersion relation (94) is satisfied. In this regime, by locally increasing the average electric field would curiously affect only the average magnetization, and dual considerations apply to the average magnetic field. It is evident that in this scenario the effects of χ_{eff}^{o} and of weak spatial dispersion cannot be neglected.
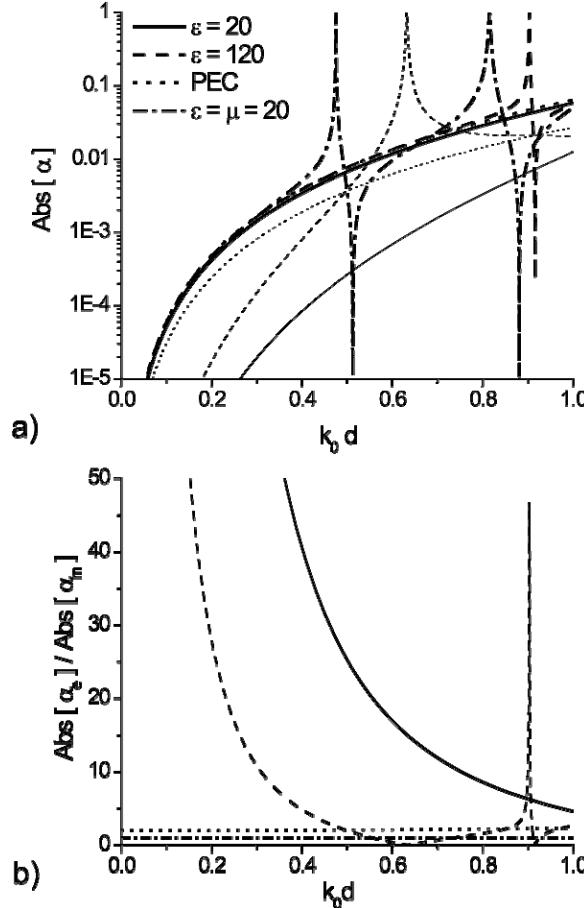

Figure 44 – (a) Frequency dispersion of the electric (thick line) and magnetic (thin) normalized polarizability of the individual inclusions for the four metamaterial arrays considered in the following figures: (solid) dielectric spheres with permittivity $\varepsilon = 20\varepsilon_0$; (dashed) dielectric spheres with $\varepsilon = 120\varepsilon_0$; (dotted) conducting spheres; (dash-dotted) magnetodielectric spheres with $\varepsilon = 20\varepsilon_0$ and $\mu = 20\mu_0$; (b) Ratio of electric over magnetic polarizability for the same geometries. Here $\gamma = 0.45$.

Near the bandgaps, there are two finite frequencies satisfying the equation

$$\alpha^{-1} = C_{int} \pm C'_{em},$$ (97)

symmetrically placed around the branch-cut point $\alpha^{-1} = C(\omega, \pi / d)$, at which all the constitutive parameters diverge. In fact, in this matched scenario the effective parameters are not bounded, but

96

$$\lim_{\left(\alpha^{-1}-C_{int}\right)\to\pm C'_{em}} \frac{\varepsilon_{eq}}{\varepsilon_0} = \lim_{\left(\alpha^{-1}-C_{int}\right)\to C'_{em}} \frac{\varepsilon_{eff}}{1-\dfrac{c_0\chi^o_{eff}}{\beta/k_0}} = \frac{\beta}{k_0}, \tag{98}$$

and analogously for μ_{eq}, ensuring that the equivalent parameters in (73) remain bounded and satisfy (94), even when all the effective constitutive parameters diverge. These two closely spaced vertical asymptotes for the effective parameters are symmetrically placed around any branch-cut point for $\left|\mathrm{Re}\left[\beta\right]\right| = \pi/d$ and they are separated by a distinct branch that crosses conditions (96) when $\alpha^{-1} = C\left(\omega, \beta = \pi/d\right)$. Around the inclusion resonance, the effective parameters may assume zero or infinite values and χ^o_{eff} cannot be neglected.

Passed any of these resonances, β assumes negative eigen-values, which corresponds to regions with effective negative index of refraction, in which both the effective parameters are negative. At the connection between negative and positive branches, when the effective parameters cross zero, in this matched lossless scenario spatial dispersion may be safely neglected, since

$$\frac{\varepsilon_{eff}}{\varepsilon_0} = \frac{\mu_{eff}}{\mu_0} = c_0\chi_{eff} = \frac{\varepsilon_{eq}}{\varepsilon_0} = \frac{\mu_{eq}}{\mu_0} = \frac{\beta}{k_0} = 0. \tag{99}$$

Only in this situation we may achieve a truly local zero permittivity and permeability, impedance matched with free-space, useful in various applications envisioned in recent papers [196]-[197]. In contrast, in the unmatched scenario, as outlined above, the effects of spatial dispersion may not be neglected in regions with near-zero effective index of refraction.

h. Numerical Examples and Further Discussion

In this section, we discuss the homogenization of four specific metamaterial geometries of interest. Although the previous formulation is applicable to arbitrary lossy, bianisotropic inclusions, arbitrary source distribution and any choice of $\left(\omega, \mathbf{\beta}\right)$, here we focus on metamaterials composed of lossless spheres and eigen-modal propagation. This has the advantage of providing a clearer picture of the difference between this homogenization approach and other quasi-static techniques and retrieval methods focused on the absence of embedded sources in the array, in order to highlight the relevant effects of spatial dispersion and magneto-electric coupling coefficient in the different propagation regimes and transition regions near the metamaterial resonances. Our numerical examples are tailored to highlight the difference between quasi-static homogenization models and this rigorous homogenization approach. For this reason, we limit our analysis to dipolar approximations and eigen-modal propagation in the long-wavelength regime, of major interest in the metamaterial community. In future works we will apply the general multipolar approach introduced in Section 2 to arbitrary metamaterial inclusions and extend our numerical analysis to the presence of embedded sources. Since we deal with spherical particles, we can use analytical closed-form expressions for α_e, α_m [200]. Finally, for the reasons outlined above and the purpose of this paper, we focus all our examples in the long-wavelength region, usually considered safe for quasi-static homogenization models, i.e., $\left(k_0 d\right) < 1$ [162]-[164]. The parameter $\gamma = a/d$ is also introduced, which defines the ratio of sphere radius over lattice period, as a measure of the array density.

97
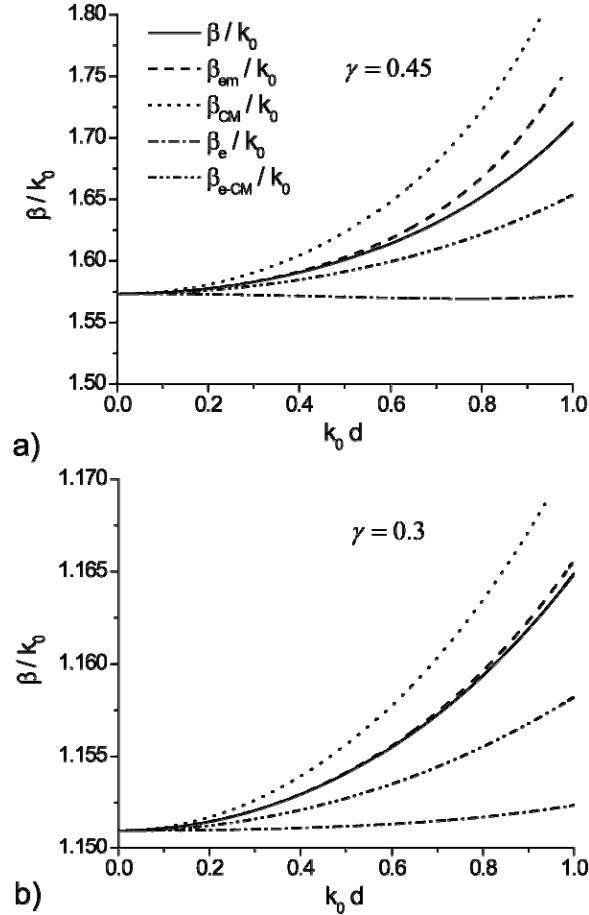
Figure 45 – Frequency dispersion of the guided wave number, and its approximations as defined in the text, for an array of dielectric spheres with $\varepsilon = 20\,\varepsilon_0$, with (a) $\gamma = 0.45$, (b) $\gamma = 0.3$.

Figure 44a shows in logarithmic scale the amplitude of the normalized polarizability coefficients (thick lines for the normalized electric polarizability, thin for the magnetic one) for four different geometries of interest: (1, solid lines) dielectric spheres with relative permittivity $\varepsilon_r = 20$ and permeability $\mu_r = 1$; (2, dashed) dielectric spheres with $\varepsilon_r = 120$ and $\mu_r = 1$; (3, dotted) perfectly conducting spheres; (4, dash-dotted) magneto-dielectric spheres with $\varepsilon_r = \mu_r = 20$. For convenience, Fig. 1b shows the ratio $|\alpha_e|/|\alpha_m|$, in order to highlight the ratio between electric and magnetic response at the inclusion level. Both plots show their variation as a function of $(k_0 d)$, for the density factor $\gamma = 0.45$. The chosen geometries represent specific situations of interest in common metamaterial arrays: in case 1 (solid lines), a regular array of dielectric spheres is considered, far from their individual resonances, but still with a good contrast compared to the background: a dominant electric polarization is expected all over the spectrum of interest; in case 2 (dashed), the permittivity is increased to support a magnetic and an electric resonance within the frequency band of interest, in analogy with established designs to realize negative metamaterial parameters [171]: in this case, more interesting features are expected in the metamaterial response near these resonances. As expected, the electric response is dominant for lower frequencies, but the first resonance is magnetic. In case 3 (dotted), conducting particles are considered, for which electric and magnetic responses are comparable, and for lower

98

frequencies the electric response is exactly twice the magnetic one; in case 4 (dash-dotted), impedance matched inclusions are employed, supporting two combined electric-magnetic resonances within the band of interest. It is noticed that in all these examples, lossless conditions (70) strictly apply.

Figure 45a shows the dispersion of normalized eigen-wave number (effective index of refraction) for the array 1 with $\gamma = 0.45$. The figure compares the exact eigen-modal solution of the guided wave number β / k_0 (solid line), as obtained from Eq. (71), with various approximate solutions obtained neglecting spatial dispersion and magneto-electric effects, as follows: the dashed line refers to the dispersion of β_{em}, obtained neglecting the magneto-electric coupling term C'_{em}, as in Eq. (81); the dotted line shows β_{CM}, which in addition neglects the dispersion effects in C_{int}, implying $C'_{em} = 0$ and C_{int} as given by Eq. (84), coinciding with the quasi-static Clausius-Mossotti homogenization model; the dash-dotted line refers to β_e, obtained neglecting the magnetic polarizability effects associated with the magnetism of the inclusions (which is small in this geometry), but still using the exact C_{int} expression; finally the dash-dot-dot line refers to β_{e-CM}, which neglects the magnetic effects and uses Eq. (84) for C_{int}. We consider all these approximate expressions to show how the different spatial and frequency dispersion terms, usually neglected in quasi-static homogenization models, affect the metamaterial homogenization accuracy. As expected, all these expressions converge to the same quasi-static limit when $(\omega, \beta) \to 0$, but the approximate expressions start deviating from the exact expression of β for relatively low values of $k_0 d$. In particular, it is surprising to notice how, by neglecting the magnetic polarizability of the particles, which in this case is orders of magnitude smaller than the electric one (see Fig. 1b), the dispersion of β_e / k_0 diverges quite drastically from the exact model, implying that the small magnetism in these dielectric particles should not be neglected, as one may be tempted to do looking at Fig. 1b. The effects of non-locality and spatial dispersion in C_{int} start playing a role much earlier in frequency than one would generally expect for such simple topology, comparing β_{CM} with β. In comparison, the magneto-electric coupling effects have a much weaker role, and start being relevant only around $k_0 d \simeq 1$. Figure 45b, in comparison, shows the same curves calculated for a less dense array, with $\gamma = 0.3$. As visible, the trend of the various curves is quite similar, although the effects of spatial dispersion are less relevant here, as the interaction among inclusions is weaker. In particular, the magneto-electric coupling effects associated with C'_{em} are negligible all over the range of frequency of interest, since β_{em} practically coincides with β in this less dense configuration. Non-local effects in C_{int} and the influence of the small magnetic properties of the inclusions have still some relevant effects in this less dense scenario.

Figure 46 shows the eigen-modal dispersion of effective constitutive parameters for this array for $\gamma = 0.45$. The top panel compares: the effective permittivity ε_{eff} (solid black line); ε_{em}, calculated after neglecting the magneto-electric coupling coefficient C'_{em}, as in Eq. (82) (dashed); ε_{loc}, calculated neglecting also the effects of spatial dispersion in C_{int}, but still considering its dependence on ω for $\beta = 0$ (dash-dotted); ε_{CM}, obtained using the quasi-static

99

expression for C_{int} given in (84) (dotted), which coincides with the Clausius-Mossotti definition for periodic arrays derived in [158]; finally ε_{eq} (solid light green), defined as in (73). All these expressions yield a purely real permittivity, as expected from the lossless assumption. However, ε_{CM} rapidly diverges from the first-principle value of permittivity ε_{eff}. The value of ε_{eff} actually decreases with frequency for any $k_0 d < 0.65$, due to the effects of frequency and spatial dispersion in the interaction constants for dense arrays. By neglecting the magneto-electric coupling, as in ε_{em} does not produce any sensible difference in the prediction of ε_{eff}, but the effects of spatial and frequency dispersion of the interaction constants are quite relevant, as seen analyzing the divergence of ε_{loc} and even more of ε_{CM} from ε_{eff}. Finally, the divergence of ε_{eq} from the correct value of ε_{eff} is a symptom of non-negligible spatial dispersion and magneto-electric coupling in the array, which are evidently not negligible in such dense arrays.

In comparison, the permeability is accurately predicted by all the approximate models, and even the local or Clausius-Mossotti approximations predict extremely well its weak dispersion, due to the significantly lower magnetic response of the spheres all over the frequency range of interest. Interestingly, only μ_{eq} shows a moderate deviation from μ_{eff}, which highlights how the effects of χ_{eff}^o may not be neglected even in this long-wavelength regime. Finally, the value of χ_{eff}^o (bottom panel) becomes relevant only towards the higher end of this frequency range, explaining the divergence of effective and equivalent parameters.

Figure 47 calculates the secondary effective parameters of this material, obtained using the different homogenization models of Fig. 3. In particular, Fig. 47a compares the exact value of normalized wave number β / k_0, as from Fig. 45a, with the approximate values $\beta_i / k_0 = \sqrt{\varepsilon_i \mu_i}$, where the pedix i stands for any of the approximate models used in Fig. 46. This plot offers several interesting insights. First of all, it is noticed that β_{eff} follows extremely well the dispersion of β_{em}, consistent with the weak effects of C'_{em} on the effective permittivity. However, both curves moderately diverge from the correct value β / k_0 in the range $0.5 < k_0 d < 1$, confirming that the effects of χ_{eff}^o cannot be neglected in this frequency range. The Clausius-Mossotti model β_{CM} fails even more substantially. Fig. 47b compares the corresponding values of effective characteristic impedance $\eta_i / \eta_0 = \sqrt{\mu_i / \varepsilon_i}$. As noticed in the previous section, χ_{eff}^o does not play a direct role in the impedance when $\chi_{eff}^e = 0$, as here, and therefore the parameters obtained neglecting C'_{em} yield an accurate approximation of the effective impedance η_{eff}. It should be noted, however, that the relation between η_{eff} and P_{av} / M_{av} may not be assumed as simple as (83), due to the effects of χ_{eff}^o for relatively larger frequencies. In the less dense array case of Fig. 45b (not reported here for brevity), as expectable the effects of non-locality and spatial dispersion are much less relevant, but still Clausius-Mossotti homogenization formulas would deviate considerably from the proper effective parameters. The use of equivalent parameters, that embed the magneto-electric effect in their same definition (73), would predict correct values of these secondary parameters, consistent with (74)-(75), ensuring that their use for scattering purposes in the eigen-modal operation is perfectly

100

legitimate, if one avoids assigning them the usual physical meaning of local constitutive parameters.
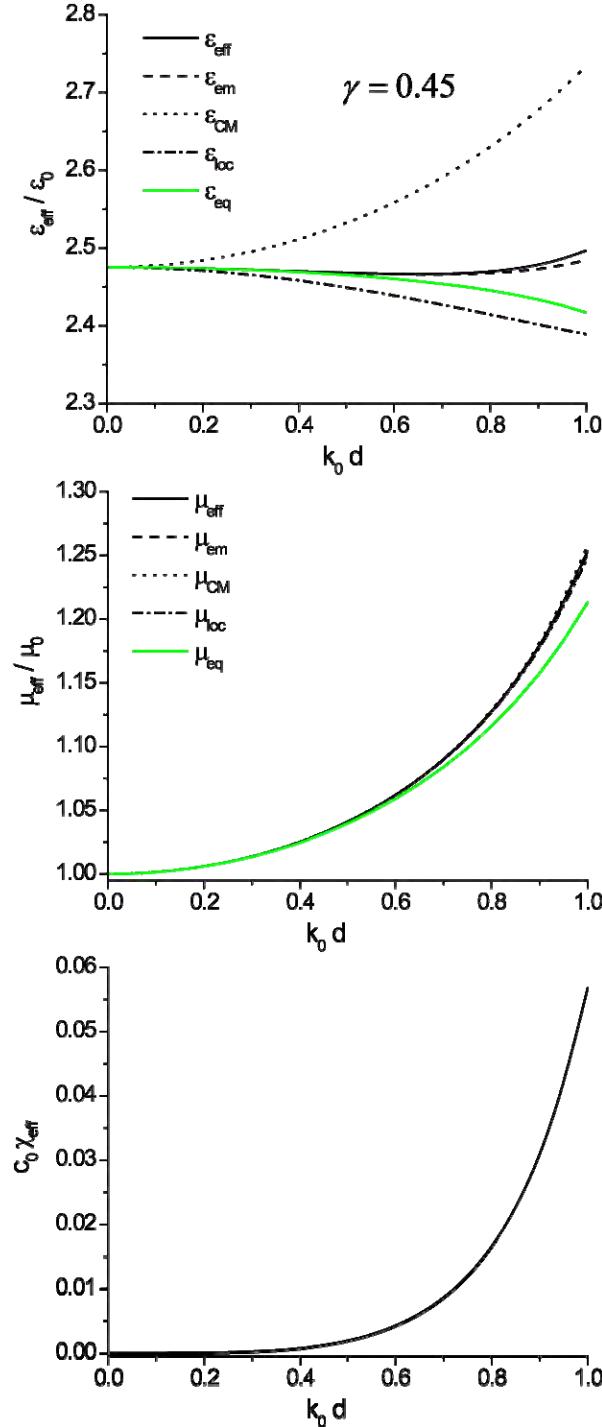

Figure 46 – Frequency dispersion of the effective constitutive parameters, and their approximations as defined in the text, for the array of Fig. 45a.

101

a)

b)
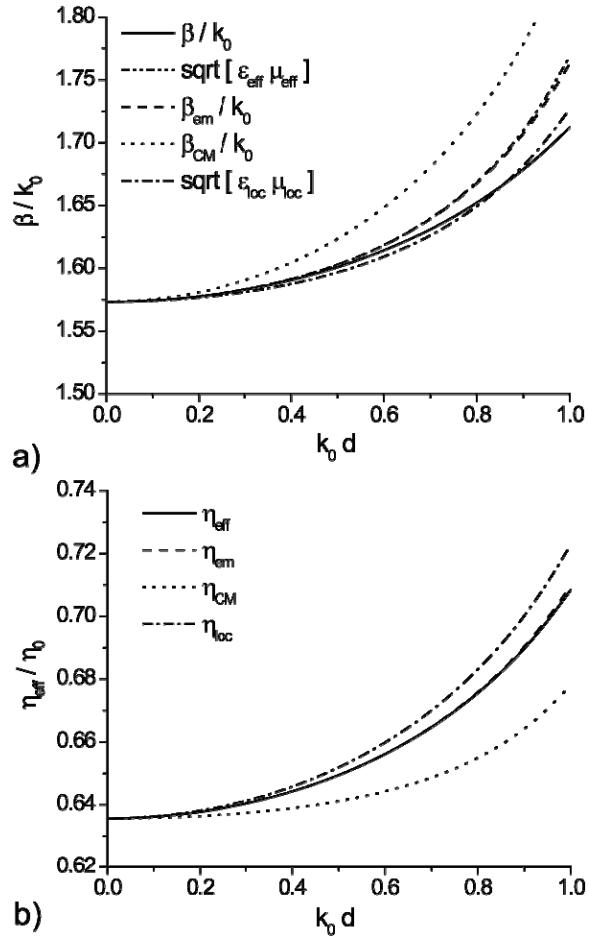
Figure 47 – Frequency dispersion of the effective wave number and characteristic impedance calculated from the constitutive parameters of Fig. 46.
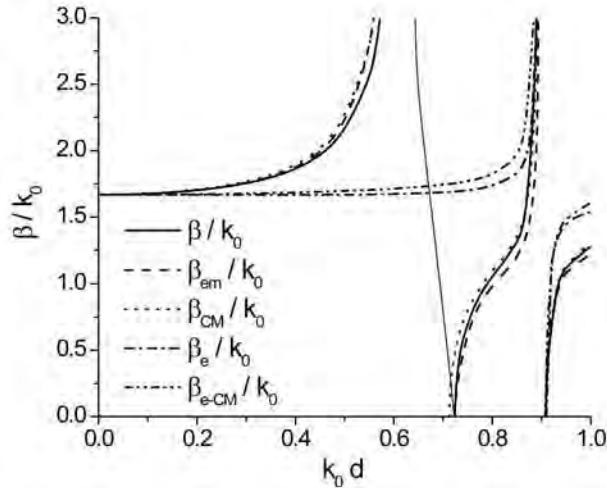

Figure 48 – Frequency dispersion of the guided wave number, and its approximations as defined in the text, for an array of dielectric spheres with $\varepsilon = 120\,\varepsilon_0$ and $\gamma = 0.45$. The thin solid line corresponds to the imaginary branch of β.
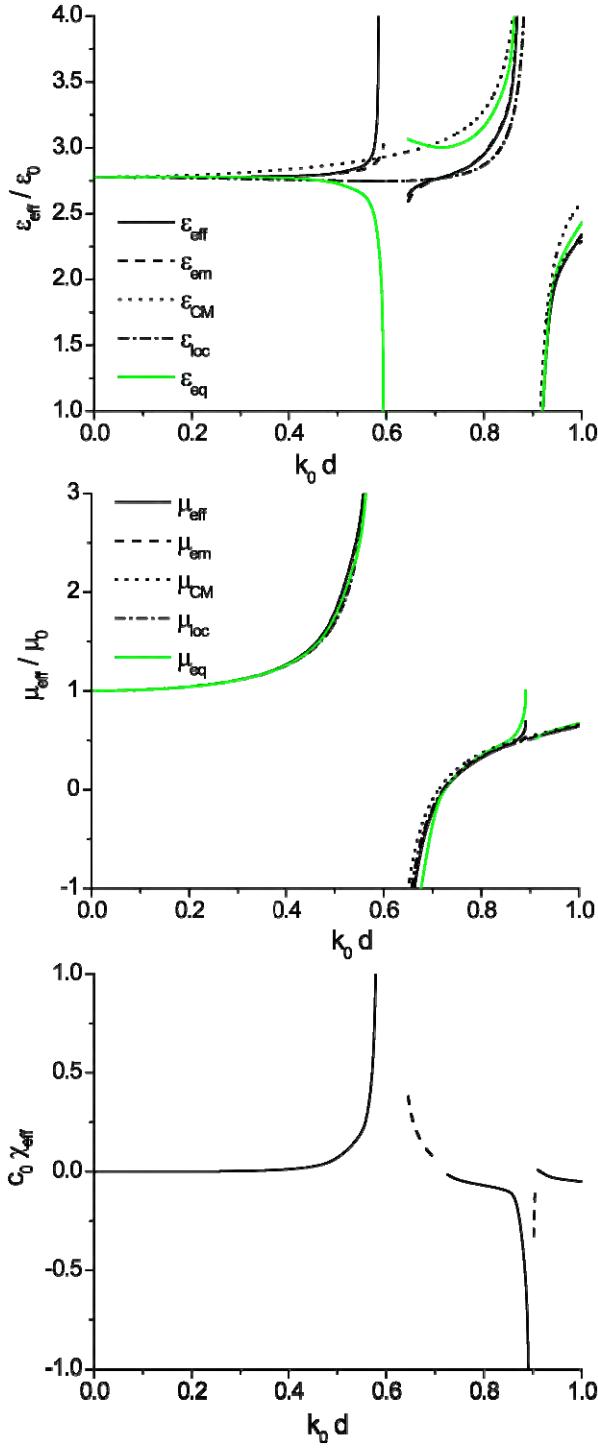
Figure 49 – Frequency dispersion of the effective constitutive parameters, and their approximations as defined in the text, for the array of Fig. 5. Dashed lines in the bottom panel refer to branches with imaginary values.

Consider now the second metamaterial of interest, composed of spheres with $\varepsilon_r = 120$, which support a magnetic and an electric resonance within the low frequency regime considered here. Figure 48 shows the eigen-wave number dispersion for such array with $\gamma = 0.45$, with symbols analogous to Fig. 2. It is immediately recognized that the exact dispersion of normalized wave

103

number β / k_0 (solid lines) is much more intricate than in the previous situation. As expected, β / k_0 initially grows with frequency, until hitting the first band-gap of the array at $(k_0 d) = 0.594$, at the magnetic resonance frequency $\alpha_m^{-1} - C = 0$. The narrow frequency region within the bandgap should be completely disregarded in terms of homogenization, since, as discussed above, the effects of array granularity plays a major role, and the same definition of averaged constitutive parameters loses its macroscopic meaning. Passed the magnetic bandgap, a branch with imaginary wave number $\beta = -j\beta_i$ is reached (thin solid line), which connects with the next real branch at $(k_0 d) = 0.723$, at the point for which $\beta = 0$. The following bandgap is then hit at the electric resonance frequency $\alpha_e^{-1} - C = 0$, at $(k_0 d) = 0.891$, and the next real branch is obtained at $(k_0 d) = 0.909$. As seen in Fig. 7, this behavior is well described by approximate dispersion relations, even neglecting the effects of C'_{em} or even the spatial dispersion in C_{int}, as in β_{em} and β_{CM} respectively, since the local inclusion resonances now dominate the spatial dispersion effects of the lattice. Of course, in this scenario it is not possible to neglect the magnetic effects in the dielectric particles, as for β_e and β_{e-CM}, since this would completely miss the first magnetic bandgap resonance.

The effective constitutive parameters of this array are reported in Fig. 49, with analogous symbols as in the previous example. If the spatial dispersion effects are negligible in evaluating $\beta(\omega)$ in Fig. 48, they play a major role in the correct definition of the constitutive parameters, in particular near the electric and magnetic resonances of the inclusions. First, it is noticed that Clausius-Mossotti formulas completely miss the relevant magneto-electric coupling arising near the bandgaps, and the permittivity especially suffers of this approximation, starting from very low frequencies. Towards the first (magnetic) resonance, ε_{em} may approximate relatively well the effective permittivity ε_{eff}, confirming that the effect of C'_{em} is small on the permittivity dispersion, dominated by the local inclusion resonances. However, the value of χ_{eff}^o assumes large values near the two resonances and it cannot be neglected in a proper homogenization model. Near the magnetic resonance, the effective permittivity experiences a sharp Lorentzian resonance, completely missed by ε_{CM} and even by ε_{loc}, which is an evident symptom of the magneto-electric coupling in the array. In contrast, the various models for magnetic permeability all have good agreements with the effective model (with the exception of a small resonant feature arising at the electric bandgap resonance of the array). In the region where β is imaginary, immediately following the bandgaps, all the models correctly predict a negative effective permeability or permittivity region, which crosses zero at $(k_0 d) = 0.723$ and $(k_0 d) = 0.909$, together with the value of β. In this negative parameter range, as expected, χ_{eff}^o is imaginary (dashed lines in the bottom panel), which ensures that the equivalent parameters are real quantities (one of them negative).

Special attention should be paid to the dispersion of the equivalent permittivity ε_{eq} in Fig. 51a (lighter green line). Its slope is negative all the way until the magnetic bandgap, producing an anti-resonance effect similar to the one extracted from retrieval procedures in various

104

metamaterial geometries near magnetic resonances [173]-[182]. It is evident from this analysis that these effects are associated to incorporating χ_{eff}^{o} in the definition of equivalent permittivity.
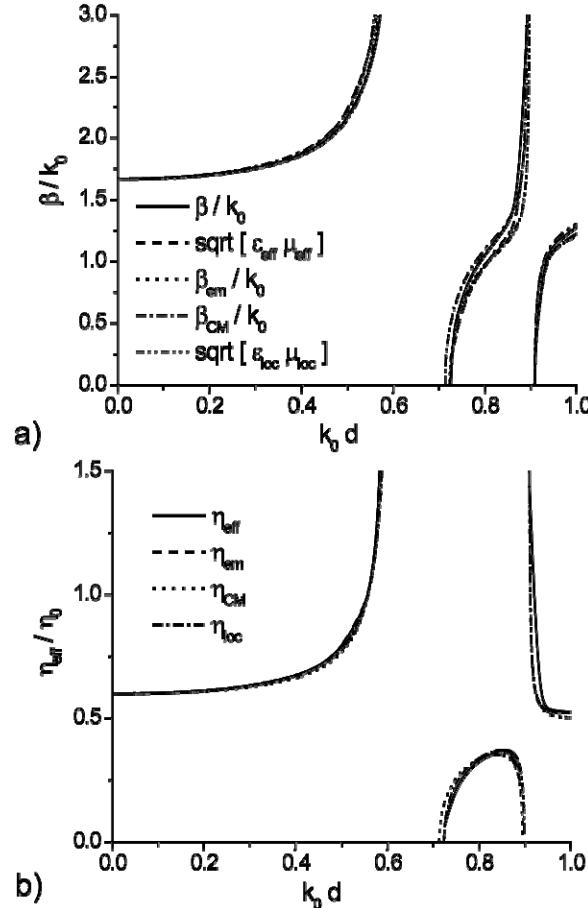

Figure 50 – (Color online): Frequency dispersion of the effective wave number and characteristic impedance calculated from the constitutive parameters of Fig. 49.

It is true that the two equivalent parameters may describe well the guidance properties of the array, but their physical meaning in this case diverges considerably from the first-principle definition of permittivity and permeability. A simple metamaterial model based on just equivalent permittivity and permeability would fail capturing the physics of the array near the first bandgap resonance, predicting $\varepsilon_{eq} = \varepsilon_0$ (87), when in reality the averaged polarization vector has a strong resonance cancelled by the coupled magnetization. These effects have been discussed in more detail in [184]. If the discrepancy between ε_{eq} and ε_{eff} may have been expected near this resonant regime, another transition region in which the equivalent parameters $\varepsilon_{eq}, \mu_{eq}$ lose their usual meaning is the region near $(k_0 d) = 0.723$, for which $\beta \simeq 0$. As confirmed by Fig. 8a, and anticipated above, in this region:

$$\varepsilon_{eff} \simeq \varepsilon_{em} \simeq \varepsilon_{loc}$$

$$\mu_{eff} \simeq 0 \qquad \qquad . \qquad \qquad\qquad\qquad\qquad\qquad (100)$$

$$\chi_{eff}^{o} \simeq 0$$

Indeed, the correct value of effective permittivity coincides with the local value ε_{loc}, since $\beta \simeq 0$, but this value is substantially different from ε_{eq}. This is due to the fact that, although the magneto-electric coefficient is near zero, the ratio χ_{eff}^{o} / β is finite, implying that ε_{eq} diverges from ε_{eff} and it loses the meaning of the average electric polarizability of the array. In this near-zero index region, the weak spatial dispersion represented by χ_{eff}^{o} may not be neglected, although the effective wavelength is very large. This confirms the results in [179] derived for periodic arrays of split-ring resonators, which discussed the presence of non-negligible spatial dispersion effects in this extremely long-wavelength ($\beta d \ll 1$) scenario.
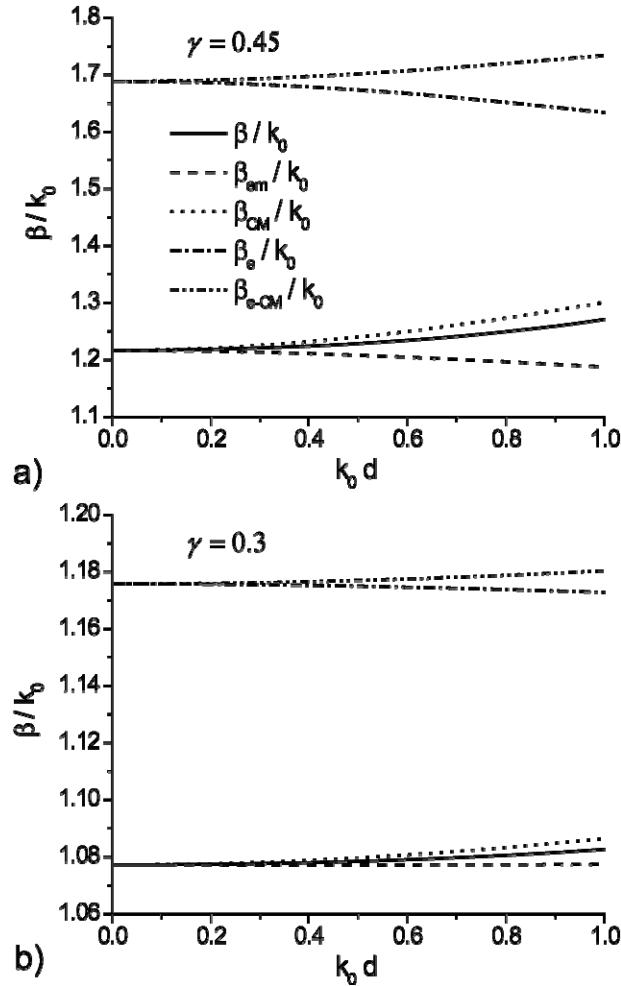

Figure 51 – Frequency dispersion of the guided wave number, and its approximations as defined in the text, with frequency for an array of conducting spheres, for (a) $\gamma = 0.45$, (b) $\gamma = 0.3$.

106
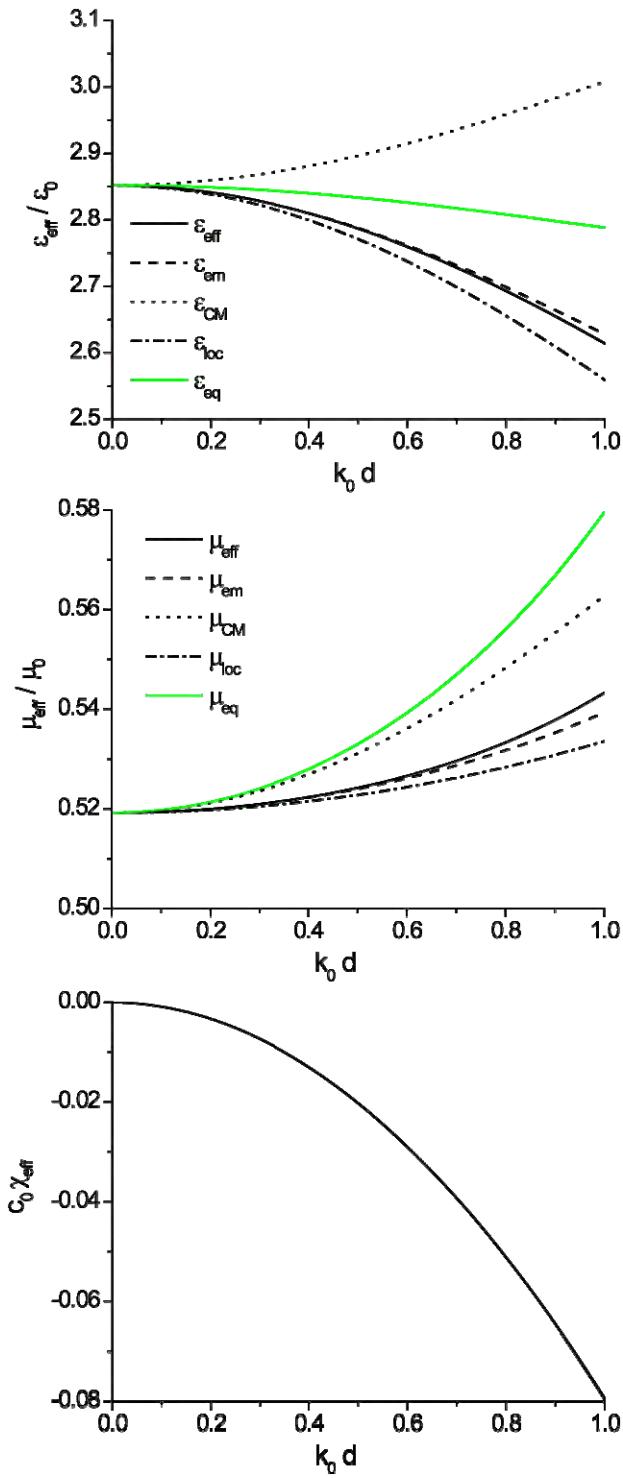
Figure 52 – Frequency dispersion of the effective constitutive parameters, and their approximations as defined in the text, for the array of Fig. 8a.

107
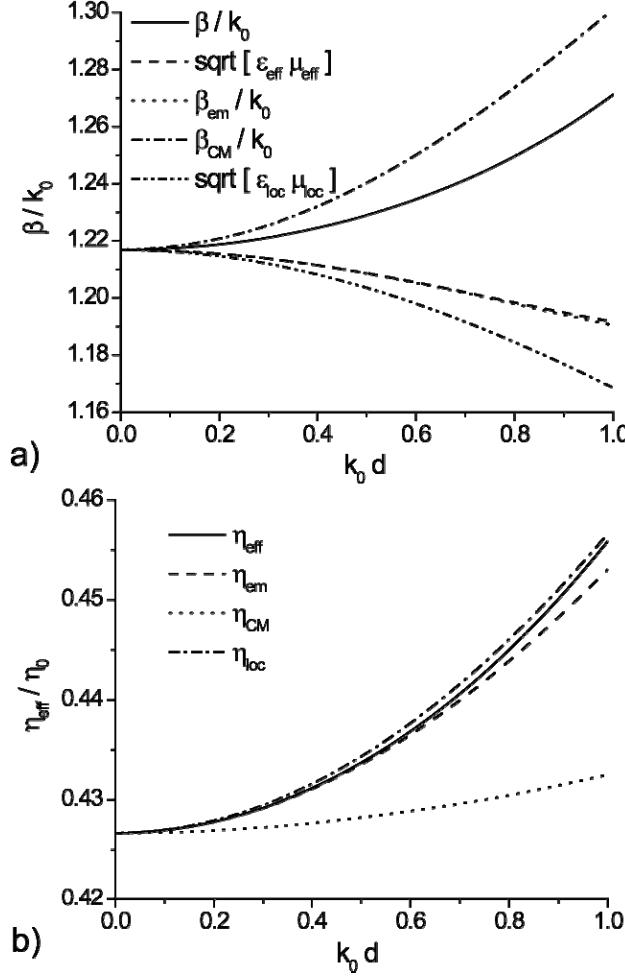
Figure 53 – Frequency dispersion of the effective wave number and characteristic impedance calculated from the constitutive parameters of Fig. 52.

Figure 50 shows the dispersion of the effective index of refraction and characteristic impedance obtained through the various parameters in Fig. 49, analogous to Fig. 47. As it is visible, all the curves agree with high accuracy within the real branches, since their dispersion is dominated by the local resonances at the inclusion level. This example clearly shows that indeed β and η for this array may be easily derived applying local concepts, like Clausius-Mossotti relations or simple retrieval procedures, since they are dominated by local resonances at the inclusion level; however, inferring from these secondary parameters the physical values of permittivity and permeability, as commonly done, may lead to physical artifacts and inconsistencies [184], since in the resonant regions the effects of χ_{eff}^{o} cannot be neglected.

As a third example, consider the case of an array of conducting particles, as in Fig. 44, dotted lines. Figure 51 shows the dispersion of wave numbers for $\gamma = 0.45$ (a) and $\gamma = 0.3$ (b), analogous to Fig. 45. In this case, the wave numbers predicted using just electric effects of the particles are evidently incorrect, since the magnetic contribution for conducting particles is never negligible. Moreover, the effect of the coupling coefficient C'_{em} is particularly relevant in this

108

conducting scenario, which shows the maximum divergence between β and β_{em}, due to the relevance of the magnetic effects even at very low frequencies.

Figure 52 shows the corresponding constitutive parameters for the case $\gamma = 0.45$. ε_{eff} also in this scenario shows a distinct negative slope, all over the range of frequencies considered here, due to non-negligible spatial and frequency dispersion. This is compensated by the positive slope of the effective permeability, which assumes, as expected, diamagnetic values [201]. Only the Clausius-Mossotti quasi-static model predicts a positive dispersion for ε_{CM}, whereas all the other models correctly follow the trend of ε_{eff}. As good confirmation of the strong influence of χ_{eff}^{o}, the deviation of the equivalent parameters ε_{eq}, and in particular μ_{eq}, from the effective parameters is pretty relevant. Figure 10, finally, shows the dispersion of the calculated wave numbers and characteristic impedances obtained using the effective constitutive parameters of Fig. 52. It is seen how all the curves agree reasonably well with the exact dispersion of η_{eff}, except the quasi-static Clausius-Mossotti formula, which neglects frequency and spatial dispersion effects of the interaction constants. The divergence of all the curves from the exact dispersion of β is particularly striking, as a symptom of the relevance of the magneto-electric coefficient χ_{eff}^{o}. We have also analyzed the less dense configuration with $\gamma = 0.3$, as in Fig. 51b (not reported here for brevity), which indeed provides analogous results, but less strong variations from the background parameters, as expected.
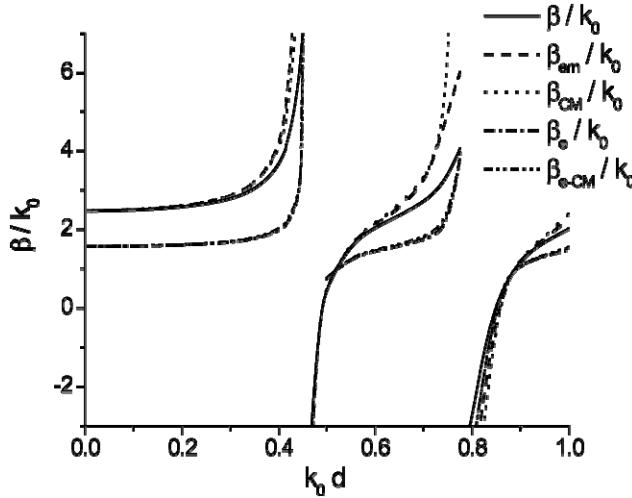

Figure 54 – Frequency dispersion of the guided wave number, and its approximations as defined in the text, for an array of magnetodielectric spheres with $\varepsilon = 20\varepsilon_0$, $\mu = 20\mu_0$, $\gamma = 0.45$.

Finally, as the fourth relevant metamaterial geometry of interest, Figs. 54-55 show the case of an array of magnetodielectric matched spheres, as in Fig. 1 (blue lines), which are able to produce degenerate electric-magnetic resonances at the same frequency, leading to negative index bands of operation [171], [173]. Figure 54 shows the eigen-wave number dispersion for this array, consistent with the previous examples. Indeed, the wave number experiences resonances near the combined electric-magnetic resonances of the inclusions, as predicted by (91). In particular, β grows from its quasi-static value until reaching the first branch-cut at $\beta = \pi / d$, at the resonant condition (95). Exactly as formulated in the previous section, the effective constitutive

109

parameters (Fig. 55) diverge twice around this resonance condition, at the frequencies (91), and the corresponding wave number enters a region of negative effective index of refraction. As expected, also χ_{eff}^{o} diverges near this resonance, and it cannot be neglected in a proper homogenization model. All the effective parameters are real for any frequency, and their value is unbounded, as described in the previous section. Consistently, the approximate models of β (in this scenario they are identically equal to the dispersion of the permittivity models in Fig. 55a, since permittivity and permeability are matched) may considerably fail near these resonances. As already mentioned in the previous section, in this matched geometry the eigen-modal characteristic impedance is always η_0, equal to the ratio M_{av}/P_{av}. Therefore, classic retrieval techniques, as well as the one employed in [173], may derive with good approximation the behavior of ε_{eff}, μ_{eff} far from the branch-cuts, for which χ_{eff}^{o} and the effects of spatial dispersion are minimal. However, near the branch-cut resonances a more refined model as the one described here is required for a proper physical description of the array.
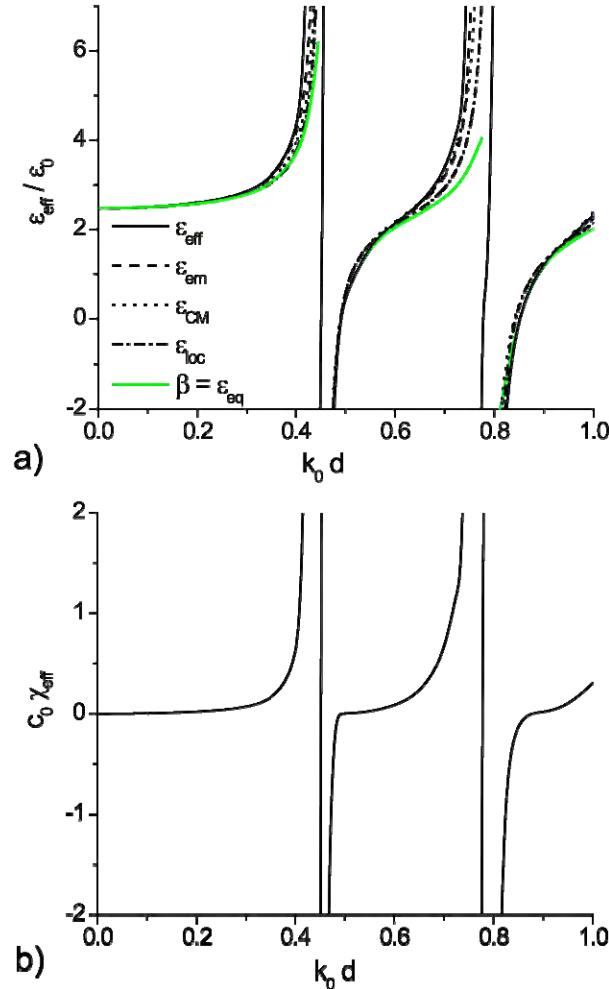

Figure 55 –Frequency dispersion of: (a) effective permittivity and its approximations (the normalized permeability and effective wave number have exactly the same dispersion in this case) and (b) magneto-electric coefficient for the array of Fig. 54.

110

We have laid out in this section the foundations of a first-principle homogenization theory to properly define quasi-local effective constitutive parameters for a periodic array of magnetodielectric and conducting inclusions. We have shown that a proper and rigorous description of the wave interaction in metamaterial arrays requires taking into account weak spatial dispersion effects and magneto-electric coupling within the lattice, even in the long-wavelength limit and for center-symmetric inclusions. In this context, we have derived closed-form analytical formulas for the rigorously defined effective constitutive relations of an arbitrary metamaterial array, highlighting the limitations of commonly used models that neglect these effects. Although our theory is very general, the numerical results presented here are focused on isotropic metamaterial arrays, lossless materials and eigen-modal propagation, in order to better highlight the specific effects of spatial dispersion, above all in the transition between different eigen-modal regions, in the long-wavelength limit. We have highlighted in our calculations the effects of neglecting spatial and frequency dispersion in the interaction constants and in the constitutive models of metamaterials formed by magnetodielectric and conducting spheres, which may cause severe artifacts and divergence from the first-principle effective parameters of the metamaterial. We believe that these results may be fundamental for a proper description of artificial materials with nonconventional properties in complex environments, for their realistic applications in practical devices of interest to the U.S. Air Force.

8. General Conclusions

We have reported here a series of basic research results as the outcome of our extensive efforts sponsored by the U.S. Air Force Research Laboratory with Contract No. FA8718-09-C-0061. We have focused in this report on the most relevant aspects of our findings, and in particular on guided and leaky-wave modes along linear arrays of nanoparticles, also considering and modeling the realistic presence of technological disorder, comparison of the guidance properties along linear and planar arrays of nanoparticles and nanovoids in different realistic geometries, guided and leaky modes along parallel arrays of nanoparticles, propagation along periodic arrays of nanoparticles and their rigorous homogenization as metamaterials and nonconventional artificial materials. We believe that these findings may be of significant importance to realize novel optical devices and exotic materials for a variety of applications of interest to the U.S. Air Force. A complete overview of our results may be found in the series of papers we have published during this effort, as reported in the following section.

9. Scientific Publications

a. Journal Papers

J1.   A. Alù, **"First-Principle Homogenization Theory for Periodic Metamaterial Arrays,"** Physical Review B, under review, online at: http://arxiv.org/abs/1012.1351.

J2.   X. X. Liu, and A. Alù, **"Homogenization of Quasi-Isotropic Metamaterials Composed of Dense Arrays of Magnetodielectric Spheres,"** Metamaterials, Special Issue for Metamaterials'2010, in press, (*invited paper*).

J3. X X. Liu, and A. Alù, ***"Limitations and Potentials of Metamaterial Lenses,"*** Journal of Nanophotonics, Special Issue on Subwavelength Imaging, in press, (*invited paper*).

J4. A. Alù, and N. Engheta, ***"Optical Metamaterials Based on Optical Nanocircuits,"*** Proceedings of IEEE, in press, (*invited paper*).

J5. J. T. Costa, M. G. Silveirinha, and A. Alù, ***"Poynting Vector in Negative-Index Metamaterials,"*** Physical Review B, Vol. 83, No. 16, 165120, April 19, 2011.

J6. A. Alù, G. D'Aguanno, N. Mattiucci, and M. Bloemer, ***"Plasmonic Brewster Angle: Broadband Extraordinary Transmission through Optical Gratings,"*** Physical Review Letters, Vol. 106, No. 12, 123902, March 23, 2011.

J7. A. Alù, P. A. Belov, and N. Engheta, ***"Coupling and Guided Propagation along Parallel Chains of Plasmonic Nanoparticles,"*** New Journal of Physics, Vol. 13, 033026 (23 pages), March 18, 2011, also in Virtual Journal of Nanoscale Science & Technology.

J8. A. Alù, ***"Restoring the Physical Meaning of Metamaterial Constitutive Parameters,"*** Physical Review B, Rapid Communications, Vol. 83, No. 8, 081102(R) (4 pages), February 17, 2011, online at: http://arxiv.org/abs/1012.1353.

J9. A. Alù, and N. Engheta, ***"Emission Enhancement in a Plasmonic Waveguide at Cut-Off,"*** Materials, Special Issue on Next Wave of Metamaterials, Vol. 4, No. 1, pp. 141-152, January 4, 2011, (*invited feature paper*).

J10. P. Y. Chen, and A. Alù, ***"Optical Nanoantenna Arrays Loaded with Nonlinear Materials,"*** Physical Review B, Vol. 82, 235405 (6 pages), December 2, 2010.

J11. X. X. Liu, and A. Alù, ***"Sub-Wavelength Leaky-Wave Optical Nanoantennas: Directive Radiation from Linear Arrays of Plasmonic Nanoparticles,"*** Physical Review B, Vol. 82, No. 14, 144305 (12 pages), October 20, 2010.

J12. A. Alù, and N. Engheta, ***"Comparison of Waveguiding Properties of Plasmonic Voids and Plasmonic Waveguides,"*** Journal of Physical Chemistry C, Special Issue for Martin Moskovits, Vol. 114, No. 16, pp 7462–7471, April 5, 2010, (*invited paper*).

J13. A. Alù, and N. Engheta, ***"Effect of Small Random Disorders and Imperfections on the Performance of Arrays of Plasmonic Nanoparticles,"*** New Journal of Physics, Vol. 12, 013015 (12 pages), January 18, 2010, also in Virtual Journal of Nanoscale Science & Technology, Vol. 21, No. 8, February 22, 2010.

b. *Book Chapters*

B1. A. Alù, and N. Engheta, ***"Optical Wave Interaction with Two-Dimensional Arrays of Plasmonic Nanoparticles,"*** in Structured Surfaces as Optical Metamaterials, A. A. Maradudin, ed., Cambridge University Press, in press.

c. Conference Papers and Abstracts

C1. X. X. Liu, and A. Alù, ***"Leaky-wave Radiation From Subwavelength Metamaterial or Plasmonic Arrays,"*** in Proceedings of the 5th European Conference on Antennas and Propagation, Roma, Italy, April 11-15, 2011, *(invited talk).*

C2. Y. Zhao, and A. Alù, ***"Broadband Circular Polarizer Formed by Stacked Plasmonic Metasurfaces,"*** in Proceedings of SPIE Photonics West, San Francisco, CA, USA, January 22-27, 2011, *(invited talk).*

C3. A. Alù, A. Yaghjian, and R. A. Shore, ***"Causality Relations in the Homogenization of Electromagnetic Metamaterials,"*** in Proceedings of 2011 Electromagnetics Contractor Meeting, San Antonio, TX, January 4-6, 2011, *(invited talk).*

C4. A. Alù, ***"Spatial and Frequency Dispersion Effects in the Homogenization of Metamaterial Arrays,"*** in Proceedings of Metamaterials 2010, Karlsruhe, Germany, September 16-19, 2010, *(invited talk).*

C5. A. Alù, and N. Engheta, ***"Electromagnetic Modeling and Limitations in the Homogenization of Metamaterials and Metasurfaces,"*** in Proceedings of Metamaterials 2010, Karlsruhe, Germany, September 16-19, 2010, *(invited talk).*

C6. P. Y. Chen, and A. Alù, ***"Optical Metamaterials and Metasurfaces Formed by Nanoantennas Loaded by Nonlinear Materials,"*** in Proceedings of Metamaterials 2010, Karlsruhe, Germany, September 16-19, 2010.

C7. A. Alù, and N. Engheta, ***"Extremely Anisotropic Boundary Conditions and Their Optical Applications,"*** in Proceedings of URSI Commission B Electromagnetic Theory Symposium 2010, Berlin, Germany, August 16-19, 2010, *(invited talk).*

C8. A. Alù, ***"Optical Leaky-Wave Nanoantenna: Complex Modes along Linear Arrays of Plasmonic Nanoparticles,"*** in Proceedings of URSI Commission B Electromagnetic Theory Symposium 2010, Berlin, Germany, August 16-19, 2010, *(invited talk).*

C9. A. Alù, and N. Engheta, ***"Homogenization of 2D and 3D Sub-diffractive Arrays of Plasmonic Nanoparticles,"*** in Proceedings of CNC/USNC/URSI Radio Science Meeting, Toronto, Canada, July 11-17, 2010, *(invited talk).*

C10. X. X. Liu, and A. Alù, ***"Plasmonic Low-Profile Nanoantenna Reflectors,"*** in Proceedings of 2010 IEEE International Symposium on Antennas and Propagation, Toronto, Canada, July 11-17, 2010.

C11. A. Alù, ***"Contribution of Higher-Order Multipole Radiation to Spatial Dispersion and Radiation Losses in Metamaterials,"*** in Proceedings of Progress in Electromagnetics Research Symposium 2010, Cambridge, MA, USA, July 5-8, 2010, *(invited talk).*

C12. A. Alù, ***"Metamaterial Antennas: From Radio to THz and Optical Frequencies,"*** in Proceedings of Tri-Service Metamaterials 2009, Atlanta, GA, U.S.A., December 8-10, 2009.

10. References

[1]   N. Engheta, and R. W. Ziolkowski (editors), Electromagnetic Metamaterials: Physics and Engineering Explorations, John Wiley & Sons, New York, 2006.

[2]   M. V. Gorkunov, S. A. Gredeskul, I. V. Shadrivov, and Y. S. Kivshar, *Phys. Rev. E* **73**, 056605 (2006).

[3]   K. Aydin, K. Guven, N. Katsarakis, C. M. Soukoulis, and E. Ozbay, *Opt. Expr.*, **12**, 5896 (2004).

[4]   L. Jylha, I. Kolmakov, S. Maslovski, and S. Tretyakov, *J. Appl. Phys.* **99**, 043102 (2006).

[5]   S. Mookherjea, and A. Oh, *Opt. Lett.* **32**, 289 (2007).

[6]   M. V. Gorkunov, S. A. Gredeskul, I. V. Shadrivov, and Y. S. Kivshar, Phys. Rev. E **73**, 056605 (2006).

[7]   A. Alù, and N. Engheta, Digest of IEEE Antennas and Propagation Society (AP-S) International Symposium, Honolulu, Hawaìi, USA, June 10-15, 2007, pp. 2897-2900, IEEE Press, (2007).

[8]   P. A. Belov, and C. Simovski, *Phys. Rev. E* **72**, 026615 (2005).

[9]   A. Alù, and N. Engheta, *Phys. Rev. B* **74**, 205436 (2006).

[10]   A. Alù, and N. Engheta, *Phys. Rev. B* **75**, 024304 (2007).

[11]   M. Rusek, J. Mostowski, and A. Orłowski, *Phys. Rev. A* **61**, 022704 (2000).

[12]   M. Rusek, and A. Orłowski, *Phys. Rev. E* **59**, 3655 (1999).

[13]   M. Rusek, A. Orłowski, and J. Mostowski, *Phys. Rev. E* **56**, 4892 (1997).

[14]   H. Benisty, D. Labilloy, C. Weisbuch, C. J. M. Smith, T. F. Krauss, D. Cassagne, A. Beraud, and C. Jouanin, *Appl. Phys. Lett.* **76**, 532 (2000).

[15]   L. C. Andreani, and D. Gerace, *Phys. Rev. B* **73**, 235114 (2006).

[16]   J. Bertolotti, M. Galli, R. Sapienza, M. Ghulinyan, S. Gottardo, L. C. Andreani, L. Pavesi, and D. S. Wiersma, *Phys. Rev. E* **74**, 0356029(R) (2006).

[17]   S. A. Tretyakov, and A. J. Vitanen, *Electrical Engineering* **82**, 353 (2000).

[18]   A. D. Yaghjian, *IEEE Trans. Antennas Propagat.* **50**, 1050 (2002).

[19]   W. H. Weber, and G. W. Ford, *Phys. Rev. B* **70**, 125429 (2004).

[20]   R. A. Shore, and A. D. Yaghjian, *Electron. Lett.* **41**, 578 (2005).

[21]   R. A. Shore, and A. D. Yaghjian, *IEICE Trans. Commun.* **E88-B**, 2346 (2005).

[22]   C. R. Simovski, A. J. Viitanen, and S. A. Tretyakov, *Phys. Rev. E* **72**, 066606 (2005).

[23]   A. F. Koenderink, and A. Polman, *Phys. Rev. B* **74**, 033402 (2006).

[24]   L. Lewin, *Polylogarithms and Associated Functions* (New York, Elsevier North-Holland, 1981).

[25]   P. B. Johnson and R. W. Christy, *Phys. Rev. B* **6**, 4370 (1972).

[26]   CST Studio Suite 2006B, www.cst.com.

[27]   P. B. Johnson, and R. W. Christy, Phys. Rev. B 6, 4370 (1972).

[28]   C. F. Bohren and D. R. Huffman, Absorption and Scattering of Light by Small Particles (Wiley, New York, 1983).

[29]   M. Quinten, A. Leitner, J. R. Krenn, F. R. Aussenegg, Opt. Lett. 23, 1331 (1998).

[30]   S. A. Tretyakov, and A. J. Vitanen, Electrical Engineering 82, 353 (2000).

[31]   M. L. Brongersma, J. W. Hartman, and H. A. Atwater, Phys. Rev. B 62, 16356 (2000).

[32]   S. K. Gray, and T. Kupka, Phys. Rev. B 68, 045415 (2003).

[33]   R. Arias, and D. L. Mills, Phys. Rev. B 68, 245420 (2003).

[34]   S. Y. Park, and D. Stroud, Phys. Rev. B 69, 125418 (2004).

[35]   W. H. Weber, and G. W. Ford, Phys. Rev. B 70, 125429 (2004).

[36] R. A. Shore, and A. D. Yaghjian, Electronics Letters 41, 578 (2005).

[37] R. A. Shore, and A. D. Yaghjian, IEICE Trans. Commun. E88-B, 2346 (2005).

[38] A. F. Koenderink, and A. Polman, Phys. Rev. B 74, 033402 (2006).

[39] A. Alù, and N. Engheta, Phys. Rev. B 74, 205436 (2006).

[40] A. Alù, and N. Engheta, Phys. Rev. B 75, 024304 (2007).

[41] A. Alù, and N. Engheta, Radio Science 43, RS4S01 (2008).

[42] S. Coyle, M. C. Netti, J. J. Baumberg, M. A. Ghanem, P. R. Birkin, P. N. Bartlett, and D. M. Whittaker, Phys. Rev. Lett. 87, 176801 (2001).

[43] H. T. Miyazaki, and H. T. Miyazaki, Phys. Rev. Lett. 96, 097401 (2006).

[44] Y. Kurokawa, and H. T. Miyazaki, Phys. Rev. B 75, 035411 (2007).

[45] F. J. Garcıa de Abajo, G. Gomez-Santos, L. A. Blanco, A. G. Borisov, and S.V. Shabanov, Phys. Rev. Lett. 95, 067403 (2005).

[46] F. J. Garcia de Abajo, "Light scattering by particle and hole arrays," Rev. Mod. Phys. 79, 1267-1290 (2007).

[47] T. A. Kelf, Y. Sugawara, J. J. Baumberg, M. Abdelsalam and P. N. Bartlett, Phys. Rev. Lett. 95, 116802 (2005).

[48] T. V. Teperik V. V. Popov, and F. J. García de Abajo, Phys. Rev. B 71, 085408 (2005).

[49] L. Chen, J. Shakya, and M. Lipson, Opt. Lett. 31, 2133 (2006).

[50] G. Gantzounis, and N. Stefanou, Phys. Rev. B 74, 085102 (2006).

[51] T. A. Kelf, Y. Sugawara, R. M. Cole, J. J. Baumberg, M. E. Abdelsalam, S. Cintra, S. Mahajan, A. E. Russell, and P. N. Bartlett, Phys. Rev. B 74, 245415 (2006).

[52] K. Y. Kim, Y. K. Cho, H. S. Tae, and J. H. Lee, Opt. Expr. 14, 320 (2006).

[53] H. T. Miyazakia, and Y. Kurokawa, Appl. Phys. Lett. 89, 211126 (2006).

[54] T. V. Teperik, V. V. Popov, F. J. García de Abajo, M. Abdelsalam, P. N. Bartlett, T. A. Kelf, Y. Sugawara, and J. J. Baumberg, Opt. Expr. 14, 1965 (2006).

[55] P. B. Catrysse, H. Shin, and S. Fan, J. Vac. Sci. Technol. B 23, 2675 (2005).

[56] A. Alù, and N. Engheta, J. Opt. Soc. Am. B 23, 571 (2006).

[57] C. Enkrich, M. Wegener, S. Linden, S. Burger, L. Zschiedrich, F. Schmidt, J. F. Zhou, Th. Koschny, and C. M. Soukoulis, Phys. Rev. Lett. 95, 203901 (2005).

[58] J. Zhou, T. Koschny, M. Kafesaki, E. N. Economou, J. B. Pendry, and C. M. Soukoulis, Phys. Rev. Lett. 95, 223902 (2005).

[59] A. Alù, A. Salandrino, and N. Engheta, Opt. Expr. 14, 1557 (2006).

[60] G. Shvets and Y. A. Urzhumov, J. Opt. A: Pure Appl. Opt. 8, S122 (2006).

[61] C. R. Simovski, A. J. Vitanen, and S. A. Tretyakov, "Resonator mode in chains of Silver spheres and its possible application," Physical Review E, vol. 72, 066606 (2005).

[62] C. R. Simovski, A. J. Vitanen, and S. A. Tretyakov, "A resonator mode in linear arrays of silver spheres and cylinders," J. Zhejiang Univ. Science A, vol. 7, no. 1, pp. 29-33 (2006).

[63] A. Karalis, E. Lidorikis, M. Ibanescu, J. D. Joannopoulos, and M. Solja, Phys. Rev. Lett. 95, 063901 (2005).

[64] N. Engheta, A. Salandrino, and A. Alù, Phys. Rev. Lett. 95, 095504 (2005).

[65] A. Alù, and N. Engheta, "Effect of Small Random Disorders and Imperfections on the Performance of Arrays of Plasmonic Nanoparticles," New Journal of Physics 12, 013015 (2010).

[66] L. J. Chu, J. Appl. Phys. 19, 1163 (1948).

[67] A. Alù, and N. Engheta, J. Appl. Phys. 97, 094310 (2005).

[68] L. Lewin, Polylogarithms and Associated Functions (New York, Elsevier North-Holland, 1981).

[69] G. V. Eleftheriades, and K. G. Balmain (eds.), Negative-Refraction Metamaterials (IEEE Press, 2005).

[70] L. Landau, and E. M. Lifschitz, Electrodynamics of Continuous Media (Pergamon Press, Oxford, UK, 1984).

[71] P. T. B. Shaffer, "Refractive Index, Dispersion, and Birefringence of Silicon Carbide Polytypes," Appl. Opt 10, 1034-1036 (1971).

[72] J. Takahara, S. Yamagishi, H. Taki, A. Morimoto, and T. Kobayashi, Opt. Lett. 22, 475-477.

[73] P. Belov and C. Simovski, Phys. Rev. E 72, 026615 (2005).

[74] K. B. Crozier, A. Sundaramurthy, G. S. Kino, and C. F. Quate , J. Appl. Phys. 94, 4632 (2003).

[75] P. J. Schuck, D. P. Fromm, A. Sundaramurthy, G. S. Kino, and W. E. Moerner, Phys. Rev. Lett. 94, 017402 (2005).

[76] C. E. Talley, J. B. Jackson, C. Oubre, N. K. Grady, C. W. Hollars, S. M. Lane, T. R. Huser, P. Nordlander, N. J. Halas., Nano Lett. 5, 1569 (2005).

[77] P. Mühlschlegel, H.-J. Eisler, O. J. F. Martin, B. Hecht, D. W. Pohl, Science 308, 1607 (2005).

[78] L. Novotny, Phys. Rev. Lett. 98, 266802 (2007).

[79] J. B. Lassiter, J. Aizpurua, L. I. Hernandez, D. W. Brandl, I. Romero, S. Lal, J. H. Hafner, P. Nordlander, and N. J. Halas, Nano Lett. 8, 1212 (2008).

[80] M. Schnell, A. García-Etxarri, A. J. Huber, K. Crozier, J. Aizpurua and R. Hillenbrand, Nat. Photon. 3, 287 (2009).

[81] A. Alù and N. Engheta, Phys. Rev. Lett. 101, 043901 (2008).

[82] Alu, A. and N. Engheta, Nat. Photon. 2, 307 (2008).

[83] R. E. Collin and F. J. Zucker, Antenna Theory, (McGraw-Hill, New York, 1969).

[84] D. R. Jackson, A. A. Oliner, "Leaky-Wave Antennas," in Modern Antenna Handbook, Ch. 7, 2008.

[85] P. Lampariello, F. Frezza, and A. A. Oliner, IEEE Trans. Microwave Theory Tech. 38, 1831 (1990).

[86] A. Lai, T. Itoh, and C. Caloz, IEEE Microw. Mag. 5, 34 (2009).

[87] L. Lei, C. Caloz, and T. Itoh, Electr. Lett. 38, 1414 (2002).

[88] L. Sungjoon, C. Caloz, and T. Itoh, IEEE Microw. Wireless Compon. Lett. 14, 183 (2004).

[89] S. A. Maier, M. L. Brongersma, P. G. Kik, S. Meltzer, A. A. G. Requicha, and H. A. Atwater, Adv. Mater. 13, 1501 (2001).

[90] R. A. Shore, and A.D. Yaghjian, Electr. Lett. 41, 578 (2005).

[91] W. H. Weeber, and G. W. Ford, Phys. Rev. B 70, 125429 (2004).

[92] R. A. Shore, and A. D. Yaghjian, IEICE Trans. Commun. E88-B, 2346 (2005).

[93] S. A. Maier, P. G. Kik, H. A. Atwater, S. Meltzer, E. Harel, B. E. Koel and A. A. G. Requicha, Nat. Mater. 2, 229 (2003).

[94] M. Quinten, A. Leitner, J. R. Krenn, F. R. Aussenegg, Opt. Lett., 23, 1331 (1998).

[95] M. L. Brongersma, J.W. Hartman, and H.A. Atwater, Phys. Rev. B 62, R16356 (2000).

[96] A. L. Aden, and M. Kerker, J. Appl. Phys. 22, 1242 (1951).

[97] J. R. Krenn, M. Salerno, N. Felidj, B. Lamprecht, G. Schider, A. Leitner, F. R. Aussenegg, J. C. Weeber, A. Dereux & J. P. Goudonnet, J. Microscopy 202, 122 (2001)

[98] S. A. Maier, P. G. Kik, and H. A. Atwater, Phys. Rev. B 67, 205402 (2003).

[99] A. Alù, and N. Engheta, in Negative Refraction Metamaterials: Fundamental Properties and Applications, G. V. Eleftheriades, and K. G. Balmain, eds., Ch. 9, pp. 339-380, IEEE Press, John Wiley & Sons Inc., Hoboken, New Jersey, 2005.

[100] A. Alu, and N. Engheta, Phys. Rev. B 74, 205436 (2006).

[101] J. Hu, and C. R. Menyuk, Adv. Opt. Photon. 1, 58 (2009).

[102] H. Limin, C. Jung-Chih, and M.P. De Lisio, IEEE Trans. Antennas Propag. 48, 1769 (2000).

[103] C. Pi-Wei, L. C Sae, and V. Nalbandian, IEEE Trans. Antennas Propag. 50, 832 (2002).

[104] W. Hong, T.-L. Chen, C.-Y. Chang, J.-W. Sheen, Y.-D. Lin, Broadband tapered microstrip leaky-wave antenna. IEEE Trans. Antennas Propag. 51, 1922 (2003).

[105] A. Drezet, A. Hohenau, A. L. Stepanov, H. Ditlbacher, B. Steinberger, N. Galler, F. R. Aussenegg, Appl. Phys. Lett. 89, 091117 (2006).

[106] J. J. Burke, G. I. Stegeman and T. Tamir, Phys. Rev. B 33, 5186 (1986)

[107] A. Bouhelier, Th. Huser, H. Tamaru, H.-J. Guntherodt, and D. W. Pohl, Phys. Rev. B 63, 155404 (2001),

[108] A. Alù, and N. Engheta, Phys. Rev. Lett. 104, 213902 (2010).

[109] J. Li, A. Salandrino, N. Engheta, Phys. Rev. B 79, 195104 (2009).

[110] A. G. Curto, G. Volpe, T. H. Taminiau, M. P. Kreuzer, R. Quidant, and N. F. van Hulst. Science 329, 930 (2010).

[111] S. Ghadarghadr, Z. Hao, and H. Mosallaei, Opt. Express 17, 18556 (2009).

[112] A. Ahmadi, S. Ghadarghadr, and H. Mosallaei, Opt. Express 18, 123 (2010).

[113] R. A. Shore, and A. Yaghjian, Complex waves on 1D, 2D, and 3D periodic arrays of lossy and lossless magnetodielectric spheres. AFRL-RY-HS-TR-2010-0019 in-house report, May 2010.

[114] S. A. Tretyakov, Analytical Modeling in Applied Electromagnetics, Artech House (2003).

[115] S. A. Tretyakov, and A. J. Viitanen, Electr. Eng. 82, 35 (2000).

[116] L. Lewin, Polylogarithms and Associated Functions, (New York: Elsevier, 1981).

[117] J. E. Sipe, and J.V. Kranendonk, Phys. Rev. A 9, 1806 (1974).

[118] O. Zhuromskyy, O. Sydoruk, E. Shamonina, and L. Solymar, J. Appl. Phys. 106, 104908 (2009).

[119] As it follows from the properties of leaky modes[83]-[84], these forward modes are inherently improper, since they grow in the transverse direction away from the array axis. Although this would violate the radiation condition for infinite arrays, these eigenmodes indeed dominate the far-field pattern of finite arrays for small $\text{Im}\left[\bar{\beta} \right]$.

[120] J. A. Dionne, L. A. Sweatlock, H. A. Atwater,, and A. Polman, Phys. Rev. B 72, 075405 (2005).

[121] A. Hohenau, A. Drezet, M. Weißenbacher, F. R. Aussenegg, and J. R. Krenn, Phys Rev B 78, 155405 (2008).

[122] A. Alù, and N. Engheta, Phys. Rev. B 75, 024304 (2007).

[123] In analogy with Refs. [119] and in agreement with Ref. [83]-[84], these backward modes are inherently proper, since they decay in the transverse direction away from the array axis. These may be considered proper physical eigensolutions of the array even in the limit of infinite geometries.

[124] R. E. Collin, Field Theory of Guided Waves, IEEE Press (1991).

[125] L. D. Landau, E. M. Lifshitz, and L. P. Pitaevskii, Electrodynamics of Continuous Media, (Oxford: Butterworth-Heinemann, 1982).

[126] S. A. Maier, P. E. Barclay, T. J. Johnson, M. D. Friedman, and O. Painter, Appl. Phys. Lett. 84, 3990 (2004).

[127] S. A. Maier, P. G. Kik, and H. A. Atwater, Appl. Phys. Lett. 81, 1714 (2002).

[128] E. Palik, Handbook of Optical Constants of Solids. (New Yotk: Academic Press, 1985).

[129] CST Design StudioTM 2009.

[130] P. B. Johnson and R.W. Christy, Phys. Rev. B 6, 4370 (2009).

[131] M. Quinten, A. Leitner, J. R. Krenn, F. R. Aussenegg, "Electromagnetic energy transport via linear chains of silver nanoparticles", Opt. Lett 23, 1331-1333 (1998).

[132] S. A. Tretyakov, and A. J. Viitanen, "Line of periodically arranged passive dipole scatterers," Electr. Engin. 82, 353-361 (2000).

[133] M. L. Brongersma, J. W. Hartman, and H. A. Atwater, "Electromagnetic energy transfer and switching in nanoparticle chain arrays below the diffraction limit," Phys. Rev. B 62, 16356-16359 (2000).

[134] S. A. Maier, P. G. Kik, H. A. Atwater, S. Meltzer, E. Harel, B. E. Koel, and A. A. G. Requicha, "Local detection of electromagnetic energy transport below the diffraction limit in metal nanoparticle plasmon waveguides," Nature Materials 2, 229-232 (2003).

[135] S. K. Gray, and T. Kupka, "Propagation of light in metallic nanowire arrays: finite-difference time-domain studies of silver cylinders," Phys. Rev. B 68, 045415 (2003).

[136] R. A. Shore, and A. D. Yaghjian, "Travelling electromagnetic waves on linear periodic arrays of lossless spheres," Electron. Lett. 41, 578-579 (2005).

[137] A. J. Viitanen, and S. A. Tretyakov, "Metawaveguides formed by arrays of small resonant particles over a ground plane," J. Opt. A: Pure Appl. Opt. 7, S133-S140 (2005).

[138] A. F. Koenderink, and A. Polman, Phys. Rev. B 74, 033402 (2006).

[139] A. F. Koenderink, Nano Letters 9, 4228 (2009).

[140] A. Alù, and N. Engheta, "Theory of linear chains of metamaterial/plasmonic particles as sub-diffraction optical nanotransmission lines," Phys. Rev. B 74, 205436 (2006).

[141] A. Alù, and N. Engheta, "Effect of Small Random Disorders and Imperfections on the Performance of Arrays of Plasmonic Nanoparticles," N. J. Phys. 12, 013015 (2010).

[142] A. Alù, and N. Engheta, "Comparison of Waveguiding Properties of Plasmonic Voids and Plasmonic Waveguides," J. Phys. Chem. C 114, 7462–7471 (2010).

[143] A. Alù, P. A. Belov, and N. Engheta, "Parallel-chain optical transmission line for a low-loss ultraconfined light beam," Phys. Rev. B 80, 113101 (2009).

[144] N. Engheta, A. Salandrino, and A. Alù, "Circuit elements at optical frequencies: nano-inductors, nano-capacitors and nano-resistors," Phys. Rev. Lett. 95, 095504 (2005).

[145] N. Engheta, "Circuits with light at nanoscales: optical nanocircuits inspired by metamaterials," Science 317, 1698-1702 (2007).

[146] A. Alù, and N. Engheta, "Optical nano-transmission lines: synthesis of planar left-handed metamaterials in the infrared and visible regimes," J. Opt. Soc. Am. B 23, 571-583 (2006).

[147] A. Alù, and N. Engheta, "Guided propagation along quadrupolar chains of plasmonic nanoparticles," Phys. Rev. B 79, 235412 (2009).

[148] J. A. Porto, P. Johansson, S. P. Apell, and T. Lopez-Rıos, Phys. Rev. B 67, 085409 (2003).

[149] L. Lewin, Polylogarithms and Associated Functions, New York, Elsevier North-Holland, 1981.

[150] X. X. Liu, and A. Alù, "Sub-wavelength leaky-wave optical nanoantennas: directive radiation from linear arrays of plasmonic nanoparticles," Phys. Rev. B 82, 144305 (2010).

[151] J. Takahara, S. Yamagishi, H. Taki, A. Morimoto, and T. Kobayashi, "Guiding of a one-dimensional optical beam with nanometer diameter," Optics Lett. 22, 475-477 (1997).

[152] A. Alù, and N. Engheta, "Anomalies of sub-diffractive guided-wave propagation along metamaterial nanocomponents," Radio Sci. 42. RS6S17 (2007).

[153] P. B. Johnson, and R. W. Christy, "Optical constants of noble metals," Phys. Rev. B 6, 4370-4379 (1972).

[154] R. E. Collin, F. J. Zucker, Antenna Theory, Part II (McGraw Hill, 1961).

[155] P. Ewald, Ann. Phys. 64, 253 (1921).

[156] J. van Kranendonk, and J. E. Sipe, in Foundations of the Microscopic Electromagnetic Theory of Dielectric Media, E. Wolf, ed., Progress in Optics (North Holland, New York, 1977).

[157] V. M. Shalaev, Phys. Rep. 272, 61 (1996).

[158] R. E. Collin, Field Theory of Guided Waves, IEEE, 1990.

[159] S. A. Tretyakov, Analytical Modeling in Applied Electromagnetics, Artech House, 2002.

[160] A. Sihvola, Electromagnetic Mixing Formulas and Applications, IEE Press, 1999.

[161] N. Engheta, and R. W. Ziolkowski (eds.), Electromagnetic Metamaterials: Physics and Engineering Explorations, John Wiley and Sons, New York, 2006.

[162] C. R. Simovski, Opt. and Spectroscopy 107, 726 (2009).

[163] C. R. Simovski, and S. A. Tretyakov, Phys. Rev. B 75, 195111 (2007).

[164] C. R. Simovski, Metamaterials 1, 62 (2007).

[165] D. R. Smith, Phys. Rev. E 81, 036605 (2010).

[166] A. D. Scher, and E. Kuester, Metamaterials 3, 44 (2009).

[167] C. R. Simovski, and S. He, Phys. Lett. A 311, 254 (2003).

[168] P. A. Belov, and C. R. Simovski, Phys. Rev. B 72, 026615 (2005).

[169] A. Alù, and N. Engheta, Phys. Rev. B 75, 024304 (2007).

[170] C. R. Simovski, AEU, Int. Journal Electron. Communicat. 52, 76 (1998).

[171] C. L. Holloway, E. F. Kuester, J. Baker-Jarvis, and P. Kabos, IEEE Trans. Antennas Propagat. 51, 2596 (2003).

[172] C. R. Simovski, P. Belov, and S. He, IEEE Trans. Antennas Propagat. 51, 2582 (2003).

[173] R. A. Shore, and A. Yaghjian, Radio Science 42, RS6S21 (2007).

[174] J. Li, and J. B. Pendry, arxiv:cond-mat/0701332.

[175] C. Fietz, and G. Shvets, Physica B 405, 2930 (2010).

[176] M. G. Silveirinha, Phys. Rev. B 76, 245117 (2007).

[177] M. G. Silveirinha, Phys. Rev. B 75, 115104 (2007).

[178] M. G. Silveirinha, J. D. Baena, L. Jelinek, and R. Marques, Metamaterials 3, 115 (2009).

[179] M. G. Silveirinha, and P. A. Belov, Phys. Rev. B 77, 233104 (2008).

[180] S. O'Brien, and J. B. Pendry, J. Phys.: Condens. Matter 14, 6383 (2002).

[181] T. Koschny, P. Markos, D. R. Smith, and C. M. Soukoulis, Phys. Rev. E 68, 065602 (2003).

[182] D. R. Smith, D. C. Vier, T. Koschny, and C. M. Soukoulis, Phys. Rev. E 71, 036617 (2005).

[183] L. Landau, E. Lifschitz, Electrodynamics of Continuous Media (Butterworth-Heinemann, 1984).

[184] A. Alù, Phys. Rev. B 83, 081105(R) (2011).

[185] V. Agranovich and V. Ginzburg, Spatial Dispersion in Crystal Optics and the Theory of Excitons (Willey-Interscience, New York, 1966).

[186] P. A. Belov, R. Marqués, S. I. Maslovski, I. S. Nefedov, M. Silveirinha, C. R. Simovski, and S. A. Tretyakov, Phys. Rev. B, Vol. 67, 113103 (2003).

[187] Here and in the following we refer to microscopic quantities as those locally varying in space, before any form of spatial averaging, in contrast to the macroscopic quantities that are obtained after averaging. In the definition of microscopic quantities, a first level of homogenization is implicit, which allows defining local fields, neglecting their variations at the atomic or molecular scale in the materials composing the inclusions. We can safely assume that these variations can be homogenized following standard macroscopic electromagnetic theory, since the atomic scale is several orders of magnitude smaller than the typical field variations considered here.

[188] J. van Bladel, Electromagnetic Fields, (IEEE Press, 2nd Ed., Hoobken, NJ, 2007).

[189] A. D. Yaghjian, Proc. IEEE 68, 248 (1980).

[190] P. A. Belov, S. I. Maslovski, K. R. Simovski, and S. A. Tretyakov, Techn. Phys. Lett. 29, 718 (2003).

[191] R. Marques, F. Medina, and R. Rafii-El-Idrissi, Phys. Rev. B 65, 144440 (2002).

[192] S. Enoch, G. Tayeb, and B. Gralak, IEEE Trans. Antennas Propagat. 51, 2659 (2003).

[193] A. Alù, M. G. Silveirinha, A. Salandrino, and N. Engheta, Phys. Rev. B 75, 155410 (2007).

[194] M. G. Silveirinha, and N. Engheta, Phys. Rev. Lett. 97, 157403 (2006).

[195] A. Alù, M. G. Silveirinha, and N. Engheta, Phys. Rev. E 78, 016604 (2008).

[196] R. W. Ziolkowski, Phys. Rev. E 70, 046608 (2004).

[197] M. G. Silveirinha, and N. Engheta, Phys. Rev. B 75, 075119 (2007).

[198] A. Alù, and N. Engheta, Opt. Expr. 15, 13773 (2007).

[199] M. G. Silveirinha, A. Alù, J. Li, and N. Engheta, J. Appl. Phys. 103, 064305 (2008).

[200] A. Alù, and N. Engheta, J Appl Phys. 97, 094310 (2005).

[201] E. N. Economou, Th. Koschny, and C. M. Soukoulis, Phys. Rev. B 77, 092401 (2008).